SEARCH FOR THE $R(3520)$ CRYPTO-EXOTIC STATE AT *BABAR*

A thesis submitted for the degree of Doctor of Philosophy
Brunel University

by
Daniel Sherwood

School Of Engineering
Brunel University

· June 2008 ·

Abstract

Motivated by the recent discoveries of exotic and possible crypto-exotic states, presented in this thesis is an inclusive search for the production of a crypto-exotic baryon state called $R(3520)$ with hidden charm in e^+e^- interactions at a centre of mass energy of 10.58 GeV in the data collected at the energy $\Upsilon(4S)$ resonance with the *BABAR* detector using a data set of $228\,\mathrm{fb}^{-1}$. Hints about the existence of the $R(3520)$ state were reported in an analysis of data from a 2m hydrogen bubble chamber experiment at CERN.

Two decay modes of the $R(3520)$ resonance were investigated in this thesis $R(3520) \rightarrow pK^+\pi^-\pi^-K^0_S$ and $R(3520) \rightarrow pK^+\pi^-K^{*-}$. The invariant mass spectra of the two final states were analysed and no evidence for the state was observed. Therefore, Upper limits were set on the differential cross section for the production of the $R(3520)$ as a function of the momentum in the centre of mass frame. Using these differential cross sections the total cross sections were calculated with two different hypotheses for the width of the resonance, $1\,\mathrm{MeV}/c^2$ and $7\,\mathrm{MeV}/c^2$, with the additional assumption that the momentum spectrum for the production of state is flat. The upper limits for the total cross section production of the $R(3520)$ for the decay mode $p\ \pi^-\ \pi^-\ K^+\ K^0_S$ were calculated to be $32\,\mathrm{fb}/\ \mathrm{GeV}/c$ ($48\,\mathrm{fb}\ \ \mathrm{GeV}/c$) with the $1\,\mathrm{MeV}/c^2$ ($7\,\mathrm{MeV}/c^2$) width. For the decay mode $p\ \pi^-\ K^+\ K^{*-}$ the upper limits on the total cross section were $62\,\mathrm{fb}/\ \mathrm{GeV}/c$ ($93\,\mathrm{fb}/\ \mathrm{GeV}/c$) for the $1\,\mathrm{MeV}/c^2$ ($7\,\mathrm{MeV}/c^2$) width hypotheses.

The studies were repeated with the additional requirement that there was an additional antiproton in the event. The invariant mass spectra were analysed and no evidence for the state was found. Therefore, upper limits were calculated on the differential cross sections and the total cross sections for the production of this state. The upper limits for the total cross section production of the $R(3520)$ for the decay mode $p\ \pi^-\ \pi^-\ K^+\ K^0_S$ were calculated to be $25\,\mathrm{fb}/\ \mathrm{GeV}$ ($36\,\mathrm{fb}/\ \mathrm{GeV}$) with the $1\,\mathrm{MeV}/c^2$ ($7\,\mathrm{MeV}/c^2$) width. For the decay mode $p\ \pi^-\ K^+\ K^{*-}$ the upper limits on the total cross section were $62\,\mathrm{fb}/\ \mathrm{GeV}/c$ ($83\,\mathrm{fb}/\ \mathrm{GeV}/c$) for the $1\,\mathrm{MeV}/c^2$ ($7\,\mathrm{MeV}/c^2$) width hypotheses. This shows that the nonobservance of the state was unaffected by the condition that the baryon number was conserved in the event.

The thesis also investigates the feasibility of using a new evolutionary algorithm, Gene Expression Programming, for an event selection problem relevant for the physics analysis presented here. The new methods allowed automatic identification of selection criteria similar to those based on cuts applied on event variables. This showed the feasibility of the new method.

It doesn't matter how beautiful your theory is, it doesn't matter how smart you are. If it doesn't agree with experiment, it's wrong. . . .

Richard Feynman

Contents

List of Figures

List of Tables

Acknowledgements

I would like to acknowledge:

Particle Physics and Astronomy Research Council(PPARC) now part of Science and Technology Facilities Council(STFC) for the opportunity and the funding of this PhD.

Dr. Liliana Teodorescu for her supervision and support.

The *BABAR* Collaboration for being friendly and trying to answer all my naive questions.

The HEP group at Brunel university for listening to me moaning on Fridays and giving me access to a cluster that has been really useful.

My colleagues — Matt for being the font of all *BABAR* related knowledge and Aidan for occasionally deputising. Israel, Neil, Dave, Amir, Jason, Richard, Craig, Amir, Aaron, Cov etc. for the lunches, the football and the occasional Monday night pint.

My family — Mum and Dad for always being on the end of the phone and putting up with my Minuit related mood swings. Holly for her organisational skills, without her not many people would have got presents. Grandma, for the conversations about sausages. Victoria, Laura, Aunty Sue and Uncle David for the pig pong.

My house-mates — Tom and Andrew for being great house-mates and making the last two years or so a lot more bearable.

All my friends, there are too many of you to mention here but you know who you are! Anyway I know the likelihood of you ever reading this is slim! The last four years would not have been the same without you all.

Chapter 1

Introduction

Hadronic spectroscopy is an important field in particle physics as it helps advance the understanding of the fundamental particles from which hadronic matter is comprised and the forces which govern their interactions. Since the discovery of the proton by Rutherford in 1919, well over 150 different hadrons have been discovered. These hadrons are classified as either mesons with a quark-antiquark ($q\,\overline{q}$) composition or baryons ($q\;q\;q$) with a triquark composition. Theoretically they are described by the quark model. However, this model does not limit the permitted states to $q\,\overline{q}$ and $q\;q\;q$ configurations: multi-quark states are permitted. These multiquark states are called exotic and crypto-exotic states. Exotic states are those with manifestly exotic quantum numbers or exotic combinations of quantum numbers which cannot be explained by $q\,\overline{q}$ by $q\;q\;q$ quark configurations. Crypto-exotic states are hadrons which have ordinary quantum numbers but have anomalous external properties such as widths or decay modes.

Whilst the ordinary mesons and baryons are well understood both theoretically and experimentally, there has been very little evidence for exotic or crypto-exotic states. Despite a number of searches over the last four decades, the literature only provides hints of the existence of such states.

Recently, a number of possible exotic or crypto-exotic states, known collectively as the "XYZ" states, have been observed at the B Factory experiments, *BABAR* and BELLE. A number of these states can be interpreted as crypto-exotic states with hidden charm.

There is very little evidence for the existence of crypto-exotic baryonic states. The only evidence is confined to two possible observations in data from bubble chamber experiments. A state with a mass of $3170\,\mathrm{MeV}/c^2$, called the $\Sigma(3170)$, was reported in two independent K^-p bubble chamber experiments at energies of $8.25\,\mathrm{GeV}/c^2$ and $6.5\,\mathrm{GeV}/c^2$. A state with a mass of $3520\,\mathrm{MeV}/c^2$, called the $R(3520)$ was reported in data from the CERN 2m bubble chamber exposed to a pion beam of $16\,\mathrm{GeV}/c^2$ which was found to decay through a K^{*-} resonance.

Motivated by the recent discoveries of exotic/crypto-exotic mesons, a search has been carried out for the $R(3520)$ state in e^+e^- interactions using data from the *BABAR* detector. This study is presented in this thesis.

Two inclusive reactions were studied $e^+e^- \to K^+p\pi^-\pi^-K^0_S\ + X$, $e^+e^- \to K^+p\pi^-K^{*-}\ + X$. In order to ensure that the baryon number was conserved, these inclusive modes were also searched for with the extra requirement that there was an additional baryon in the final state.

Also, a novel event selection method based on a new evolutionary algorithm, called Gene Expression Programming (GEP) was investigated in this thesis. The suitability of the method for the development of event selection criteria in $K^0_S \to \pi^+\pi^-$ decays has been evaluated and the results obtained have been compared with those from two manual optimisation studies. As this method is at an early development stage, it has not been used in the physics analysis of the $R(3520)$ state.

The contribution of the author to the studies presented in this thesis consists of performing the analysis for the searches for the $R(3520)$ in data collected by the *BABAR* collaboration. The Monte Carlo simulated data used in this thesis were also produced by the *BABAR* collaboration. To the GEP analysis, the author contributed by performing the manual optimisation of the selection cuts, and by processing some of the GEP runs described in the text.

This thesis is organised as follows:

Chapter 2 presents an introduction to the topic giving a brief description of the standard model and the quark model, the nature of exotic and crypto-exotic states, and a review of the experimental evidence for these states.

Chapter 3 describes the experimental complex used for this study: the asymmetric energy PEP-II collider and the *BABAR* detector.

Chapter 4 presents the software used for the reconstruction of the events, for particle identification, and Monte Carlo simulation at *BABAR*.

Chapter 5 describes the data sample and the event selection method used in this analysis. Optimisation studies were carried out to find the best selection criteria to select K^0_S and K^{*-} candidates that appear in the decay modes of the $R(3520)$ and are presented in this chapter.

Chapter 6 describes the search for the inclusive production of the $R(3520)$ state, in e^+e^- collisions at an c.m. energy of $10.58\,\mathrm{GeV}/c^2$. The state was reconstructed in two final states — $p\ \pi^-\ \pi^-\ K^+\ K^0_S$ and $p\ \pi^-\ K^+\ K^{*-}$.

Chapter 7 presents calculations of the cross sections of the processes studied. As no evidence for a signal was observed and upper limits were set on the differential cross sections of these processes as a function of the momentum in the c.m. frame, and on the integrated cross section.

Chapter 8 describes the search for the inclusive production of the $R(3520)$ state with an additional $\overline{p}$ in the final state. No evidence for a signal was observed and upper limits were set on the differential cross sections as a function of the momentum in the c.m. frame, and the integrated cross section.

Chapter 9 describes the new method for event selection based on an evolutionary algorithm called Gene Expression Programming.

Chapter 10 summarised the conclusions of this thesis.

Chapter 2

Hadronic spectroscopy — exotic and crypto-exotic states

2.1 Standard Model

Throughout history, mankind has striven to understand the nature of the universe. During this journey, man has uncovered the smaller and smaller building blocks that constitute the observed matter. For example, observations of atoms lead to the discovery that atoms consisted of a nucleus surrounded by orbiting electron. In turn this lead to the discovery that the nucleus was comprised of smaller particles — protons and neutrons. From this, the realisation followed that these nucleons were not fundamental particles but were composed of even smaller particles — the quarks. The quarks are thought to be fundamental. The electrons are also thought to belong to a family of elementary particles — the leptons. Along with these particles of matter, a number of forces that govern how these particles interact with each other have been discovered.

The Standard Model (SM) of particle physics is the current best theory that describes the nature of these particles and the forces which control their interactions. The SM evolves constantly to incorporate new knowledge as it is accumulated. Phenomena that are beyond the standard model today may be incorporated into the standard model tomorrow.

In the SM, all matter is composed from two types of particles, quarks and leptons which are both fermions obeying Fermi-Dirac statistics. Six distinct varieties of leptons have been discovered and their properties are tabulated in Table 2.1. An antimatter partner exists for each of the six types of lepton with an identical mass and opposite charges and quantum numbers.

The second kind of fundamental particle are the quarks which are also available in six different flavours and for each quark there is a corresponding antiquark. Their properties are listed in Table 2.2.

Table 2.1: Properties of the leptons. [1]

Particle Name	Particle Symbol	Spin($\hbar$)	Charge(e)	Mass (MeV/c^2)	Anti-particle
electron	e^-	$\frac{1}{2}$	-1	0.511	e^+
electron neutrino	ν_e	$\frac{1}{2}$	0	$< 3 \times 10^{-6}$	$\bar{\nu_e}$
muon	μm	$\frac{1}{2}$	-1	106	μ^+
muon neutrino	ν_μ	$\frac{1}{2}$	0	< 0.19	$\bar{\nu_\mu}$
tau	τ^-	$\frac{1}{2}$	-1	1780	τ^+
tau neutrino	ν_τ	$\frac{1}{2}$	0	< 18.2	$\bar{\nu_\tau}$

The main difference between quarks and leptons is that quarks can interact via the strong nuclear force whilst the leptons cannot. In addition to an electrical charge, quarks have a strong colour charge. This charge is analogous to the electrical charge but three distinct colour charge states exist which are commonly known as red (r), blue (b) and green (g). Antiquarks carry anti-colour charges of anti-red($\bar{r}$), anti-green($\bar{g}$) or anti-blue($\bar{b}$).

Table 2.2: Properties of the quarks. [1]

Particle Name	Particle Symbol	Spin($\hbar$)	Charge(e)	Mass (GeV/c^2)	Anti-particle
Down	d	$\frac{1}{2}$	$-\frac{1}{3}$	0.003 to 0.007	$\overline{d}$
Up	u	$\frac{1}{2}$	$\frac{2}{3}$	0.0015 to 0.003	$\overline{u}$
Strangeness	s	$\frac{1}{2}$	$-\frac{1}{3}$	0.095 ± 0.025	$\overline{s}$
Charm	c	$\frac{1}{2}$	$\frac{2}{3}$	1.250 ± 0.090	$\overline{c}$
Bottom	b	$\frac{1}{2}$	$-\frac{1}{3}$	4.200 ± 0.070	$\overline{b}$
Top	t	$\frac{1}{2}$	$\frac{2}{3}$	174.2 ± 3.3	$\overline{t}$

Free quarks have never been observed despite many searches. Therefore, it is conjectured that quarks exist only in bound states. Thus, the properties of individual quarks, such as the mass, are difficult to measure and are subject to large errors.

Quarks exist only in colour neutral composite states. There have been searches for coloured states and none have been found. There are states called baryons which are composed from three quarks with different colours (rgb). There are also states called mesons composed from a quark and an antiquark such that the colour and anti-colour cancel out, e.g. ($r\bar{r}$). Anti-baryons are the third configuration and these consist of three antiquarks with different anti-colours.

The forces of nature are found to act as only four fundamental forces — electromagnetic force, gravitational force, the weak nuclear force and the strong nuclear force. At high energies, the weak nuclear force and electromagnetic force act as a single force — the electroweak force. It is possible that all of the four forces are manifestations of a single unified force, that is only evident at energies that are much higher than those which can currently be studied. In the standard model, forces are mediated by bosons which obey Bose-Einstein statistics. The properties of the force carrying bosons are given in Table 2.3.

Table 2.3: Properties of the gauge bosons [1]. The Higgs and Graviton have not (yet) been discovered, therefore there are no measurements of their properties — The values in parentheses are those predicted by the Standard Model.

Particle Name	Particle Symbol	Spin($\hbar$)	Charge(e)	Mass (GeV/c^2)
Photon	γ	1	0	$< 6 \times 10^{-17}$
Gluon	γ	1	0	0(Predicted)
W	$W^{\pm}$	1	±1	80.403 ± 0.029
Z	c	1	0	91.188 ± 0.002
Graviton	G	(2)	$-\frac{1}{3}$	?
Higgs	$H^0, H^{\pm}$?	0	(0,$\pm$1)	?

The electromagnetic force is mediated by the photon, whereas the the weak nuclear force is mediated by three particles, the W^+, the W^-, and the Z^0. The strong nuclear force is mediated by eight varieties of gluons which carry a colour charge like the quarks. The boson that transmits the force of gravity is called the Graviton, but this has not been discovered yet.

The Higgs mechanism [2] was suggested to answer the problem of the origin of the masses within the standard model. This proposes spontaneous symmetry breaking along with a coupling to a new boson, the Higgs boson, which would couple more strongly to the observed particles with the highest masses. The Higgs boson remains undiscovered, but searches using future experiments should reveal if it exists and if so what properties it may have.

There is another slight problem with the standard model which should be noted. Following the big bang, equal quantities of matter and antimatter should have been created. As the universe cooled this matter and antimatter should have annihilated to leave a universe full of photons but depopulated of both matter and antimatter. Today however, there is an excess of matter in the universe and there is no evidence for the presence of antimatter on a macroscopic scale. As the majority of the visible matter is composed of baryons, some process must have occurred in the early universe that allowed this baryon asymmetry to develop. Andrei Dmitrievich Sakharov [3] proposed the three conditions necessary for this asymmetry to occur: the non-conservation of baryon number, the occurrence of CP-violation, and the universal departure from thermodynamic equilibrium. CP combines two symmetries — charge conjugation C in which particles and anti-particles are interchanged, and parity P in which the space is replaced by a mirror image of the space, which are conserved in the interactions of electromagnetism, gravity and the strong nuclear force, however they are violated by certain rare weak interactions. CP-violation was discovered in neutral K decays in 1964 [4], and more recently in neutral B meson decays [5] [6]. More information about CP violation can be found in the PDG [1] and the references found therein. The amount of measured CP violation in the standard model is insufficient to account for the observed universe which could imply that our current understanding is incomplete and that sources exist in new physics, beyond the standard model. Although, evidence for neutrino masses could imply the occurrence of CP-violation in the lepton sector which may account for some of this discrepancy.

2.2 Quantum chromodynamics

The theory of Quantum Chromodynamics (QCD) describes the interactions under the strong nuclear force. In QCD, hadrons are interpreted as bound states of quarks which are held together through gluon mediated non-Abelian gauge interactions. The theory of QCD has been tested in over 40 years of experiments and is an integral part of the standard model. QCD has two peculiar properties — asymptotic freedom and confinement. With asymptotic freedom, reactions at very high energies the interactions between quarks and gluons are weak which allows the use of perturbation theories. Asymptotic freedom in the strong interaction was discovered independently by Gross and Wilczek [7] and by Politzer [8]. The property of confinement means that the force between quarks does not reduce as the quarks are separated. Due to confinement, an infinite amount of energy would be required to separate two quarks. Although this property of QCD has not been proved analytically, it is believed to be true because it would explain why no free quarks have ever been observed. The property of confinement has been verified using lattice QCD computations.

The study of QCD evolved out of the quark model which was described first in the seminal papers of Gell-Mann [9] and Zweig [10]. The quark model was developed to try and find a fundamental reason why the spectroscopy and quantum numbers of the known mesons and baryons were described so well by the broken SU(3) symmetry called the "Eightfold Way" [11] [12] [13]. The eightfold way was for particle physics what Mendeleev's table was for chemistry. The quark model [9] proposed that baryons and mesons were composed from smaller fundamental particles with fractional charges — the quarks. In this model baryons consisted of three quarks whilst mesons were considered to be a quark antiquark pair. The baryon numbers of quarks and antiquarks were proposed to be $\frac{1}{3}$ and $-\frac{1}{3}$, respectively. These quarks were not to be associated with any particle known at the time and formed a unitary triplet composed from a doublet (u,d) and a singlet (s) with strangeness zero and one, respectively.

In order to explain the independence of the strong nuclear interactions to electrical charge the concept of isospin had been introduced. In this description, protons and neutrons were both considered to be nucleons with similar interactions under the strong nuclear force but different values of isospin (I_Z). For isospin, the operators which corresponded to the isospin vector's three components were considered to be the generators in the algebra of the SU(2) symmetry group. Broken SU(3) symmetry developed from the desire to extend this description to include the hyper-charge. The hyper-charge

Y is given by $Y = S + B$, where S and B are the strangeness and the baryon number respectively. An operator that corresponded to the hyper-charge was added along with four other operators that corresponded to quantities known as v-spin and u-spin. The resulting eight operators were assumed to correspond to those of the algebra of SU(3), thus the eightfold way. There were now super-multiplets which corresponded to the irreducible multiplets of SU(3) in the same manner in which the isospin multiplets corresponded to the irreducible multiplets of SU(2). In the same manner that the SU(2) isospin multiplets were broken due to the electric charge the SU(3) symmetries were broken by the hyper-charge of the strong nuclear force. In the unitary triplet description of the quark model, such symmetry breaking would result from mass difference between the s and (u, d) quarks [9].

In the broken SU(3) symmetry scheme and therefore also the quark model, the lowest multiplets are a singlet and an octet. The known pseudoscalar mesons the (K, π, $\overline{K}$) had properties which were consistent with belonging to the octet. In 1962 the missing isoscalar state η was discovered and the singlet state η' was discovered in 1964. An octet of vector mesons was also predicted despite the fact that only ρ and ω were known at the time. However, the predicted K^* (892) and $\overline{K}^*$ (892) states were discovered shortly after to complete the octet.

In the baryon sector the singlet state was discarded. When the colour charge is included in the model it turns out that this ground state is forbidden by Fermi-Dirac statistics. The properties of the known baryon states $[N, \mathit{\Lambda}, \mathit{\Sigma}, \mathit{\Xi}]$ were consistent with belonging to an octet with positive parity and spin $J = \frac{1}{2}$.

Probably the greatest success of QCD was the explanation of the nature of the $\Delta(1232)$ and the $\mathit{\Omega}^-$ baryons. The Δ states decay to πN. The $\Delta(1232)^{++}$ baryon discovered by Fermi et al. [14] in 1951 had troubled physicists since. In the quark model the $\Delta(1232)^{++}$ is composed of three u quarks with aligned spins, which is forbidden clearly by the Pauli exclusion principle. The $\mathit{\Omega}^-$ discovered in 1964 [15] is composed of three s quarks with aligned spin and this would be forbidden on the same grounds. This is solved in QCD by giving the quarks an additional degree of freedom, the colour charge. The colour charge was introduced in 1965 independently by Han and Nambu [16], and Greenberg [17].

Han and Nambu noted that the quarks may interact via eight types of gluons. Evidence for gluons was discovered in three jet events at PETRA in 1979 [18]. The model of QCD has been successfully extended to cover the strong interactions of the c, b and t quarks, which have since been discovered.

QCD does not preclude the existence of multi-quark states. In fact, provision is made for the existence of mesons composed of two quarks and two antiquarks, and baryons composed of four quarks and an antiquark, in the papers of both Zweig and Gell-Mann. It is also possible that states constructed entirely from gluons (glueballs) or baryons or mesons containing gluons in addition to quarks and antiquarks (quark-gluon hybrids). The existence or absence of such states is important as it allows us to learn more about the quarks and the forces that bind them together.

2.3 Exotic and crypto-exotic states

Since the birth of the quark model there have been searches for states, which do not conform to the q–$\overline{q}$ or three quark configurations. There are three kinds of such states called exotic states, which can be searched for. These definitions are taken from the proceedings of lectures given by Landsberg at a summer school in 1992 [19].

Exotic states of the first kind are those with manifestly exotic quantum numbers such as electrical charge(Q), isospin(I) and strangeness(S). Examples of such exotic states would include mesons with $Q > 2$, $I > 1$ or $S \geq 2$, and baryons with $Q > 2$, $I > \frac{3}{2}$ or $S > 0$. These particles could no be explained by $q\ \overline{q}$ or $q\ q\ q$ quark configurations and therefore would be exotic states.

Exotic states of the second kind are defined as those with exotic combinations of quantum numbers such as, spin (J), parity (P) and charge conjugation (C). Quarks have an intrinsic spin $S = 1/2$. Consequently a meson consisting of a quark and an antiquark can only form a system with intrinsic spin 0 or 1. The quark and antiquark can have relative orbital angular momentum, L, which is combined vectorally to give the spin of the meson, J, where $J = L + S$. This fixes the parity and charge conjugation of the meson to be $P = (-1)^{L+1}$ and $P = (-1)^{L+S}$, respectively. This means that a $q\ \overline{q}$ quark state can only have the following combinations of quantum numbers: $P = C = (-1)^J$ or $(-1)^{J+1}$ and also $C = (-1)^J$ and $P = (-1)^{J+1}$. There cannot be $q\ \overline{q}$ states which have $C = (-1)^{J+1}$ and $P = (-1)^J$ or with $J + 1$ and $C = -1$. This is because if $J = 0$ then $S = L = 0, 1$ and $C = +1$. The exotic configurations of J^{PC} are 0^{--}, 0^{+-}, 1^{-+}, 2^{+-}, 3^{-+}... It is possible for all types of exotic mesons such as tetraquarks, hybrids and glueballs to have these values of J^{PC}.

Collectively, exotic states of the first and second types are known as **open exotic states**.

Exotic states of the third kind are also known as **crypto-exotic states**. They have external quantum numbers, which do not give away their complex internal states. This information can only be gleaned indirectly by examining features of their characteristics such as anomalously narrow widths, anomalous decay channels and special production mechanisms. Exotic states of all varieties can belong to this class. The state searched for in the analysis presented in this thesis is a possible example of a crypto-exotic baryon.

2.4 Experimental evidence for exotic and crypto-exotic states

Until recently there had been very little evidence for the production of exotic states. However, recently there have been a number of mesonic states that have been observed mainly in the charmonium sector, which could be interpreted as states with exotic internal structure, some with hidden charm. A short review of the experimental status of exotic and crypto-exotic mesons and baryons is presented in this section.

2.4.1 Exotic and Crypto-Exotic Mesons

The Light Quark Sector

The internal structure of the well identified scalar mesons $a(980)$ and $f(980)$ has long been debated. Frequently, they have been identified as P-wave $q\,\overline{q}$ states [20] because the axial and tensor nonets are both well identified [1]. However, there are problems with the $q\,\overline{q}$ assignment because the $f(980)$ couples more to s quarks than to either u or d. Many interpretations have been proposed for these states. One interpretation was that the $f(980)$ and $a(980)$ are both $K\,\overline{K}$ molecules [21] [22] with no strange or isoscalar partners. An alternative model is the bag-model description [23] [24] [25] [26] which defines a nonet of crypto-exotic ($q\,q\,\overline{q}\,\overline{q}$) states therefore going beyond a $q\,\overline{q}$ description. A recent paper by Maiani et al. [27] interprets this as a nonet of diquark-antidiquark states. These tetraquark models imply the existence of strange and isoscalar members of the nonet the κ and the σ. Although there is some evidence for both of these states, there is much debate about whether either of these states exist.

One problem with the $q\,\overline{q}$ model is that there are too many high mass isoscalar states with quantum numbers $J^{PC} = 0^{++}$. The existence of glueball states is predicted in lattice gauge calculations such as those by Morningstar et al. [28]. The first of these glueball states should have a mass in the range 1.4-1.8 GeV/c^2 and should mix with other $J^{PC} = 0^{++}$ states. This would perturb the mass spectra and lead to the observation of too many states in this region. A good candidate for a glueball state consisting was observed at Mark-3 in the radiative decays of J/ψ mesons with a mass of approximately 1.7 GeV/c^2 at Mark-3 [29]. A state recently observed at BES [30] with a mass of approximately 1.81 GeV/c^2 would be another good candidate for a glueball state. The presence of such states requires a description that goes beyond the standard $q\,\overline{q}$ model.

States described as quark-gluon hybrids can have exotic quantum numbers that are forbidden in the $q\,\overline{q}$ model, such as $J^{PC} = 1^{-+}$. One such state was predicted by gluon-flux tube models [31] at a mass of roughly 1.9 GeV/c^2. Models based on lattice-gauge calculations [32] [33] predict a state at approximately this mass, whilst the predictions based on the bag model [34] predict this at lower mass of which one would have $J^{PC} = 1^{-+}$. Partial wave analyses from the E852 experiment at BNL using data from the interactions of 18 GeV/c pions with a liquid hydrogen target have yielded two such states. The first was observed at a mass of $1.370\pm0.016^{+0.050}_{-0.030}$ GeV/c^2 with a width of $0.385\pm0.040^{+0.065}_{-0.105}$ GeV/c^2, in the reaction $\pi^- p \rightarrow \eta\pi^-\, p$ [35] [36]. This state was confirmed by the E862 experiment at BNL in the reaction $\pi^- p \rightarrow \eta \pi^0 \ n$ [37]. The second was observed [38] [39] in the reaction $\pi^- p \rightarrow \eta' \pi^- \ p$ at a mass of $1.590 \pm 0.010^{+0.015}_{-0.010}$ GeV/c^2 with a width of $0.340 \pm 0.040 \pm 0.050$ GeV/c^2. These states indicate mesons with a non $q \ \overline{q}$ structure.

The $D_{sJ}(2632)$ state

The SELEX collaboration claimed to observe the $D_{sJ}(2632)$ meson [40]. The narrow state was observed to decay to $D_s^+ \eta$ and $D^0 \ K^+$ with a significance of 7σs and was interpreted as a $[c \ d \ ][\overline{s} \ \overline{d} \ ]$tetraquark state [41]. However, searches by *BABAR* [42] and FOCUS and CLEO, referenced in a review paper [43] have all failed to confirm this state's existence and the current view is that this may be an experimental artifact [43].

States with hidden charm

A number of charmonium like states have been discovered recently in B meson decays by the B Factory experiments, *BABAR* and BELLE. Collectively, these new states are known as the "XYZ" mesons. Two of these states have been interpreted as the η_C' and χ_C' charmonium states. However, the remainder have properties which cannot be explained by the charmonium model. The current experimental status was reviewed recently by Olsen [44] and more information can be found there. The properties of these states are listed in Table 2.4.

Table 2.4: The "XYZ" mesons

State	Experiment	Reaction	Decay mode	Mass (MeV/c^2)	Width (MeV/c^2)	J^{PC}
$X(3872)$	BELLE [45] [46], *BABAR*	$B \rightarrow KX$	$J/\psi \ \pi^+ \ \pi^-$	3871.4 ± 0.6	< 2.3	1^{++}
	CDF [47] [48], D0 [49]	$p \ \overline{p}$				
$X(3875)$	BELLE [50], *BABAR* [51]	B	$D^0 \ \overline{D}^0 \ \pi^0$	3875.5 ± 1.5	$3.0^{+2.1}_{1.7}$	$?^{??}$
$X(3940)$	BELLE [52]	$e^+e^- \rightarrow J/\psi X$	$D\overline{D}^*$	3942 ± 9	37 ± 17	$?^{?+}$
$Y(3940)$	BELLE [53], *BABAR* [54]	$B \rightarrow K \ Y$	$\omega J/\psi$	3943 ± 7	87 ± 34	$?^{++}$
$Z(3940)$	BELLE [55]	$\gamma\gamma$	$D\overline{D}$	3929 ± 5	29 ± 10	2^{++}
$Y(4008)$	BELLE [56]		$\pi^+ \ \pi^- \ J/\psi$	$4008 \pm 40^{+114}_{-28}$	$226 \pm 44 \pm 87$	1^{--}
$Y(4160)$	BELLE [57]	$e^+e^- \rightarrow J/\psi Y$	$D^* \ \overline{D}^*$	4156 ± 29	139^{+113}_{-65}	$?^{++}$
$X(4260)$	*BABAR* [58], CLEO [59] BELLE [56]	$e^+e^- \rightarrow \gamma X$	$J/\psi \ \pi^+ \ \pi^-$	4264 ± 12	83 ± 22	1^{--}
$Y(4350)$	*BABAR* [60], BELLE [61]	$e^+e^- \rightarrow \gamma Y$	$\pi^+\pi^-\psi'$	4361 ± 13	74 ± 18	1^{--}
$Z(4430)$	BELLE [62]	$B \rightarrow KZ$	$\pi^+\psi'$	$4433 \pm 4 \pm 2$	44^{+18+30}_{-13-13}	
$Y(4660)$	BELLE [61]	$e^+e^- \rightarrow \gamma Y$	$\pi^+\pi^-\psi'$	4664 ± 12	48 ± 15	1^{--}

The nature of these states are uncertain and possible interpretations include various charmonium states, hybrid charmonium states, and tetraquark states in either a diquark-antidiquark configuration or a deuteron like molecule.

The $X(3872)$ state has been interpreted as a $D^0\ \overline{D}^{*0}$ molecule [63] [64] [65] [66] [67] or a $[c\ d\ ][\overline{c}\ \overline{d}\ ]$ tetraquark [68] [69] [70]. The mass difference between the $X(3875)$ and the $X(3872)$ could either a threshold effect or, alternatively, an indication that the $X(3875)$ was the $[c\ u\ ][\overline{c}\ \overline{u}\ ]$ partner to the $X(3872)$ predicted by the diquark-antidiquark model [68]. The $X(3940)$ state could be interpreted in a number of ways including a hybrid charmonium state [71]. Although the $X(3940)$ is not seen to decay to $\omega J/\psi$ the upper limit on this is not stringent enough to rule out that the $Y(3940)$ is not the same state.

It is unclear whether $Y(4008)$ is a new "XYZ" state, a threshold effect or the $\psi(4040)$ state.

The $X(4260)$ state could have a number of interpretations including the first orbital excitation of a $[c\ s\ ][\overline{c}\ \overline{s}\ ]$ tetraquark [72], a hybrid charmonium state [73] [74] [71], a $\chi_c - \rho^0$ molecule [75], and the 4S charmonium state [76]. The $Y(4350)$ state has a number of interpretations including a $3^3D_1\ c\ \overline{c}$ state [77] and a charmonium hybrid state [73]. If the $Z(4430)$ state is interpreted as a meson then it cannot be a $c\ \overline{c}$ charmonium or a $c\ \overline{c}$ gluon hybrid as both of these would be electrically neutral. The remaining interpretation is a crypto-exotic tetraquark state with hidden charm. Maiani et al. [78] propose this to be a diquark-antidiquark state with quark content $[c\ u\ ][\overline{c}\ \overline{d}\ ]$ whilst others [79] [80] [81] [82] [83] advocate a $D^*\ \overline{D}^{**}$ molecule. The $Y(4660)$ state has a number of interpretations including a $5^3S_1\ c\ \overline{c}$ state [77] and a charmonium hybrid [73].

In the strange meson sector, one state with a mass of $2170 \pm 15 \pm 10\,\mathrm{MeV}/c^2$ and a width of $58 \pm 16 \pm 20\,\mathrm{MeV}/c^2$ was observed by BABAR in 2006 and it was called the $Y_S(2145)$ [84]. This state was reported in the invariant mass distribution $f(980)\phi$ produced in $e^+e^- \rightarrow \gamma f(980)\phi$ interactions. This state was also recently observed by BES2 [85] in the $J/\psi \rightarrow \eta f(980)\phi$ decay mode with a mass and a width consistent with the BABAR measurement. The quantum numbers of the state were $J^{PC} = 1^{--}$ and the state can be interpreted in a number of ways including as a strangeonium hybrid [86] or a $(s\ s\ \overline{s}\ \overline{s})$ tetraquark state [77].

In the bottomonium sector the decay $\Upsilon(5S) \rightarrow \Upsilon(nS)\pi^+\pi^-$ was found to occur with an anomalously large width at BELLE [87] which could explained by the existence of a state analogous to the $Y(4260)$ state called the Y_b which could be interpreted as a $(b\ u\ \overline{b}\ \overline{d})$ tetraquark which overlaps with the $\Upsilon(5S)$ state [88].

2.4.2 Exotic baryons — pentaquarks

Searches for exotic baryons are nothing new, in fact particle physics has a rich history of searching for such states. Since the early days of the quark model, evidence for these states has been searched for in the partial wave analysis of data from KN interactions in elastic, charge exchange and inelastic scattering. The results for the Z^* states as they were known were summarised briefly in a paper by Hey et al. [89]. The only structures were found in the P_{01} and P_{03} amplitudes at masses between 1.8 and 1.9 GeV/c^2. In the 1986 edition of the particle data book [90] the PDG had dismissed the Z^* issue as being inconclusive. From the 1988 edition of the PDG [91] onwards the $Z*$ states were only mentioned in a reference to the 1986 edition. After this the study of exotic baryons received very little interest except from theorists interested in the chiral soliton models as proposed by Skyrme [92].

For a brief period in the middle of this decade the possible discovery of the pentaquark was again a hot topic in particle physics. Searches for pentaquark states were carried out by seemingly every major particle physics collaboration and over 500 theory papers have been written about the subject. The catalyst for this interest was the discovery of a narrow baryonic resonance with positive strangeness at a mass of 1.54 GeV/c^2 in the invariant mass distribution of the $K^+ \; n$ system. This resonance, called the Θ^+ was observed in photo-production off a neutron target by the LEPS collaboration at the SPring-1 experiment [93]. This search had been inspired by a 1997 theory paper by Diakonov et al. [94] who had predicted using a chiral soliton model a narrow $S = +1$ state at approximately the same mass. More positive claims for the existence of the Θ_5^+ followed and these are summarised graphically in Figure 2.1 which was taken from a review paper by Dzierba et al. [95]. For each of these observations the collaboration and the reaction studied are tabulated along with the mass, width and statistical significance in Table 2.5.

Another state, with a mass of 1.862 ± 0.002 GeV/c^2 and a width < 0.018 GeV/c^2 the Ξ_5^{--} was observed in the $\Xi^-\pi^-$ invariant mass distribution with a significance of 4.0σ's by the NA49 collaboration [96] in $p\,p$ interactions. In the same analysis, indications of its neutral partner, the Ξ_5^0 baryon, were observed at the same mass in the invariant mass distribution of $\Xi^-\pi^+$. These were interpreted as baryons with $I = 3/2$ and $S = 2$ and quark content $d\ s\ d\ s\ \overline{u}$ and $d\ s\ u\ s\ \overline{d}$, respectively. As can be seen in Table 2.6, there is no experimental evidence which confirms the existence of this state. The analysis method has been questioned publicly by members of the same collaboration [97].

A charmed state, the Θ_C was observed by the H1 Collaboration [98] at HERA in the invariant mass distributions of $D^{*-}\ p$ and $D^{*+}\ \overline{p}$ with a mass of $3.099 \pm 0.003 \pm 0.005$ GeV/c^2 and a width comparable to the detector resolution (12 MeV/c^2). However, no corroborating evidence has been found for this state in a number of experiments including ZEUS [99], the pair experiment of H1 at HERA, which should operate under the same conditions.

Since the initial observations of the pentaquarks the majority of the results have been negative. The negative results are tabulated alphabetically in Table 2.6 which is an updated version of that presented by Dzierba [95]. There have been negative results from roughly 20 experiments in 30 reactions. These

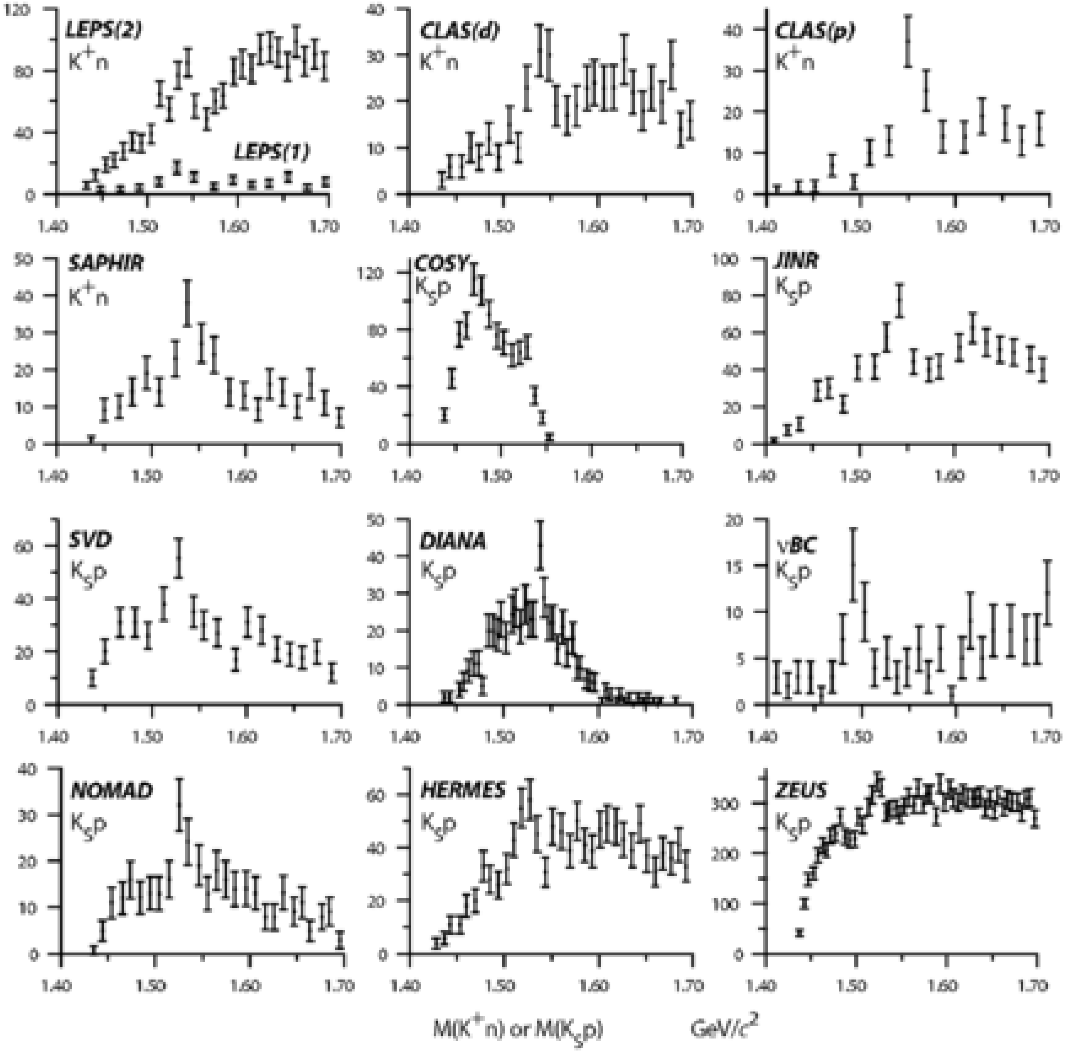

Figure 2.1: Invariant mass distributions for the results listed in Table 2.5 for the decay modes K^+ n or K_S^0 p in the range 1.4-1.7 GeV/c^2 with purely statistical error bars. [95]

Table 2.5: Results from the experiments reporting the observation of the $\Theta^+(1540)$ in the invariant mass distributions of either n K^+ or p K_S^0.

Experiment	Reaction	Mass	Width	σs	Reference
		(MeV/c^2)	(MeV/c^2)		
LEPS(1)	$\gamma C^{12} \rightarrow K^+K^-X$	1540 ± 10	< 25	4.6	[100]
LEPS(2)	$\gamma d \rightarrow K^+K^-X$				[93]
CLAS(d)	$\gamma d \rightarrow K^+K^-(n)p$	1555 ± 10	< 26	7.8	[101]
CLAS(p)	$\gamma p \rightarrow K^+K^-(n)\pi^+$	1542 ± 5	< 21	5.2	[102]
SAPHIR	$\gamma p \rightarrow \overline{K}^0K^+(n)$	1540 ± 6	< 25	4.8	[103]
COSY	$pp \rightarrow \Sigma^+K^0p$	1530 ± 5	< 18	$4-6$	[104]
JINR	$p(C_3H_8) \rightarrow K_S^0pX$	1540 ± 8	9.2 ± 1.8	5.5	[105]
SVD	$pA \rightarrow K_S^0pXA = (C, Si, Pb)$	1526 ± 4	< 24	5.6	[106]
DIANA	$K^+Xe \rightarrow K^0p(Xe)'$	1539 ± 2	< 0.9	4.4	[107] [108]
ν BC(ITEP)	$\nu Ne \rightarrow K_S^0pX$	1533 ± 5	< 20	6.7	[109]
NOMAD	$\nu_\mu A \rightarrow K_S^0pXA = (Fe, Al, Pb)$	1528.7 ± 2.5	< 21	4.4	[110] [111]
HERMES	$e^+d \rightarrow K_S^0pX$	1528 ± 3	13 ± 9	5	[112]
ZEUS	$e^-p \rightarrow e^-K_S^0pX$	1522 ± 3	8 ± 4	5	[113]

include a number of inclusive high statistics searches at experiments where hyperons are produced in far greater quantities than those which claim positive observations. The negative results also include a number of high statistics updates of the same reactions under the same experimental conditions which originally produced positive results. However, as the possible mechanisms for the production of the $\Theta^+(1540)$ are unknown it is possible the conditions at these experiments are not optimal for pentaquark production.

Table 2.6: Recent negative searches for pentaquark states. For each of the pentaquark states (P): a - indicates that the state was not searched for, a $\Uparrow$ indicates the state was observed, and a $\Downarrow$ indicates that no evidence was found for the state.

Experiment	Search Reaction	Θ^+	Ξ_5	Θ_c	Reference
ALEPH	Hadronic Z^0 decays	$\Downarrow$	$\Downarrow$	$\Downarrow$	[114]
BABAR	$e^+e^- \rightarrow PX$	$\Downarrow$	$\Downarrow$	$\Downarrow$	[115] [116]
BABAR	e^- Secondary Interactions	$\Downarrow$	-	-	[117]
BELLE	$KN \rightarrow PX$	$\Downarrow$	-	$\Downarrow$	[118]
BELLE	$B^0 \rightarrow \overline{p}pK^0$	$\Downarrow$	-	-	[119]
BES	$e^+e^- \rightarrow J/\psi\,(\psi(2S)) \rightarrow \Theta\bar{\Theta}$	$\Downarrow$	-	$\Downarrow$	[120]
CDF	$p\overline{p} \rightarrow PX$	$\Downarrow$	$\Downarrow$	$\Downarrow$	[47] [121] [122] [123]
CLAS	$\gamma p \rightarrow K^+K^-p$	$\Downarrow$	-	-	[124]
CLAS	$\gamma p \rightarrow \overline{K}^0K^+n \Vert \overline{K}^0K^0p$	$\Downarrow$	-	-	[125]
CLAS	$\gamma D \rightarrow \Lambda nK^+$	$\Downarrow$	-	-	[126]
CLAS	$\gamma D \rightarrow pK^-K^+n$	$\Downarrow$	-	-	[127]
COMPASS	$\mu^+(^6LiD) \rightarrow PX$	$\Downarrow$	$\Downarrow$	-	[128]
DELPHI	Hadronic Z^0 Decays	$\Downarrow$	-	-	[129]
E690	$pp \rightarrow PX$	$\Downarrow$	$\Downarrow$	-	[130]
E522	$\pi^-p \rightarrow K^-PX$	$\Downarrow$	-	-	[131]
FOCUS	$\gamma p \rightarrow PX$	$\Downarrow$	$\Downarrow$	$\Downarrow$	[132] [133] [134]
H1	$e^-p \rightarrow PX$	$\Downarrow$	-	$\Uparrow$	[135] [98]
HERA-B	$pA \rightarrow PX$	$\Downarrow$	$\Downarrow$	-	[136] [137]
HERMES	$e^+D \rightarrow K^0_spX$	$\Uparrow$	$\Downarrow$	-	[112] [138]
HyperCP	$(\pi^+, K^+p)Cu \rightarrow PX$	$\Downarrow$	-	-	[139]
LASS	$K^+p \rightarrow K^+n\pi^+$	$\Downarrow$	-	-	[140]
NOMAD	$\nu_\mu A \rightarrow K^0_spXA = (Fe, Al, Pb)$	$\Downarrow$	-	$\Downarrow$	[111] [141]
L3	$\gamma\gamma \rightarrow \Theta\bar{\Theta}$	$\Downarrow$	-	-	[142] [129]
OBELIX	$\overline{p}^4He \rightarrow PK^0_sX \Vert PK^-XP\Lambda X$	$\Downarrow$	-	-	[143]
PHENIX	$AuAu \rightarrow PX$	$\Downarrow$	-	-	[144]
SELEX	$(\pi, p, \Sigma)p \rightarrow PX$	$\Downarrow$	-	-	[145]
SPHINX	$pC(N) \rightarrow \Theta^+C(N)$	$\Downarrow$	-	-	[146] [147]
WA89	$\Sigma^-N \rightarrow PX$	$\Downarrow$	$\Downarrow$	-	[148] [149]
ZEUS	$e^-p \rightarrow PX$	$\Uparrow$	$\Downarrow$	$\Downarrow$	[113] [113] [150] [99]

Theoretical interpretations

Aside from the chiral soliton models such as those proposed by Diakonov et al. [94] which predicted the existence of the Θ^+ baryon. More models were developed to describe the internal structure of pentaquarks.

The model developed by Karliner and Lipkin [151] proposed that pentaquarks could be considered to be composed of a diquark and triquark cluster. With each of these clusters having isospin zero and being colour nonsinglet with the identical flavours separated. The clusters are kept outside the range of the colour magnetic force by a centrifugal barrier. The two clusters are held together by the colour electric forces.

A second model of this type was proposed by Jaffe and Wilczek [152]. In this model pentaquark states are viewed as being composed from two diquark clusters combined with a bachelor antiquark.

Finally it should be possible to investigate the possible existence of a crypto-exotic state using lattice gauge techniques. These were used for the pentaquark candidates and a 2005 paper [153] discussed the current status of such calculations and concluded that there was no evidence for the existence of such states. Although they conclude that the “absence of evidence” should not be considered to be “evidence of absence” at this stage of the investigations.

2.4.3 Crypto-exotic baryons

For crypto-exotic baryons the experimental evidence is limited to two possible observations which date from the 1980’s and 1990’s.

The $\Sigma^+(3170)$ state

The $\Sigma^+(3170)$ state was reported by Amirzadeh et al. [154] in data from two independent bubble chamber experiments where K^- beams were fired at a hydrogen target. The first experiment was based at CERN and used a 2m bubble chamber with an incident 8.25 GeV/c K^- beam. The second experiment took place at Argonne and used a 12’ bubble chamber and an incident 6.5 GeV/c K^- beam. In the missing mass spectrum of the system recoiling against a π^-, a peak was observed at a mass of 3.170 GeV/c^2 with a width of 20 MeV/c^2.

The selected events were required to contain more than one strange particle. This could either be the signature of a Ξ or three strange particles originating from the production vertex. In each of the events at least one neutral strange particle was required.

The significance of the peak was reported to be 3σ in the experiment which used the 8.25 GeV/c K^- beam. A cut was applied which constrained the direction of the π^- to be in the backwards hemisphere and the significance of the peak increased to 5.5σ. The cross section for the production of the state at 8.25 GeV/c was found to be $0.7 \pm 0.2\,\mu$b.

In the 6.25 GeV/c experiment the significance of the peak was about 4σ. The cross section for the production of the $\Sigma^+(3170)$ was evaluated to be $1.0 \pm 0.3\,\mu$b.

In Figure 2.2 the combined missing mass distribution from the two experiments are plotted with units of Number of events/20 MeV/c^2 in Figure 2.2a) and with units of Number of Events/5 MeV/c^2 in

Figure 2.2b).

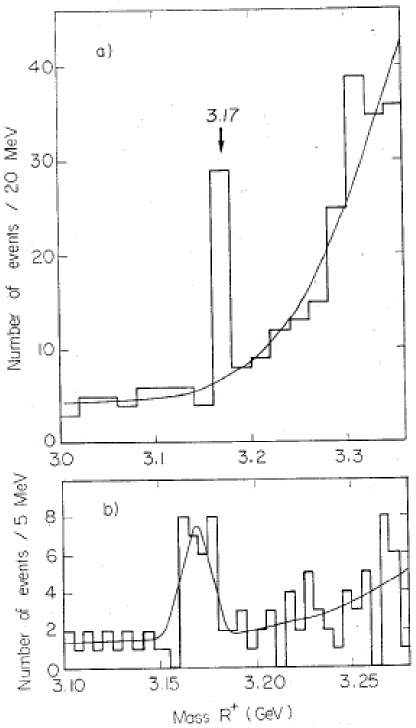

Figure 2.2: Invariant mass distribution of the $\Sigma^+(3170)$ candidates for the decay mode $p\ K^+\ K^0_S\ \pi^-\ \pi^-$ [154]

The state was observed to decay through the following decay modes: $\Sigma\ K\ \overline{K}$ plus two pions, $\Lambda K\ \overline{K}$ plus two pions, and $\Xi\ K$ plus three pions. Events containing a single strange particle were examined however no evidence was found and upper limits were set. No evidence for the negative or neutral partners of this mode was observed. The state was proposed to be a pentaquark with a quark content of $(q\ q\ s\ s\ \overline{s})$. This assignment was based on the narrow width and the dominance of decay modes containing multiple strange particles.

The $\Sigma^+(3170)$ state was also searched for by Aston et al. [155] at the Large Aperture Solenoid Spectrometer (LASS), in the interactions of a 11 GeV/c K^- beam with a liquid hydrogen target. The state was searched for in the decay mode $\Xi^- K\ + \pi$'s in the missing mass spectra of the state recoiling against the slowest pion. No evidence was found for this state and an upper limit (with 95% confidence level) of 0.7 μb was set on the production of this state.

The $R(3520)$

The existence of the $R(3520)$ state was suggested by Karnaukhov et al. [156] by analysing the experimental data from the CERN 2m hydrogen bubble chamber exposed to a 16 GeV/c pion beam. In the invariant mass spectrum of the $p\ K^+\ K^0_S\ \pi^-\ \pi^-$ system, a peak at a mass of 3.520 ± 0.003 GeV/c^2 with a width of 7^{+20}_{-7} MeV/c^2 was observed. In the invariant mass spectrum of the $p\ K^-\ K^0_S\ \pi^+\ \pi^-$ system a similar peak was not observed.

In this study 1684 four-prong events which contained a K^0_S vertex in addition to four charged tracks (two positive and two negative) were analysed. Events in which there was some ambiguity between the K^0_S and Λ^0 hypotheses for the vertex were not included as in an earlier study 80% of these candidates were found to be Λ^0s. In order to improve the momentum resolution tracks with a $\Delta p/p > 10\%$ were removed.

For each four-prong event, the invariant mass of every combination was calculated with the pion, kaon and proton mass hypotheses applied to each of the four charged tracks. For the $p\ K^+\ \pi^-\ \pi^-\ K^0_S$ system there are two possible assignments (K^+,p,$\pi^-\ \pi^-$,K^0_S) and (p,K^+,$\pi^-\ \pi^-$,K^0_S), which were both considered separately.

These candidates were also weighted with an average weight of 1.13 to account for losses in the detector. The candidates were weighted before the fit of the invariant mass distribution was performed.

The ionization energy was used for particle identification. The momentum thresholds for the separation of pions from kaons, and the separation of protons from kaons, were 0.7 GeV/c and 1.2 GeV/c, respectively. The ionization measurements were only available for less than 20% of the 4×1684 tracks. If there was no ionization information for a track then all particle hypotheses were considered for that track. This reduced the number of weighted candidates to 1057 and 2183 for the assignments $p\ K^+\ \pi^-\ \pi^-\ K^0_S$ and $p\ K^-\ \pi^+\ \pi^-\ K^0_S$, respectively.

This invariant mass distribution of the $p\ K^+\ \pi^-\ \pi^-\ K^0_S$ system reported in this experiment is shown in Figure 2.3.

The data were analysed further to investigate the influence of the $K^0\ \pi^-$ structures on the peak. The mass spectra of the events in the peak and the adjacent regions was investigated and reproduced in Figure 2.4. It was found that more than two thirds of the events had a $\pi^-\ K^0_S$ combination with a mass in the range 0.7-1.05 GeV/c^2. It was also found there was a bump at 1.3 GeV/c^2 which could correspond to higher K^* resonances. When the events with $\pi^-\ K^0_S$ masses in the range 0.7-1.05 GeV/c^2 were excluded the peak in the distribution shown in Figure 2.3 disappeared. These observations led to the conclusion that the $R(3520)$ decayed through a K^{*-} resonance. This indicated that the $R(3520)$ state decayed through a $\overline{K}^0$ and that $R(3520)$ had strangeness $S = 0$.

The data was also analysed to investigate the influence of the K^{*+} on the peak. The positive charged tracks which were not identified as protons were assigned the pion mass. These were combined with the K^0_S and the invariant mass of the combination was calculated. Those events with a $\pi^+\ K^0_S$ mass in the K^{*+} mass region (0.8-0.95 GeV/c^2) were removed. This removed roughly a third of the candidates and did not reduce the size of the peak. From this it was concluded that the peak was not a reflection

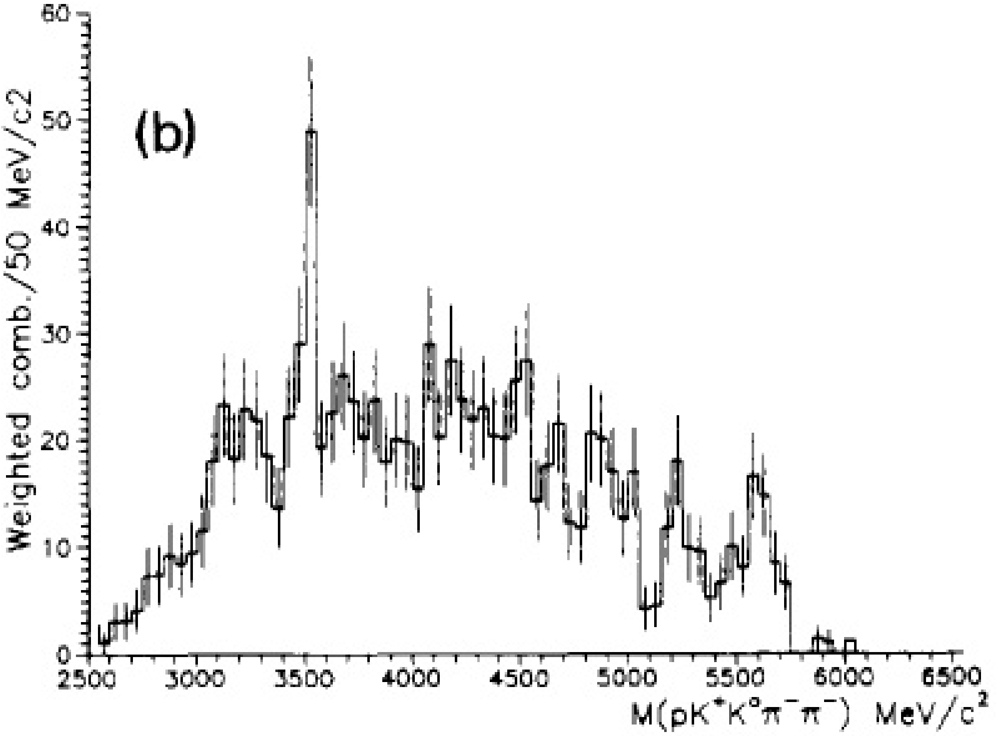

Figure 2.3: Invariant mass distribution of the $R(3520)$ candidates for the decay mode $p\ K^+\ K^0_S\ \pi^-\ \pi^-$ [156]

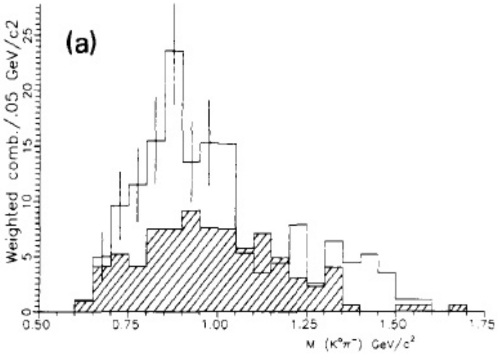

Figure 2.4: Invariant mass distribution of the $K^0_S\ \pi^-$ system for 154 combinations for events from the interval 3.45-3.55 GeV/c^2. The shaded area represents the distribution of the $K^0_S\ \pi^-$ mass for events in the intervals adjacent to the peak normalised to the background. [156]

of the K^{*+}.

It was also analysed the rapidity region in which the peak occurred. It was found that the peak disappeared outside the rapidity region $-0.18 < y < 0.38$, which indicated that the peak appeared only in central collisions.

With the cuts on the mass of the $K_S^0\ \pi^-$ combination and the rapidity applied, the significance of the peak increased from 5 to 8.9 standard deviations. The number of candidates in the fitted peak above a linear background was 37 before the cuts and 42 after the cuts. The invariant mass distribution of the $p\ K^-\ K_S^0\ \pi^+\ \pi^-$ system after the application of the cuts is displayed in Figure 2.5.

The cross section for the production of this state was evaluated to be $16 \pm 3\,\mu$b. Due to the decay mode and the narrowness of the peak the state was suggested to have a $(u\ u\ d\ c\ \overline{c})$ quark content.

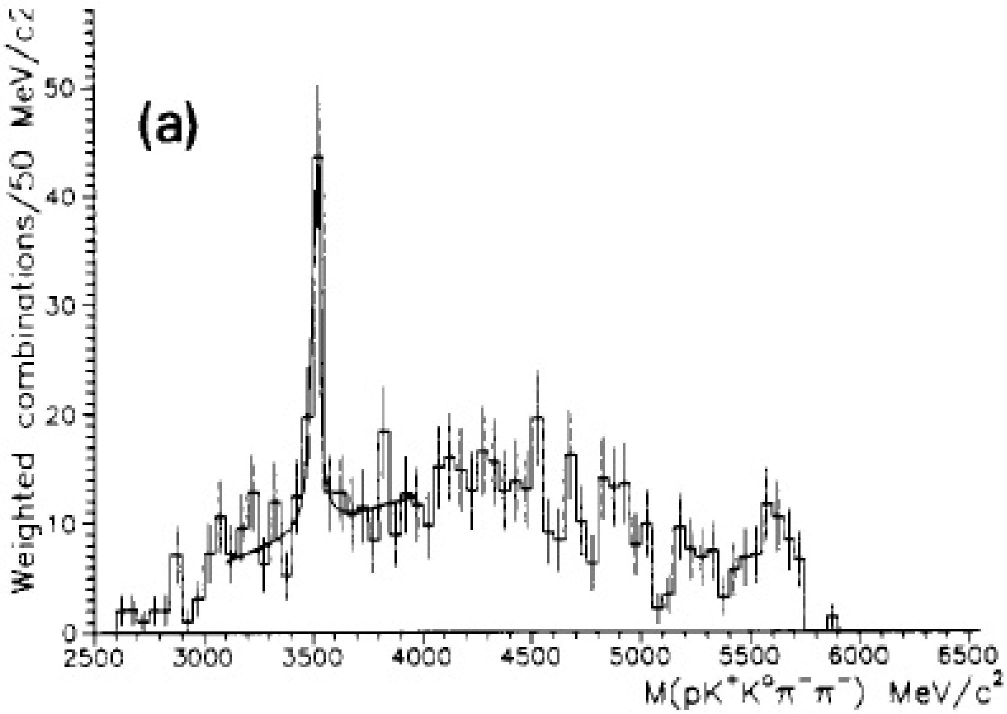

Figure 2.5: Invariant mass distribution of the $R(3520)$ candidates for the decay mode $p\ K^+\ K_S^0\ \pi^-\ \pi^-$ [156] for events passing the cuts on rapidity and the $\pi^-\ K_S^0$ mass.

This state was also searched for by the SPHINX experiment [157] which was a fixed target experiment that used a 70 GeV proton beam. It was searched for, however, in different final states and negative results were reported. Upper limits were set at the 95% confidence level on the cross section of the production of the state for the decay modes $R(3520) \to \phi p$, $R(3520) \to \Lambda(1520)K^+$, $R(3520) \to pK^+K^-$ at < 0.27 nb/nucleon, < 3.4 nb/nucleon, and < 2.6 nb/nucleon, respectively. These upper limits were 4-5 orders of magnitude lower than those given in [156]. However, because these upper limits are for different final states, there is no direct contradiction.

Theoretical interpretations of crypto-exotic states

In a paper by Landsberg [19], it was noted that the quark configuration proposed by Karnaukhov et el. [156] for the $R(3520)$ state was problematic as the production cross section was 2-3 orders of magnitude greater than the production of the J/ψ which also has hidden charm. The second issue raised in this paper was that the $R(3520)$ has approximately the same mass as the only observed doubly charmed baryonic state in the PDG [1], the Σ_{cc}^{+}. However, as the Σ_{cc}^{+}, has also not been confirmed this is not that much of a problem.

A more detailed study was performed by Lutz and Hofmann [158]. They modelled the masses, widths, and decay modes of exotic and crypto-exotic states with charm, $C = -1, 0, 1, 2, 3$. There predictions were based on the chiral soliton models given in [92]. In chiral soliton models, nucleons are considered to be solitons in a field of pseudoscalar mesons which are the Goldstone bosons of these interactions. In the paper by Diakonov et al. [94] which predicted the Θ_5^+, the nucleons are considered to be solitons in a pion field. The coupled channel models of Lutz and Hofmann [158] are more complex and consider the S-wave scattering of the pseudoscalar mesons off baryon fields. These predications are based on calculations for SU(4) flavour space and SU(3) colour space. In the coupled channel models the exotic or crypto-exotic states were defined as a superposition of bound molecular states composed from a baryon and meson.

In this study a number of crypto-exotic baryons containing a $c\ \bar{c}$ pair with $C = 0$ were predicted with masses below $4\,\mathrm{GeV}/c^2$. The widths of such states are expected to be small due to OZI rule [19]. A narrow nucleon resonance was found with at a mass of $3.52\,\mathrm{GeV}/c^2$, or the $R(3520)$ state. The state was a coupled channel bound state of the $\eta_C N$ and $\bar{D}\Sigma_C$ which decayed dominantly in the $\eta' N$ channel. Its decay is driven by the exchange of charm via the t-channel. The width estimated using SU(4) was about $150\,\mathrm{MeV}/c^2$. With moderate breaking of the SU(4) symmetry, the width was reduced to 5-20 MeV/c^2 which is consistent with that measured by Karnaukhov et al. [156]. This state belonged to an SU(3) octet of states which decay predominately through an η' meson. The isospin singlet, doublet, and triplet had masses of $3.58\,\mathrm{GeV}/c^2$, $3.80\,\mathrm{GeV}/c^2$, and $3.93\,\mathrm{GeV}/c^2$, respectively.

An even stronger coupled charm bound state of the $(\bar{D}_s \Lambda_c)$, $(\bar{D}_s \Sigma_c)$ systems was predicted. This state had a mass which was close to the $3.17\,\mathrm{GeV}/c^2$ measured by Amirzadeh et al. [154]. The decays of this state were suppressed into channels involving the η' meson because it was an SU(3) singlet. Therefore, a width $< 1\,\mathrm{MeV}/c^2$ was predicted, which was compatible with that measured by Amirzadeh et al. [154].

Interesting results were also obtained in the sector with $C = -1$ where the pentaquark states predicted by Lipkin [159] were confirmed by Lutz and Hofmann. Exotic states were predicted with $S = -1$ and $S = -2$ with masses of $2.78\,\mathrm{GeV}/c^2$ and $2.84\,\mathrm{GeV}/c^2$. The $\Lambda_c(2593)$ was recovered as a narrow state which coupled strongly to the (DN) and $(D_s\Lambda)$ states. The $\Xi_c(2780)$ was interpreted as a bound state of the $(\overline{K}\Sigma_c)$, $(\eta\Xi_c)$ system. It was argued that the $\Lambda_c(2880)$ discovered by the CLEO collaboration could not be an s-wave state. About ten more narrow s-wave states were predicted with masses below $3\,\mathrm{GeV}/c^2$. These included narrow $\Xi_c(2680)$ and $\Xi_c(2760)$ states which coupled strongly to the $(D\Sigma)$, $(D_S\Xi)$ and $(D\Lambda)$, $(D_S\Xi)$ states, respectively. Also predicted were narrow $\Lambda_c(2815)$ and $\Sigma_C(2630)$ states which coupled strongly to the (DN),$(D_S\Sigma)$ states. States were also predicted with $C = 2$ and $C = 3$

Chapter 3

PEP-II and the *BABAR* detector

3.1 Introduction

The primary purpose behind the design and construction of the *BABAR* experiment was to create an ideal environment for precision studies of time dependent *CP* violation in the decays of neutral B mesons. The designs of every facet of the detector have been optimised to achieve these goals. However the detector has also the capability to provide precision measurements of decays of other processes, such as the decays of charm mesons and baryons, τ leptons or searches for the rare processes which become accessible at high luminosities. The detector was constructed at the Stanford Linear Accelerator Centre (SLAC) in order to take advantage of the 2km long SLAC linear accelerator (LINAC). The physics requirements, design and performance of the PEP-II B factory and the *BABAR* detector are described and discussed in this chapter.

3.2 The PEP-II B factory

3.2.1 Overview

The PEP-II B Factory is an asymmetric-energy e^+e^- collider, which operates at a centre of mass (CM) energy of 10.58 GeV. This energy corresponds to the $\Upsilon(4S)$ resonance, which decays almost exclusively to form pairs of B^+B^- and $B^0\overline{B}^0$ mesons in equal proportions. Therefore, this energy is ideal for the study of *CP* violating B mesons. The cross-sections for the production of fermion pairs at this energy are given in Table 3.1 and are taken from the *BABAR* Physics Book [160].

PEP-II has two storage rings the High Energy Ring (HER) containing 9.0 GeV/c electrons and the Low Energy Ring (LER) containing 3.1 GeV/c positrons. They are described fully in [161]. The beams are guided through vacuum tubes by magnets before being focused to collide in the *BABAR* detector.

Table 3.1: The cross-sections for the production in e^+e^- annihilations at this energy of 10.58 GeV. The figures for e^+e^- scattering only correspond to within the coverage of the detector. [160]

e^+e^-	Cross-section (nb)
$b\overline{b}$	1.05
$c\overline{c}$	1.30
$s\overline{s}$	0.35
$u\overline{u}$	1.39
$d\overline{d}$	0.35
$\tau^+\tau^-$	0.94
$\mu^+\mu^-$	1.16
e^+e^- (Bhabha)	40

The asymmetry in the energy of the two beams results in a Lorentz boost to the $\Upsilon(4S)$ resonance of $\beta\gamma = 0.56$. As the $\Upsilon(4S)$ resonance is only slightly over the threshold for the production of $B\overline{B}$ pairs the B mesons are produced almost at rest. The boost allows both B mesons to be reconstructed individually and their lifetimes to measured from their decay lengths. The lifetimes are important for the measurement of any (CP) time dependence of the decay-rates. It is also important that the $B\overline{B}$ pair produced are coherent, which enables their flavours to be tagged.

This boost makes it possible to reconstruct the decay vertices of both B mesons. This allows the relative decay times of the B mesons to be determined and therefore the time dependence of the decay rates can be determined.

PEP-II is also operated at an CM energy of 10.54 GeV, which is 40 MeV below the $\Upsilon(4S)$ resonance and hence below the threshold for $B\overline{B}$ production. Roughly 10% of data is taken at this energy, this data is called off-peak data. The data taken at this energy allows the study of the backgrounds from continuum ($q\overline{q}$) events ($e^+e^- \to c\overline{c}, s\overline{s}, , u\overline{u}, d\overline{d}$), which is important in B physics. Data taken at a CM energy of 10.58 GeV is called on-peak data in this thesis.

3.2.2 The injection system

An overview of the 3 km long LINAC and the PEP-II storage rings is shown in Figure 3.1. The LINAC system consists of an electron gun and a positron source which are followed by damping rings that focus the electrons and positrons before they are accelerated and injected into the PEP-II rings. Bunches of electrons are produced by the electron gun by using polarised laser light to remove electrons from a semiconductor surface. The electrons are accelerated to about 10 MeV and are focused by a number of cycles of a damping ring where the electrons perpendicular momentum is reduced through the emission of synchrotron radiation. These focused electrons are accelerated by the LINAC to an energy of 9 GeV using a series of klystrons and injected into the HER. Positrons are produced through the collision of 30 GeV electrons with a stationary tungsten target. Positrons are collected and focused in their own damping ring. The positrons bunches are then accelerated to an energy of 3.1 GeV by the LINAC and injected into the LER.

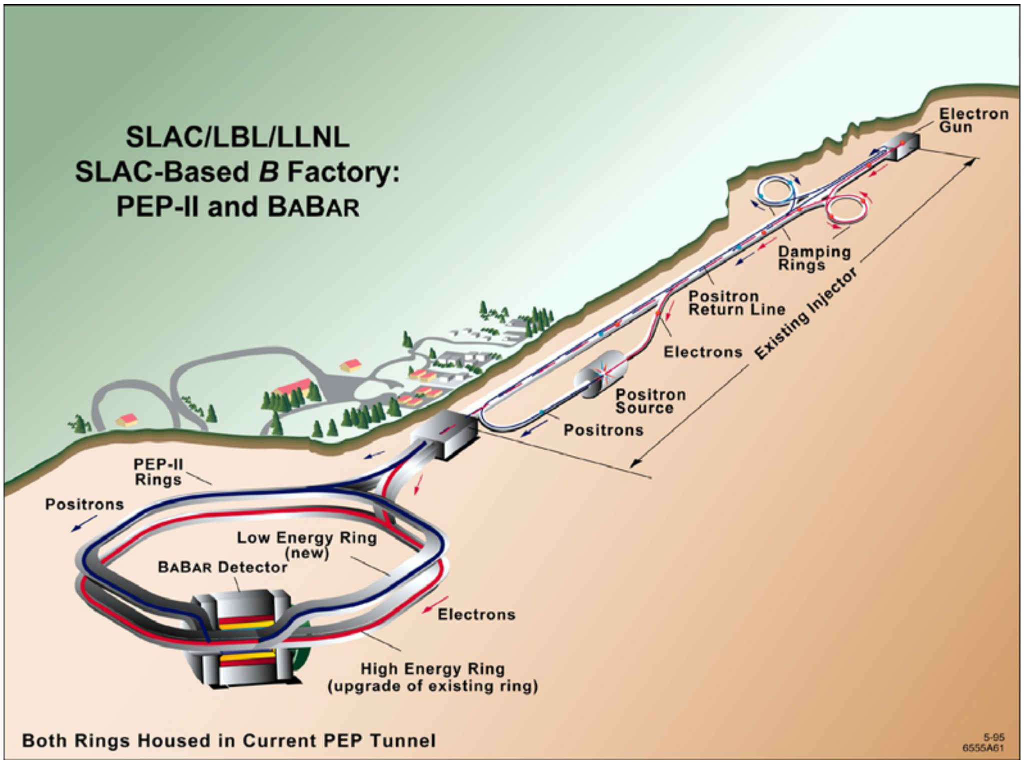

Figure 3.1: Overview of the Stanford Linear Accelerator Centre showing the Linear Accelerator and the PEP-II Storage Rings

3.2.3 The PEP-II beam

The parameters of the two beams are given in Figure 3.2.

Table 3.2: PEP-II Beam Parameters

Parameters	Design	Present
Energy HER (GeV)	9.1	9.1
Energy LER (GeV)	3.0	3.0
Current HER (A)	0.75	1.9
Current LER (A)	2.15	2.95
Number of Bunches	1658	1725
Luminosity ($10^{33} cm^{-2} s^{-1}$)	3	12
Luminosity (pb^{-1})	135	600

To optimise the performance of the *BABAR* detector it is necessary to monitor the luminosity, the beam energies and the position and size of the radiative region.

Luminosity is measured in *BABAR* is measured primarily by the production of electron-positron and muon-antimuon pairs, as both processes are well understood. The uncertainty in the measurement of the absolute value of the luminosity is 1.5%. Both the beam energies are calculated online using the total magnetic bending strength and deviation in the accelerating frequencies central values. The beam energies measured are accurate to within 1.1 MeV using data that corresponds to an integrated luminosity of $1\,\mathrm{fb}^{-1}$.

Beam position and size are measured by analysing the distance of closest approach (DOCA) to the collision axis of tracks in well measured two track events. The position and size are measured to an accuracy of a few μm in the transverse plane and $100\,\mu$m along the collision axis.

3.2.4 The interaction region

To achieve the required high luminosities the beams are divided into around 1500 small bunches to minimise the interference between the beams. The beams must be focused at the interaction point and then brought apart immediately to avoid secondary collisions. If the beams were not separated, secondary collisions would occur at a distance of ±62 cm from the interaction point with PEP-II operating at the design parameters.

Figure 3.2 shows a plan view of the interaction region. A number of magnets are used to bring the beams together so they collide head on and then to bring the beams apart again. The dipoles labelled B1 are located ± 21 cm about the interaction point and lie within the detector and therefore limit the acceptance of *BaBar* detector. The QF2 quadrapoles are used to focus the positrons in the LER. The Q4 and Q5 quadrapoles are used to focus the electrons in the HER. The Interaction Region is surrounded by water-cooled beryllium beam pipe. The inside of this pipe is coated with gold to reduce the synchrotron radiation.

3.2.5 Machine backgrounds

It is important that the machine backgrounds are monitored and well understood. Machine backgrounds cause the degradation of physics measurements and increase the trigger rate, which increases the dead-time of the detector and this makes it more likely that interesting physics events will be lost. They also contribute to the radiation damage in the detector.

The main sources of machine background are the synchrotron radiation, the beam-gas interactions, the beam-beam interactions and the radiative Bhabha scattering.

Synchrotron radiation is emitted as charged particles are accelerated in an electromagnetic field. It is more of an problem in the *BaBar* detector than at other electron positron colliders due to the complex optics described in Section 3.2.4 which are situated close to the detector in order to collide the two beams head on. Aspects of the interaction region, including the beam orbits, vacuum-pipe apertures

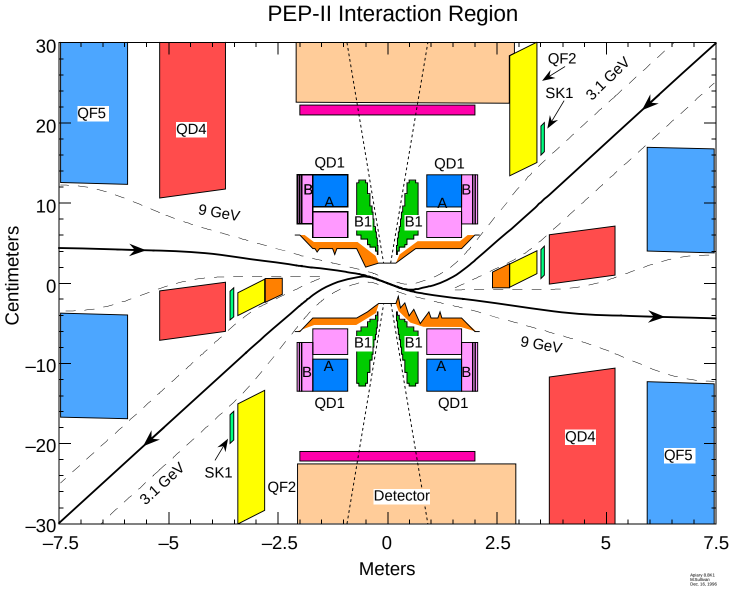

Figure 3.2: The PEP-II Interaction Region [162] The vertical scale is exaggerated

and radiation masks have been designed to reduce the impact of the synchrotron radiation. The majority of the synchrotron radiation is channelled away from the *BaBar* detector and the remainder is forced to be scattered multiple times before entering the detector's acceptance region.

Interactions between the beams and the residual gas in the beam pipe are another source of machine background. The particles in the beams undergo Bremsstrahlung and Coulomb scattering with the gas molecules and also the beam-pipe and detector. If either the scattering angle or energy loss caused by these interactions is large enough then beam particles are removed from the beams acceptance and can interact with the detector. The rate of beam-gas interactions is proportional to both the beam current and beam pressure, which also increases with the luminosity. This background has reduced with time as the synchrotron radiation removes the gas from the beam pipe.

Another source of machine backgrounds are beam-beam interactions. Particles in one beam can be deflected by the electric field of the other beam, removing them from the beams acceptance. These particles are then more likely to interact with the beam pipe or gas.

A further source of background is radiative Bhabha scattering. As Bhabha scattering is the scattering of a positron and electron they are inevitable in an electron-positron collider. The electrons and positrons lose energy and collide with the sides of the beam-pipe. When these interactions occur close to the IP debris from electromagnetic showers is picked up the *BaBar* detector. The process is proportional to the luminosity.

A number of systems exist to monitor the instantaneous and total radiation doses received by the subsystems within the *BaBar* detector. If the radiation levels get too high then the beam is cut off.

3.2.6 Performance

Since startup PEP-II has worked exceptionally well. The instantaneous and integrated luminosities specified in the design were both achieved in the first year of operation and the collider has consistently improved ever since. These improvements have been achieved by the improvement of PEP-II to allow for higher currents and smaller bunch spacing and also by changing the process in which the beams were filled.

Initially the beams worked with fill cycles of 40-50 minutes followed by a period of 3 minutes to replenish the beams. This was improved by the introduction of trickle injection in which both electrons and positrons are constantly injected at a rate of roughly 10Hz into the two storage rings. This removes the dead-time from process therefore increasing the achievable luminosity.

Figure 3.3 shows the daily and total integrated luminosities delivered by PEP-II and recorded by the *BaBar* detector at 15/05/2007. The effects of the introduction of trickle injection in March 2004 and improvements to PEP-II on the luminosity can be seen.

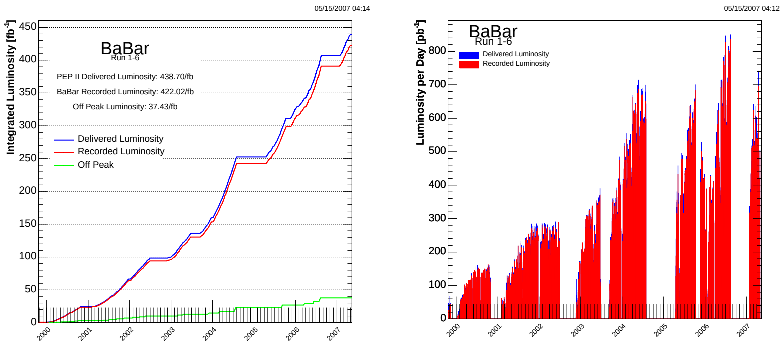

Figure 3.3: The daily (left) and total (right) integrated luminosities delivered by PEP-II and recorded by the *BaBar* detector [163].

3.3 The *BaBar* detector

The *BaBar* detector is described fully in the eponymous paper [162], all numbers quoted in this chapter are taken from there unless specified otherwise. The *BaBar* detector is a general purpose detector designed for measuring asymmetries in CP violation in the decays of B mesons. The detector is also well equipped for the study of other rare processes such as the decays of D mesons and τ

leptons and for spectroscopic studies that become attainable at high luminosities. To maximise the potential for physics analyses using the asymmetric PEP-II machine, the *BABAR* detector is offset from the interaction point by 37 cm along the z axis. This offset allows for the maximum possible coverage in the centre of mass frame of the $\Upsilon(4S)$. The *BABAR* detector was designed to fulfil the following requirements:

- high reconstruction efficiency for charged and neutral particles,
- good momentum resolution for charged particles in the range 60 MeV/c to 4 GeV/c,
- good angular resolution and energy resolution for neutral particles in the range 20 MeV to 4 GeV,
- Excellent particle identification for, $e^{\pm}$, $\mu^{\pm}$, $\pi^{\pm}$, $K^{\pm}$, p, $\overline{p}$, over a large range of momenta,
- vertex resolution that must be sufficient to measure the differences between B decay times. This is also required in order to vertex τ and charm decays,
- efficient and flexible trigger system that selects the interesting physics events whilst reducing the event rate to a level that the data acquisition system can deal with,
- the detector must be able to operate at the high radiation conditions expected at high luminosities without a reduction in performance.
- large quantity of data.

The actual performance achieved using the *BABAR* detector is discussed in quantitative terms in later sections.

The *BABAR* detector is shown in Figure 3.4 (longitudinal cross section) and Figure 3.5 (end view). The detector consists of the following sub-detectors:

- Silicon Vertex Detector — SVT: used for determining the vertex positions of particles decaying close to the interaction point.
- Drift Chamber — DCH: The main component of the tracking system
- Detector of Internally Reflected Cherenkov Light — DIRC: used for particle identification.
- Electromagnetic Calorimeter — EMC: used to measure the energies of particles.
- 1.5T magnet: used to bend the paths of charged particles which is necessary for momentum based particle identification.
- Instrumented Flux Return — IFR: used to detect muons and neutral hadrons.

Each of these sub-detector systems is discussed in detail later in this chapter.

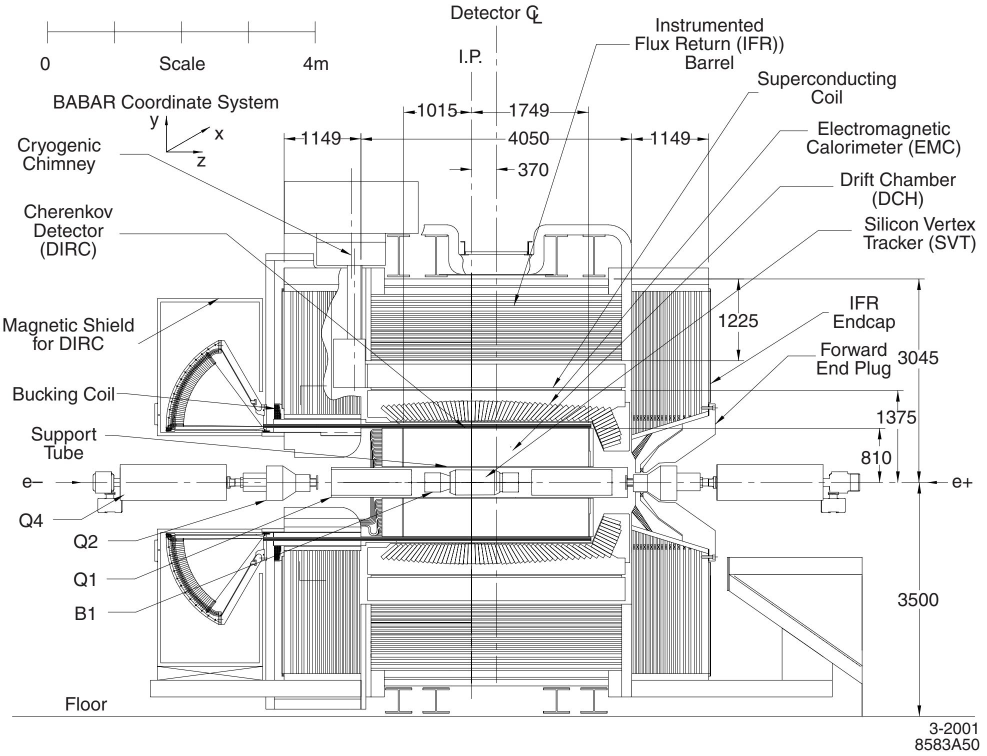

Figure 3.4: Longitudinal section of the *BABAR* detector [162]

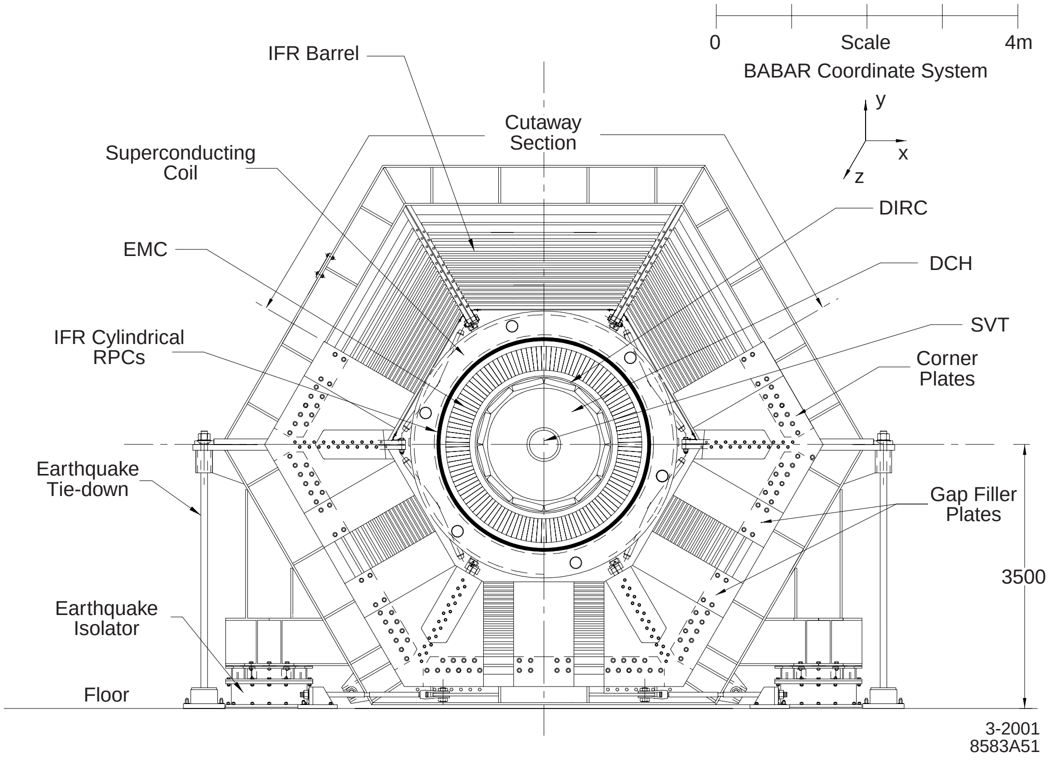

Figure 3.5: End view of the *BABAR* detector [162]

3.3.1 The *BaBar* coordinate system

The *BaBar* detector has a right handed coordinate system that is centred on the interaction point. The z axis corresponds to the central axis of the drift chamber and points in the direction of the HER. It differs from the direction of the HER by 20 mrad. The y axis points vertically upwards and the x axis points horizontally away from the centre of the PEP-II rings. The polar and azimuthal angles, θ and ϕ, are defined as in the standard polar coordinate system. When the asymmetric nature of the detector is described the forward region is that in the positive $+z$ direction and the backward region is in the negative $-z$ direction.

The tracks of particles within the detector are characterised using five parameters which are calculated at the point of closest approach to the z axis. These parameters are:

- d_0 — the distance of closest approach to the z axis,
- z_0 — the distance from the origin along the z axis at which d_0 is measured,
- ϕ_0 — the azimuthal angle of the track,
- λ — the dip angle of the track with respect to the $x-y$ plane,
- ω — the curvature of the track which is related to the transverse momentum of the track, p_T, by the formula $\omega = 1/p_T$.

3.4 The Silicon Vertex Tracker

3.4.1 Physics requirements

The Silicon Vertex Tracker (SVT) is the innermost tracking detector. Its main purpose is to provide precision measurements of the positions of the vertices of short lived particles, such as B mesons, D mesons and τ leptons. This is required for the study of time-dependent CP violating decays. In order to separate the vertices from two B mesons, the SVT is required to have a resolution along the z axis of $80\,\mu$m. While, to separate the vertices of D mesons in decays such as $B^0 \to D^+D^-$ a resolution of $100\,\mu$m in the $x-y$ plane is required.

The SVT is very important for detecting low momenta particles, such as the soft pion from D^* decays, because only charged particles with transverse momenta greater than 120 MeV/c can be detected reliably with the Drift Chamber. It provides measurements of the ionization loss $\mathrm{d}E/\mathrm{d}x$, which is used for particle identification for charged tracks with a momentum less than 700 MeV/c.

3.4.2 Design

The SVT consists of 5 layers of double sided silicon strip sensors that surround the beam-pipe. The innermost three layers (1-3) are flat whilst the outer two layers (4 and 5) are arch shaped. Each sensor has a strip on each side which are mounted orthogonally to each other. The strips used for measuring ϕ are mounted parallel to the beam axis whilst those for measuring z are mounted transversely. The transverse and longitudinal cross sections of the SVT is shown in Figure 3.6 and Figure 3.7, respectively. The layout of these sensors are as shown in the figure with each layer consisting of 6, 6, 6, 16 and 18 modules respectively. The three inner layers provide impact parameter measurements, whilst the outer two layers are needed for pattern recognition and low momentum tracking.

The SVT sensors are built on high resistivity $(6 - 15k\Omega/cm)$ n type Silicon substrates with p+ strips and n+ strips on either side. Insulation of the n+ strips is provided by individual p-stops. When a charged particle passes through the strip electron hole pairs are produced and a current flows between a pair of strips. As you know which two strips were involved you have the position of the event. As well as the sensors, the design of the front end electronics had to meet stringent requirements. A custom chip the ATOM IC was deigned to meet these requirements.

The angular coverage of the SVT is limited by the B1 magnets and extends to a polar angle with respect to the beam line of 20.1° in the forward direction and 150.2° in the reverse direction.

The SVT was required to be capable of withstanding a total dose of 2MRad of ionising radiation. The expected typical daily doses of radiation were 1Rad for the horizontal plane adjacent to the beam pipe and 0.1Rad elsewhere. There are systems installed, which monitor the radiation dose received by the SVT and cut off the beam if required. The SVT is required to be reliable and robust, because the SVT is inaccessible during detector operations.

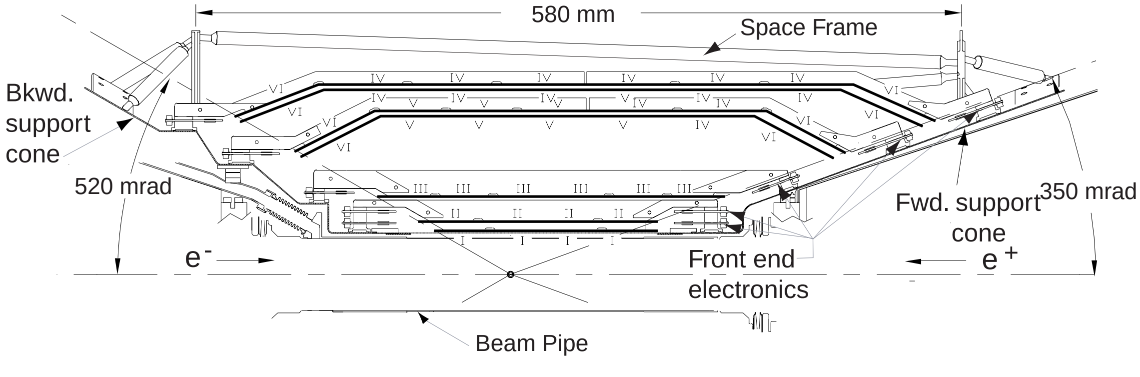

Figure 3.6: Longitudinal schematic view of SVT [162]

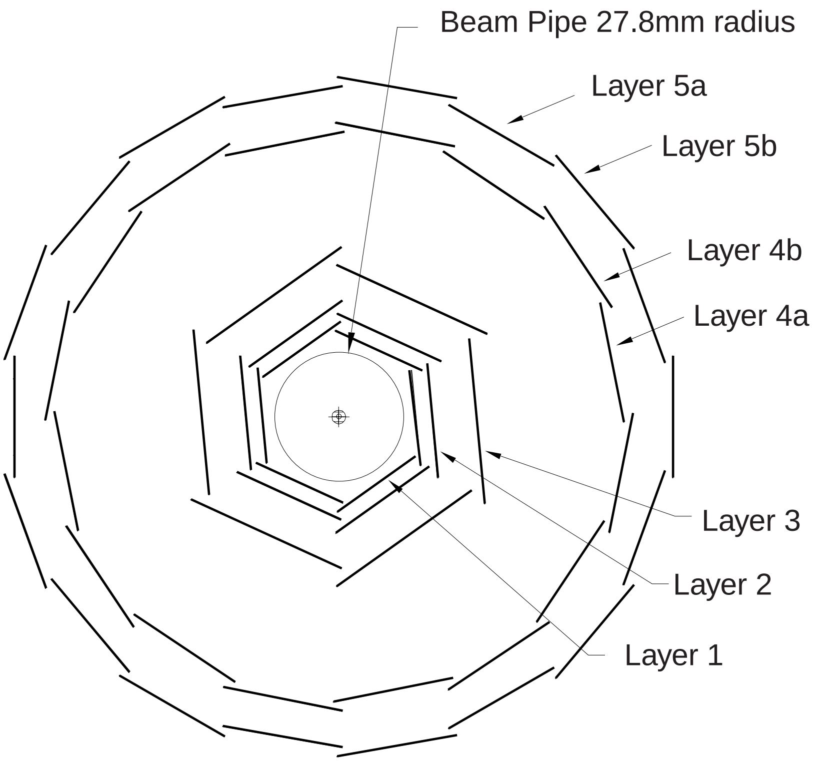

Figure 3.7: Transverse schematic view of SVT [162]

3.4.3 Performance

Good alignment of the SVT is essential to get accurate measurements of the position and momentum. The local alignment measures the position of the modules with respect to each other and the global alignment measures the position of the SVT with respect to the other detector subsystem. Tracks from $e^-e^- \rightarrow \mu^+\mu^-$ and cosmic ray events are used to calibrate the position of the SVT.

A resolution along the z axis better than $23\,\mu$m allows B decays to be fully reconstructed making the SVT critical for the measuring time dependent CP violation. A resolution in the x-y plane of less than $29\,\mu$m enables D mesons to be separated from B^0 decays. The three dimensional vertex resolution is better than $70\,\mu$m. Stand-alone tracking of particles with momentum less under 120 MeV/c is provided with a tracking efficiency of greater than 70%.

The dE/dx resolution is approximately 14% this allows the 2 standard deviation separation of pions and kaons with a momentum below 500 MeV/c and of kaons and protons below 1 GeV/c.

During a $1\,\mu$s window the occupancy of the SVT is 3% for the inner layers mainly due to beam induced background and 1% in the outer layers where noise hits dominate. Excluding the 9 out 208 defective read out sections, a combined hardware and software efficiency of 97% is measured.

3.5 The Drift Chamber (DCH)

3.5.1 Physics requirements

The drift chamber (DCH) is the principal tracking system of the *BABAR* detector and works in conjunction with the SVT. It is required to make precision measurements of the momenta and angular momenta of charged particles. These measurements are required to enable the reconstruction of exclusive B and D meson decays with small backgrounds.

The DCH is solely responsible for the reconstruction of vertices from decays and interactions that occur outside the SVT volume. These include the decays of K^0_S mesons and $\mathit{\Lambda}$ baryons. In order to achieve this the DCH measures the longitudinal positions of tracks as well as their transverse momenta and positions.

The DCH also provides information to the charged particle trigger. For particles with low momenta the DCH provides particle identification information by measuring the ionization loss, $\mathrm{d}E/\mathrm{d}x$. In the barrel region this information is used in conjunction with that from the DIRC, but the particle identification of charged tracks in both extreme forwards and backwards directions is solely reliant on the DCH. The material in front of and inside the DCH is kept to a minimum in order to reduce multiple scattering which is a major limiting factor on the determination of track parameters.

The DCH provides tracking and timing information to the trigger and must be capable of performing in the presence of large beam generated backgrounds.

3.5.2 Design

The drift chamber is situated outside the SVT and forms a cylinder almost 3 m long with a radius of 809 mm, the inner radius, inside which the SVT is situated, is 236 mm. The longitudinal cross section of the DCH is shown in Figure 3.8. The interaction point is not located in the centre of this cylinder but is shifted in the direction of the boost in the $+z$ direction. This is due to the asymmetric nature of the beams which causes the majority of charged tracks to travel in the forward direction. The boost allows the more accurate reconstruction of these tracks.

The DCH consists of 40 cylindrical layers of small hexagonal cells. These cells provide up to 40 measurements of the position and ionization loss for charged particles with momenta greater than 180 MeV/c. Information about the longitudinal position is obtained by orienting the wire in 24 of the 40 layers at a small angles to the beam. The layers are grouped in fours to form 10 super-layers. The super-layers are split into axial (A), and positive and negative stereo (U and V), the super layers are ordered AUVAUVAUVA. Figure 3.9 shows the layout and orientation of the drift cells in the first four super-layers. It can be seen that the wires in super-layers 2 and 3 are oriented at a small angle whilst those in super-layers 1 and 4 are not. The stereo angle is shown in the right column in units of mrad The stereo angle in the super-layer vary from ±45 mrad in the inner layers to ±76 mrad in the ninth super-layer.

The DCH is filled with gas, which is an 80:20 mixture of helium and isobutane. This has a radiation length of 807m, this along with the low mass aluminium wires reduces multiple scattering in the detector. It has a Lorentz angle of 32° which gives a uniform relationship between time and distance enabling a good spatial resolution. The $\mathrm{d}E/\mathrm{d}x$ resolution of the DCH is 6.9%.

Each of the hexagonal drift cell consists of a single gold plated Tungsten-Rhenium sense wire surrounded by 6 field wires. The sense wire is $20\,\mu$m in diameter and the diameters of the field wires are either $80\,\mu$m or $120\,\mu$m. The drift wires are made from gold plated aluminium. A high positive voltage is applied to the sense wires whilst the field wires are grounded. The design voltage was 1960V, but because a number of DCH cells were damaged during the commissioning of the detector some data in run one was taken at a voltage of 1900V. The voltage was raised to 1930V for the Run2 data taking period and this voltage has been applied ever since.

The main purpose of the drift chamber is to measure the curvature of a charged track and hence its momentum. This is done by combining a number of hits together to form a track. A DCH hit occurs when a charged particle passes through a drift cell and ionises the gas molecules which liberates electrons. The liberated electrons are accelerated by the electrons and ionise further gas molecules causing an avalanche of charge to travel towards the sense wire. The gain is approximately 5×10^4 at an operating voltage of 1960V. The drift times are determined using the leading edge of this charge avalanche. The resolution of the drift times is 1 ns and this can be used to extract position information. The total amount of charge deposited is used to determine the energy loss as particles travel though the drift chamber.

Figure 3.10 shows the isochrones, contours of equal drift times in two layers. The isochrones are roughly circular close to the sense wires but near the guard wires at the edge of the cells the isochrones are more irregularly shaped. Ions that originate in the gaps between super-layers are picked up in the surrounding layers after a time lag of a few μs. This does not affect the drift times but does have an impact on the measurement of $\mathrm{d}E/\mathrm{d}x$.

The inner cylindrical wall is kept as thin as possible to allow SVT and DCH tracks to be matched, improve high momentum tracks' resolution and minimise the background from photon conversions and interactions. Material in the outer wall and in the forward direction are also minimised to reduce the effect on the DIRC and EMC.

The electronics from the drift chamber are installed in three front end assemblies. The signals from the drift chamber super-layers are amplified and digitised by amplifier digitiser boards and the output is organised by a readout interface board. This information is passed to the trigger and data input output modules.

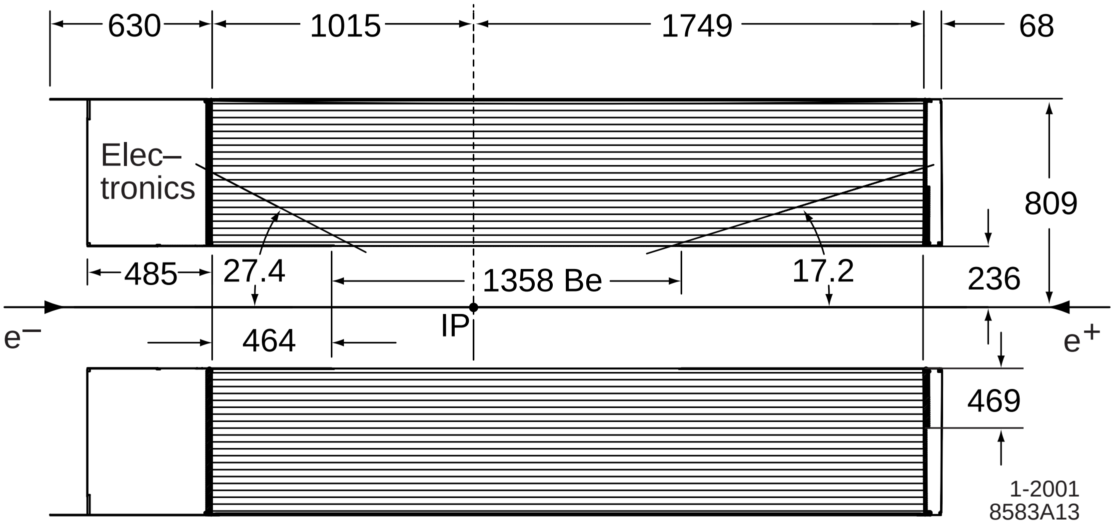

Figure 3.8: Schematic view of the longitudinal section of the drift chamber [162]

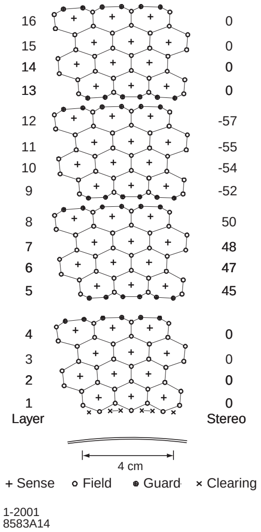

Figure 3.9: Schematic layout of the drift cells in the four innermost super-layers. The lines between the field wires have been added to aid visualisation of the cell boundaries. The column of numbers on the right are the stereo angles (mrad) of the sense wires in each layer. [162]

3.5.3 Performance

The relationship between the track positions and drift times in the DCH is calibrated using two-prong events such as $e^-e^- \to \mu^+\mu^-$ and Bhabbha scattering. The calibration is done for each of the DCH cells, the tracks are fitted excluding the point from the cell in question. The drift distance is then

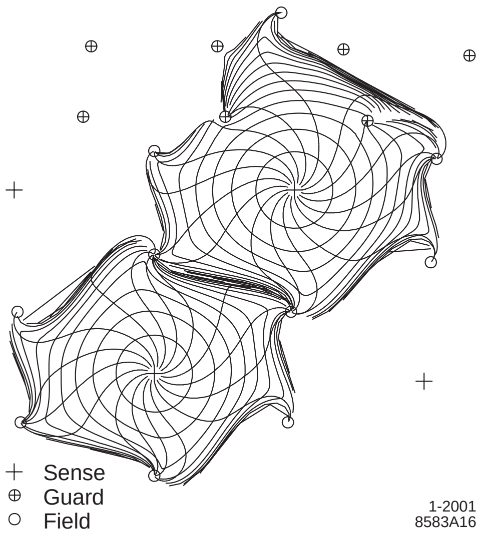

Figure 3.10: Drift cell isochrones, contours of equal drift times. The isochrones are spaced by 100ns [162]

estimated by calculating the distance of closest approach of this track. The measurements of $\mathrm{d}E/\mathrm{d}x$ are also calibrated to account for biases from various sources such as the temperature and pressure of the gas.

The track reconstruction efficiencies are determined using the method described in the *BABAR* tracking efficiency studies [164] and [165]. The *BABAR* detector has two tracking detectors the DCH and the SVT. This makes it possible to measure the efficiency of tracks in the DCH using the number of hits in the SVT. The method started with a track in the SVT and measured how often a corresponding track was found in the DCH. The tracking efficiency was studied for tracks with a transverse momentum $p_T > 100\,\mathrm{MeV}/c$.

To calculate the raw track reconstruction efficiency tracks that have as least 10 hits in the SVT were compared. The number of these tracks that pass the selection criteria for GoodTracksLoose was divided by the number that pass the selection criteria for GoodTracksVeryLoose. The selection criteria for GoodTracksLoose and GoodTracksVeryLoose are listed in Table 4.1 in Section 4.2.1. For tracks with $p_T > 100\,\mathrm{MeV}/c$ the only difference between these two selection criteria is that at least 12 hits in the DCH were required to pass the GoodTracksLoose selection criteria. Thus, this method calculates the tracking efficiency of the DCH.

Sometimes, through the combination of noise hits, it is possible to form fake tracks in the SVT. It is possible to determine how many fake tracks are formed using data from Bhabha events. The detection rate of these fake tracks is calculated by dividing the number of fake tracks by the total number of Bhabha events.

Based on the assumption that fake tracks are as common in Bhabha events as in events of other types, it is possible to determine the total expected number of fake tracks, N_f, by multiplying this rate by the total number of events.

Thus the tracking efficiency ϵ_{TRK} is given by

$$\epsilon_{TRK} = \frac{\text{Number of GoodTracksLoose with 10 SVT hits}}{\text{Number of GoodTracksVeryLoose with 10 SVT hits} - N_f} \tag{3.1}$$

The track reconstruction efficiency was investigated as a function of the tracks transverse momentum p_T, the angles ϕ and θ of the tracks in the lab frame along with the track multiplicity. The output of this study was a look up table binned in these four quantities with the tracking efficiency correction calculated for each of these bins. Because the tracking efficiencies are dependent on the conditions in the detector, the efficiency corrections are applied separately for events from each of the different data taking periods used within this analysis. One condition that affects the track reconstruction efficiency is the voltage between the field and sense wires in the drift chamber.

The track reconstruction efficiency in the DCH is shown in Figure 3.11. The track reconstruction efficiency is shown as a function of the transverse momentum and angle θ in the lab frame. The average track reconstruction efficiency with the detector is 96.1% $\pm$ 1% at both the design voltage and 1930V.

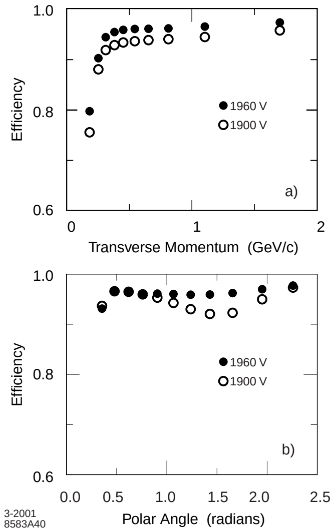

Figure 3.11: Track reconstruction efficiency in the Drift Chamber at operating voltages of 1960V and 1900V. The top plot (a) shows the efficiency as function of the tracks' transverse momenta. The lower plot shows the efficiency as a function of θ. [162]

Figure 3.12 shows the resolution of the impact parameters d_0 and z_0 as a function of the tracks transverse momentum. The resolution of these parameters is an important aspect of this analysis as they are used as selection criteria to determine whether the tracks in an event originate from the beam.

The resolution in the transverse momentum was derived using cosmic muons and found to be described by the formula

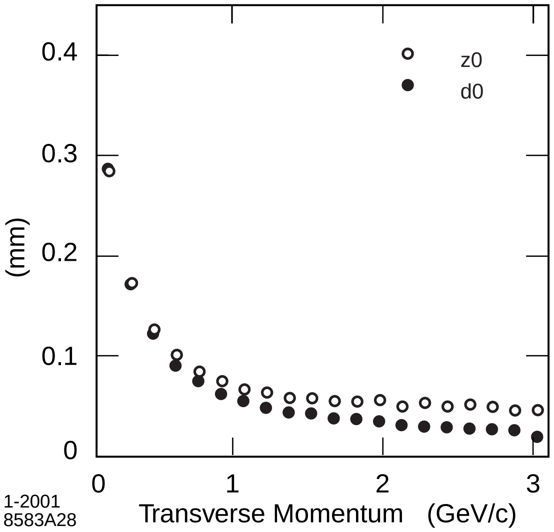

Figure 3.12: The resolution of the parameters d_0 and z_0 as a function of the transverse momentum. [162]

$$\frac{\sigma_{p_T}}{p_T} = ((0.13 \pm 0.01)\% \times p_T) + (0.45 \pm 0.03)\% \tag{3.2}$$

where p_T is the transverse momentum given in units of GeV/c. This is in good agreement with the design values and that obtained using Monte Carlo simulations.

Figure 3.13 shows dE/dx measured in the DCH as a function of the track momenta. The curves show the Bethe-Bloch predictions for charged particles of different masses. The RMS resolution is 7.5%, which is close to the design value of 7%. This is important for the identifications of particles with low momenta in this analysis.

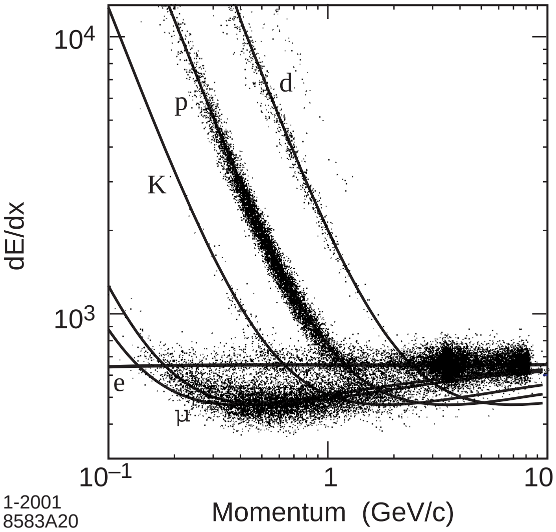

Figure 3.13: Measurement of dE/dx in the DCH as a function of the track momenta. The curves show the Bethe-Bloch predictions [162]

3.6 The Cherenkov Detector (DIRC)

The Detector of Internally Reflected Cherenkov Light (DIRC) is the main particle identification system for charged particles at BABAR. Differentiating between pions and kaons is important for tagging the flavour of one of the B mesons whilst reconstructing the other decay. It is also useful for differentiating between rare two-body decays $B^0 \rightarrow \pi^+\pi^-$ and $B^0 \rightarrow K^{\pm}\pi^{\mp}$. This means that the π/K separation is required to be better than 4σ for decays from the pion Cherenkov threshold to 4.2 GeV/c. For particles with a momentum less than 700 MeV/c the dE/dx information from the DCH and SVT is used for particle identification.

The DIRC is required to be thin and uniform in terms of radiation lengths so as not to effect the energy measurements from the calorimeter.

3.6.1 Design

Cherenkov light is produced when charged particles travel through a medium faster than the speed of light in that medium. The angle at which the Cherenkov light is emitted, the Cherenkov angle, θ_c is related to the velocity of the particle, v, by the equation $\cos\theta_c = 1/n\beta$, where n is the refractive index of the medium and $\beta = v/c$ and c is the speed of light. The DIRC takes advantage of the fact that when the Cherenkov light is reflected off a flat surface, the angles of reflection are maintained. The DIRC is made of 144 4.9 m long bars, which are manufactured from fused silica. These bars are oriented parallel to the beam and arranged in blocks of 12 bars to form a dodecagonal barrel. The refractive index of fused silica is 1.473, which enables the bars to act both as a medium for producing Cherenkov radiation and also a waveguide. A schematic of one of these fused silica bars is shown in Figure 3.14.

Cherenkov light travelling forwards is reflected by a mirror that is placed at the front end of the DIRC in order to avoid instrumenting both ends. The light that has been guided to the rear end of the detector is allowed to exit through a fused silica wedge into the standoff box which is an expansive region filled with purified water. Water has been used because it has approximately the same refractive and chromacity indices as the fused silica which minimises any refraction at the surface where the two materials meet. Light is focused by a pinhole defined by the aperture of the bar. The light travels though about a metre of water before being detected by an array of 10,752 photo-multiplier tubes (PMT)s. Each PMT is 2.82 cm in diameter. In front of each PMT is a hexagonal light catcher, which increases the effective active surface area to 90%.

Between the main detector body and the stand off box is a bucking coil which reduces the magnetic field around the PMTs.

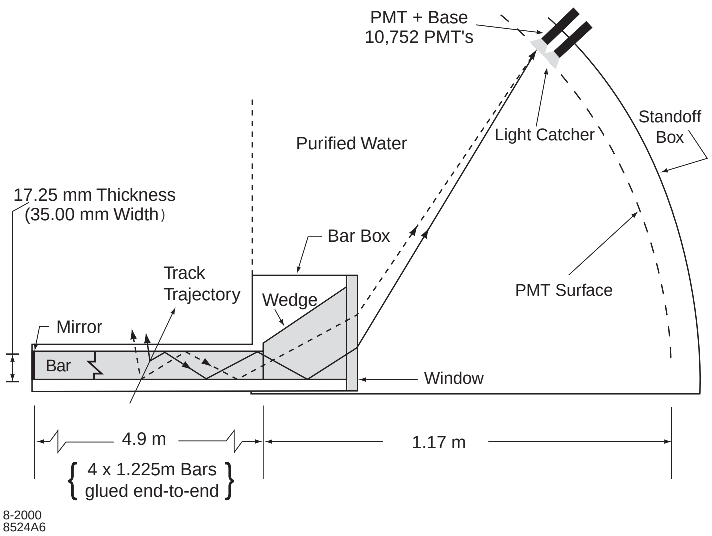

Figure 3.14: Schematics of a DIRC fused silica bar and the imaging region [162]

The DIRC is essentially a three dimensional imaging device using the position and arrival time from the PMTs. The vector between the middle of the bar and the centre of each PMT is a measurement of the photon propagation angles. As the track positions and angles are already known, these vector angles can be used to calculate the Cherenkov angles. An extra constraint is provided by the arrival times of the photons. The front end electronics measures the arrival times of the Cherenkov photons with an accuracy limited by the 1.5ns transit time spread of the PMT. It has a pipeline to deal with the latency in the Level-1 trigger.

The DIRC has a coverage of 94% in the azimuthal angle and 83% in polar angle. It contributes 17% of a radiation length for tracks travelling perpendicularly.

3.6.2 Performance

The angular resolution and time resolution of the DIRC are measured using dimuon events. The angular resolution of single photon is roughly 1 mrad. The measured time resolution is 1.7 ns. The resolution in the Cherenkov angle of a track is inversely proportional to the square root of the number of Cherenkov photons. This angular resolution is typically 2.5 mrad. The $\pi^{\pm}$-$K^{\pm}$ separation that is achieved as a function of momentum is shown by Figure 3.15. It can be seen that at a momenta of 3 GeV/c a $\pi^{\pm}$-$K^{\pm}$ separation of 4 is achieved.

3.7 Electromagnetic Calorimeter (EMC)

The Electromagnetic Calorimeter, EMC, is a positional calorimeter. The EMC is important because it is the only detector capable of detecting photons and therefore the detector is required to efficiently

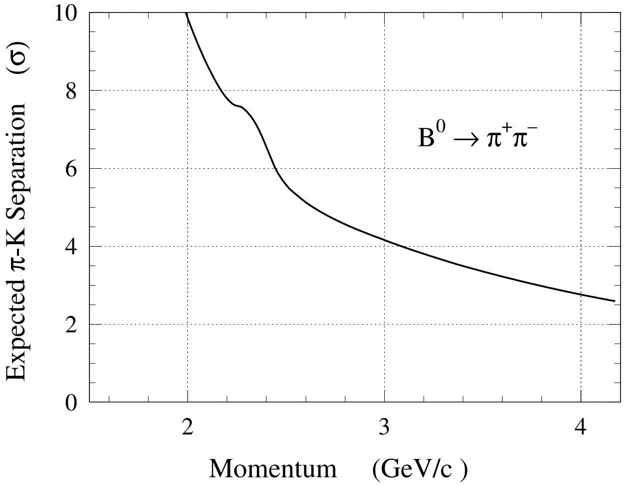

Figure 3.15: The separation between kaons and pions achieved with the DIRC as a function of momentum [162]

detect photons with good angular and energy resolution. The EMC detects electromagnetic showers over energies ranging from 20 MeV to 9 GeV. This allows the detection of photons from the decays of π^0 and η which are commonly found in B meson decays. The energies of the photons in 50% of these decays are below 200 MeV. The EMC is required to detect photons from radiative and electromagnetic processes which can have energies up to 9 GeV. These processes are used extensively in calibration. The EMC is used in the identification of electrons, which contributes to flavour-tagging in the semi-leptonic decays of neutral B mesons, the reconstruction of vector mesons such as the J/ψ and the reconstruction of semi-leptonic B and D meson decays. The EMC outputs cluster and timing information to the Level 1 Trigger every 269 ns.

3.7.1 Design

The EMC is manufactured from a total of 6580 Thallium doped Caesium Iodide (CsI(Tl)) scintillating crystals. It consists of a cylindrical barrel and a conical forward end-cap. The barrel section consists of 48 rings, each containing 120 identical crystals. The end-cap consists of 820 crystals arranged in 8 rings. The crystals are arranged so they are pointed towards the IP in ϕ and in the general direction of the Interaction Point (IP) in θ. They are not pointed directly at the IP in order to stop photons being lost in the gaps between the crystals. The layout of the crystals in the EMC is shown in Figure 3.16. The EMC has full coverage in ϕ and covers angles in θ between 15.8° to 141°. This corresponds to 90% coverage in the centre of mass frame.

The crystals were made from CsI(Tl) as this has a high light yield and small Moliere radius, enabling the EMC to have excellent angular and energy resolution. The short radiation length allows

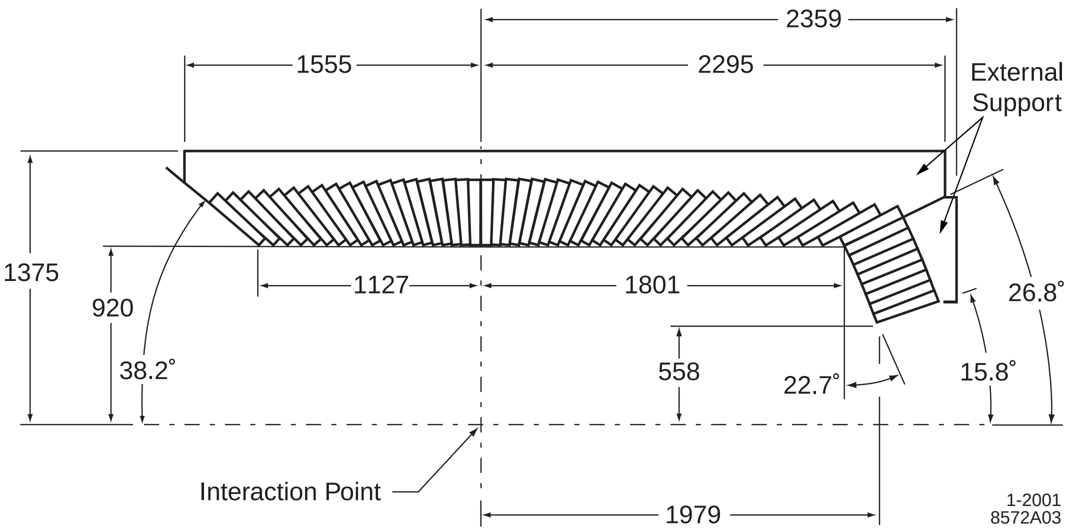

Figure 3.16: Side-view of top half of EMC [162]

for electromagnetic showers at the energies typically found at BaBar to be contained within shorter crystals, which means that the design of the EMC can be relatively compact. The schematic of a typical crystal is shown in Figure 3.17.

The crystals are trapezoidal in shape and there length ranges from 29.6 cm in the backward direction to 32.4 cm in the forward direction. This corresponds to a radiation length X_0 between 16.1 and 17.6. The front face of each crystal is typically 4.7 cm × 4.7 cm which is comparable with the size of the Moliere radius. This means that the energy is spread into neighbouring crystals creating clusters. In order to minimise the leakage of photons to and from adjacent crystals, each crystal is surrounded with a reflective coating. An aluminium foil coating is used to shield the crystals.

The scintillated light from each crystal is collected by two silicon photo-diodes glued to the back of each crystal. The signals from the two photo-diodes from each crystal are amplified, digitised and sent along a fibre optic cable to the readout modules. When a L1 trigger signal is received all samples within a time widow of 1 μs are selected for feature extraction.

3.7.2 Performance

The total energy collected by the two photo-diodes is not equal to the amount of energy that is deposited in the crystal. Therefore, each crystal needs to be calibrated in order to determine the relationship between the physical energy deposited and the light yield that is collected. The calibration utilises photons and electrons of known energies. At low energies photons from a 6.13 MeV radioactive source are used. At higher energies the relationship between the angles and the energies of the photons from Bhabha events is utilised. In addition to the calibration of individual crystals the cluster energy needs

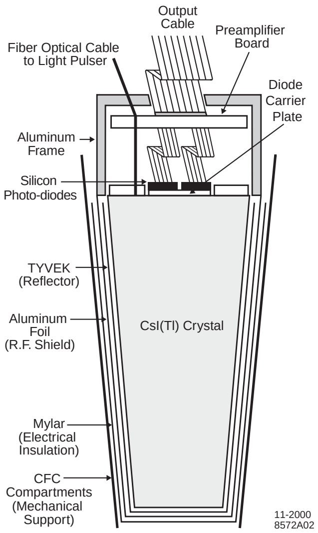

Figure 3.17: Schematic of an EMC Crystal [162]

to be calibrated. This is necessary because the energy deposited within a single crystal is unlikely to be the total energy of the incident particle which is necessary for improved positional resolution. Corrections are required for the leakage between crystals, absorption by the material in front of and between the crystals and also any energy deposited that is not associated with the incident particle. For energies below 0.8 GeV this cluster calibration uses $\pi^0 \rightarrow \gamma\gamma$ decays.

The energy resolution is parameterised in the following formula ($\oplus$ corresponds to the addition of the two terms in quadrature)

$$\frac{\sigma_E}{E} = \frac{(2.32 \pm 0.32)\%}{\sqrt[4]{E(\,\mathrm{GeV})}} \oplus (1.85 \pm 0.12)\% \tag{3.3}$$

The energy dependent term originates primarily from photon statistics but is also sensitive to noise in the photon detection and electronics. The constant term arises due to variations in the light collection, leakage or adsorption in the material in between and in front of the crystals and any uncertainties from the calibration process. The energy resolution is plotted in Figure 3.18. The energy resolution varies from about 5% at 6.13 MeV to 1.9% at 7.5 GeV.

The angular resolution of the EMC for photons from π^0 decays is parametrised in the following way.

$$\sigma_\theta = \sigma_\phi = \frac{(3.87 \pm 0.32)\%}{\sqrt{E\,\mathrm{GeV}}} \oplus (0.00 \pm 0.04) mrad \tag{3.4}$$

The angular resolution as a function of energy determined from π^0 decays is shown in Figure 3.19. The reconstructed π^0 mass width is measured to be 135.1 MeV/c^2 and this is stable over the full

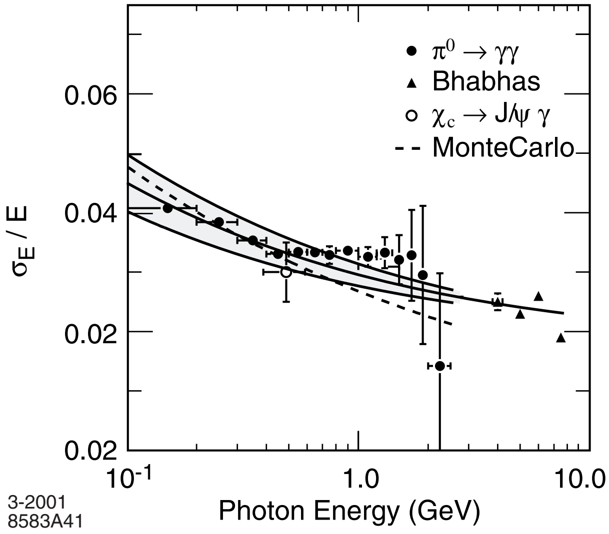

Figure 3.18: The energy resolution of the EMC for electrons and photons originating from various processes [162]

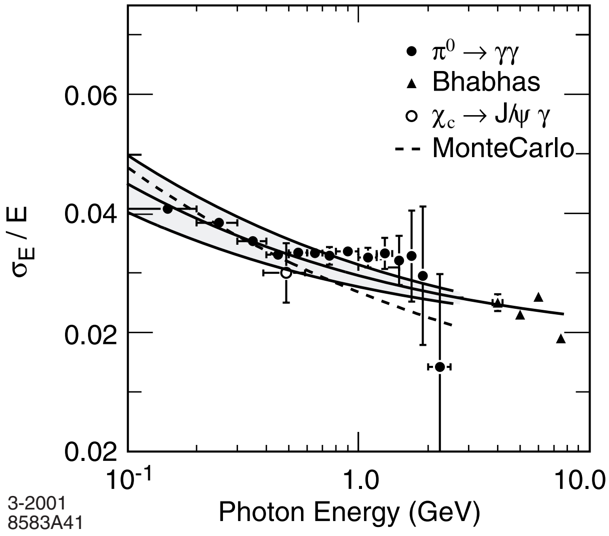

Figure 3.19: The angular resolution as a function of energy of the EMC for electrons and photons from π^0 decays [162]

energy range of the photons.

Electrons are separated from charged hadrons mainly using the energy measurements from the EMC. This information is combined with that from the DCH and the DIRC. The most important variable for the discrimination of hadrons is the ratio of the energy to the track momentum. Photons and electrons typically deposit all their energy within the EMC, whilst muons travel straight through the EMC depositing very little energy. Pions and kaons can interact causing hadronic showers or travel through the EMC without interacting. The lateral and longitudinal shapes of hadronic showers and electromagnetic showers are different, which allows for further discrimination. The electron efficiency and pion misidentification probability as a function of the particle momentum and polar angle in the laboratory frame in Figure 3.20 and electrons are identified with an efficiency of 94.8% in the momentum range $0.5 < p < 2\,\mathrm{GeV}/c$.

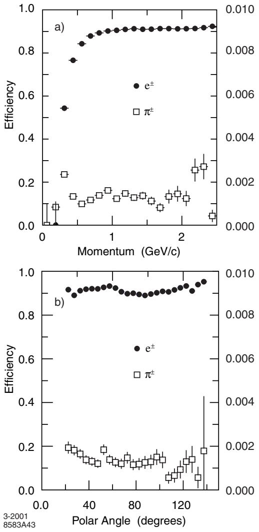

Figure 3.20: The electron efficiency and pion reconstruction efficiency as a function of (a) the particles' momentum and (b) the polar angle in the laboratory frame. [162]

3.8 Instrumented Flux Return

The instrumented flux return (IFR) identifies muons and detects K_L^0, neutrons and other neutral hadrons. The IFR is the flux return for the 1.5T magnet and provides much of the support structure for the rest of the detector. The detection of muons is important for tagging the flavour of neutral B mesons via semi-leptonic decays, the reconstruction of vector mesons including the J/ψ and the study of semi leptonic and rare decays of B mesons, D mesons and τ leptons. The detector is designed to resolve muons at momenta below $1\,\mathrm{GeV}/c$. The detection of K_L^0 is important as it allows the study of exclusive B decays such $B^0 \to J/\psi\, K_L^0$.

3.8.1 Design

The layout of the IFR is shown in Figure 3.21.

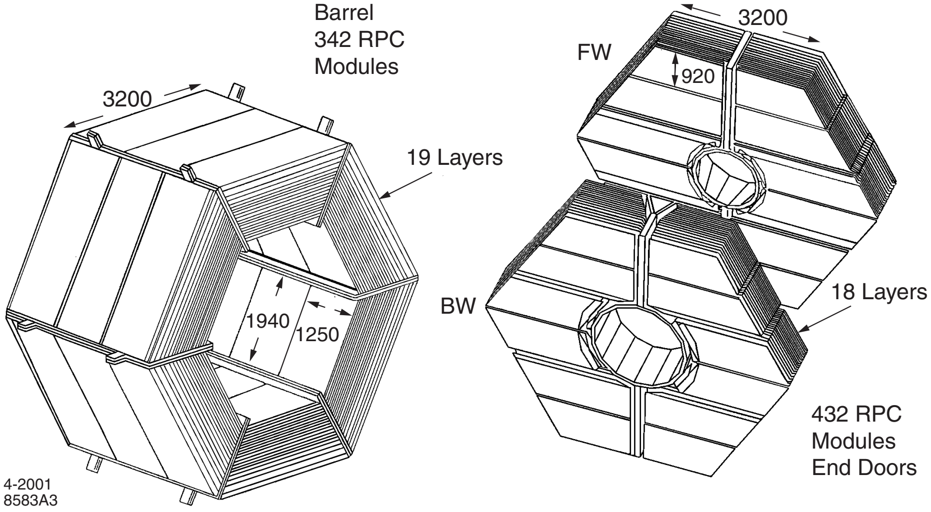

Figure 3.21: Overview of the IFR showing the barrel and the forward (FW) and backward end-caps [162]

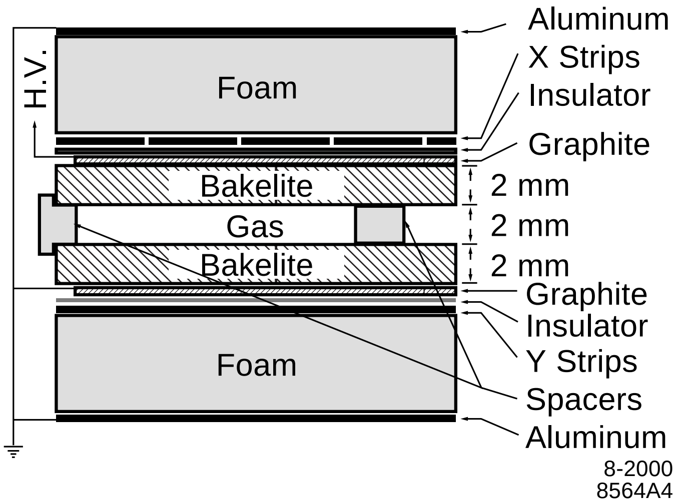

Figure 3.22: Cross section of a planar RPC [162]

The IFR uses the steel flux return of the magnet as a muon filter and neutral hadron absorber. The detectors are resistive plate chambers (RPC) with a two coordinate readout. The cross section of an RPC is shown in Figure 3.22. There are 19 layers of RPC's in the barrel and 18 in the end-cap. The RPCs consist of two sheets of 2mm thick Bakelite separated by 2 mm of gas. The Bakelite is coated with graphite, the two graphite surfaces are connected to high voltage and the readout is made through aluminium electrodes. The RPCs detect streamers from ionising particles via capacitive readout strips with a time resolution of 1-2 ns and a position resolution of a few mm. The strips are connected to front end cards which each handle 16 channels. Signals from 3300 FECs are connected to eight custom IFR crates which process the strip readings and time information and output the data to the readout modules.

During the operation of the *BABAR* experiment, the performance of the RPC modules has reduced significantly with time. The 18 layers of RPCs in the barrel were replaced with Limited Streamer Tubes, LSTs. In order to increase the efficiency of the muon detection 6 of the RPC layers were replaced with brass absorbers. The LSTs consist of a resistive tube, which acts as the cathode, with a wire strung down the centre, which acts as the anode. A high positive voltage is applied to the anode and the cathode is connected to ground.

3.8.2 Performance

The IFR at *BABAR* suffered from a number of problems A mean muon detection efficiency of 90% in the momentum range $1.5 < p < 3\,\mathrm{GeV}/c$ was achieved in the summer of 1999. This efficiency had dropped to under 50% in 2002. Because this efficiency would decrease further, the end-cap RPCs were replaced with more efficient double gap chambers and the six barrel sections were replaced with LSTs. The detection efficiency returned to 90%.

The K^0_L detection efficiency varies between 20% and 40% in the momentum range between 1 to $4\,\mathrm{GeV}/c$.

3.9 Trigger

The purpose of the *BABAR* trigger is to select interesting physics events whilst rejecting background events, thus reducing the total event rate to an acceptable level (below 120Hz), so that the data can be processed by the data acquisition system and stored. The trigger efficiency is required to be high stable and well understood. At the design luminosity the total rate of the background events from synchrotron radiation, beam gas interactions and radiative Bhabha scattering is roughly 20kHz. As the *BABAR* experiment is now operating well in excess of the design luminosity, the rate of the background events will be higher. The trigger is also required to select events for diagnostic, efficiency and background studies.

The *BABAR* trigger system at *BABAR* is implemented in a two-level hierarchy. There is a Level 1 trigger implemented in hardware followed by a Level 3 trigger in software.

3.9.1 Level 1 trigger

The Level 1 trigger, L1T, is the first stage and is implemented in hardware. The bunch crossing rate of PEP-II is about 238MHz and the L1 trigger is required to reduce the total event rate to under 2kHz. There is no event data as such from the L1T and the selections are based on the event topology. The L1T is divided into three independent systems the Drift Chamber Trigger (DCT), the Electromagnetic Calorimeter Trigger (EMT) and the IFR Trigger (IFT), which deal respectively with data from the DCH, EMC and IFR. The information from the SVT cannot be processed quickly enough to be used in the trigger.

Each of these trigger systems produces trigger primitives which are used to inform a higher level trigger that a certain criteria has been met. The combined primitives provide a summary of the energy and momentum of the particles detected. These primitives are passed on to a Global Level Trigger (GLT), which is activated if various logical combinations occur .

The DCT takes data from each of the 7104 cells. Track segments are found and these are combined to form complete tracks which are compared with a momentum threshold. The output from the DCT is ϕ maps for short tracks, long tracks and high p_T tracks. The EMT analyses the sum of energy deposited in the calorimeter crystals. The IFT is used for triggering on $\mu^+\mu^-$ and cosmic rays for mainly diagnostic purposes.

The outputs from each of these triggers are sent to a global trigger which is operated as logical OR. These outputs are filtered and events matching certain criteria are passed on to the level 3 trigger. The efficiency of the Level 1 trigger are greater than 99.9% for $b\ \overline{b}$ events, 99.9% for charmonium events and 98.2% for $u\ d\ s$ events. The output from the Level 1 trigger is roughly 1kHz.

3.9.2 Level 3 trigger

The second part of the *BABAR* trigger system is the Level-3 Trigger. The level 3 trigger software is run on the Online Event Processing (OEP) computer farm, consisting of several hundred nodes and each event is processed by a single node. The software has access to all of the data from the event. The purpose of the Level-3 trigger is to reduce the data rate from 1kHz to below 120Hz, which is the rate at which the online prompt reconstruction system can accept data. The L3T trigger is activated when a L1A signal is received from the L1T. Algorithms are run to find tracks and clusters and events can be reconstructed and selections on the topology of clusters and tracks are applied.

The desired physics events consist of 13% of the total output from the L3T trigger whilst those required for calibration make up 40%. The efficiencies of the Level 3 trigger are greater than 99.9% for $\overline{b}$ events, 98.9% for charmonium events and 95.8% for $u\ d\ s$ events.

The output lines from the L3T can be rescaled in order to reduce the amount of data recorded from high luminosity processes such as Bhabha scattering and $e^- e^- \to \mu^+ \mu^-$ events. These events are required for calibration and luminosity measurements but at nowhere near the vast rate at which they occur.

A number of events, which do not meet the Level-3 trigger are accepted anyway at a set prescaled rate. This enables the efficiencies to be calculated and these events are known as "Level-1 Pass Through" Events.

All events that are accepted by the L3T are written out of the buffers and stored permanently.

3.10 The Data acquisition system

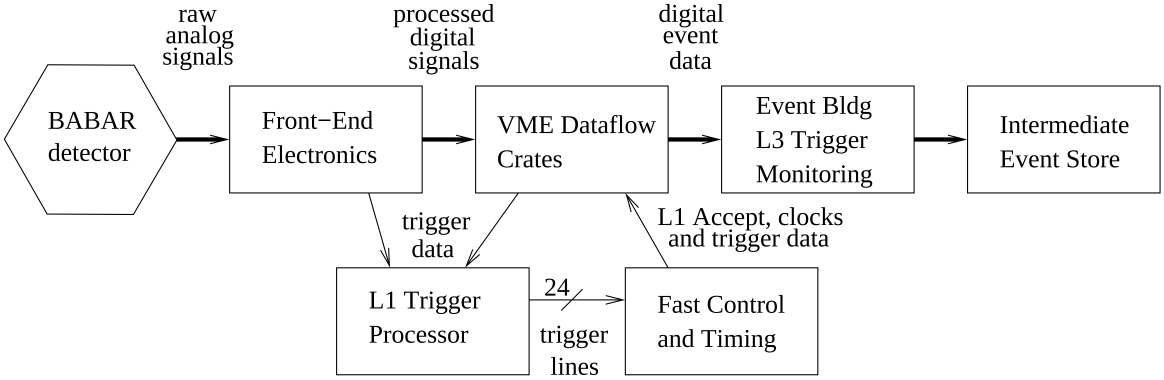

Figure 3.23: Schematic diagram of the data acquisition process at *BaBar* [162]

A schematic of the data acquisition DAQ system is shown in 3.23. The DAQ system links the detector and the trigger system with the *BaBar* online computing system. The main goal of the DAQ process is to transfer the data from the detector to the event store whilst minimising the deadtime. The DAQ system starts from the front end electronics FEEs, which take the raw measurements from the individual detector subsystems and perform some amplification and signal shaping. The FEEs pass data to the L1T and if this data passes the trigger conditions it is allowed to pass through the dataflow crates to the L3T. If this data is accepted by the L3T then it is written to disk and stored in the event store. The DAQ system can also interface with the trigger system, which is required for calibration purposes. The conditions of the detector are stored. These include the luminosities and currents of the beams, the temperature, gas supply purity, the status of the high voltage supply and so on. These are stored in a conditions database and can be associated with the data from events taken at the time. These conditions are used in further processing of the *BaBar* data as well as being used in the generation of Monte Carlo simulated events (discussed in Section 4.4).

3.11 Online reconstruction and data quality

The data that are written to disk are processed by the Online Prompt Recognition (OPR) software. This takes raw data from the detector, such as the DCH hits and crystal energies, and converts these into the physical quantities used in analyses, such as particle energies and momenta.

The OPR process consists of two parts: firstly Prompt Calibration (PC), secondly Event Reconstruction (PC).

PC is run over small subsets of data that are large enough to monitor the data quality and calculate calibration constants. PC is performed on four dedicated computer farms at SLAC and is typically done within a few hours of the data being written to disk.

ER is a longer process that is run over every event and is normally completed within a few days of the events being logged. Reconstruction routines are run in which charged tracks and energy clusters are reconstructed from the raw detector hits. These routines are discussed in Sections 4.2.1 and 4.2.2. The ER software is run on 10 dedicated computer farms spread between SLAC and in Padova, Italy.

The data quality is monitored, in both PC and ER, by the Data Quality Group (DQG). This group consists of experts on each of the detectors' subsystems, who check that the event distributions from each subsystem are acceptable and that data have not been lost through detector failures or distorted due factors such as high backgrounds.

When modifications are made to the *BABAR* reconstruction software, the data are reprocessed in PC and ER. Only data which are deemed usable for physics by the Data Quality Group are used in physics analyses.

Chapter 4

Offline event reconstruction and Monte Carlo simulation

4.1 Introduction

The event reconstruction routines at *BABAR* used the raw hits from the *BABAR* detector and converted them into the tracks and clusters that are stored in the event store. Particle Identification routines were run to identify the charged tracks. Tracks were vertexed together to reconstruct K_S^0, K^{*-}, and $R(3520)$ candidates for further use in the analysis. Monte Carlo simulated events were also required for the interpretation of the data.

4.2 Track and cluster reconstruction

4.2.1 Track reconstruction

The track reconstruction algorithms in the online prompt reconstruction, OPR, used the tracks found by the Level 3 Trigger as a start point. A fitting technique based on a Kalman filter [166] was applied to the DCH hits associated with these tracks. This technique also made allowances for the variations in the magnetic field and interactions with the material in the detector. Additional hits that were consistent with being associated with these tracks were included and the Kalman fit was performed again. These tracks were used to give an improved estimate of the collision time. Additional track finding code was applied to the DCH hits from tracks that did not span the whole DIRC or originate from the interaction point. All the tracks from the DCH were extrapolated back into the SVT and hits consistent with these tracks were added to these and a further Kalman fit is performed. Hits in the SVT which are inconsistent with the DCH hits are subjected to a final track finding algorithm to search for those mainly low momentum tracks that interact only with the SVT.

The performance and efficiency of the track finding algorithms described here are discussed in Section 3.5.3.

Depending on their quality, these tracks were banked in lists in the Event Store which were used for further processing. The selection criteria that were used for the tracking lists in BABAR were detailed in Table 4.1 [167]. The cuts given in the table are the tracks': minimum transverse momentum (p_T), maximum momentum p, minimum χ^2, maximum distance of closest approach to the z-axis ($DOCA_{XY}$), maximum distance from the origin along the z axis at which $DOCA_{XY}$ is measured ($DOCA_Z$), and the minimum and maximum angles (θ). This analysis used tracks from the ChargedTracks list in the reconstruction of the K_S^0 candidates and the GoodTracksAccLoose list was used for the other tracks involved in this analysis.

Table 4.1: Requirements of the tracking lists used at BABAR

List	# DCH Hits	$p_T >$ GeV/c	$p <$ GeV/c	$\langle\chi^2\rangle >$	$DOCA_{XY} <$ cm	$\lvert DOCA_Z\rvert <$ cm	$\theta >$ rad	$\theta <$ rad
ChargedTracks	0	NA	NA	NA	NA	NA	NA	NA
ChargedAccTracks	0	NA	NA	NA	NA	NA	0.41	2.54
GoodTracksVeryLoose	0	0	10	0	1.5	10	NA	NA
GoodTracksLoose	12	0.1	10	0	1.5	10	NA	NA
GoodTracksAccLoose	12	0.1	10	0	1.5	10	0.41	2.54
GoodTracksTight	20	0.1	10	0	1	3	NA	NA

4.2.2 EMC cluster recognition

Clusters were found by looking for individual crystals that had energy deposits of greater than 10 MeV. The neighbouring crystals were examined and those with an energy deposit greater than 1 MeV were added to the cluster, the crystals surrounding the cluster are examined and those with high enough energy were added. This process continued until there were no adjoining crystals with the requisite energy can be found.

When a cluster was found a bump finding algorithm was run over all its constituent crystals to determine whether the cluster originated from multiple showers. The algorithm looked for local energy maxima within the cluster. A further algorithm tried to associate these clusters with tracks. If these clusters can be associated with a track then the cluster was stored with the track. Any unmatched cluster was assumed to originate from a neutral particle and was stored in a list in the event store.

4.2.3 Vertexing

Vertexing is the process of finding the best estimate of the intersection point of a number of tracks in three dimensions. Due to the errors present in all the measurements there is no unique point through which all the reconstructed tracks pass the problem therefore needs to be solved with some kind of optimisation process.

In this analysis the vertexing was done using the TreeFitter vertexer which is described in a paper by W. Hulsbergen [168]. The TreeFitter vertexer was based on a Kalman Filter and allowed the entire decay chain to be fitted at once calculating the correlations between all the candidates. The Kalman filter is a least χ^2 fitting method which adapts a set of parameters to a set of data points. Geometric constraints were applied which ensured that the tracks originated from the same vertex. Kinematic constraints were also applied which ensure that the momentum, of the tracks originating from the same vertex, was conserved at the vertex.

4.3 Particle identification (PID)

After the track reconstruction and cluster finding processes had been completed, Particle Identification, PID, selectors were used to process each track. Information from a number of the subdetectors in the *BaBar* detector was used in the PID selectors. The information used depends on the type of particle being selected and is also constrained by the interactions of each individual track.

Each PID selector used probability distribution functions (PDF) to evaluate the likelihood that a track is the type of particle that the selector was designed to select. At *BaBar*, five different mass hypotheses for charged particles were used, these were in increasing order of mass: electron; muon; pion; kaon and proton. The PID selectors can be run in a number of modes which allow the user to strike the balance between purity and efficiency in the analysis.

Control samples are important in designing PID selectors and measuring the purities, efficiencies and misidentification rates achieved with the selectors. These control samples are not selected using PID information, instead well known physics processes and kinematics are used to select the highly pure samples.

For kaons the $D^{*+} \to D^0\pi^+, D^0 \to \pi^+K^-$ decay was used, because the kaon and pion can be separated by kinematics. For pions the $K^0_S \to \pi^+\pi^-$ decay were used, the K^0_S candidates decay away from the interaction region and are easy to identify. For protons the $\Lambda \to p\pi^-$ is used, because Λ decay away from the interaction region. For muons $e^+e^- \to \mu^+\mu^-\gamma$ events are used. For electrons, radiative Bhabha events are used.

The final state analysed in this thesis involves four pions, a kaon and a proton in the final state.

So the proton, kaon and pion selectors are of interest in this analysis. However, electron and muon selectors are also used as electron and muon vetos are present in some of the PID selectors.

The analysis uses the likelihood selectors for the selection of kaons, protons and pions these are described in more detail on the PID web-page [169].

The idea behind the likelihood selectors is to calculate a likelihood for each particle hypothesis L_i. This likelihood is calculated using the formula below:

$$L_i = L_{i_{SVT}} \times L_{i_{DCH}} \times L_{i_{DIRC}} \tag{4.1}$$

where, $L_{i_{SVT}}$, $L_{i_{DCH}}$, and $L^{i_{DIRC}}$ are the likelihoods for that particle hypothesis from the SVT, DCH and respectively.

The likelihoods for the DCH and SVT the measured $\mathrm{d}E/\mathrm{d}x$ is compared with the $\mathrm{d}E/\mathrm{d}x$ expected from the Bethe-Bloch parameterisation. The quantity used is the pull which is equal to the difference between the measured and expected values of $\mathrm{d}E/\mathrm{d}x$ divided by the error. Then the DCH likelihood is calculated using a Gaussian PDF and the SVT likelihood is calculated using a Bifurcated Gaussian PDF.

The DIRC likelihood cannot be calculated in this manner because there are heavy tails on the distributions of the fitted Cherenkov angle and the number of photons. The global likelihood for the DIRC also suffers from these heavy tails. To reduce the effect of these tails, a new likelihood is constructed using the Cherenkov angle, number of photons and track quality. This new likelihood is found from a lookup table that is binned in momentum in the laboratory frame, the measured Cherenkov angle and finally a probability calculated using the track quality and the number of photons. Only three bins are used for the Cherenkov angle, these bins correspond to the bands for pions, kaons and protons.

These lookup tables were filled using Monte Carlo truth-matched tracks. The likelihoods in these lookup tables are the probabilities that the Monte Carlo truth-matched tracks have the measured quantities of that bin.

The binned DIRC likelihoods are designed to deal with the tails in the response of the DIRC, especially those near the particle thresholds. At higher momentum the binned likelihood does not separate well the Cherenkov angle bands. To improve matters these binned likelihoods are multiplied by a Gaussian likelihood based on the Cherenkov angle for tracks with a momentum greater than 1.5 GeV/c.

The likelihood selectors consist of cuts on the relevant likelihood ratios. Table 4.2 lists the requirements of the likelihood selectors used in this analysis. This information is taken from the PID web-page [170]. For each selector the cuts on the quantities $\frac{L_K}{L_K+L_\pi}$, $\frac{L_K}{L_K+L_p}$, $\frac{L_p}{L_p+L_\pi}$ are given where these quantities are the likelihood the track is a kaon and not a pion, the likelihood the track is a proton and not a kaon and the likelihood the track is proton not a pion. The final two columns in the table detail whether the muon and electron vetos are applied. The electron veto are only applied above a momentum threshold p the value of these momentum thresholds are also given in the table.

Table 4.2: Requirements of the LH based PID selectors used at *BABAR*

List name	$\frac{L_K}{L_K+L_\pi}$	$\frac{L_K}{L_K+L_p}$	$\frac{L_p}{L_p+L_\pi}$	!eLHTight	!muLHTight
p Selectors					
pLHVLoose		< 0.75	> 0.5		
pLHLoose		< 0.3	> 0.5	$p < 0.75$ OR true	
pLHTight		< 0.2	> 0.75	$p < 0.75$ OR true	
pLHVTight		< 0.1	> 0.96	$p < 0.75$ OR true	true
K Selectors					
KLHVLoose	> 0.50	> 0.018		$p < 0.40$ OR true	
KLHLoose	> 0.8176	> 0.018		$p < 0.40$ OR true	
KLHTight	> 0.9	> 0.2		$p < 0.40$ OR true	
KLHVTight	> 0.9	> 0.2		$p < 0.40$ OR true	true
π Selectors					
piLHVLoose	< 0.98		< 0.98		
piLHLoose	< 0.82		< 0.98	true	
piLHTight	< 0.5		< 0.98	true	
piLHVTight	< 0.2		< 0.5	true	true

4.4 Monte Carlo simulation

Monte Carlo simulated data plays an important role in particle physics, without it the interpretation of real data would be impossible. In this analysis, Monte Carlo simulated data were used in order to evaluate selection criteria and to calculate the signal efficiencies.

The first strange involved the event generator `EvtGen` [171], which was used to generate $\overline{b}$ and hadronic continuum events ($q\overline{q}$, where $q = u$, d, s, c) using `JETSET` [172]. Other Monte Carlo generators were used within *BABAR* to model Bhabba, $\mu^+\mu^-$ $\tau^+\tau^-$ and two photon events. Although none of these were used directly within this analysis, they were used indirectly for purposes including the evaluation of tracking efficiencies.

Each event was generated from the 3-momenta of the electron and positron and a primary vertex position. As a part of this process the beam energies and the position of the primary decay vertex of an event were varied to reflect what happens in the PEP-II collider. Gaussian distributions of ranges $160\,\mu$m and $8\,\mu$m were used to smear the x and y coordinates, respectively. The z coordinate of the interaction region was allowed to vary along a uniform distribution over a range of 1cm. The electron and positron form an intermediate particle, which was then allowed to decay. For each event a list of the decay particles was generated along with the vector 4-momentum and vertex positions for each particle in this list.

The next stage involved the simulation of the passage of the generated particles though a model of the *BABAR* detector. The interactions with the detector were simulated using `GEANT` 4 model of the detector. `GEANT` 4 [173] outputed a detector hit when a passing particle interacted with part of a sub-detector.

The response of the *BABAR* electronics system to these detector hits was modelled by `SimApp`. `SimApp` modelled the flow of the data from the interactions with Front End Electronics through the Trigger system right though to the DAQ crates. The simulated data was outputed in the same format as that produced by the *BABAR* detector. In order to make the simulation as realistic as possible the conditions and dead channels recorded during the running of the detector were also used within the simulation.

Real beam background events recorded with the *BABAR* detector were added to simulated data at this stage. Because the trigger conditions that were used when these beam background events were recorded, the probability that interesting physics events were incorporated in these events was slim.

The final stage in the production of Monte Carlo simulated data was to process it with the same reconstruction software as was used for data. The only major difference was that the truth information was stored along with the data for each event. The truth information contained the decay chains, momenta, and vertex positions, of the particles generated in each Monte Carlo event. This enables the reconstructed variables to be compared with their generated values.

In the study presented in this thesis the Monte Carlo simulated data used in this analysis was generated by the *BABAR* collaboration.

Monte Carlo samples were used for optimising the selection criteria for K^0_S and K^{*-} candidates. Their contents are detailed in Table 4.3 and Table 4.4, respectively. The various components were mixed in the proportions given in the *BABAR* Physics Book [160].

Table 4.3: MC data sample used for K^0_S selection study

Data Type	Data Set	Number of Events
Data	AllEventsSkim-Run1-OnPeak-R16a	2,000,000
$u\ d\ s$ MC	SP-998-AllEventsSkim-R16a	836,000
$c\overline{c}$ MC	SP-1005-AllEventsSkim-R16a	520,000
B^+B^- MC	SP-1235-AllEventsSkim-R16a	216,000
$B^0\overline{B}^0$ MC	SP-1237-AllEventsSkim-R16a	216,000
$\tau^+\tau^-$ MC	SP-3429-AllEventsSkim-R16a	356,000
Total MC		2,144,000

For detection efficiency studies, two signal Monte Carlo data samples were generated using the

Table 4.4: MC data sample used for $K^{*\pm}$ selection study

Data Type	Data Set	Number of Events
$u\ d\ s$ MC	SP-998-AllEventsSkim-R16a	12,540,000
$c\overline{c}$ MC	SP-1005-AllEventsSkim-R16a	7,800,000
B^+B^- MC	SP-1235-AllEventsSkim-R16a	3,240,000
$B^0\overline{B}^0$ MC	SP-1237-AllEventsSkim-R16a	3,240,000
$\tau^+\tau^-$ MC	SP-3429-AllEventsSkim-R16a	5,790,000
Total MC		13,044,000

method described in [115] and used in searches for the Θ^+ and Ξ^{--} at *BABAR*. They were produced using `EvtGen` with the special parameter settings of the `JETSET` generator. An existing baryon, the Σ_c^0 was used as a substitute for $R(3520)$ with the mass, width and decay channel forced appropriately. The production mode for the substitute was assumed to be through the decay of the $c\ \overline{c}$ states produced in e^+e^- interactions. The substitute's mass and width were set to $3.52\,\mathrm{GeV}/c^2$ and $0.001\,\mathrm{GeV}/c^2$ respectively which are similar to the values given for these parameters in [156]. Two samples of signal Monte Carlo simulated data were generated, one in which the substitute particle's decay mode was forced to $K_S^0\ \pi^-\ \pi^-\ p\ K^+$ and another one where the decay mode was forced to $K^{*-}\ \pi^-\ p\ K^+$. From the generated events those which contained at least one of the substitute particles were retained. The samples of signal Monte Carlo simulated data with the decay modes $K_S^0\ \pi^-\ \pi^-\ p\ K^+$ and $K^{*-}\ \pi^-\ p\ K^+$ are referred to in this thesis as SP6050 and SP6051, respectively.

Chapter 5

Event selection

A search has been carried out for the $R(3520)$ state in e^+e^- interactions. Two inclusive reactions were studied $e^+e^- \to K^+p\pi^-\pi^-K^0_S+X$, and $e^+e^- \to K^+p\pi^-K^{*-}+X$. The decay mode $K^+\ p\ \pi^-\ \pi^-\ K^0_S$ was analysed because the $R(3520)$ state was reported in this system by Karnaukhov et al. [156]. The decay mode $K^+\ p\ \pi^-\ K^{*-}$ was studied as Karnaukhov et al. [156] reported that the state decayed through a K^{*-}.

In order to ensure that the baryon number was conserved, these inclusive modes were also searched for with the extra requirement that there was an additional baryon in the final state.

5.1 Datasets

The data sample used in this analysis comprises the Runs 1-4 data collected with the *BaBar* detector at the PEP-II asymmetric e^+e^- storage ring from 1999 until 2004 and amounts to an integrated luminosity of $227.89\,\mathrm{fb}^{-1}$. Of this data roughly 90% (10%) was taken above (below) the resonance of the $\Upsilon(4S)$ at a c.m. energy of $\sqrt{s} = 10.58\,\mathrm{GeV}(10.54\,\mathrm{GeV})$.

In order to reduce the volume of data processed, a skim was written and included in the R16c skim-cycle. The skim was a fast filter that only processed events with at least 6 tracks. From these events those which contained at least one K^0_S identified with the KsDefaultMass criteria, one p identified with the pLHLoose criteria, one K^+ identified with the KLHLoose criteria and two π^- identified with the piLHVeryLoose criteria were selected.

All data and Monte Carlo were processed with software from the Analysis-26 release of the *BaBar* analysis software with the recommended extra-tags.

5.2 K^0_S selection

5.2.1 Variables used in the K^0_S selection

The sample of K^0_S candidates that were used in this study were selected from those candidates which met the KSTight selection criteria. These candidates were reconstructed from pairs of oppositely charged tracks with the mass of a charged pion assigned to both of these tracks. These pairs of charged tracks were vertexed together using the TreeFitter vertexer with geometric constraints. The TreeFitter vertexer, described in [168], used a Kalman filter to perform a χ^2 fit at the vertex. This allowed the entire decay chain to be vertexed at once, by calculating the correlations between all the candidates. The geometric constraints required that the two tracks originated from the same point in space. Only K^0_S candidates that had a χ^2 probability of the vertex greater than 0.001 and a flight length significance F_{Sig} greater than 3 were selected. The candidates mass calculated at the point of closest approach (POCA) was required to be within $\pm\,50\,\mathrm{MeV}/c^2$ of the K^0_S PDG mass [1].

To improve the purity of the K^0_S sample, the selection criteria introduced by W. Dunwoodie and J. Coleman in [115] were used. They are briefly described here.

In the standard lists and vertexers, which were used to select K^0_S candidates at BABAR, no geometric requirements were placed on the distance between two tracks that were combined to reconstruct a K^0_S candidate, at their POCA. This caused oddities in the position of the vertex of these K^0_S candidates. This included the reconstruction of K^0_S candidates with vertices in the IFR and K^0_S candidates with tracks separated by distances of several meters at their POCA. Therefore, the distance of closest approach, DOCA, between the two charged tracks was used as a selection criteria.

The path of the reconstructed K^0_S candidates (the vector sum of the π^+ π^- momenta at their POCA) should pass close to the interaction point (IP) for most physical processes of interest. The collision axis was defined in [115]. R_{XY} was defined to be the distance of closest approach to the collision axis in the XY plane. R_Z was defined to be the position along the Z axis where this distance of closest approach is measured.

When reconstructing K^0_S candidates, it is possible to reconstruct vertices that are inverted with respect to their outward direction from the collision axis. These vertices should have a negative signed flight length. The signed flight length (SFL) was defined by the following formula:

$$SFL = (\pm 1) \times \sqrt{(X_V - X^{AP}_{K^0_S})^2 + (Y_V - Y^{AP}_{K^0_S})^2 + (Z_V - Z^{AP}_{K^0_S})^2} \tag{5.1}$$

where,

(X_V, Y_V, Z_V) was the position of the vertex of the K^0_S candidate and

$(Z^{AP}_{K^0_S}, Z^{AP}_{K^0_S}, Z^{AP}_{K^0_S})$ was the point of closest approach between the the fitted momentum of the K^0_S

candidate and the collision axis.

The sign of SFL is given by $\hat{n}.\hat{p}$, where

$\hat{n}$ was a unit vector in the direction from $(X^{AP}_{K^0_S}, Y^{AP}_{K^0_S}, Z^{AP}_{K^0_S})$ to (X_V, Y_V, Z_V) and $\hat{p}$ was a unit vector in the direction of the reconstructed K^0_S momentum.

5.2.2 Cut variable optimisation procedure

Cuts on the variables described before were applied for this analysis and the values of the cuts were optimised such that the signal significance was maximised. The signal significance was defined by:

$$S_{Sig} = \frac{S}{\sqrt{S+B}} \tag{5.2}$$

where S_{Sig} in the signal significance of the cut, S is the number of signal candidates and B is the number of background candidates.

Each of these selection criteria was optimised individually, with each new cut being introduced one after the next.

The dataset used in the optimisation procedure was a sample of SP6 generic Monte Carlo simulated data, which was detailed in Section 5.1.

The number of signal candidates that passed a selection criteria was obtained by performing a χ^2 fit on the invariant mass distribution of the K^0_S candidates. In this fit an asymmetric double Gaussian probability distribution function (PDF) was used to model the signal combined with a quadratic PDF to model the background.

In each stage of the optimisation process, the fit parameters were obtained from the χ^2 fit of the invariant mass distribution of the K^0_S candidates selected with the selection criteria, which had already been finalised at that stage of the analysis. For each new cut variable, a fit was made to the invariant mass distribution without any cut on that variable. In this first fit all of the fit parameters were allowed to float. The fit parameters which corresponded to the shape of the signal function, the central value, width parameters and the fraction of candidates contained in each of the asymmetric Gaussians were fixed at the values obtained from this first fit. Subsequent fits were made whilst the cut variable was varied. Four fit parameters were allowed to float in these subsequent fits, these were the number of signal events and the three parameters describing the quadratic background function.

After each fit, the number of signal candidates, S, was obtained through integrating the signal function over a mass window of $\pm\ 10\,\mathrm{MeV}/c^2$ about the PDG mass of the K^0_S, defined in [1]. The number of background candidates, B, was obtained by integrating the background PDF over the same mass region.

5.2.3 Results of the cut optimisation

The variables used for K_S^0 selection were $DOCA_{\pi^+\pi^-}$, R_Z, R_{XY}, $|\cos\theta^{\pi^+}_{Helicity}|$, SFL and F_{Sig}. Their distributions are shown in Figure 5.1. The cut values were optimised in the order $DOCA_{\pi^+\pi^-}$, R_Z, R_{XY}, SFL, $|\cos\theta^{\pi^+}_{Helicity}|$, F_{Sig}, following the procedure described in the previous section. The candidates removed are shaded on the plots in Figure 5.1.

Figure 5.2 shows the variation of the signal significance as a function of the values of the cuts applied on: $DOCA_{\pi^+\pi^-}$, R_Z, R_{XY}, SFL and F_{Sig}. The optimal values of these cut variables are shown by arrows and they are: $DOCA_{\pi^+\pi^-} \leq 0.32\,\text{cm}$; $|R_Z| < 2.9\,\text{cm}$; $R_{XY} \leq 0.13\,\text{cm}$; $SFL \geq 0\,\text{cm}$; $F_{Sig} > 4$.

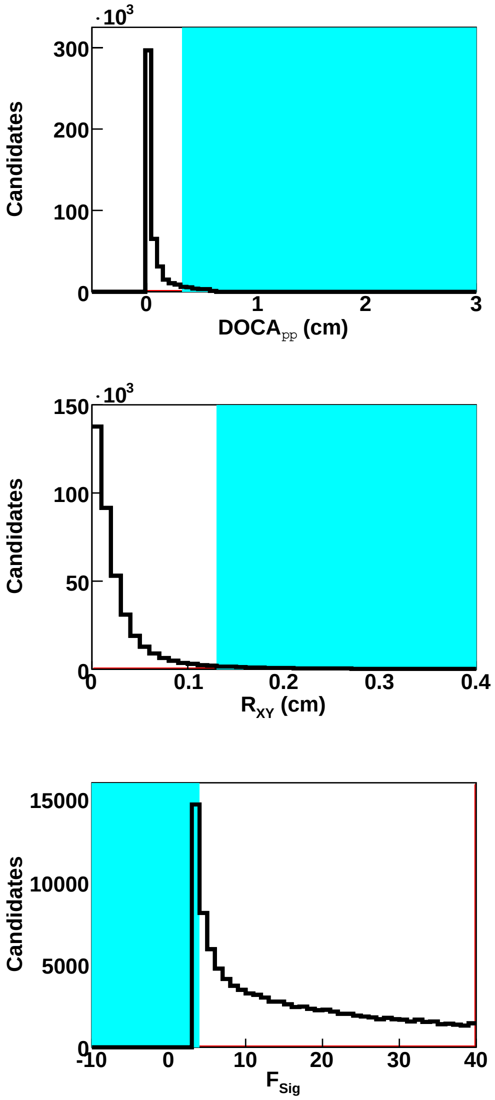

Figure 5.1: Distributions of $DOCA_{\pi^+\pi^-}$, R_Z, R_{XY}, SFL, F_{Sig}, the cut variables used to select K_S^0 candidates. The candidates removed by the cuts are shaded.

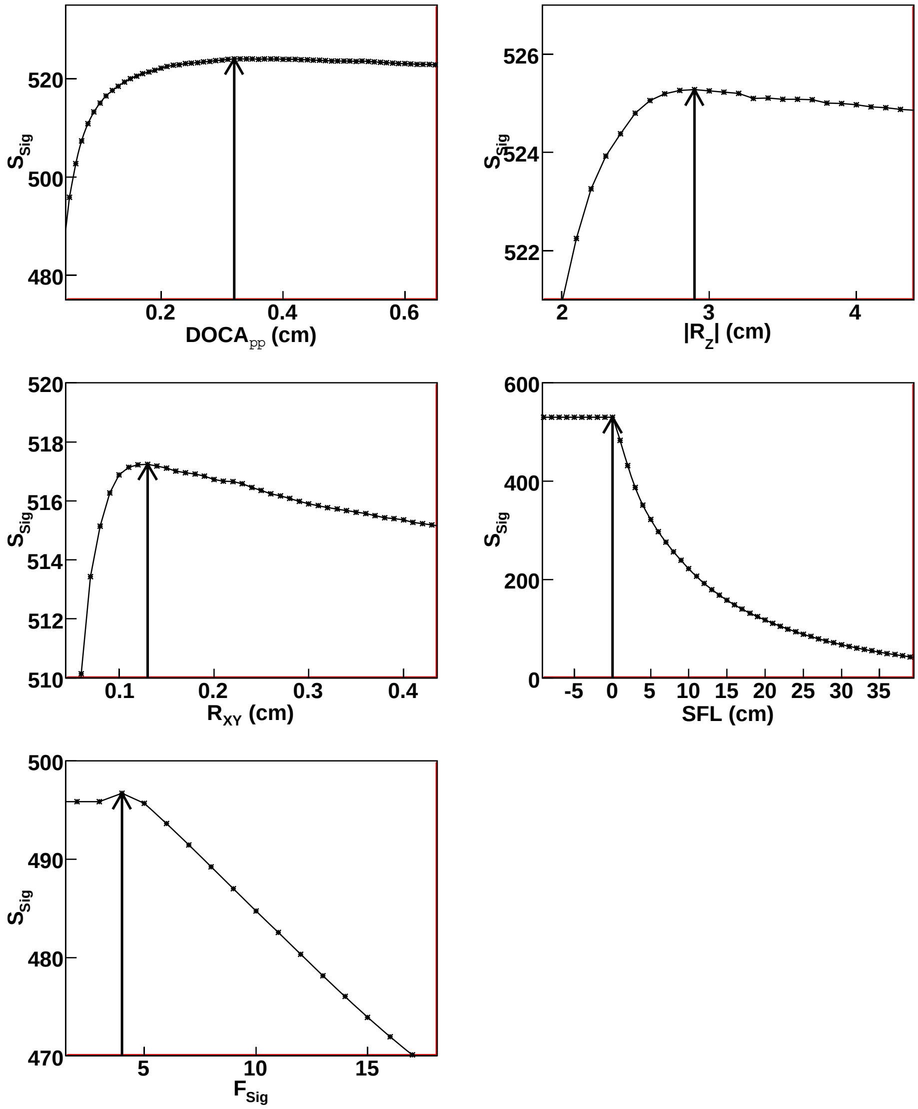

Figure 5.2: Signal significance as a function of the values of the cuts applied on $DOCA_{\pi^+\pi^-}$, $|R_Z|$, R_{XY}, SFL, F_{Sig} for K_S^0 candidates. The values at which the cuts were made are shown by arrows.

The distribution of the magnitude of the cosine of the helicity angle of the daughter pions is shown in Figure 5.3-left. It can be seen from this graph that two peaks were visible at $\cos\theta^{\pi^+}_{Helicity} = \pm 0.85$. These were due to background from Λ^0. This background can be seen more clearly in the plot of the K^0_S invariant mass versus $|\cos\theta^{\pi^+}_{Helicity}|$ shown in Figure 5.3-right. Two bands can be seen clearly at ±0.85, which corresponded to Λ^0 and $\bar{\Lambda}^0$, respectively. In order to remove the contamination from Λ^0 and $\bar{\Lambda}^0$ a cut of $|\cos\theta^{\pi^+}_{Helicity}| \leq 0.8$ was applied, which resulted in a loss of approximately 11% of signal events but improved the sample purity by 2.1%. The removed candidates are shaded in Figure 5.3

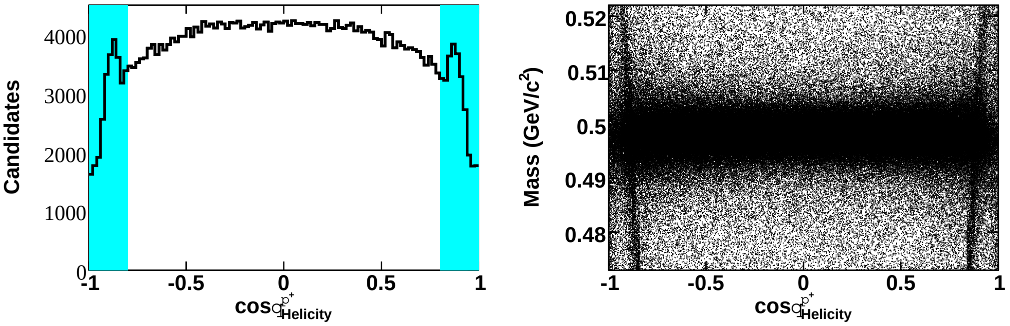

Figure 5.3: Distribution of the cosine of the helicity angle of the K^0_S daughters, $\cos\theta^{\pi^+}_{Helicity}$ (left), distribution of the cosine of the helicity angle of the K^0_S daughters, $\cos\theta^{\pi^+}_{Helicity}$, versus K^0_S mass (right). The candidates removed by the cut are shaded.

The summary of this optimisation analysis is shown in Table 5.1 which presents the effect of adding each of the cuts in turn. The quantities given are: the number of signal candidates, S, the number of background candidates, B, the total number of signal and background candidates, $S+B$, the purity of the sample, $S/(S+B)$, the signal significance S_{Sig}, the χ^2 value of the fit, and the number of degrees of freedom of the fit, NDF.

Table 5.1: The effectiveness of K^0_S selection criteria

Selection Criteria	S	B	$S+B$	$\frac{S}{S+B}$	S_{Sig}	χ^2	N.D.F.
KSTight	323339	80703	404042	0.800	508.7	296.6	190
$DOCA_{\pi^+\pi^-} \leq 0.32\,\text{cm}$	314181	49034	363215	0.865	521.3	340.8	190
$\|R_Z\| \leq 2.9cm$	313359	46302	354632	0.884	526.2	369.0	190
$R_{XY} \leq 0.13cm$	308738	30689	339427	0.910	529.9	330.5	190
$SFL \geq 0$	308835	30448	339283	0.910	530.2	334.4	190
$\|cos\theta^{\pi^+}_{Helicity}\| \leq 0.8$	274734	20222	294956	0.931	505.9	278.6	190
$F_{Sig} \geq 4$	271578	15423	286901	0.947	507.0	328.0	190

5.2.4 Optimisation of the PID variables

Following the optimisation of the continuous variables described before, the effect of using PID selectors to improve the K_S^0 selection was studied. The effect of the requirement that both daughters of a K_S^0 candidate were identified as pions with various PID selectors was studied. The results of this study are shown in Table 5.2. The sample of K_S^0 candidates were selected using the cuts optimised in Section 5.2.3.

Table 5.2: The effectiveness of using PID selectors to select the K_S^0 daughters

Selection Criteria	S	B	$S+B$	$\frac{S}{S+B}$	S_{Sig}	χ^2	N.D.F.
No PID	271578	15423	286901	0.947	507.0	328.0	190
piLHVLoose	269910	13586	283496	0.952	506.9	335.5	190
piLHLoose	266580	12940	279520	0.954	504.2	346.0	190
piLHTight	258466	11482	270848	0.954	496.6	325.0	190
piLHVTight	243954	11722	255676	0.954	482.5	322.2	190

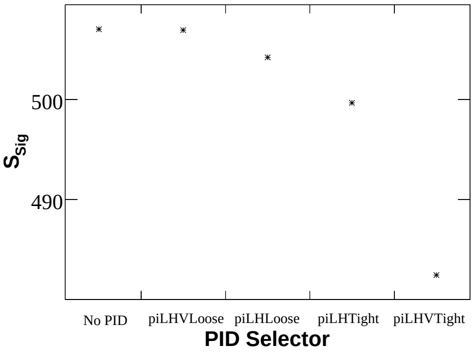

Figure 5.4: Signal significance for K_S^0 candidates obtained with various PID selectors applied on the K_S^0 daughters.

Figure 5.4 shows the signal significances obtained with various PID selectors applied to the daughters of the K_S^0 candidates. It can be seen that the signal significance achieved was almost identical with the use of no PID selector and the piLHVLoose selector. With tighter PID selection than piLHVLoose applied to both daughters of the K_S^0 candidate, the signal significance reduced because less signal candidates were selected. The piLHVLoose PID selector has been chosen for both K_S^0 daughters, because the purity of the K_S^0 sample is improved by 0.5% with no real reduction in the signal significance.

The feasibility of applying cuts on the likelihood ratios used for particle identification to select K_S^0 was also studied.

The quantities that were tested are: $L_{\pi|K}$, the likelihood that a candidate is a pion and not a kaon; $L_{\pi|e}$, the likelihood that a candidate is a pion and not an electron; $L_{\pi|p}$, the likelihood that a candidate is a pion and not a proton. These likelihoods are used in the likelihood based PID selectors used at

BABAR [170] and are defined by the formulae below, where L_{π}, L_e, L_K and L_p are the likelihoods that the candidate is a pion, electron, kaon or proton respectively.

$$L_{\pi|K} = \frac{L_{\pi}}{L_{\pi} + L_K} \tag{5.3}$$

$$L_{\pi|e} = \frac{L_{\pi}}{L_{\pi} + L_e} \tag{5.4}$$

$$L_{\pi|p} = \frac{L_{\pi}}{L_{\pi} + L_p} \tag{5.5}$$

The effect of using the product of these three pion likelihoods, $L_{\pi|}$, was also considered. This should contain all the PID information that is associated with a track.

$$L_{\pi|} = L_{\pi|p} \times \; L_{\pi|K} \times \; L_{\pi|e} \tag{5.6}$$

As each K^0_S has two daughters, the likelihoods from both daughters are multiplied together to make a single likelihood. Thus the likelihoods used were: $L^{K^0_S}_{\pi|e}$, which is the likelihood that both daughters of a K^0_S candidate are pions and not electrons, $L^{K^0_S}_{\pi|K}$, which is the likelihood that both daughters of a K^0_S candidate are pions and not kaons, $L^{K^0_S}_{\pi|p}$, which is the likelihood that both daughters of a K^0_S candidate are pions and not protons, $L^{K^0_S}_{\pi|}$, which is the likelihood that both daughters of a K^0_S candidate are pions and not electrons, kaons or protons.

$$L^{K^0_S}_{\pi|e} = L^{\pi^+}_{\pi|e} \times \; L^{\pi^-}_{\pi|e} \tag{5.7}$$

$$L^{K^0_S}_{\pi|K} = L^{\pi^+}_{\pi|K} \times \; L^{\pi^-}_{\pi|K} \tag{5.8}$$

$$L^{K^0_S}_{\pi|p} = L^{\pi^+}_{\pi|p} \times \; L^{\pi^-}_{\pi|p} \tag{5.9}$$

$$L^{K^0_S}_{\pi|} = L^{\pi^+}_{\pi|} \times \; L^{\pi^-}_{\pi|} \tag{5.10}$$

The distributions of $L^{K^0_S}_{\pi|e}$, $L^{K^0_S}_{\pi|K}$, $L^{K^0_S}_{\pi|p}$ and $L^{K^0_S}_{\pi|}$ are shown in Figure 5.5. In each of these distributions there is a peak at 1, as expected, where both daughters are identified as pions. In the $L^{K^0_S}_{\pi|e}$ and $L^{K^0_S}_{\pi|}$ distributions there is small peak near zero, which occurs when at least one daughter is identified as an electron. Very small bumps are visible in the distributions around 0.5, these correspond to the situation where a daughter is assigned two different particle hypotheses with equal likelihood.

The distributions of the signal significance as a function of cuts on $L_{\pi|e}^{K_S^0}$, $L_{\pi|K}^{K_S^0}$, $L_{\pi|p}^{K_S^0}$ and $L_{\pi|}^{K_S^0}$ are shown in Figure 5.6. The highest signal significances were obtained with no cut applied. No advantage was gained by the use of any of these cuts, therefore none are applied in this analysis.

5.2.5 Summary of the K_S^0 selection criteria

In conclusion, the selection criteria that have been used for the selection of K_S^0 in this analysis are:

- $P(\chi^2) \geq 0.001$,
- $F_{Sig} \geq 4$,
- DOCA between the two K_S^0 daughters ≤ 0.32 cm,
- $|R_Z| \leq 2.9$ cm,
- $R_{XY} \leq 0.13$ cm,
- SFL ≥ 0 cm,
- helicity angle $|\cos\theta_h| \leq 0.8$,
- both K_S^0 daughters identified as piLHVLoose,
- mass within a $\pm 0.010\,\mathrm{MeV}/c^2$ window around the PDG mass.

The invariant mass distribution of the selected K_S^0 candidates is shown in Figure 5.7. The distribution labelled Final is that after the application of all of the optimised cuts which is to be compared with the invariant mass distribution labelled Initial obtained using the KSTight criteria. The fits for each curve are also displayed. The optimised cuts reduce approximately 85% of the background for a loss of approximately 15% of the signal. The majority of this loss of signal is due to the cut on the helicity angle (11%).

5.2.6 K_S^0 multiplicity

Multiple K_S^0 candidates are reconstructed in a large number of events. Figure 5.8 shows the multiplicity of K_S^0 candidates after the application of the optimised cuts. The multiplicity of all the reconstructed K_S^0 candidates is shown by solid black lines and the multiplicity of the Monte Carlo truth-matched K_S^0 candidates shown by dashed red lines. It can be seen that the distribution after truth-matching is similar to that before truth-matching, which indicates that the majority of the multiple K_S^0 candidates are real. Hence, the reconstruction of the multiple K_S^0 candidates is not a major problem in this

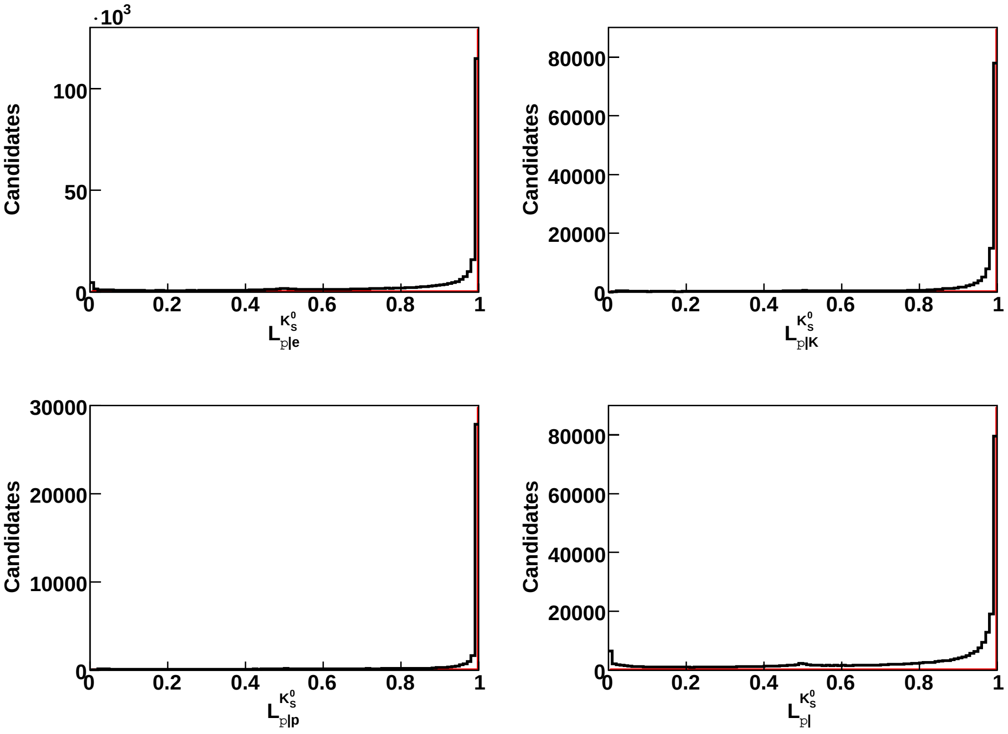

Figure 5.5: Distribution of the PID variables $L^{K_S^0}_{\pi|e}$, $L^{K_S^0}_{\pi|K}$, $L^{K_S^0}_{\pi|p}$ and $L^{K_S^0}_{\pi|}$ for K_S^0 candidates.

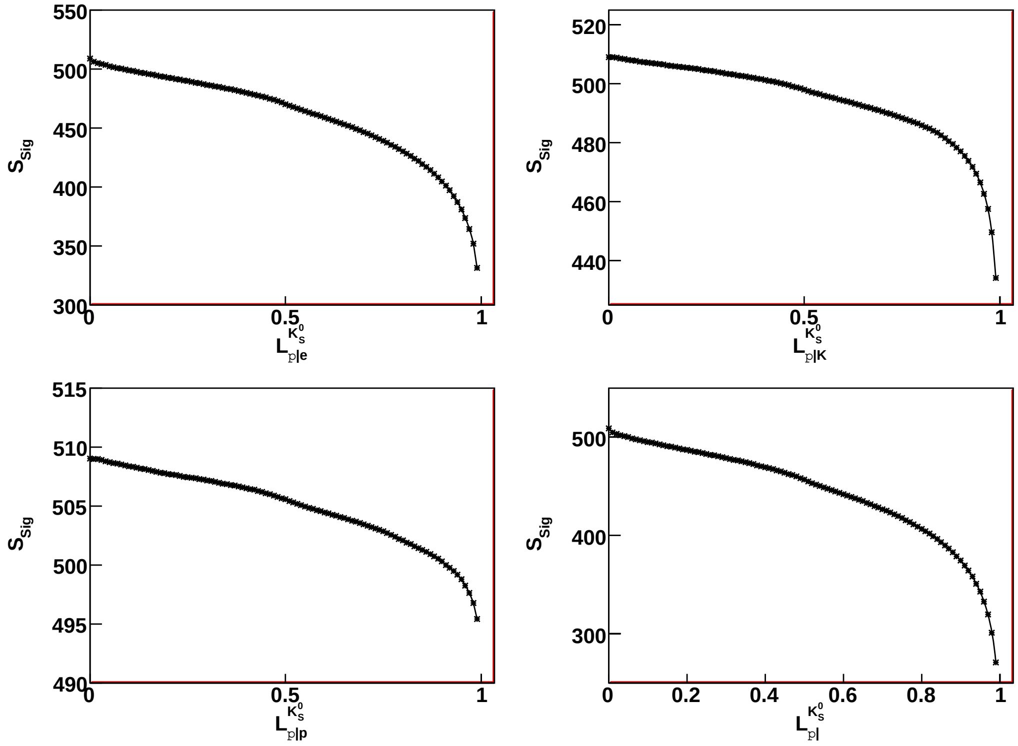

Figure 5.6: Signal significance as a function of the values of the cuts applied on $L^{K_S^0}_{\pi|e}$, $L^{K_S^0}_{\pi|K}$, $L^{K_S^0}_{\pi|p}$ and $L^{K_S^0}_{\pi|}$ for K_S^0 candidates.

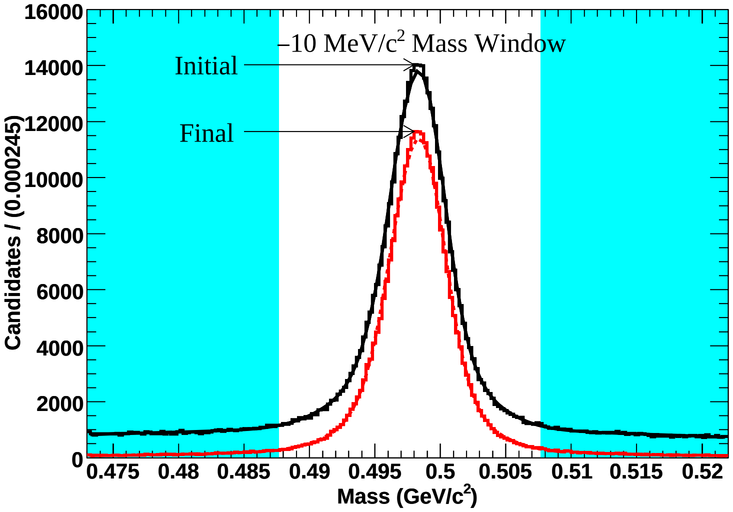

Figure 5.7: Invariant mass distributions of K_S^0 candidates in Monte Carlo simulated data before and after applying the optimised cuts. The candidates removed by the cut of $\pm 10\,\mathrm{MeV}/c^2$ around the K_S^0 PDG mass are shaded.

analysis. It was investigated further in order to identify an adequate method for the removal of overlapping candidates, which might be used further for K^{*-} selection. This study is described in the next section.

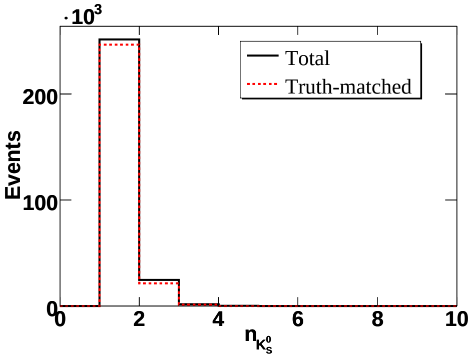

Figure 5.8: Distribution of the multiplicity of the reconstructed K_S^0 candidates in an event (solid line). The multiplicity of the truth-matched K_S^0 candidates is also displayed on the plots (dashed line).

5.2.7 Overlapping candidates

In a small proportion of the K_S^0 candidates the same pion track is used to reconstruct two or more K_S^0 candidates. These are overlapping candidates. Because a pion can be the daughter of only one of these K_S^0 candidates it is desirable to remove these extra overlapping candidates.

The removal of these overlapping candidates involved selecting the best K_S^0 candidate using some selection criteria, from the list of K_S^0 candidates preselected using the optimised cuts and then looping though the K_S^0 candidates and discarding any with overlapping daughters. This process was repeated until every K_S^0 in the event had been processed. To determine whether a selected K_S^0 candidate was signal or background the truth information from the Monte Carlo was used. If the candidate was truth matched as a K_S^0 and both daughters were truth matched as pions from the same generated K_S^0 candidate then it was considered to be signal. Otherwise, the candidate was considered to be part of the background.

The criteria that were tested for the best candidate selection are listed in in Table 5.3 together with the corresponding results. The quantities given are: the total number of candidates, $T + F$; the number of background candidates that fail the truth matching, F; the number of signal candidate that pass the truth matching, T; purity of the data sample, $T/(T + F)$; signal significance $T/\sqrt{T + F}$. These quantities are displayed both for the whole of our sample of overlapping K_S^0 candidates and also for those that lie in the 10 MeV/c^2 mass window around the K_S^0 PDG mass.

Table 5.3: Effectiveness of the best candidate selection criteria

	Complete Sample					10 MeV/c^2 Mass Window				
Selection Criteria	$T+F$	F	T	$\frac{T}{T+F}$	$\frac{T}{\sqrt{T+F}}$	$T+F$	F	T	$\frac{T}{T+F}$	$\frac{T}{\sqrt{T+F}}$
No Selection	3331	1512	1819	0.546	31.5	2342	600	1742	0.744	36.0
Random	1792	778	1014	0.566	24.0	1286	313	973	0.757	27.1
$L_{\pi\|K}^{K_S^0}$	1791	622	1169	0.653	27.6	1384	249	1135	0.820	30.5
$L_{\pi\|p}^{K_S^0}$	1788	739	1049	0.587	24.8	1319	297	1022	0.775	28.1
$L_{\pi\|e}^{K_S^0}$	1791	789	1002	0.559	23.7	1284	319	965	0.752	26.9
$L_{\pi\|}^{K_S^0}$	1794	718	1076	0.600	25.4	1320	284	1036	0.785	28.5
$DOCA_{\pi^+\pi^-}$	1793	469	1324	0.738	31.3	1483	204	1277	0.861	33.2
F_{Sig}	1792	251	1541	0.860	36.4	1586	108	1478	0.932	37.1
R_{XY}	1787	307	1480	0.828	35.0	1556	138	1418	0.911	35.9
$P(\chi^2)$	1793	456	1337	0.746	31.6	1488	200	1288	0.866	33.4
K_S^0 $\|M_{\pi^+\pi^-} - M_{PDG}\|$	1793	259	1534	0.856	36.2	1705	200	1505	0.883	36.4
K_S^0 $\|M_{\pi^+\pi^-} - M_{FIT}\|$	1795	265	1530	0.852	36.1	1702	206	1499	0.881	36.3

The total number of K_S^0 candidates selected using the best candidate selection varied depending on which parameter is used for selection. This happened because there were K_S^0 candidates whose daughters both overlapped with other K_S^0 candidates. In this situation the choice of K_S^0 candidate affected the total number of candidates selected.

As a benchmark K_S^0 candidates were selected randomly. The purity of the data sample increased but the signal significance decreased compared with the case with no best candidate selection.

Similar signal significances and sample purities were obtained using the PID variables, $L_{\pi|K}^{K_S^0}$, $L_{\pi|p}^{K_S^0}$, $L_{\pi|e}^{K_S^0}$ and $L_{\pi|}^{K_S^0}$ compared with those obtained using a random number, because the daughters of the true K^0_S were not always the two pions with the highest PID likelihoods. PID information was most useful when one daughter of a K^0_S candidate was not a pion. This rarely occurs, because the K^0_S daughters have been selected with the piLHVLoose PID selector and pions are more common than kaons, protons or electrons in these events. The most useful of these variables was $L^{K^0_S}_{\pi|K}$ because it discriminates against K^0_S candidates reconstructed with both overlapping protons or kaons. This was because the protons have a dE/dx and Cherenkov angles that were further away from the pion bands than the kaon bands. Hence, the protons will be more like kaons than pions.

The highest sample purities and signal significances were obtained using F_{Sig} to select the best K^0_S candidates. Using the mass difference from either the PDG mass or the K^0_S mass obtained from the fit were also good solutions for selecting the best K^0_S candidate. The majority of the background candidates removed using the mass differences were outside the mass window. Unsurprisingly, most of the signal K^0_S inside the mass window are selected.

The final observation was that the maximum possible gain in the signal significance that can be achieved by selecting the best K^0_S candidate selection was very small. The total number of candidates, over the full mass window, was reduced by roughly 1540 out of a total of 295333 or 0.52%. This was because the sample of K^0_S was already very pure.

5.3 $K^{*\pm}$ selection

The $K^{*\pm}$ particles were reconstructed in the decay mode $K^{*\pm} \to K^0_S\pi^\pm$. The K^0_S candidates that met the criteria defined in Section 5.2 were selected and a mass constraint was applied to each of these candidates. The $\pi^\pm$ candidates selected met both the piLHLoose and the GoodTracksAccLoose criteria. The K^0_S and $\pi^\pm$ candidates were vertexed together using the TreeFitter vertexer with geometric and lifetime constraints. The TreeFitter vertexer is described in [168]. The initial selection of $K^{*\pm}$ candidates consisted of those $K^{*\pm}$ candidates within a mass window of $\pm 175\,\mathrm{MeV}/c^2$ around the PDG mass [1]. The effects of the application of a number of different selection criteria on this $K^{*\pm}$ sample were investigated.

Each of the investigated section criteria were optimised following the same selection method as for the K^0_S selection described in Section 5.2. The invariant mass distribution of $K^{*\pm}$ was fitted with a PDF containing a Breit-Wigner PDF to model the signal and a polynomial PDF constructed from the first six Chebychev polynomials to model the background.

5.3.1 Optimisation of the cuts for the $K^{*\pm}$ candidates

The distributions of the variables investigated, $P(\chi^2)$, $DOCA_{K^0_S\pi^-}$, $\pi^\pm\ R_Z$, $\pi^\pm\ R_{XY}$, R_Z, R_{XY}, $\cos\theta^{K^0_S}_{Helicity}$ are shown in Figure 5.9. $\pi^\pm\ R_Z$, and $\pi^\pm\ R_{XY}$ are the DOCAs to the collision axis of the bachelor pion, whilst R_Z and R_{XY} are the corresponding variables for the reconstructed $K^{*\pm}$ candidates. The cut variables were optimised in the order $P(\chi^2)$, $DOCA_{K^0_S\pi^-}$, $|\pi^\pm\ R_Z|$, $\pi^\pm\ R_{XY}$, $|R_Z|$, R_{XY}, $\cos\theta^{K^0_S}_{Helicity}$. The candidates removed by the cuts are shaded in Figure 5.9.

Figure 5.10 shows the variation of the signal significance as a function of the values of the cuts applied on the variables listed before. A cut of $P(\chi^2) > 0.001$ was found to be optimal. The signal significance was found to be almost constant for cuts on $|R_Z|$ and $|\pi^\pm\ R_Z|$ between 2.5 and 5, therefore cuts of $|R_Z| < 2.9$ cm and $|\pi^\pm\ R_Z| < 2.9$ cm were applied to be consistent with those applied for K^0_S. The signal significance was found to be almost constant for cuts on R_{XY} and $\pi^\pm\ R_{XY}$ between 0.1 and 0.25, therefore cuts of $R_{XY} \leq 0.13$ cm and $\pi^\pm\ R_{XY} \leq 0.13$ cm were applied to be consistent with those applied for K^0_S. No advantage is gained by the use of the cuts on $DOCA_{K^0_S\pi^-}$ or $\cos\theta^{K^0_S}_{Helicity}$, therefore none are applied in this analysis.

The values of the cuts used in this analysis are indicated by arrows in Figure 5.10.

The results of the optimisation study are summarised in Table 5.4. The meanings of the quantities tabulated are the same as those in the K^0_S optimisation study.

Table 5.4: Effectiveness of the $K^{*\pm}$ selection criteria

Selection Criteria	S	B	$S+B$	$\frac{S}{S+B}$	S_{Sig}	χ^2	N.D.F.
Initial Selection	384696	3524363	3909059	0.098	194.6	193.6	193
$P(\chi^2) \geq 0.001$	375587	3027123	3402710	0.110	203.6	193.3	193
$\pi\vert R_Z\vert \leq 2.9cm$	374015	3014896	3388911	0.110	203.2	192.8	193
$\pi R_{XY} \leq 0.13cm$	365830	2906405	3272235	0.112	202.24	194.7	193
$\vert R_Z\vert \leq 2.9cm$	365789	2905626	3271415	0.112	202.24	194.1	193
$R_{XY} \leq 0.13cm$	365194	2795200	3260394	0.112	202.25	197.3	193

5.3.2 Optimisation of the PID variables

The feasibility of applying cuts on the likelihood ratios used for particle identification to select $K^{*\pm}$ candidates was studied.

As each $K^{*\pm}$ candidate has two daughters, the likelihoods of each daughter are multiplied together to get a single likelihood that the three tracks involved in the reconstruction of a $K^{*\pm}$ are pions. Thus the likelihoods used were: $L^{K^{*\pm}}_{\pi|e}$ which is the likelihood that all three tracks used to reconstruct a $K^{*\pm}$ candidate are pions and not electrons, $L^{K^{*\pm}}_{\pi|K}$ which is the likelihood that all three tracks used to reconstruct a $K^{*\pm}$ candidate are pions and not kaons, $L^{K^{*\pm}}_{\pi|p}$ which is the likelihood that all three

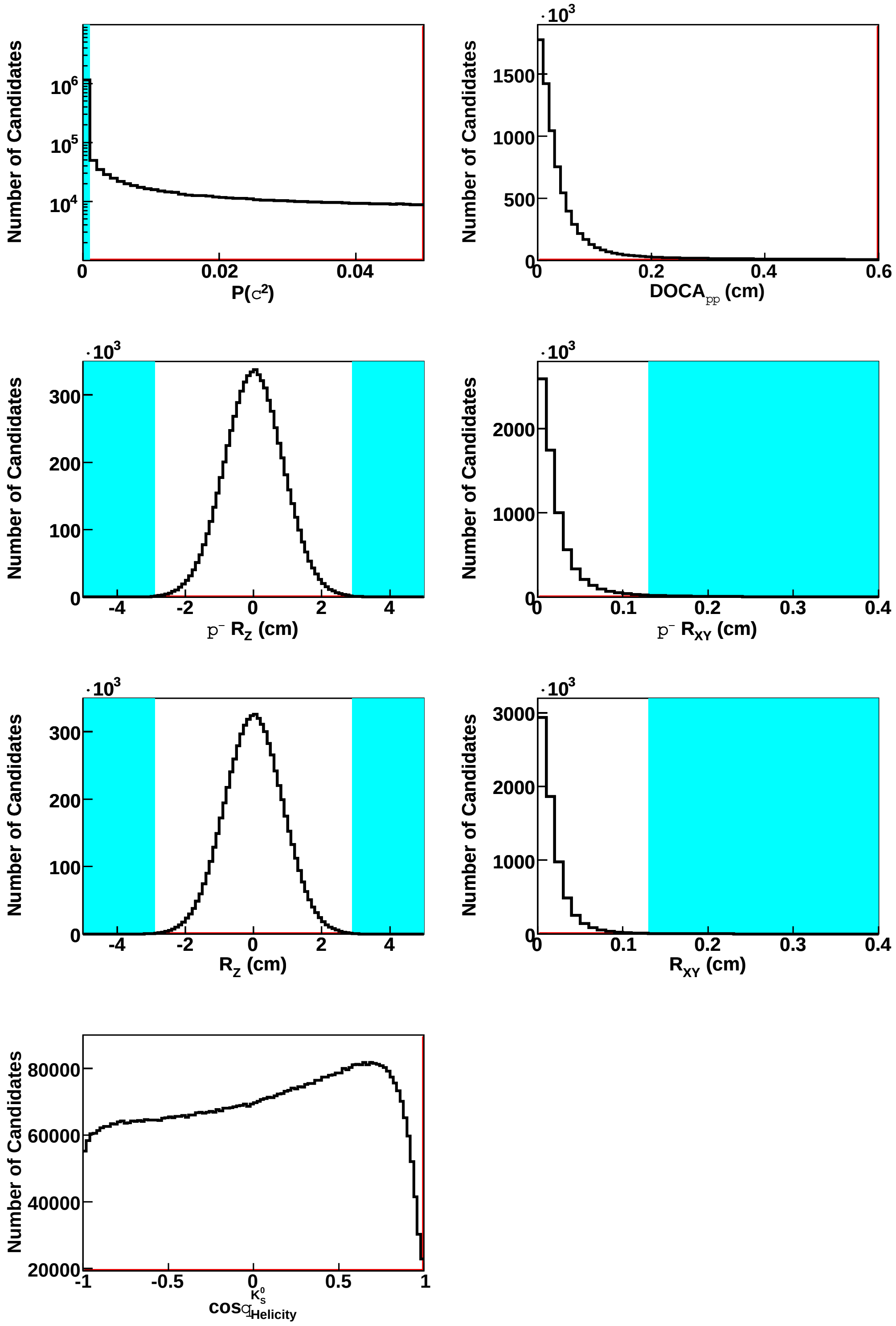

Figure 5.9: Distributions of $P(\chi^2)$, $DOCA_{K^0_S\pi^-}$, $\pi^\pm$ R_Z, $\pi^\pm$ R_{XY}, R_Z, R_{XY}, $\cos\theta^{K^0_S}_{Helicity}$. The candidates removed by the optimised cuts are shaded.

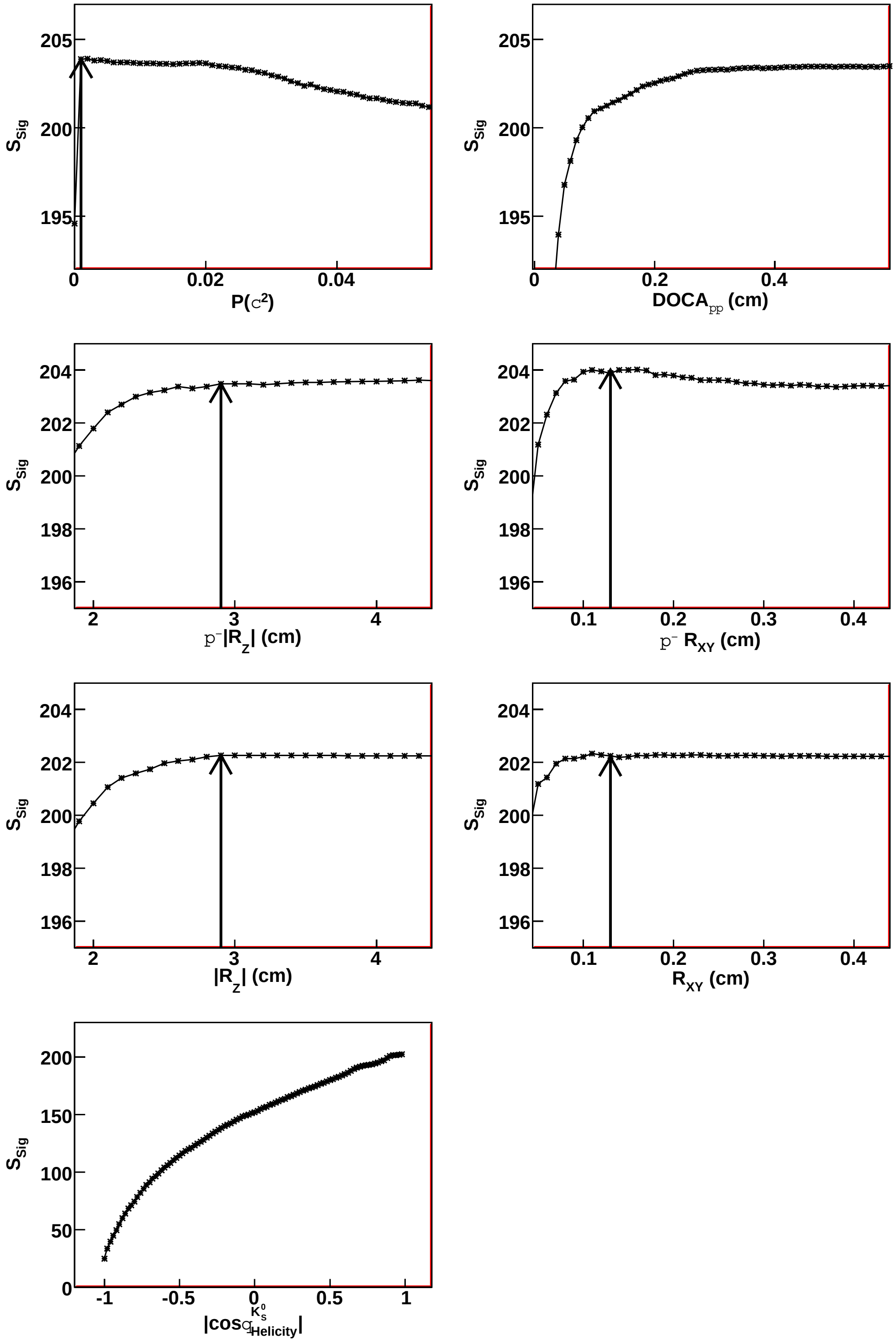

Figure 5.10: Signal significance as a function of the values of the cuts applied on $P(\chi^2)$, $DOCA_{K_S^0\pi^-}$, $|\pi^{\pm}\ R_Z|$, $\pi^{\pm}\ R_{XY}$, $|R_Z|$, R_{XY}, $\cos\theta^{K_S^0}_{Helicity}$ for $K^{*\pm}$ candidates. The values at which the cuts are made are shown by arrows.

tracks used to reconstruct a $K^{*\pm}$ candidate are pions and not protons, $L^{K^{*\pm}}_{\pi|p}$ which is the likelihood that all three tracks used to reconstruct a $K^{*\pm}$ candidate are pions and not electrons, protons, or kaons.

$$L^{K^{*\pm}}_{\pi|e} = L^{K^0_S}_{\pi|e} \times\ L^{\pi^\pm}_{\pi|e} \tag{5.11}$$

$$L^{K^{*\pm}}_{\pi|K} = L^{K^0_S}_{\pi|K} \times\ L^{\pi^\pm}_{\pi|K} \tag{5.12}$$

$$L^{K^{*\pm}}_{\pi|p} = L^{K^0_S}_{\pi|p} \times\ L^{\pi^\pm}_{\pi|p} \tag{5.13}$$

$$L^{K^{*\pm}}_{\pi|} = L^{K^0_S}_{\pi|} \times\ L^{\pi^\pm}_{\pi|} \tag{5.14}$$

The distributions of $L^{K^{*\pm}}_{\pi|e}$, $L^{K^{*\pm}}_{\pi|K}$, $L^{K^{*\pm}}_{\pi|p}$ and $L^{K^{*\pm}}_{\pi|}$ are shown in Figure 5.11. In each of these distributions there is a peak at 1 as expected where all of the three tracks used to reconstruct the $K^{*\pm}$ are identified as pions. In the $L^{K^{*\pm}}_{\pi|e}$ and $L^{K^{*\pm}}_{\pi|}$ distributions there is a small peak near zero, which occurs when the daughter pion of the $K^{*\pm}$ or a daughter of the K^0_S are identified as electrons. Very small bumps are visible in the distributions around 0.5 which correspond to the situation where one of the three pions used to reconstruct the $K^{*\pm}$ is assigned two different particle hypotheses with equal likelihood.

The distributions of the signal significance as a function of cuts on $L^{K^{*\pm}}_{\pi|e}$, $L^{K^{*\pm}}_{\pi|K}$, $L^{K^{*\pm}}_{\pi|p}$ and $L^{K^{*\pm}}_{\pi|}$ are shown in Figure 5.12. The highest signal significances are obtained with no cut applied. No cuts are applied on any of the PID variables in this analysis.

5.3.3 Final $K^{*\pm}$ selection

In conclusion, the selection criteria which have been finalised for the selection of $K^{*\pm}$ candidates in this analysis are:

- $P(\chi^2) \geq 0.001$,
- $|R_Z|$ of the daughter pion $\leq 2.9\,\text{cm}$,
- R_{XY} of the daughter pion $\leq 0.13\,\text{cm}$,
- $|R_Z|$ of $K^{*\pm}$ candidate $\leq 2.9\,\text{cm}$,
- R_{XY} of $K^{*\pm}$ candidate $\leq 0.13\,\text{cm}$,

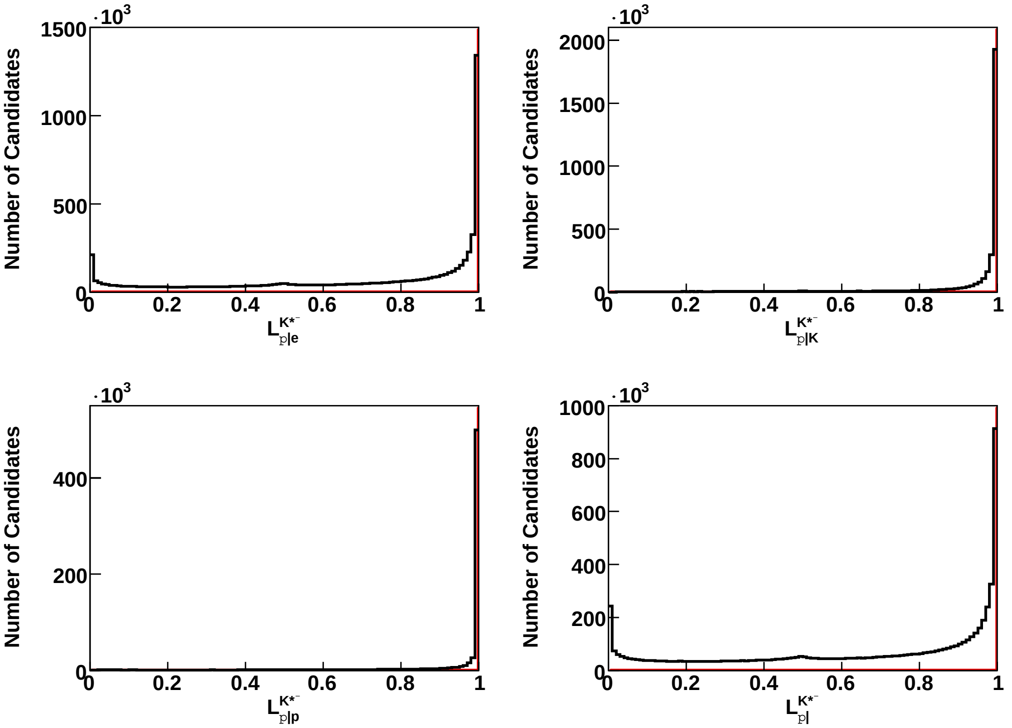

Figure 5.11: Distribution of the PID variables $L_{\pi|e}^{K^{*\pm}}$, $L_{\pi|K}^{K^{*\pm}}$, $L_{\pi|p}^{K^{*\pm}}$ and $L_{\pi|}^{K^{*\pm}}$ for $K^{*\pm}$ candidates.

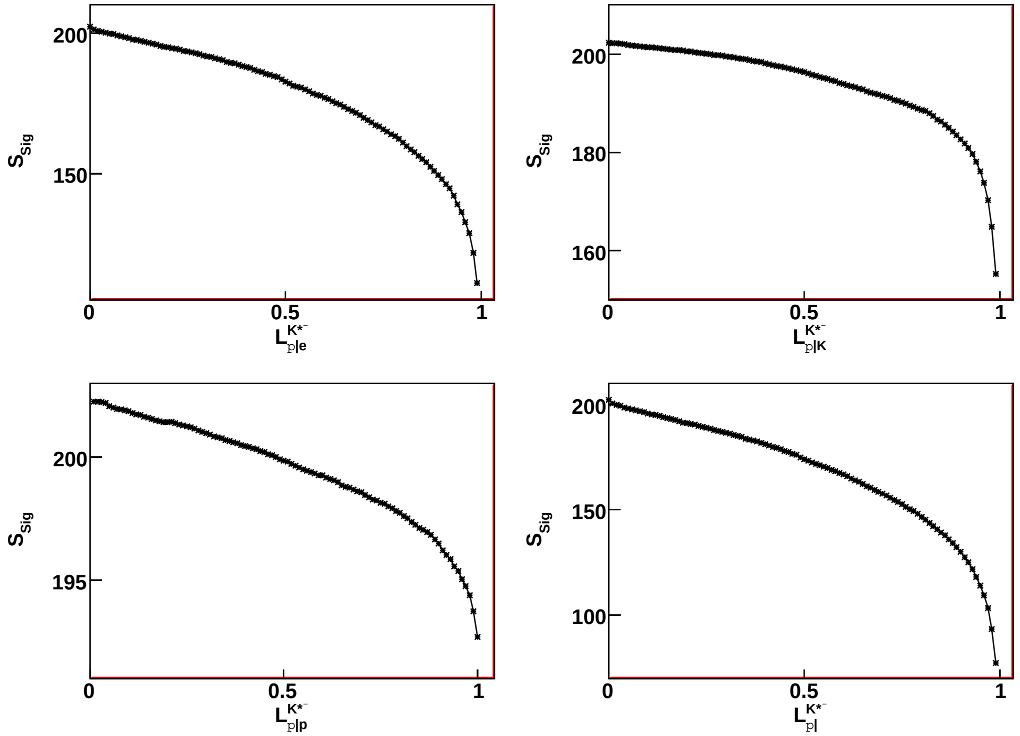

Figure 5.12: Signal significance as a function of the values of the cuts applied on $L_{\pi|e}^{K^{*\pm}}$, $L_{\pi|K}^{K^{*\pm}}$, $L_{\pi|p}^{K^{*\pm}}$ and $L_{\pi|}^{K^{*\pm}}$ for $K^{*\pm}$ candidates.

- mass within ±75 MeV/c^2 window of the PDG $K^{*\pm}$ mass value.

The invariant mass distribution of the selected $K^{*\pm}$ candidates is shown in Figure 5.13. The distribution labelled Final is after the application of all of the optimised cuts to be compared with the invariant mass distribution labelled Initial obtained without cuts. The fits to each invariant mass distribution are also displayed. These cuts reduce approximately 39% of the background for a drop in the signal of approximately 2%.

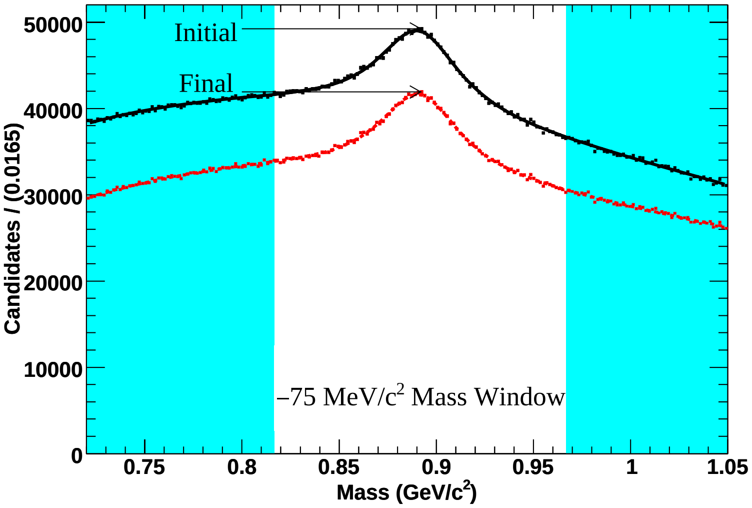

Figure 5.13: Invariant mass distributions of $K^{*\pm}$ candidates in Monte Carlo simulated data before and after the application of the optimised cuts. The candidates removed by the cut of ±75 MeV/c^2 around the $K^{*\pm}$ PDG mass are shaded.

5.3.4 $K^{*\pm}$ multiplicity

Multiple $K^{*\pm}$ candidates are reconstructed in a large number of events. Figure 5.14 shows the multiplicity of $K^{*\pm}$ candidates after the application of the optimised cuts. The $K^{*\pm}$ multiplicity is shown both for the entire sample and also within the mass window. For comparison the multiplicity of truth-matched candidates are shown on the plots by a dashed line. In the entire sample there are on average, over two $K^{*\pm}$ candidates reconstructed in an event and with a substantial tail at higher multiplicities. The maximum number of truthed $K^{*\pm}$ candidates in an event is three, which indicates that the majority of the multiple candidates are fake. However, the truth-matching is not perfect for $K^{*\pm}$ candidates. Some $K^{*\pm}$ candidates are produced through three-body decays of heavier particles. These decays can contain $K^{*\pm}$ candidates however these candidates will be truth-matched as the mother of the $K^{*\pm}$. This means that the number of truth-matched $K^{*\pm}$ candidates is less than the number of $K^{*\pm}$ generated in the Monte Carlo. It is expected that these $K^{*\pm}$ candidates will have similar properties, therefore the conclusions based on truth-matching will be valid. The mass cut reduces the average multiplicity of the $K^{*\pm}$ candidates but there are still events containing over 15 candidates. Various methods for the removal of overlapping $K^{*\pm}$ candidates were investigated. This study is described in the Section 5.3.5.

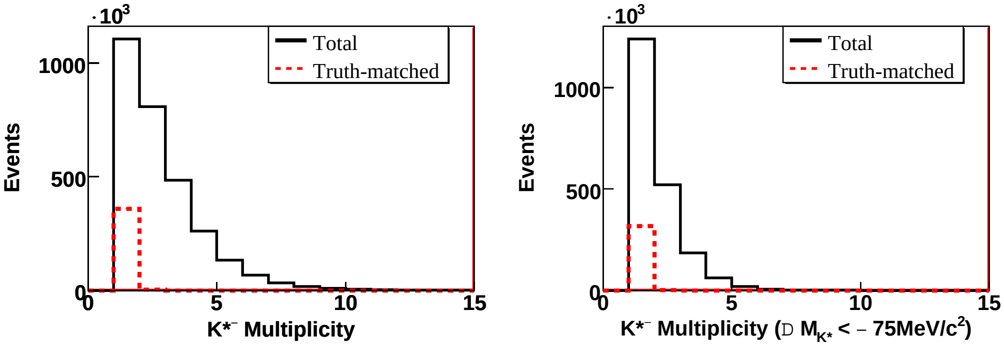

Figure 5.14: Distributions of the multiplicities, $n_{K^{*\pm}}$, of $K^{*\pm}$ candidates in the entire sample (left) and within the ±75 MeV/c^2 mass window around the PDG value (right). For comparison the distributions of the multiplicities of truth-matched $K^{*\pm}$ candidates are also shown (dashed red).

The effect of applying cuts on the $K^{*\pm}$ multiplicity is shown in Table 5.5. It can be seen that the purity of the sample increases with tighter cuts on the $K^{*\pm}$ multiplicity, $n_{K^{*\pm}}$, slightly until $n_{K^{*\pm}} < 7$, more and more afterwards. Also the signal significance increases slightly with tighter cuts up to $n_{K^{*\pm}} < 7$ and decreases significantly after this value. If a cut is applied at $n_{K^{*\pm}} < 7$ the loss in signal is 15% with 25% reduction in background.

Figure 5.16 shows the invariant mass distribution of $K^{*\pm}$ candidates after various cuts on the multiplicity and the multiplicity of $K^{*\pm}$ candidates in a window of ±75 MeV/c^2 around the $K^{*\pm}$ PDG mass after various cuts on the multiplicity. The distributions with no multiplicity cut and cuts of $n_{K^{*\pm}} < 7$ and $n_{K^{*\pm}} < 5$ are plotted. The effect of these cuts was investigated for the selection of $R(3520)$ candidates.

5.3.5 Overlapping candidates

In a large number of the $K^{*\pm}$ candidates, the same pion tracks or K^0_S candidates are used to reconstruct two or more $K^{*\pm}$ candidates. As a pion or K^0_S can only be part of one $K^{*\pm}$ candidate it is desirable to remove these extra overlapping candidates. Therefore, the effectiveness of using various criteria to select the best $K^{*\pm}$ candidates was evaluated.

The procedure for this study was similar to that for overlapping K^0_S candidates described in Section 5.2.7. Similarly, as with the K^0_S study any $K^{*\pm}$ candidates that had any overlapping daughters or granddaughters with the selected candidates were discarded. As in the K^0_S study, the $K^{*\pm}$ and its

Table 5.5: Effectiveness of a cut on the $K^{*\pm}$ multiplicity

$K^{*\pm}$ Multiplicity	S	B	$S+B$	$\frac{S}{S+B}$	$\frac{S}{\sqrt{S+B}}$	χ^2	N.D.F.
< 2	97074	437691	534765	0.182	132.75	198.0	193
< 3	198922	1103527	1302449	0.153	174.3	205.3	193
< 4	268412	1720590	1989002	0.135	190.3	210.7	193
< 5	313783	2168725	2482508	0.126	199.2	214.4	193
< 6	336963	2456811	2793774	0.121	201.6	201.0	193
< 7	352598	2631026	2983624	0.118	204.1	204.7	193
< 8	358414	2732267	3090681	0.116	203.9	202.4	193
< 9	361542	2792637	3154179	0.115	203.6	181.2	193
< 10	363523	2827883	3191406	0.114	203.5	195.9	193
< 11	364132	2850707	3214839	0.113	203.1	198.4	193
< 12	366166	2863934	3229990	0.113	203.7	199.4	193
< 13	364845	2875275	3240120	0.112	202.7	198.1	193
< 14	366650	2888098	3246748	0.112	203.5	199.2	193
< 15	365140	2886323	3251463	0.112	202.5	198.4	193
No Cut	365194	2895200	3260394	0.111	202.3	197.3	193

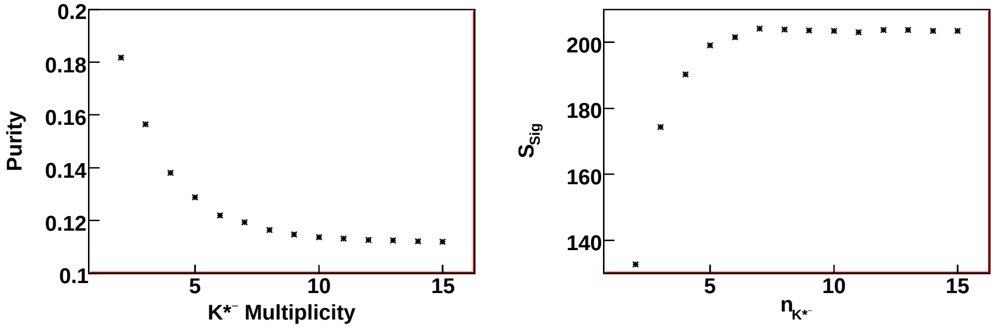

Figure 5.15: Sample purities (left) and signal significances (right) after cuts on the multiplicity of $K^{*\pm}$ candidates in an event.

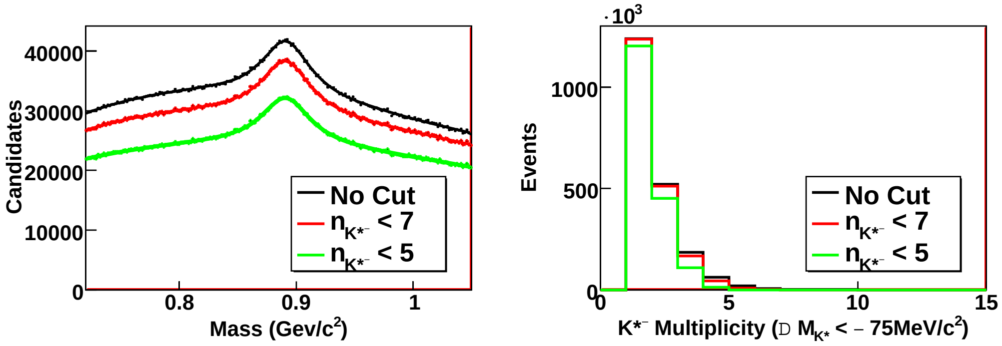

Figure 5.16: Invariant mass distribution of $K^{*\pm}$ candidates after cuts on the multiplicity of $K^{*\pm}$ candidates in an event(left). Distribution of the multiplicity of $K^{*\pm}$ candidates within a $\pm 75\,\mathrm{MeV}/c^2$ window around the PDG mass after cuts on the total $K^{*\pm}$ multiplicity(right).

daughters were truth-matched.

The criteria that were tested for the best candidate selection are listed in Table 5.6 with the corresponding results. The meanings of the quantities presented are the same as those for the K_S^0 analysis of overlapping candidates. These quantities are displayed both for the complete sample of overlapping $K^{*\pm}$ candidates and for those that lie in the 75 MeV/c^2 mass window around the $K^{*\pm}$ PDG mass.

Table 5.6: Effectiveness of the best candidate selection criteria for $K^{*\pm}$ candidates

	Complete Sample					75 MeV/c^2 Mass Window				
Selection Criteria	$T+F$	F	T	$\frac{T}{T+F}$	$\frac{T}{\sqrt{T+F}}$	$T+F$	F	T	$\frac{T}{T+F}$	$\frac{T}{\sqrt{T+F}}$
None	6880410	6516035	364365	0.053	138.9	3260180	2938131	322049	0.099	178.4
Random	3099440	2910025	189415	0.061	107.6	2122077	1891614	230463	0.109	158.3
$L_{\pi\|K}^{K^*}$	3100671	2911375	189296	0.061	107.5	2123028	1893191	229837	0.108	157.7
$L_{\pi\|p}^{K^*}$	3103067	2911375	193291	0.062	109.7	2123885	1891561	232324	0.109	159.4
$L_{\pi\|e}^{K^*}$	3102893	2905824	197069	0.064	111.9	2123028	1889060	234598	0.110	161.0
$L_{\pi\|}^{K^*}$	3105285	2910119	195166	0.063	110.8	2124246	1890320	233926	0.110	160.5
$DOCA_{K_S^0\pi}$	3103074	2904040	199034	0.064	113.0	2123585	1887115	236470	0.111	162.3
R_{XY}	3103074	2908234	195182	0.063	110.8	2123774	1889836	233988	0.110	160.6
$P(\chi^2)$	3100293	2906123	194800	0.063	110.6	2122842	1888712	234130	0.110	160.7
Δ_M	3100486	2882201	278295	0.090	158.0	2122168	1861093	261075	0.123	179.2

The first observation is that the process of best candidate selection is less effective for $K^{*\pm}$ candidates than for K_S^0 candidates because there are generally more $K^{*\pm}$ candidates in an event.

If the mass cut is applied before the best candidate is selected then the signal significance and sample purity are higher than the case where the best candidate is selected before the mass cut is applied because there are fewer background candidates after the mass cut has been applied.

As a benchmark $K^{*\pm}$ candidates were selected randomly. The sample purity increased but the signal significance decreased compared with the case without best candidate selection.

When any of the PID variables $L_{\pi|K}^{K^*}$, $L_{\pi|p}^{K^{*\pm}}$, $L_{\pi|e}^{K^{*\pm}}$, $L_{\pi|}^{K^{*-}}$ are used to select the best $K^{*\pm}$ candidates the results were similar to those obtained using a random selection. As was seen from the K_S^0 selection study the sample of K_S^0 candidates used in the reconstruction of $K^{*\pm}$ candidates was very pure. Hence, the majority of the background was from tracks being combined with a true K_S^0. Most of these tracks were pions, therefore these PID variables were of limited use. The most useful of these variables was $L_{\pi|e}^{K^{*\pm}}$ as there is more contamination from electrons and muons than there is from kaons and protons.

When the variables R_{XY}, $DOCA_{K_S^0\pi^\pm}$, $P(\chi^2)$ were used to select the best $K^{*\pm}$ candidates the sample purities and signal significances obtained were similar with a slight improvement over those obtained using a random number. This similarity is because most of the true $K^{*\pm}$ candidates will be produced along with one or more tracks in the decay of some heavier particle. When these tracks are combined with the K^0_S candidate the resulting $K^{*\pm}$ candidates will have similar properties thus making the selection essentially random.

The only criteria that improves the sample purity and signal significance compared with those without best candidate selection is the mass difference between the reconstructed $K^{*\pm}$ mass and the PDG value. Figure 5.17 shows the invariant mass distributions of the $K^{*\pm}$ candidates before and after the selection of the best $K^{*\pm}$ candidates using the mass difference. The distribution before best candidate selection is displayed with a solid black line and the distribution after best candidate selection is shown with a dashed red line. However, using the mass difference alters the shape of the $K^{*\pm}$ mass distribution from a Breit-Wigner on cubic background to a distribution that approximates a bifurcated exponential. This biases against valid $K^{*\pm}$ candidates with masses away from the PDG value and as the $K^{*\pm}$ is a resonance these could be true candidates. However this is clearly the most effective method of best candidate selection for $K^{*\pm}$ candidates and is the only method of removing overlapping candidates that is worth considering for $K^{*\pm}$. The analyses for the $R(3520)$ production were performed both with and without best candidate selection.

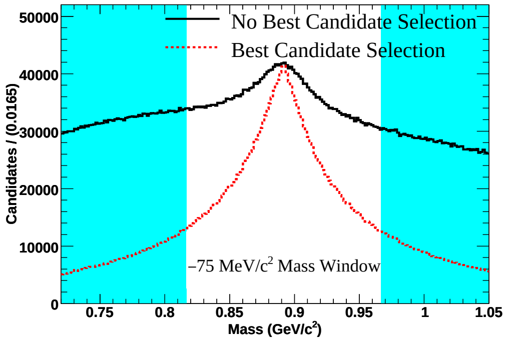

Figure 5.17: Invariant mass distributions of $K^{*\pm}$ candidates in Monte Carlo simulated data before and after the selection of the best $K^{*\pm}$ candidates using the difference between the reconstructed $K^{*\pm}$ mass and the PDG value. The candidates removed by the cut of $\pm 75\,\mathrm{MeV}/c^2$ around the $K^{*\pm}$ PDG mass are shaded.

The effects of selecting the best K^0_S candidates before selecting the best $K^{*\pm}$ candidates were investigated in order to check if the results improved. The K^0_S candidates were selected using the flight significance. The same criteria described before were used to select the $K^{*\pm}$ candidates. The results of this study are listed in Table 5.7.

When no best candidate selection was applied on the $K^{*\pm}$ the application of best candidate selection on the K^0_S reduces the total number of $K^{*\pm}$ candidates by 24825 over the whole range and by 10190 inside the mass window. This only includes 567 truthed candidates in the full range and 494 within the mass window. In each case the sample purities and signal significances of the $K^{*\pm}$ sample are exactly the same after the best candidate selection of the K^0_S The improvements are small because

Table 5.7: Effectiveness of best candidate selection criteria for $K^{*\pm}$ candidates with best candidate selection applied on the K^0_S.

	Complete Sample					75 MeV/c^2 Mass Window				
Best $K^{*\pm}$ Selection Criteria	$T+F$	F	T	$\frac{T}{T+F}$	$\frac{T}{\sqrt{T+F}}$	$T+F$	F	T	$\frac{T}{T+F}$	$\frac{T}{\sqrt{T+F}}$
None	6855585	6491777	363808	0.053	139.0	3249270	2927715	321555	0.099	178.4
Random	3092247	2902947	189300	0.061	107.7	2117358	1887038	230320	0.109	158.3
$L^{K^*}_{\pi\|K}$	3093496	2904321	189175	0.061	107.5	2118214	1888560	229654	0.108	157.8
$L^{K^*}_{\pi\|p}$	3095921	2902755	193166	0.062	109.8	2119088	1886951	232137	0.110	159.5
$L^{K^*}_{\pi\|e}$	3095822	2898897	196925	0.064	111.9	2118930	1884514	234416	0.111	161.0
$L^{K^*}_{\pi\|}$	3097605	2902581	195024	0.063	110.8	2119155	1885679	233715	0.110	160.5
$DOCA_{K^0_S\pi}$	3096131	2897245	198886	0.064	113.0	2118943	1882260	236283	0.112	162.3
R_{XY}	3096622	2901628	194994	0.063	110.8	2119155	1885437	233718	0.110	160.6
$P(\chi^2)$	3093955	2899304	194651	0.063	110.7	2118213	1884275	233938	0.110	160.7
Δ_M	3092637	2814566	278071	0.090	158.1	2117405	1856534	260871	0.123	179.3

only 0.33% of the $K^{*\pm}$ candidates are removed when the best K^0_S candidates are selected. The effect being so small, the best candidate selection of K^0_S is not used further in this analysis.

5.4 Proton, kaon and pion selection

The protons, kaons and pions used in this analysis were selected using the BABAR likelihood based PID selectors, these are described in [169]. The pions, kaons and protons were selected using the piLHLoose, KLHTight and pLHTight selectors respectively. The cuts used by these PID selectors are documented in [170] and were described in Section 4.3. The cuts for these PID selectors are detailed in Table 4.2.

The cuts on $|R_Z|$ and R_{XY} used to select K^0_S and $K^{*\pm}$ candidates were also applied for the pions, protons and kaons to ensure that they originated from the same fiducial volume close to the collision axis.

5.5 Control samples

In order to verify that the selection criteria used in this analysis were working correctly, a number of multi-particle final states were reconstructed with these selection criteria. The invariant masses of these states were calculated and in their distributions known particles were observed proving the correctness of the selection criteria. Throughout this paper, whenever a mode is given, the charge conjugate is also implied.

Figure 5.18a shows the invariant mass distribution of the $\pi^\pm$ $\pi^\pm$ $K^\mp$ final state. Peaks can be seen in the distribution at 1.87 GeV/c^2 corresponding to $D^{\pm}$ and at 2.01 GeV/c^2 corresponding to $D^{*\pm}$. Figure 5.18b shows the invariant mass distribution of the $\pi^{\pm}$ K^0_S $K^{\mp}$ final state. The peak at 1.87 GeV/c^2 from D^0 can clearly be seen. Figure 5.18c shows the invariant mass distribution of the p K^0_S final state. The peak from Λ_c^+ can clearly been seen at 2.29 GeV/c^2.

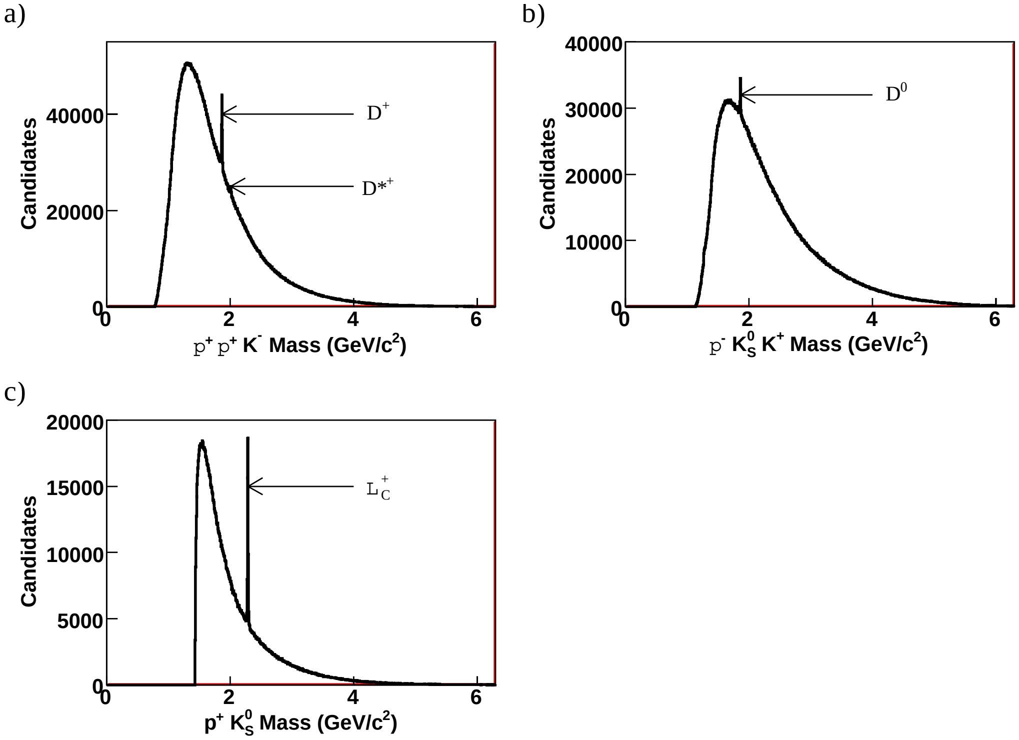

Figure 5.18: Invariant mass distributions of the multi-particle final states: π^+ π^+ K^- (a); π^- K^0_S K^+ (b); p K^0_S (c). The charge conjugate modes are included in these distributions.

Chapter 6

Search for the $R(3520)$ resonance

6.1 Loose selection of the $R(3520)$ candidates

$R(3520)$ was reconstructed in two decay modes — $p\ K^0_S\ K^+\ \pi^-\ \pi^-$ and $p\ K^{*-}\ K^+\ \pi^-$. $227\,\mathrm{fb}^{-1}$ of data were used in this search. Throughout this thesis, whenever a mode is given, the charge conjugate is also implied. The K^0_S and $K^{*\pm}$ candidates were selected using the criteria described in Section 5.2 and Section 5.3, respectively. These K^0_S candidates were combined with a tightly identified proton, a tightly identified kaon and two loosely identified pions to reconstruct $R(3520)$ candidates. The cuts on $|R_Z|$ and R_{XY} used to select K^0_S and $K^{*\pm}$ candidates were also applied for the pions, proton and kaon to ensure that they originated from the same fiducial volume close to the collision axis.

In summary the following criteria were used to select the $R(3520)$ candidates.

$p\ K^0_S\ K^+\ \pi^-\ \pi^-$ decay mode

- K^0_S identified as described in Section 5.2,
- both π^- identified as piLHLoose and GoodTracksAccLoose,
- $|R_Z|$ of both $\pi^- \leq 2.9\,\mathrm{cm}$,
- R_{XY} of both $\pi^- \leq 0.13\,\mathrm{cm}$,
- K^+ identified as KLHTight and GoodTracksAccLoose,
- $|R_Z|$ of $K^+ \leq 2.9\,\mathrm{cm}$,
- R_{XY} of $K^+ \leq 0.13\,\mathrm{cm}$,
- p identified as pLHTight and GoodTracksAccLoose,

- $|R_Z|$ of $p \leq 2.9\,\mathrm{cm}$,
- R_{XY} of $p \leq 0.13\,\mathrm{cm}$.

$p\ K^{*\pm}\ K^+\ \pi^-$ decay mode

- K^{*-} identified as described in Section 5.3,
- π^- identified as piLHLoose and GoodTracksAccLoose,
- $|R_Z|$ of π^- from $R(3520) \leq 2.9\,\mathrm{cm}$,
- R_{XY} of π^- from $R(3520) \leq 0.13\,\mathrm{cm}$,
- $K^\pm$ identified as KLHTight and GoodTracksAccLoose,
- $|R_Z|$ of $K^+ \leq 2.9\,\mathrm{cm}$,
- R_{XY} of $K^+ \leq 0.13\,\mathrm{cm}$,
- p identified as pLHTight and GoodTracksAccLoose,
- $|R_Z|$ of $p \leq 2.9\,\mathrm{cm}$,
- R_{XY} of $p \leq 0.13\,\mathrm{cm}$.

6.2 Invariant mass distributions of the $R(3520)$ candidates

The invariant masses of the $R(3520)$ candidates were calculated and their distributions were plotted in Figure 6.1 and Figure 6.2 for the decay modes $p\ K^0_S\ K^+\ \pi^-\ \pi^-$ and $p\ K^{*-}\ K^+\ \pi^-$, respectively. Plot a) in these figures shows the full spectrum while b), c) and d) show the spectrum in the ranges 2-3 GeV/c^2, 3-4 GeV/c^2, and 4-5 GeV/c^2, respectively.

A maximum likelihood fit was performed on each of the invariant mass distribution with a function of the form,

$$\Delta m^{c_1} \exp -(c_2\Delta m + c_3\Delta m^2 + c_4\Delta m^3 + c_5\Delta m^4) \tag{6.1}$$

where Δm is the difference between the $R(3520)$ candidates invariant mass and the mass threshold. The mass threshold is the sum of the invariant masses of the constituent particles involved in the reconstruction of the $R(3520)$ candidate. Mass thresholds of 2.20874 GeV/c^2 and 2.464 GeV/c^2 are used for the decay modes $p\ K^0_S\ K^+\ \pi^-\ \pi^-$ and $p\ K^{*-}\ K^+\ \pi^-$, respectively. Equation 6.1 was found to model well the invariant mass distribution of the combinatorial background in the range between the mass threshold and infinity. A similar equation was used by the FOCUS collaboration in [132] to describe the background in a search for the Θ^+.

6.3 The multiplicity of the $R(3520)$ candidates per event

Multiple $R(3520)$ candidates were reconstructed in the majority of events in which there was at least one candidate that passes the selection criteria. These multiple $R(3520)$ candidates had one or more daughters which overlapped with other candidates in an event. Figure 6.3 shows the multiplicities of $R(3520)$ candidates per event for the decay modes $p\ K_S^0\ K^+\ \pi^-\ \pi^-$ (left) and $p\ K^{*-}\ K^+\ \pi^-$ (right), respectively. The distributions have a number of peaks which are explained further.

$p\ K_S^0\ K^+\ \pi^-\ \pi^-$ decay mode

The number of $R(3520)$ candidates in an event are related to the number of kaons, protons, K_S^0 and pions in the event. The multiplicity of $R(3520)$ candidates in an event is directly proportional to both the numbers of protons and kaons of the appropriate sign in that event because only one proton and one kaon are required to reconstruct a $R(3520)$ candidate.

Figure 6.4 (left) shows the contribution to the multiplicity from the pions and the K_S^0 in the event. This is calculated by dividing the number of $R(3520)$ candidates by the product of the number of kaons and protons of the correct sign in the event. The most pronounced peaks in this distribution are at 1, 3, 6, 10, 15. There are also events with 2, 4, 9, 12, 20 candidates and also a small number of events with higher multiplicities.

The relationship between the multiplicity of $R(3520)$ candidates and the number of pions in an event is somewhat more complex. There are a number of different ways in which the pions in an event can be combined with a proton and a kaon to reconstruct a $R(3520)$ candidate. This is because two pions of the same sign are required to reconstruct a $R(3520)$ candidate and there is also an additional pion of the same sign in the K_S^0 candidate. It is made even more difficult by the fact that the ChargedTracks criteria used to select the tracks for the reconstruction of the K_S^0 candidates are different to the piLHLoose criteria used to select the two pions used in the reconstruction of the $R(3520)$ candidates.

For the events containing only a single K_S^0 candidate the multiplicity distribution depends only on the number of pions in the event. The number of different combinations of selecting two from the n pions in the list of pions passing the selection criteria for the $R(3520)$ (C_2^n) is given by the relationship below, which is the series of triangular numbers. This sequence accounts for the peaks in the multiplicity distribution at 1, 3, 6, 10, 15, 21, 28, etc.

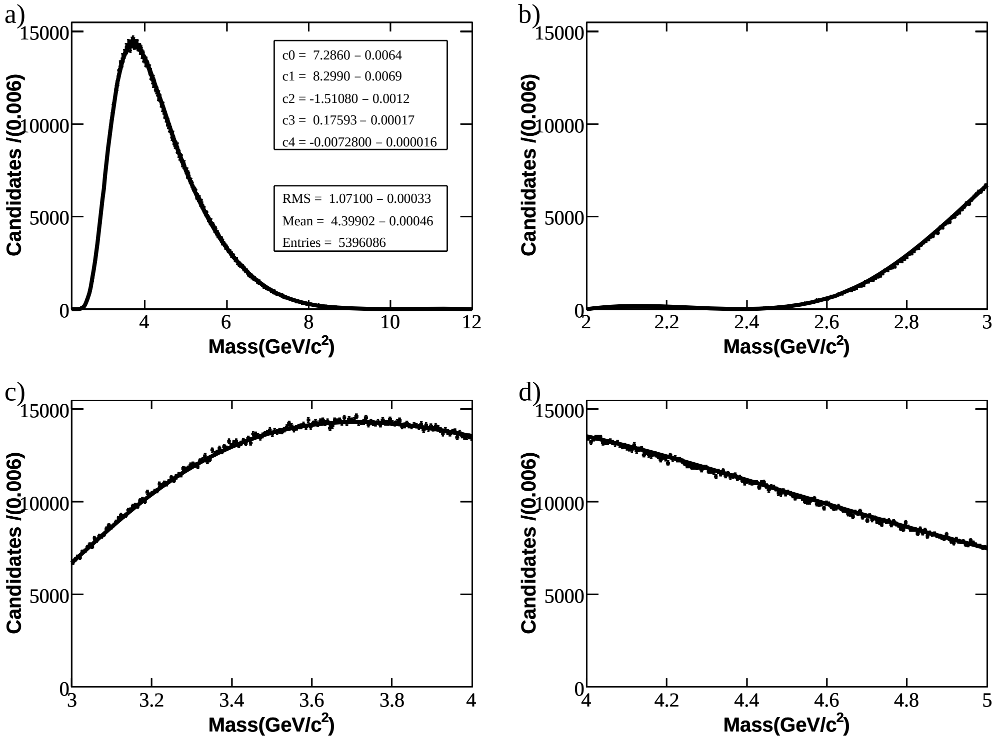

Figure 6.1: Invariant mass distributions of the $R(3520)$ candidates for the $p\ K^0_S\ K^+\ \pi^-\ \pi^-$ decay mode.

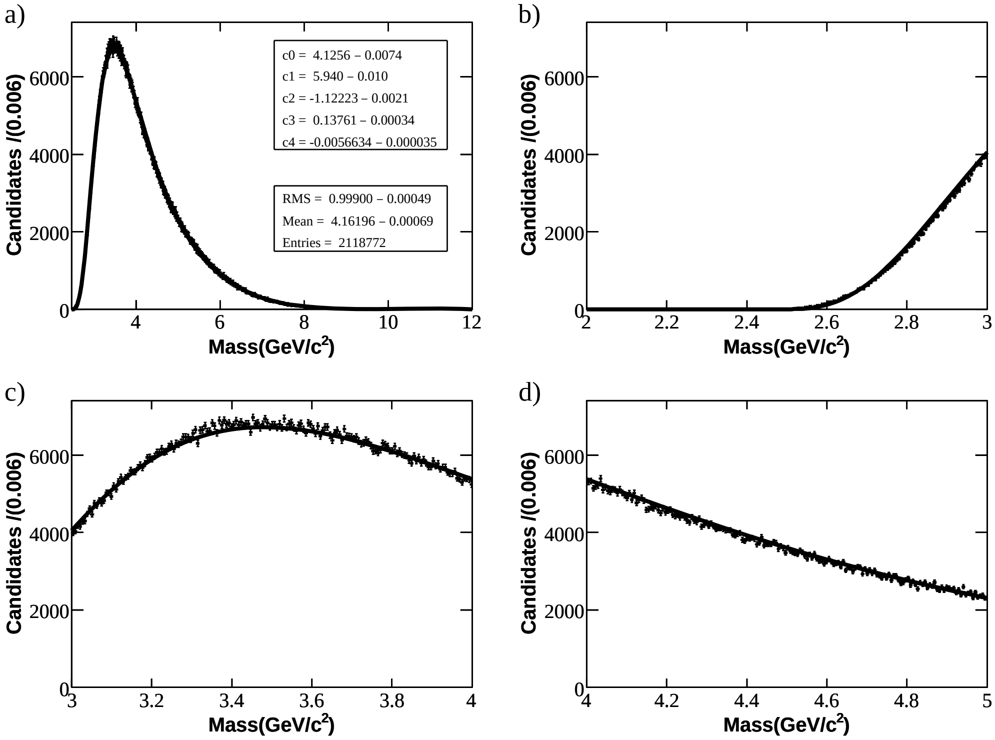

Figure 6.2: Invariant mass distributions of the $R(3520)$ candidates for the $p\ K^{*-}\ K^+\ \pi^-$ decay mode.

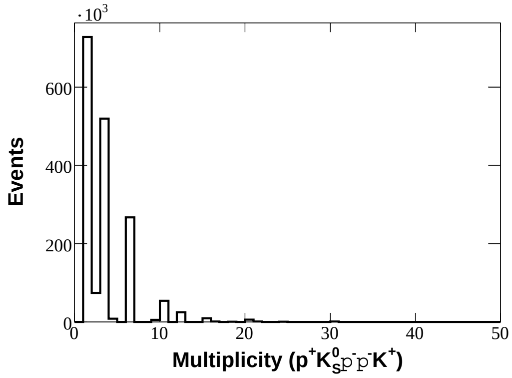

Figure 6.3: Multiplicities of $R(3520)$ candidates per event for the decay modes $p\ K^0_S\ K^+\ \pi^-\ \pi^-$ (left) and $p\ K^{*-}\ K^+\ \pi^-$ (right)

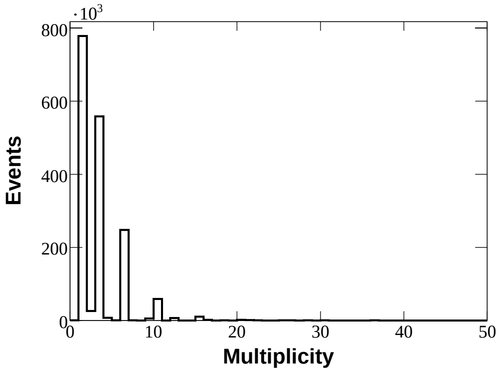

Figure 6.4: Contributions of the number of π^- and K^0_S to the $R(3520)$ multiplicity for the decay mode $p\ K^0_S\ K^+\ \pi^-\ \pi^-$ (left). Contributions of the number of π^- and K^0_S to the $R(3520)$ multiplicity for the decay mode $p\ K^{*-}\ K^+\ \pi^-$ (right). These are obtained by dividing the number of $R(3520)$ candidates by the product of the number of K^+ and the number of p in that event.

$$multiplicity = C_2^n = \frac{n!}{2!(n-2)!} = \frac{n(n-1)}{2} \tag{6.2}$$

When there are two K_S^0 candidates in an event there are three distinct situations that can occur. The selection criteria for the pion tracks used to reconstruct a $R(3520)$ candidate can be met by either zero, one or two of the pion tracks that are used to reconstruct the two K_S^0 candidates.

In the case where neither of the relevant pions used to reconstruct the two K_S^0 candidates pass the selection criteria to be used in the reconstruction of $R(3520)$ candidates the multiplicity is given by the relationship below. There is no overlap between the pions in the K_S^0 candidates and the pions in the $R(3520)$ candidate so the multiplicity is simply C_2^n multiplied by two. This will give rise to the peaks in the distribution at 2, 6, 12, 20, etc.

$$multiplicity = 2 \times C_2^n = n(n-1) \tag{6.3}$$

In the situation where the daughter of one of the K_S^0 candidates meets the selection criteria for pions used in the reconstruction of $R(3520)$ candidates, there are C_2^n combinations from the K_S^0 containing the pion that is not in the $R(3520)$ pion list and C_2^{n-1} combinations from the K_S^0 with a pion in the $R(3520)$ pion list. The multiplicity distribution is given by the equation below, which is the reason there are peaks at square numbers 1, 4, 9, 16, etc.

$$multiplicity = C_2^n + C_2^{n-1} = \frac{n(n-1)}{2} + \frac{(n-1)(n-2)}{2} = (n-1)^2 \tag{6.4}$$

When the daughter pions from both of the K_S^0 candidates also meet the selection criteria for the pions used to reconstruct the $R(3520)$ candidates, there will be C_2^{n-1} combinations from each K_S^0 candidate. Then the multiplicity will be given by the equation below which gives peaks in the distribution at 2, 6 ,12 etc.

$$multiplicity = C_2^{n-1} + C_2^{n-1} = (n-1)(n-2) \tag{6.5}$$

It is possible to derive similar formula for events containing three or more K_S^0. In general, the multiplicity of the $R(3520)$ candidates in an event coming from the the numbers of K_S^0 and π^- candidates is given by

$$multiplicity = mn(n-1)/2 - (n-1)l \tag{6.6}$$

where m is the number of K_S^0 candidates, n is the number of pions used to reconstruct the $R(3520)$ candidates and l is the number of pions used to reconstruct both $R(3520)$ and K_S^0 candidates. For the case with $m = 2$ K_S^0 candidates in an event this gives the multiplicities $n(n-1)$, $(n-1)(n-1)$, and $(n-1)(n-2)$ for events where 0, 1 and 2 pions are in the $R(3520)$ pion list, respectively (previous formulae).

A potential problem caused by the reconstruction of multiple $R(3520)$ candidates in an event is that it is possible to create fake peaks in the mass spectra. These peaks arise because the invariant mass of the $R(3520)$ is calculated from the sum of the four momentum of the six constituent tracks. As each $R(3520)$ candidate contains three pions of the same sign it is possible to interchange the position of these pions in the decay and then combine them to reconstruct up to three different candidates from the same six tracks. Obviously, these candidates will have roughly the same invariant mass. In order to stop this scenario from occurring, there is a check for these clone candidates, and only the one of these clone $R(3520)$ candidates that is reconstructed using the K_S^0 that has the highest F_{Sig} is selected. This reduces the multiplicity of candidates in some events and reduces the average multiplicity.

p K^{*-} K^+ π^- decay mode

The multiplicities of $R(3520)$ candidates for the decay mode K^{*-} π^- K^+ p are difficult to calculate because different selection criteria are applied for each of the three π^- that are used to reconstruct the $R(3520)$ (one in each of the K_S^0, K^{*-}, and $R(3520)$ particles).

Changing the order of these pions will result in the reconstruction of different $R(3520)$ candidates. These pions can be used in each of the three positions to create different $R(3520)$ candidates. This situation arises because the pions used to reconstruct the K_S^0 have different selection criteria than those in the $K^{*\pm}$ and the $R(3520)$ candidate. This means that all three pions are distinguishable in the reconstruction of the $R(3520)$ candidates.

The multiplicity of $R(3520)$ candidates per event is directly proportional to the number of kaons and to the number of protons in the event. The contribution to the multiplicity from the π^- and K^{*-} which is the multiplicity of $R(3520)$ candidates divided by the product of the number of K^+ and the number of p in the event, is shown in Figure 6.4 (right).

With a proton, a kaon, a π^+ and only three π^- in an event it is possible to reconstruct up to six different $R(3520)$ candidates with the same six tracks and therefore the same mass. This will happen rarely, because it relies on the three π^- being combined with a single π^+ to create three K_S^0 candidates who pass all of the cuts. These K_S^0 candidates would have to combine with both the other two π^- to reconstruct valid K^{*-} candidates.

A similar worse case scenario with four π^- in a single event could result in the reconstruction of up to 24 different $R(3520)$ candidates.

The π^- from the K^{*-} and the π^- from the $R(3520)$ can be swapped in approximately 21% of candidates. This number was obtained by comparing the numbers of $R(3520)$ candidates in signal Monte Carlo before and after the removal of the cloned candidates.

To ensure that only one of these clone candidates is selected the procedure below was followed. The $R(3520)$ clone candidates, which are reconstructed using the best K^0_S candidate, are chosen using F_{Sig} of the K^0_S candidate. This selection ensures that only two from a possible six clone $R(3520)$ candidates are valid. From the remaining two $R(3520)$ candidates, the $R(3520)$ clone candidate, which is reconstructed from the best K^{*-} candidate, is selected using the mass difference between the reconstructed mass and the PDG value [1] of the K^{*-} candidate.

Multiple candidates are the largest source of background in this analysis. In the sample of data the average multiplicity is 3.456 and there can only be one true $R(3520)$ candidate per event. This means that there are on average 2.456 extra candidates in every signal or background event in this analysis. Eliminating this background would be beneficial to this analysis.

6.4 Tighter selection of the $R(3520)$ candidates

In an attempt to reduce the background, additional cuts were applied on the $R(3520)$. The cut variables considered were the $P(\chi^2)$, R_Z and R_{XY} of the reconstructed $R(3520)$ candidates. In the studies of the selection of K^0_S and K^{*-} candidates the $DOCA$ between the two daughters was found to be a useful selection criteria. It is desirable to have a similar selection criteria for $R(3520)$ candidates. The DOCAs between each pair of tracks that are used in the reconstruction of the $R(3520)$ were calculated. The largest of these DOCAs is selected and this DOCA is defined as the multi-track DOCA or, $DOCA_{MT}$.

The distributions of the variables $P(\chi^2)$, $DOCA_{MT}$, R_Z, R_{XY}, for $R(3520)$ candidates for the decay modes $p\ K^+\ K^0_S\ \pi^-\ \pi^-$ and $p\ K^+\ K^{*-}\ \pi^-$ are shown in Figure 6.5 and Figure 6.6, respectively. The candidates removed are shaded on the plots. The cut values have been chosen to be consistent with those used for K^0_S and K^{*-} selection. The applied values of these cut variables are: $P(\chi^2) > 0.001$; $DOCA_{MT} \leq 0.32\,\mathrm{cm}$; $|R_Z| < 2.9\,\mathrm{cm}$; $R_{XY} \leq 0.13\,\mathrm{cm}$.

In the case where the $R(3520)$ candidate decays though a $K^{*\pm}$, the $K^{*\pm}$ can be considered either as a single track in the direction of its momentum or as two separate tracks, considering the direction of the K^0_S's momentum and the π^- track separately. Both versions were investigated. In Figure 6.6 the line displayed in solid black corresponds to the $DOCA_{MT}$ calculated considering the $K^{*\pm}$ candidate to be a single track, the line displayed in dashed red corresponds to the $DOCA_{MT}$ calculated considering the K^0_S and $\pi^\pm$ from the $K^{*\pm}$ candidate separately. It can be seen that the average $DOCA_{MT}$ of the $R(3520)$ candidates is smaller when the $K^{*\pm}$ is considered as a single track than when the K^0_S and π^- are considered individually. When the K^{*-} is considered to be a single track, the DOCA is calculated between six different pairs of tracks, when the K^0_S and π^- are considered individually the DOCA is calculated between ten pars of tracks, hence there is therefore more chance that the $DOCA_{MT}$ will be larger for an $R(3520)$ candidate. However, in the region where the cut is applied the two versions of $DOCA_{MT}$ give similar values. Hence for this cut K^{*-} is considered to be a single track.

The invariant masses of the $R(3520)$ candidates were calculated and their distributions were plotted in Figure 6.7 and Figure 6.8 for the decay modes $p\ K^0_S\ K^+\ \pi^-\ \pi^-$ and $p\ K^{*-}\ K^+\ \pi^-$, respectively. Plot a) in these figures shows to full spectrum while b), c) and d) show the spectrum in the ranges 2-3 GeV/c^2, 3-4 GeV/c^2, and 4-5 GeV/c^2, respectively. A maximum likelihood fit was performed on each of the invariant mass distributions with a function of the form given by the formula 6.1.

From these plots it can be seen that the cut on $P(\chi^2)$ is the most powerful of the cuts. The cuts on the $DOCA_{MT}$, $|R_Z|$ and R_{XY} do not remove many $R(3520)$ candidates. This is because these cuts have already been applied to the daughters of these candidates.

Figure 6.9 shows the multiplicities of $R(3520)$ candidates after tighter selection for the decay modes $p\ K^+\ \pi^-\ \pi^-\ K^0_S$ (left) and $p\ K^+\ \pi^-\ K^{*-}$ (right), respectively.

The combination of these cuts reduced the average multiplicity of $R(3520)$ candidates for the decay mode $p\ K^+\ \pi^-\ \pi^-\ K^0_S$ from 4.19 to 3.79. For the decay mode $p\ K^+\ \pi^-\ K^{*-}$ the average multiplicity of $R(3520)$ candidates was reduced from 3.65 to 3.42.

The upper limits on the cross section for the production of the $R(3520)$ with this tighter selection were calculated.

6.5 Effects of the cut on the $K^{*\pm}$ multiplicity

The invariant mass distributions of the $R(3520)$ candidates after cuts on the multiplicity of $K^{*\pm}$ candidates in an event were plotted in Figure 6.10 for the decay mode $p\ K^{*-}\ K^+\ \pi^-$. Plot a) in these figures shows the full spectrum while b), c) and d) show the spectrum in the ranges 2-3 GeV/c^2, 3-4 GeV/c^2, and 4-5 GeV/c^2, respectively. A maximum likelihood fit was performed on each of the invariant mass distribution with a function of the form given by the formula 6.1.

The mass distributions do not change much when a cut on events with a $nK^{*\pm} < 7$ is applied. The effects of a cut of $nK^{*\pm} < 5$ are more pronounced. There is a bigger difference between the three curves at lower masses than at higher masses.

The distribution of the multiplicity of $R(3520)$ candidates after cuts on the $K^{*\pm}$ multiplicity is shown for $R(3520)$ candidates for the decay mode $p\ K^+\ \pi^-\ K^{*-}$ in Figure 6.11. It can be seen that the cut on the $K^{*\pm}$ multiplicity does not have a significant effect on the $R(3520)$ multiplicity distributions. This is because the proportion of the events with $nK^{*\pm} \geq 5$ ($nK^{*\pm} \geq 7$) is only 3.5%

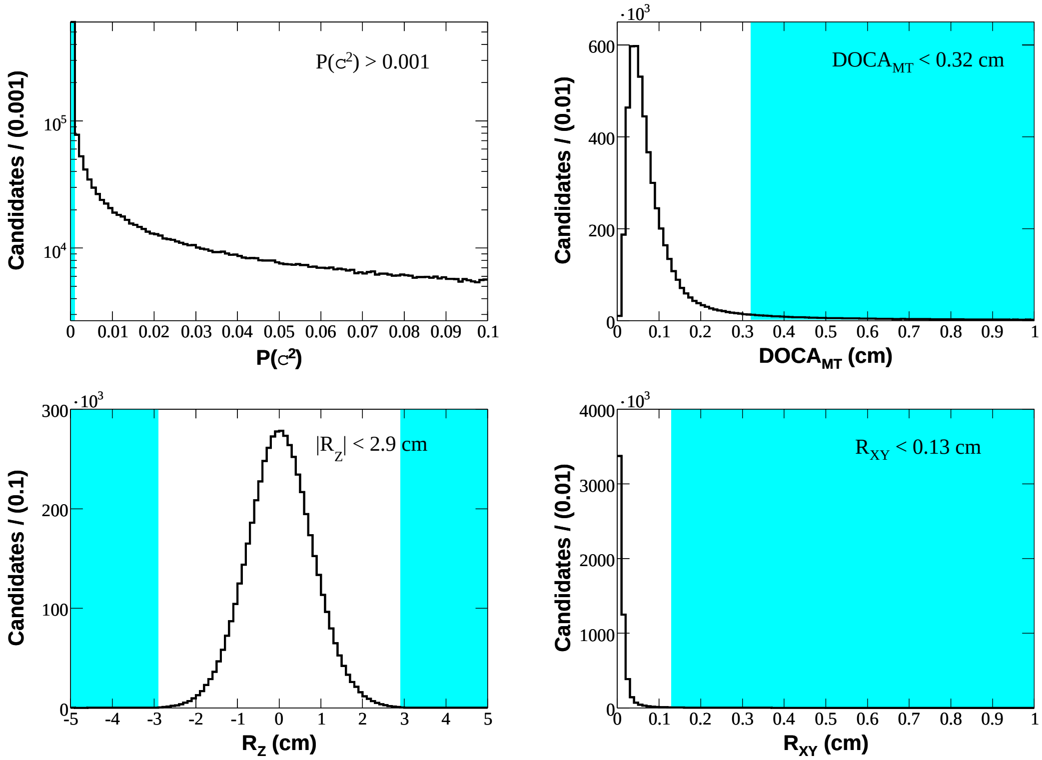

Figure 6.5: Distributions of $P(\chi^2)$, $DOCA_{MT}$, R_Z, R_{XY} variables used to select $R(3520)$ candidates in the decay mode $p\ K^+\ K_S^0\ \pi^-\ \pi^-$. The candidates removed by the cuts are shaded.

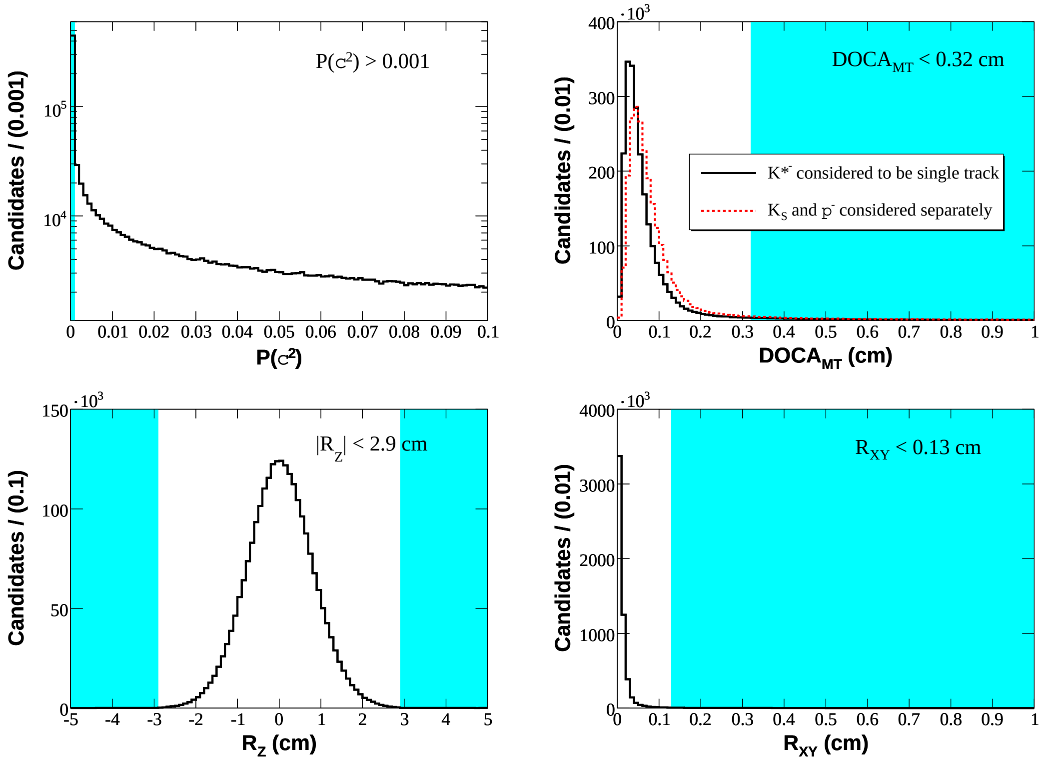

Figure 6.6: Distributions of $P(\chi^2)$, $DOCA_{MT}$, R_Z, R_{XY} variables used to select $R(3520)$ candidates in the decay mode $p\ K^+\ K^{*-}\ \pi^-$. The candidates removed by the cuts are shaded.

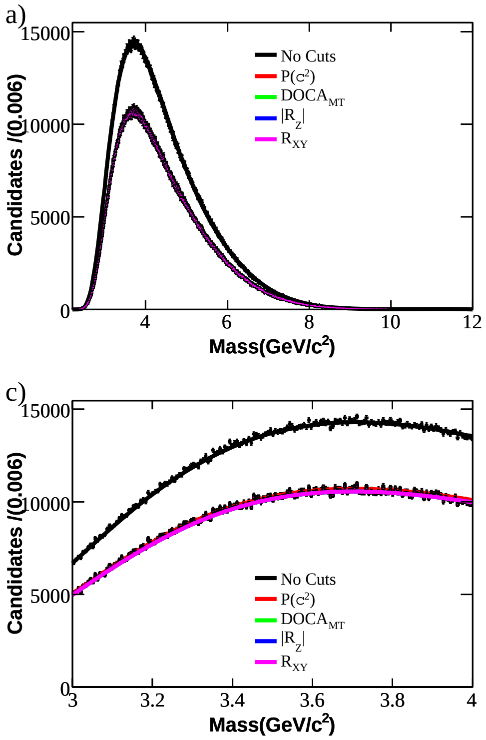

Figure 6.7: Invariant mass distributions of $R(3520)$ candidates after tighter selection for the decay mode $p\ \pi^-\ \pi^-\ K^+\ K^0_S$.

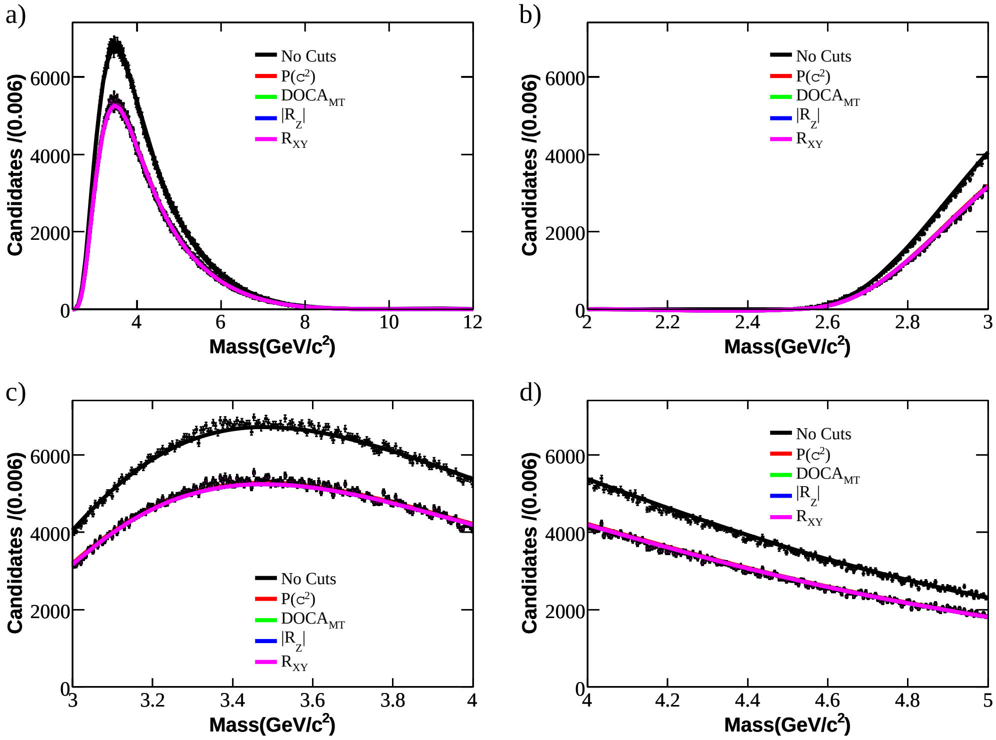

Figure 6.8: Invariant mass distributions of the $R(3520)$ candidates after the tighter selection for the decay mode $p\ \pi^-\ K^+\ K^{*-}$.

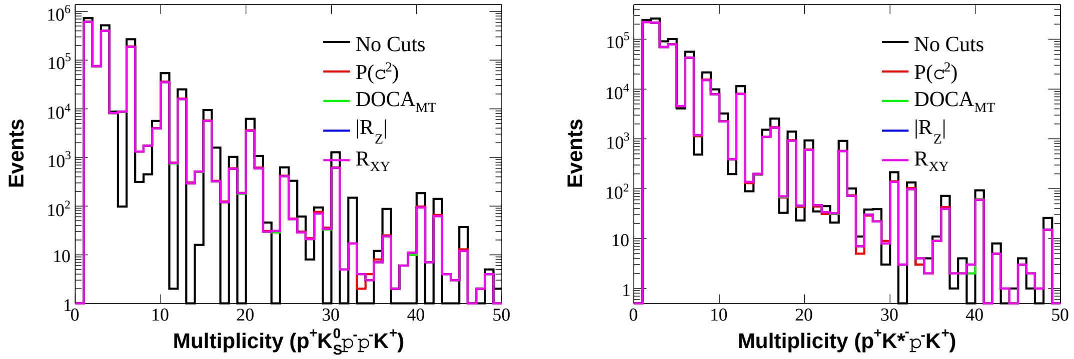

Figure 6.9: Multiplicities of $R(3520)$ candidates after tighter selection for the decay modes $p\ \pi^-\ \pi^-\ K^+\ K^0_S$ (left) and $p\ K^+\ \pi^-\ K^{*-}$ (right).

(0.54%).

The upper limits on the cross section for the production of the $R(3520)$ with these cuts on the $K^{*\pm}$ multiplicity selection were not calculated as it only affects a small proportion of the events.

6.6 Best candidate selection of the K^0_S and K^{*-} candidates

The effects of selecting the best K^0_S and K^{*-} candidates were investigated. The best K^0_S candidates were selected as described in section 5.2.7 using the F_{Sig}. The best $K^{*\pm}$ candidates were selected as described in section 5.3.5 using the difference of the $K^{*\pm}$ candidates mass from the PDG value.

The invariant mass distributions of the $R(3520)$ candidates were plotted before and after the selection of the best K^0_S and $K^{*\pm}$ candidates in Figure 6.12 and Figure 6.13 for the decay modes $p\ K^0_S\ K^+\ \pi^-\ \pi^-$ and $p\ K^{*-}\ K^+\ \pi^-$, respectively. The plots are shown before (after) the selection of the best K^0_S or K^{*-} candidates in black (red). Plot a) in these figures shows the full spectrum while b), c) and d) show the spectrum in the ranges 2-3 GeV/c^2, 3-4 GeV/c^2, and 4-5 GeV/c^2, respectively. A maximum likelihood fit was performed on each of the invariant mass distributions with a function of the form, 6.1.

The multiplicity distributions of the $R(3520)$ candidates are shown in Figure 6.14 before and after the best K^0_S and K^{*-} candidates for the decay modes $p\ K^0_S\ K^+\ \pi^-\ \pi^-$ (left) and $p\ K^{*-}\ K^+\ \pi^-$ (right), respectively.

The selection of the best K^0_S candidates has a small effect on the multiplicity of $R(3520)$ candidates for the decay mode $p\ K^0_S\ K^+\ \pi^-\ \pi^-$ This is because $R(3520)$ candidates are only removed from the events with overlapping K^0_S candidates which constitute a small proportion of the total. The selection of the best $K^{*\pm}$ candidates reduces the average multiplicity of $R(3520)$ candidates for the decay mode $p\ K^{*-}\ K^+\ \pi^-$ by about a third.

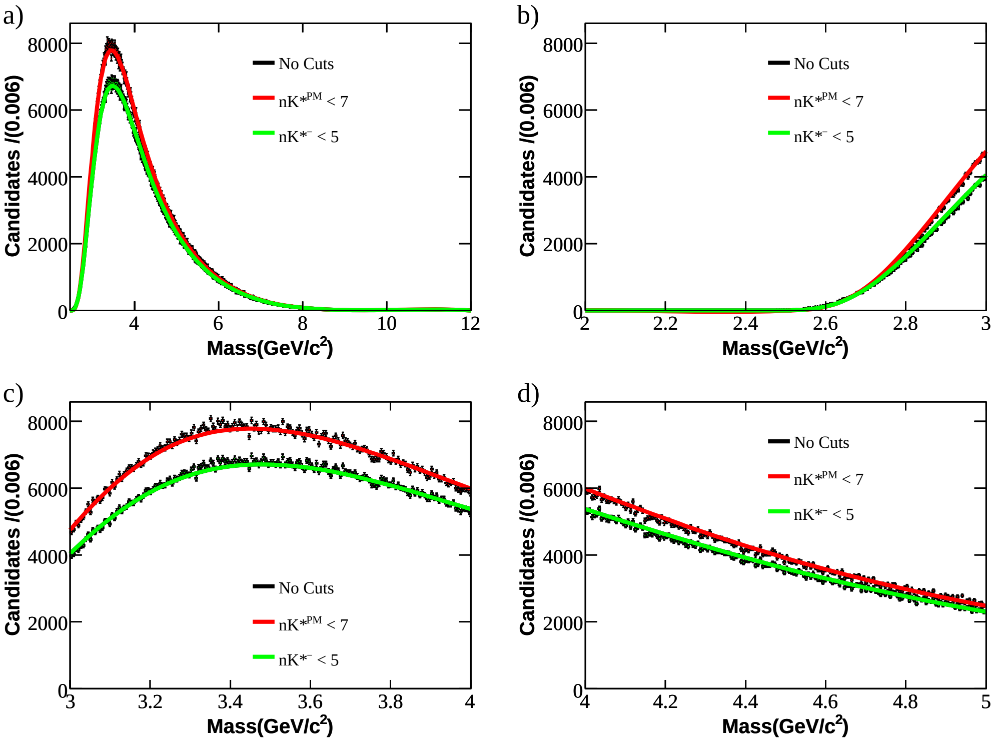

Figure 6.10: Invariant mass distributions of $R(3520)$ candidates after the application of cuts on the $K^{*\pm}$ multiplicity for the decay mode $p\ \pi^-\ K^+\ K^{*-}$.

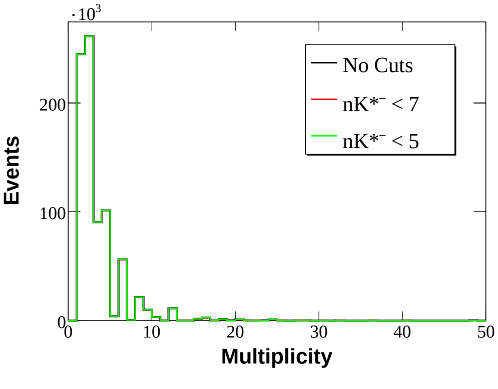

Figure 6.11: Multiplicity of $R(3520)$ candidates for the decay mode $p\ \pi^-\ K^+\ K^{*-}$ after the application of cuts on the $K^{*\pm}$ multiplicity

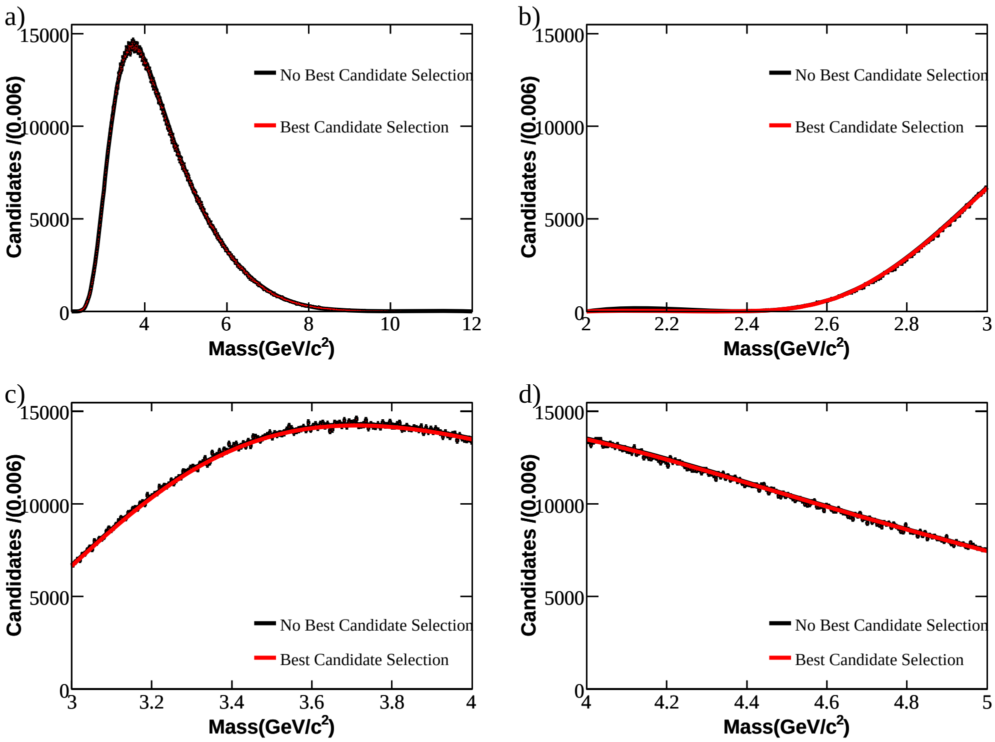

Figure 6.12: Invariant mass distributions of the $R(3520)$ candidates before and after selection of the best K_S^0 candidates for the decay mode $p\ \pi^-\ \pi^-\ K^+\ K_S^0$.

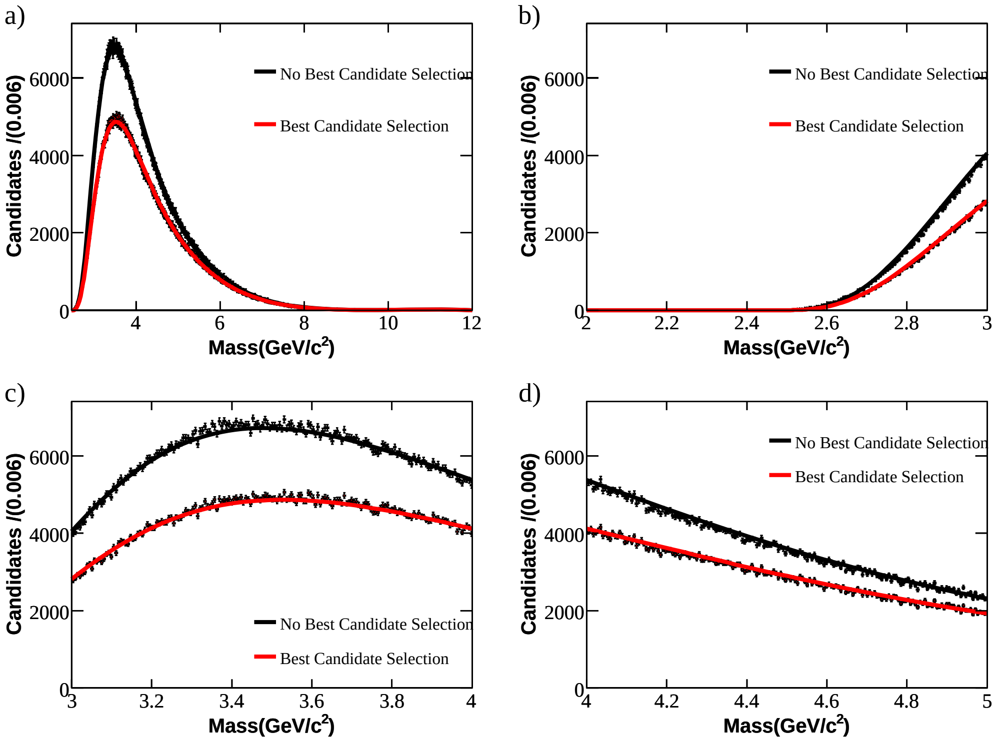

Figure 6.13: Invariant mass distributions of the $R(3520)$ candidates before and after the selection of the best K^{*-} candidates for the decay mode $p\ \pi^-\ K^+\ K^{*-}$.

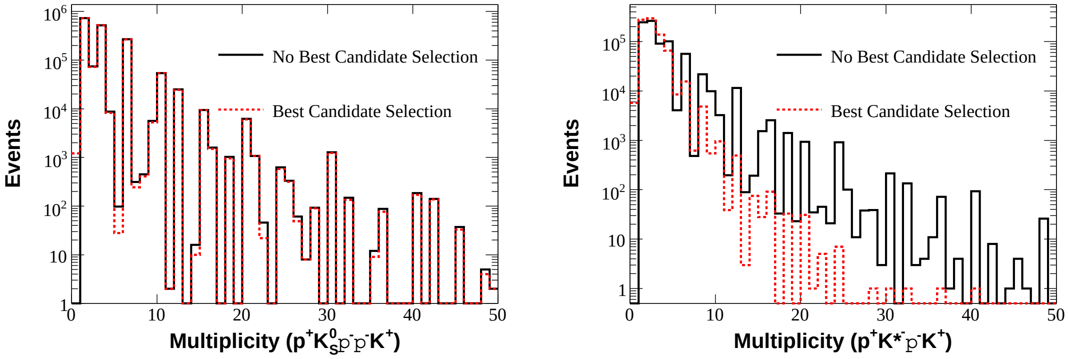

Figure 6.14: Distributions of the multiplicity of $R(3520)$ candidates per event for the decay modes $p\ \pi^-\ \pi^-\ K^+\ K^0_S$ (left) and $p\ \pi^-\ K^+\ K^{*-}$ (right) before and after the selection of the best K^0_S or K^{*-} candidates. The solid black (dashed red) show the distribution before (after) this selection.

The upper limits on the cross section for the production of the $R(3520)$ with and without the selection of the best K^0_S and $K^{*\pm}$ candidates were calculated.

Chapter 7

Upper limits on the differential cross section

7.1 Calculation of the upper limits on the differential cross section

7.1.1 Introduction

Since the production mechanism and therefore the momentum spectrum are unknown for the $R(3520)$ candidates, the differential cross section $d\sigma/dp*$ per unit c.m. momentum, $p*$, was measured or limited. The differential cross section is given by:

$$\frac{d\sigma}{dp*} = \frac{N}{\epsilon_{COR} \times L \times B \times \Delta p*} \tag{7.1}$$

where N is the number of signal candidates, ϵ_{COR} is the signal efficiency after the appropriate corrections have been applied (these corrections are described in Section 7.1.3), $L = 227.89\,\mathrm{fb}^{-1}$ is the integrated luminosity, B is the branching fraction of the reconstructed mode and $\Delta p*$ is the width of the momentum bin. The number of signal candidates, N, was returned from an extended maximum likelihood fit performed on the histogram of the invariant mass distribution in a $p*$ bin.

If the signal is consistent with zero, limits on the differential production cross section can be derived as a function of $p*$:

$$\frac{d\sigma}{dp*} \leq \frac{N^{max}}{\epsilon_{COR} \times L \times B \times \Delta p*} \tag{7.2}$$

where N^{max} is the 95% confidence level upper limit on the number of signal candidates returned from the unbinned extended maximum likelihood fit on data. The error on the number of signal candidates was taken to be the asymmetric parabolic error returned from the MINOS fit in Minuit [174]. A one-sided 95% confidence level was calculated for N^{max} with the restriction that the central value was not allowed to be negative,

$$N^{max} = max(N, 0) + 1.64 * \sqrt{\sigma_{Fit}^2 + \sigma_{Syst}^2} \tag{7.3}$$

where σ_{Fit} is the error on N returned from the fit and σ_{Syst}^2 is the sum in quadrature of the systematic errors on the measurements of B, L and ϵ_{COR}.

In order to extract N^{max} a fit of the invariant mass distribution of $R(3520)$ candidates was performed in each momentum bin with the sum of two Probability Distribution Functions (PDFs): a double Voigtian PDF used to describe the signal, and a polynomial PDF constructed from the first three Chebychev polynomials used to describe the background. The fits were performed in two stages. A unbinned maximum likelihood fit was performed to calculate the parameters which describe the shape of the signal PDF. An unbinned extended maximum likelihood fit was then used to calculate the yield.

In order to determine the parameters that describe the double Voigtian signal PDF (the mean, sigmas and fraction of candidates in the first Voigtian) a maximum likelihood fit on the invariant mass distribution of a sample of signal Monte Carlo data was performed. The two Voigtian components of the signal PDF had a common mean and the width was fixed to $1\,\mathrm{MeV}/c^2$, the generated width of the resonance. Samples of signal Monte Carlo data were generated as described in Section 4.4. These samples of signal Monte Carlo data contained a mixture of signal $R(3520)$ and combinatorial background. This background was removed using the truth information in the Monte Carlo simulation. The fit was performed on this sample of signal candidates.

To extract the yield from the real data and from the Monte Carlo simulated data, for each p* bin, unbinned extended maximum likelihood fits were performed on the invariant mass distributions of the $R(3520)$ candidates. In order for the extended maximum likelihood fit to converge the parameters which describe the shape of the signal double Voigtian PDF were fixed at the values returned from the fit on the truth matched sample of signal candidates described above. The parameters that were allowed to float in the extended maximum likelihood fit were: the two parameters describing the shape of the background PDF along with the number of signal candidates, $nSig$, and the number of background candidates, $nBkg$.

7.1.2 Signal efficiency

The signal efficiency, ϵ_{RAW}, is given by

$$\epsilon_{RAW} = \frac{N^{Signal}_{Reconstructed}}{N^{Signal}_{Generated}} \tag{7.4}$$

where, $N^{Signal}_{Reconstructed}$ and $N^{Signal}_{Generated}$ are the numbers of signal candidates reconstructed and generated in the Monte Carlo simulation, respectively.

$N^{Signal}_{Reconstructed}$ was either obtained from an extended maximum likelihood fit on a sample of signal Monte Carlo simulated data or from the the same sample using the truth information in the Monte Carlo simulation. Results obtained with both methods will be presented further.

7.1.3 Corrections to the signal efficiency

To account for differences observed between the signal efficiency in the real data and in the Monte Carlo simulated data, a set of corrections related to the tracking, PID, and K^0_S efficiencies were applied.

Tracking correction

Some differences in the signal efficiency were observed when the data and the Monte Carlo simulated data were processed with the track finding and reconstruction algorithms. The ratio between the tracking efficiencies in the real and Monte Carlo simulated data was used to apply a tracking correction to the signal efficiency.

The track reconstruction efficiencies were determined using the method described in the *BABAR* tracking efficiency studies [164] and [165] and are briefly summarised here.

The *BABAR* detector has two tracking detectors the DCH and the SVT. This makes it possible to measure the efficiency of the tracks in the DCH using the number of hits in the SVT. The method started with a track in the SVT and measured how often a corresponding track was found in the DCH. The tracking efficiency was studied for tracks with a transverse momentum $p_T > 100\,\mathrm{MeV}/c$.

To calculate the raw track reconstruction efficiency, tracks that have as least 10 hits in the SVT were compared. The number of these tracks that pass the selection criteria for GoodTracksLoose was divided by the number of the tracks that pass the selection criteria for GoodTracksVeryLoose. The selection criteria for GoodTracksLoose and GoodTracksVeryLoose are listed in the *BABAR* documentation [167] and are reproduced in Table 4.1. For tracks that had $p_T > 100\,\mathrm{MeV}/c$ the only difference between these two selection criteria is that at least 12 hits in the DCH were required to pass the GoodTracksLoose selection criteria. Thus, this method calculates the tracking efficiency of the DCH.

Sometimes, through the combination of noise hits, it is possible to form fake tracks in the SVT.

It is possible to determine how many fake tracks are formed using data from Bhabha events. The detection rate of these fake tracks was calculated by dividing the number of fake tracks by the total number of Bhabha events. Based on the assumption that fake tracks are as common in Bhabba events as in events of other types, it is possible to determine the total expected number of fake tracks, N_f, by multiplying this rate by the total number of events.

The raw tracking efficiency corrected for fake tracks ϵ_{TRK} is given by

$$\epsilon_{TRK} = \frac{\text{Number of GoodTracksLoose with 10 SVT Hits}}{\text{Number of GoodTracksVeryLoose with 10 SVT Hits} - N_f} \tag{7.5}$$

The tracking efficiency was investigated as a function of the tracks transverse momentum, p_T, the angles of the tracks ϕ and θ in the lab frame along with the track multiplicity. The output of this study was a look up table binned in these four quantities with the tracking efficiency correction calculated for each of these bins. Because the tracking efficiencies are dependent on the conditions in the detector, the efficiency corrections are applied separately for events from each of the different data taking periods used within this analysis. One condition that affects the track reconstruction efficiency is the voltage between the field and sense wires in the drift chamber. During Run 1, the first data taking period, this voltage was altered from 1960V to 1900V, therefore, the data taken at each of these voltages were considered separately and different tracking corrections were applied. During Runs 2-4, a voltage of 1930V was used, therefore a single tracking correction was applied for each of these data taking period.

This was done for both data and Monte Carlo simulated data and the ratio between the tracking efficiencies in the real and Monte Carlo simulated data was used to apply a tracking correction to the signal efficiency.

The total tracking correction for a $R(3520)$ candidate was calculated by multiplying the tracking efficiencies of the two pions, the kaon and the proton together. This quantity was used as a weight which was applied individually to each of the $R(3520)$ candidates.

An extended unbinned maximum likelihood fit was performed on the invariant mass with the $R(3520)$ candidates weighted using the tracking efficiencies. The tracking efficiency correction applied was the ratio of the then number of signal $R(3520)$ candidates with and without the tracking correction.

PID correction

Some differences between the performance of the PID selectors on the data and on the Monte Carlo simulated data were seen at BABAR. The efficiencies for each of the PID selectors were calculated using control samples of data and Monte Carlo simulated data. The PID correction for a particular PID selector is the ratio between the efficiencies of that PID selector in real data and Monte Carlo simulated data. The PID corrections and the procedure for applying them are described in [175] and are briefly summarised here.

The control samples were divided into bins of the tracks momentum, and the angles of the track θ and ϕ. The PID efficiencies were calculated in each of these bins for charged pions, kaons, protons, electrons and muons of both signs. The PID correction along with the error on the PID correction and a status, which depicted the reliability of the PID selector, were calculated for each bin.

The PID correction that was returned for a track using a particular selector was dependent on the truth information in the Monte Carlo simulation that was associated with that track. For example, the weight that was returned for a generated electron that was reconstructed as kaon would be the ratio of the electron misidentification rates and not the ratio of the kaon efficiencies.

If the PID efficiency was close to one in the real data and close to zero in the Monte Carlo simulated data then it was possible to get candidates with PID corrections that were very large. These could have caused major variations in the mass distribution and therefore would have had a large effect on the correction. As the errors associated with the PID correction for such candidates were much larger than the PID correction itself, the PID correction was consistent with one. Therefore no PID corrections were applied to such candidates.

The total PID correction for a $R(3520)$ candidate is calculated by multiplying the PID corrections from the two pions, the kaon and the proton together. This quantity was used as the PID correction which was applied as a weight to each of the $R(3520)$ candidates, individually.

K_S^0 correction

Similarly, a correction is applied to account for the difference between the reconstruction of K_S^0 decays in the data and in the Monte Carlo simulation. The efficiencies for tracks which originate within $R_{XY} < 1.5\,\mathrm{cm}$ were well modelled in the Monte Carlo simulation. Most K_S^0 candidates decay outside this region therefore the tracks from these decays were simulated more poorly. A study to investigate the differences between K_S^0 decays in data and Monte Carlo simulated data at BABAR is described in [176].

The output from this study was a binned look up table giving the corrections to the efficiency from K_S^0 reconstruction as a function of p_T (the transverse momentum), θ_{LAB} (the angle in the lab frame) and d_{XY} (the flight length in the XY plane). Because the K_S^0 reconstruction efficiencies were dependent on the detector and trigger efficiencies, which vary with time, different corrections were applied for events from each of the four data taking periods used in this analysis.

This analysis follows the K_S^0 correction recipe given by the tracking efficiency task force in [177]. However, this prescription was only applicable if the number of K_S^0 candidates in the final state was known in advance. Also, the method was only directly applicable to events containing either one or two K_S^0 candidates. Because there were events containing four or more K_S^0 candidates present in this analysis, this recipe has been adapted to account for these events. In this analysis the K_S^0 correction has been applied on a candidate by candidate basis as opposed to an event by event basis.

Corrected efficiency

The corrected signal efficiency, ϵ_{COR}, is the raw signal efficiency multiplied by the product of the tracking, PID and K_S^0 corrections.

$$\epsilon_{COR} = \epsilon_{RAW} \times W_{TRK} \times W_{PID} \times W_{K_S^0} \tag{7.6}$$

where, W_{TRK} is the tracking correction, W_{PID} is the PID correction, $W_{K_S^0}$ is the K_S^0 correction and ϵ_{RAW} is the raw efficiency.

7.1.4 Systematic errors

Systematic errors from uncertainties on the limited statistics of the signal Monte Carlo data, on the tracking correction to the signal efficiency, on the PID correction to the signal efficiency, on the K_S^0 correction to the signal efficiency, on the measurement of the luminosity and on the branching fraction were evaluated and applied. The relative systematic errors from these sources were summed in quadrature.

The procedures described in recommended statistical methods for the BABAR experiment are presented in [178], which includes a chapter on systematic errors, were followed in this analysis. The content of this chapter is also contained in a number of statistics textbooks, including [179].

The systematic error on a parameter can be determined by taking two different measurements of the parameter. When the measurements are both extreme and there is an equal probability that either of these is correct, the systematic error can be taken to be the difference between the two values divided by 2. This is the method applied in this analysis.

Systematic error on the signal efficiency due to the limited size of the signal Monte Carlo simulated data

There is an uncertainty due to the fact that the signal efficiency and the shape of the signal PDF have been determined using a finite sample of Monte Carlo simulated data.

The signal efficiency is the probability that a generated $R(3520)$ candidate will be detected. For each candidate there are two possible outcomes therefore in $N_{Generated}^{Signal}$ trials $N_{Observed}^{Signal}$ will follow a binomial probability distribution with a probability ϵ_{RAW}. From the formula for the variance of a binomial distribution it is possible to derive that the systematic error due to the limited statistics of the sample of the Monte Carlo simulated data $\Delta\epsilon^{MC}_{RAW}$ is given by

$$\Delta\epsilon^{MC}_{RAW} = \sqrt{\frac{\epsilon_{RAW}(1-\epsilon_{RAW})}{N^{Signal}_{Generated}}} \tag{7.7}$$

Systematic error associated with the corrections to the signal efficiency

The systematic errors associated with the tracking, PID, and K^0_S corrections to the signal efficiency were calculated by dividing the difference between the signal efficiencies before and after the application of the correction by two.

So, the systematic error associated with the application of a correction to the signal efficiency, $\Delta\epsilon^{i}_{RAW}$, is given by

$$\Delta\epsilon^{i}_{RAW} = \frac{|\epsilon_i - \epsilon_{RAW}|}{2} \tag{7.8}$$

where, $i = TRK||PID|KS$, ϵ_i, is the signal efficiency after the tracking, PID weighting or K^0_S correction has been applied and ϵ_{RAW} is the signal efficiency before the correction has been applied.

Systematic error associated with the luminosity measurement

The luminosity L at e^+e^- colliders is measured by

$$L = \frac{N}{\sigma_{VIS}} \tag{7.9}$$

where N is the number of events observed and σ_{VIS} is the visible cross section of some process in the detector. $\sigma_{VIS} = \epsilon \times \sigma_{th}$, where ϵ is the reconstruction efficiency of the detector and σ_{th} is the theoretical cross section of the process considered.

The process that is used to determine the luminosity in the detector should be, ideally, both common and well understood. It is desirable to use two or more different processes to measure the luminosity in the detector as this provides a cross check and allows the reduction of the systematic errors.

At BABAR the luminosity was measured using the rates of $e^+e^- \to e^+e^-(\gamma)$ and $e^+e^- \to \mu^+\mu^-(\gamma)$. These measurements can reveal time dependent effects and variations in the efficiencies of the detector and trigger. Because the cross sections of both processes are large, for any reasonably sized sample of events the statistical error will be dwarfed by the systematic errors on the luminosity. These systematic errors on the luminosity originate from a number of sources including uncertainties in the raw cross sections, tracking, Bremsstrahlung in the e^+e^- measurement and background and stability issues in the $\mu^+\mu^-$ measurement. A dedicated study at BABAR showed that the combined total systematic error on the luminosity from these sources is 1.1% [180].

Systematic error on the branching fraction

The branching fractions used in this analysis were taken from [1] and are $B(K^0_S \rightarrow \pi^+\pi^-) = 69.2\% \pm 0.05\%$, $B(K^0 \rightarrow K^0_S) = 50\%$, and $B(K^{*+} \rightarrow K^0\pi^+) = 50\%$. These branching fractions are well understood and therefore the systematic errors associated with using them were very small.

Systematic error due to the fit procedure

The systematic effects which originated from the fit were also considered. The background function was varied and this was found to have a negligible effect. Various signal functions were also investigated, including Breit Wigner, Voigtian and double Voigtian. The effects of these on the upper limit were negligible. To investigate possible resolution effects, Voigtian and double Voigtian PDF were fitted across the complete sample of signal Monte Carlo simulated data instead of that in the relevant p* bin and this was found to have a negligible effect on the limits. The cross section is dependent on the width and this was covered by using two different width hypotheses which gives a systematic range. Variation of the central mass window had no effect beyond that introduced by the statistical fluctuations. The chosen mass of 3520 MeV/c^2 was not at a point where there is a large downwards fluctuation therefore these effects were neglected.

Total systematic error

The total relative systematic error, $\frac{\sigma_{Syst}}{N^{MAX}}$, is given by,

$$\frac{\sigma_{Syst}}{N^{MAX}} = \sqrt{\left(\frac{\Delta\epsilon^{MC}_{RAW}}{\epsilon_{RAW}}\right)^2 + \left(\frac{\Delta\epsilon^{K^0_S}_{RAW}}{\epsilon_{RAW}}\right)^2 + \left(\frac{\Delta\epsilon^{TRK}_{RAW}}{\epsilon_{RAW}}\right)^2 + \left(\frac{\Delta\epsilon^{PID}_{RAW}}{\epsilon_{RAW}}\right)^2 + \left(\frac{\Delta L}{L}\right)^2 + \left(\frac{\Delta B}{B}\right)^2} \tag{7.10}$$

where, $\Delta\epsilon^{MC}_{RAW}$ is the systematic error from the limited statistics of the Monte Carlo data, $\Delta\epsilon^{K^0_S}_{RAW}$ is the systematic error on the signal efficiency, ϵ_{RAW}, associated with the reconstruction of K^0_S candidates, $\Delta\epsilon^{TRK}_{RAW}$ is the systematic error associated with the tracking correction to the signal efficiency, $\Delta\epsilon^{PID}_{RAW}$ is the systematic error associated with the PID correction on the signal efficiency, ΔL is the systematic error associated with the measurement of the luminosity, L, and ΔB is the systematic error associated with the measurement of the branching fraction, B.

7.2 Experimental results of the upper limits on the differential cross section — $\Gamma = 1\,\mathrm{MeV}/c^2$ hypothesis

The results from the calculations of the upper limit on the differential cross section for the production of $R(3520)$ candidates at *BABAR* are presented in this section. The data was divided into four momentum bins. Each quantity is given for each bin. The calculation is described in detail in section 7. The $p\ \pi^-\ \pi^-\ K^+\ K^0_S$ and $p\ \pi^-\ K^+\ K^{*-}$ results use the SP6050 and SP6051 samples of signal Monte Carlo simulated data, respectively, which were produced as described in Section 4.4.

As shown in Section 6.3 it was possible to reconstruct multiple candidates from the same six tracks. To prevent the double counting in the maximum likelihood fits which determine the yield and the signal efficiency the procedure described in Section 6.3 was used. This is valid because the only quantity that is of interest in this analysis is the invariant mass of the $R(3520)$ candidates. $R(3520)$ candidates which are constructed using the same six tracks with the same particle assignment will have the same invariant mass therefore for the purpose of performing the maximum likelihood fit, it makes no difference which of these candidates is chosen. However, the order in which the tracks are combined together is important for the truth matching process. The method used to select the $R(3520)$ candidate will ensure that the truth matched candidate is selected on the majority of occasions. However, sometimes the wrong duplicate candidate will be chosen in this case if the six tracks used in the reconstruction have the correct particle assignment and are the same six tracks used to reconstruct the truth matched candidate then the duplicate candidate is considered to be truth matched.

7.2.1 Loose selection of the $R(3520)$ candidates

The invariant mass distributions for the decay modes $p\ \pi^-\ \pi^-\ K^+\ K^0_S$ and $p\ \pi^-\ \pi^-\ K^+\ K^0_S$ are shown in Figure 7.1 and Figure 7.2, respectively. In each figure, the top four plots are for signal Monte Carlo simulated data and the bottom four plots are for real data. The solid lines show the extended maximum likelihood fit on these distributions and the dashed line shows the background component of these fits. The numbers of signal and background candidates are given on the plot.

Results of the calculation of the upper limits on the differential cross section for the production of $R(3520)$ candidates for the decay modes $K^0_S\ K^+\ p\ \pi^-\ \pi^-$ and $K^{*-}\ K^+\ p\ \pi^-$ are tabulated in Table 7.1 and Table 7.1, respectively. The signal efficiencies have been calculated using both the number of signal candidates returned from extended maximum likelihood fits and the number of signal candidates determined from the Monte Carlo truth information.

From the tabulated results it can be seen that the corrected efficiency increases with the p*. There are a number of reasons for that. Firstly, for the decays of $R(3520)$, with higher p* it is more likely that

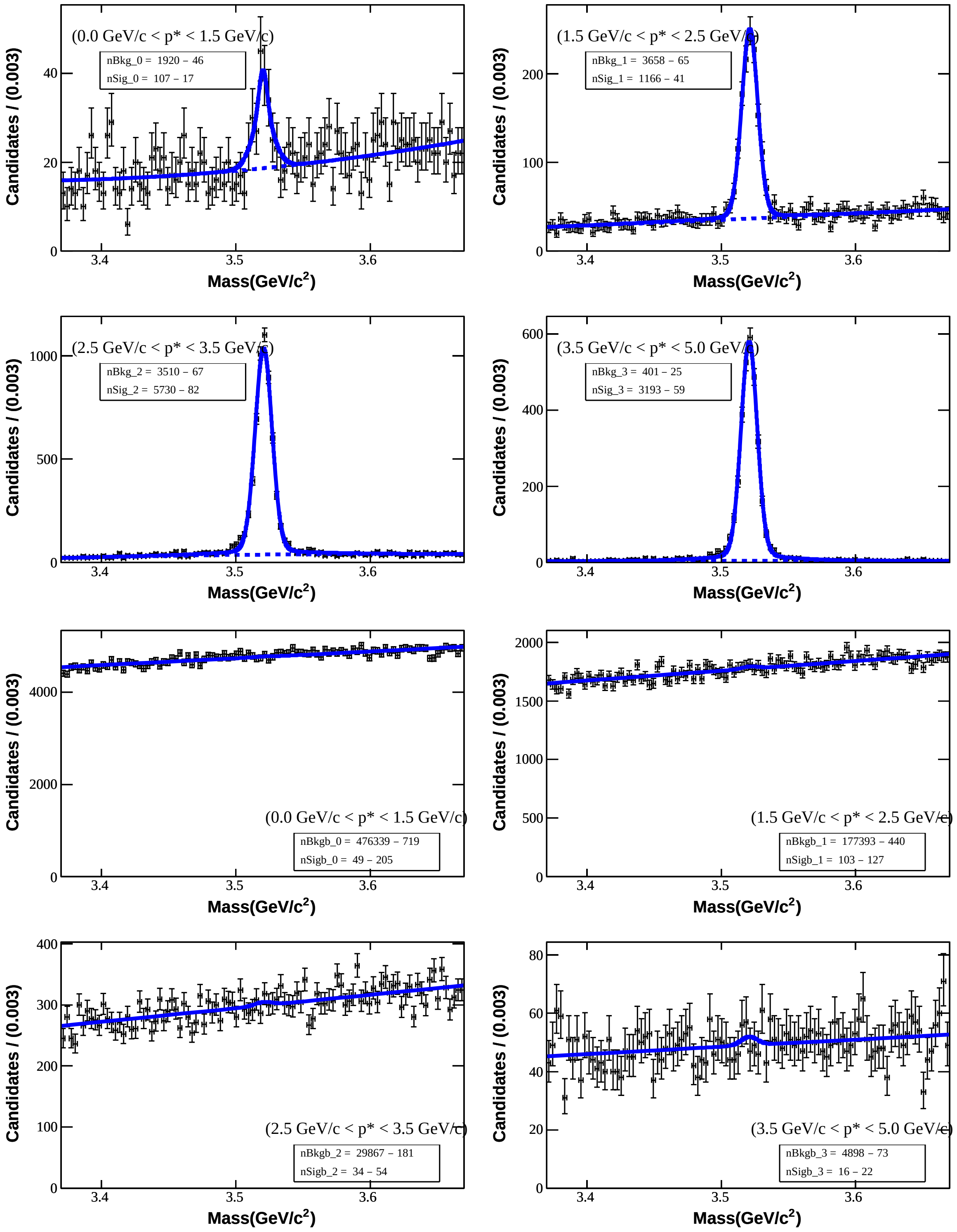

Figure 7.1: Invariant mass distribution of $R(3520)$ candidates in the SP6050 Monte Carlo (top four plots) and data (bottom four plots) for each $p*$ bin for the decay mode $p\ \pi^-\ \pi^-\ K^+\ K^0_S$.

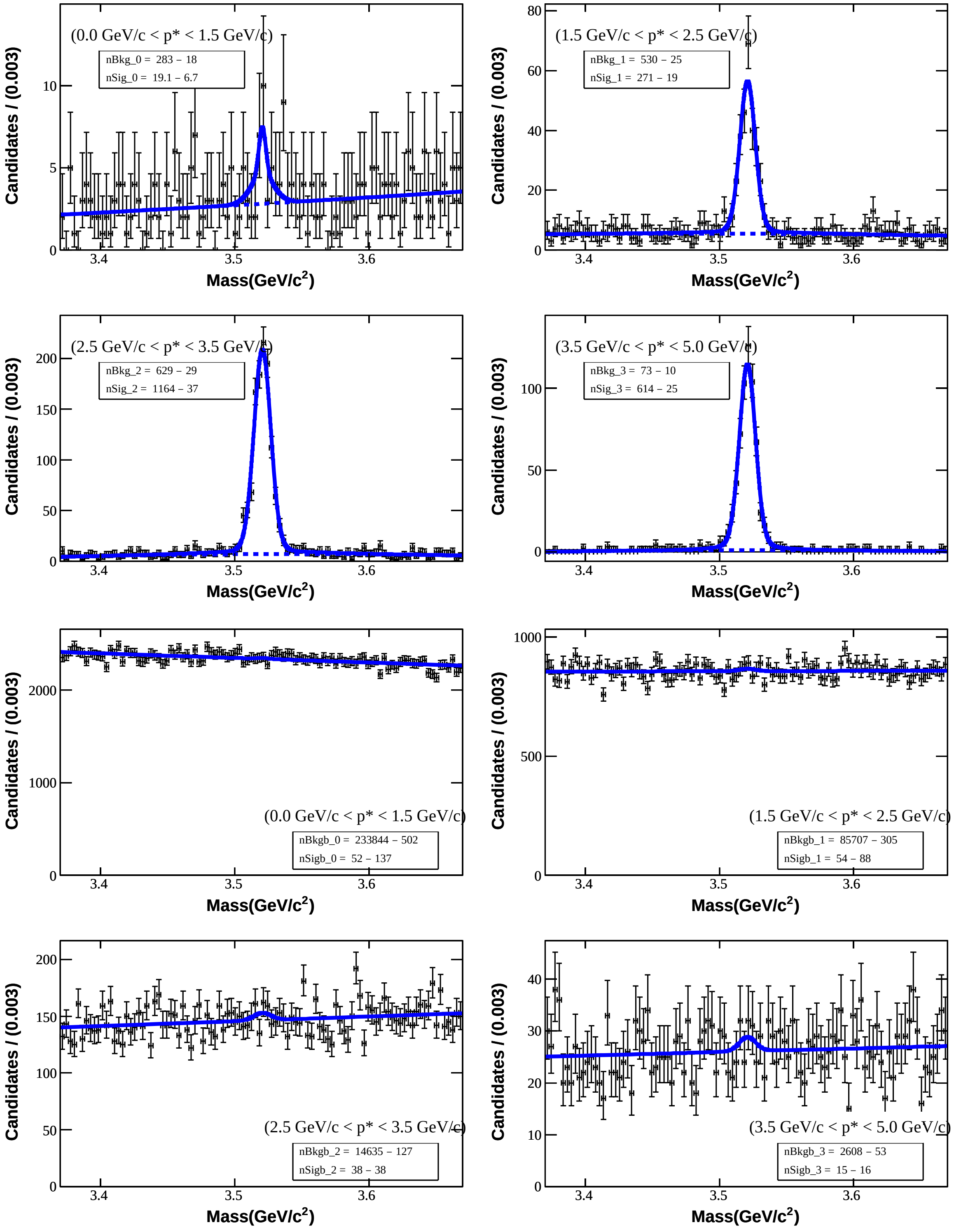

Figure 7.2: Invariant mass distribution of $R(3520)$ candidates for the decay mode $p\ \pi^-\ K^+\ K^{*-}$ in the SP6051 Monte Carlo simulated data (top four plots) and data (bottom four plots) for each $p*$ bin.

Table 7.1: Upper limit on the differential cross section on the production of the $R(3520)$ for the decay mode K^0_S K^+ p π^- π^- using SP6050 Monte Carlo.

Bin	1		2		3		4	
Method	Fit	Truth	Fit	Truth	Fit	Truth	Fit	Truth
p* (GeV/c)	0.00-1.50		1.50-2.50		2.50-3.50		3.50-5.00	
Fitted Yield	$49.32^{+203.65}_{-205.76}$		$102.71^{+127.43}_{-127.55}$		$33.61^{+54.27}_{-53.59}$		$16.38^{+22.32}_{-21.53}$	
Shift	0.00		0.00		0.00		0.00	
Raw Efficiency (%)	5.93	6.67	7.08	7.23	8.73	8.90	10.05	10.16
Track eff. corr.(%)	96.20	96.10	95.91	95.83	95.76	95.78	95.91	95.92
PID eff. corr. (%)	99.02	98.79	98.67	98.32	97.95	97.97	97.93	97.97
K^0_S eff. corr. (%)	97.82	102.10	100.18	100.55	101.55	100.53	101.04	100.67
Corrected Efficiency (%)	5.53	6.47	6.72	6.85	8.32	8.39	9.54	9.61
Raw UL (events)	385.34		312.97		123.16		53.20	
MC Stat error	9.39	8.82	2.82	2.79	1.26	1.25	1.68	1.67
Tracking Syst error	1.90	1.95	2.05	2.09	2.12	2.11	2.04	2.04
PID Syst error	0.49	0.60	0.67	0.84	1.03	1.02	1.03	1.01
K^0_S Syst error	1.09	1.05	0.09	0.27	0.78	0.26	0.52	0.33
Total Syst.	9.72	9.18	3.72	3.76	2.99	2.89	3.09	3.05
Corrected UL	391.79	391.11	314.27	314.30	123.44	123.42	53.35	53.34
Luminosity (fb^{-1})	227.89		227.89		227.89		227.89	
Branching Fraction	0.35		0.35		0.35		0.35	
Upper Limit (fb/ GeV/c)	59.93	51.14	59.34	58.17	18.82	18.65	4.73	4.69

Table 7.2: Upper limit on the differential cross section of the production of the $R(3520)$ for the decay mode K^{*-} K^+ p π^- using SP6051 Monte Carlo.

Bin	1		2		3		4	
Method	Fit	Truth	Fit	Truth	Fit	Truth	Fit	Truth
p* (GeV/c)	0.00-1.50		1.50-2.50		2.50-3.50		3.50-5.00	
Fitted Yield	$51.85^{+137.46}_{-137.53}$		$54.09^{+87.86}_{-87.47}$		$38.01^{+38.54}_{-37.80}$		$14.90^{+16.11}_{-15.31}$	
Shift	0.00		0.00		0.00		0.00	
Raw Efficiency (%)	4.71	4.68	7.24	6.75	7.63	7.50	8.35	8.09
Track eff. corr.(%)	96.02	95.82	95.73	95.77	95.82	95.84	95.67	95.87
PID eff. corr. (%)	93.22	95.47	98.06	98.31	97.75	97.76	97.50	97.53
K^0_S eff. corr. (%)	96.32	100.95	100.85	100.23	102.37	100.87	102.00	100.61
Corrected Efficiency (%)	4.06	4.32	6.86	6.37	7.31	7.08	7.94	7.61
Raw UL (events)	278.66		199.06		101.61		41.48	
MC Stat error	22.32	22.40	5.85	6.07	2.82	2.84	3.86	3.93
Tracking Syst error	1.99	2.09	2.14	2.11	2.09	2.08	2.16	2.06
PID Syst error	3.39	2.26	0.97	0.84	1.12	1.12	1.25	1.24
K^0_S Syst error	1.84	0.48	0.42	0.11	1.19	0.43	1.00	0.30
Total Syst.	22.76	22.64	6.41	6.58	4.02	3.88	4.84	4.75
Corrected UL	306.89	306.61	201.15	201.26	102.18	102.14	41.80	41.78
Luminosity (fb^{-1})	227.89		227.89		227.89		227.89	
Branching Fraction	0.17		0.17		0.17		0.17	
Upper Limit (fb/ GeV/c)	127.73	119.96	74.41	80.11	35.43	36.57	8.90	9.29

the decay products will have momentum which is higher than the threshold in the GoodTracksAccLoose selection criteria. Secondly, the higher the p* of the generated $R(3520)$ candidates the more jetlike their decays will be therefore it is more likely that all five tracks will be within the acceptance of the detector hence the efficiency was higher at high p*.

7.2.2 Best candidate selection of the K_S^0 and K^{*-} candidates

The procedure followed to select the best K_S^0 and K^{*-} candidates was that described in Section 5.2.7 and Section 5.3.5, respectively. The K_S^0 candidates selected are those with the largest flight length significance and the K^{*-} candidates which are selected are those with the mass closest to the mass given in the PDG book [1].

The invariant mass distributions for the decay modes $p\ \pi^-\ \pi^-\ K^+\ K_S^0$ and $p\ \pi^-\ K^+\ K^{*-}$ are shown in Figure 7.3 and Figure 7.4, respectively. In each figure, the top four plots are for signal Monte Carlo simulated data and the bottom four plots are for data. The solid lines show the result of the extended maximum likelihood fit on these distributions, the dashed line shows the background component of these fits. The numbers of signal and background candidates are given on the plot.

Results are tabulated in Table 7.3 and Table 7.4 for the calculation of the upper limits on the differential cross section for the production of $R(3520)$ candidates for the decay modes $K_S^0\ K^+\ p\ \pi^-\ \pi^-$ and $K^{*-}\ K^+\ p\ \pi^-$, respectively. The signal efficiencies have been calculated both using the number of signal candidates returned from extended maximum likelihood fits and also using the number of signal candidates determined from the Monte Carlo truth information.

7.2.3 Tighter selection of the $R(3520)$ candidates

The invariant mass distributions of the $R(3520)$ candidates with the tighter selection criteria (see Section 6.4) applied for the decay modes $p\ \pi^-\ \pi^-\ K^+\ K_S^0$ and $p\ \pi^-\ K^+\ K^{*-}$ are shown in Figure 7.5 and Figure 7.6, respectively. In each figure, the top four plots are for signal Monte Carlo simulated data and the bottom four plots are for real data. The solid lines show the result of the extended maximum likelihood fit on these distributions, the dashed line shows the background component of these fits. The numbers of signal and background candidates are given on the plot.

Results are tabulated in Table 7.5 and Table 7.6 for the calculation of the upper limits on the differential cross section for the production of $R(3520)$ candidates for the decay modes $K_S^0\ K^+\ p\ \pi^-\ \pi^-$ and $K^{*-}\ K^+\ p\ \pi^-$, respectively. The signal efficiencies have been calculated both using the number of signal candidates returned from extended maximum likelihood fits and also using the number of signal candidates determined from the Monte Carlo truth information.

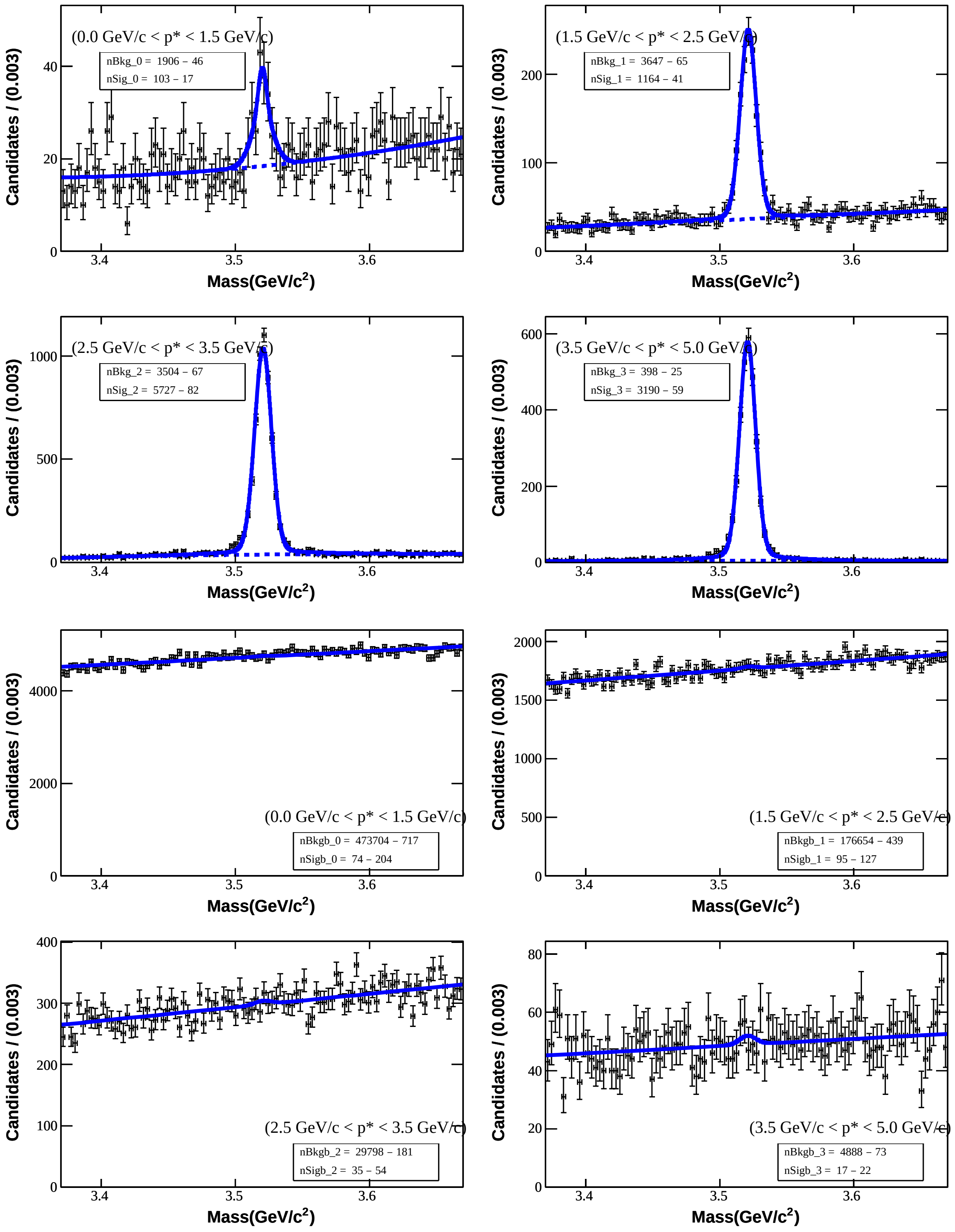

Figure 7.3: Invariant mass distributions of $R(3520)$ candidates in the SP6050 sample of Monte Carlo (top four plots) and data (bottom four plots) for the decay mode $p\ \pi^-\ \pi^-\ K^+\ K^0_S$ with best candidate selection applied on the K^0_S for each $p*$ bin.

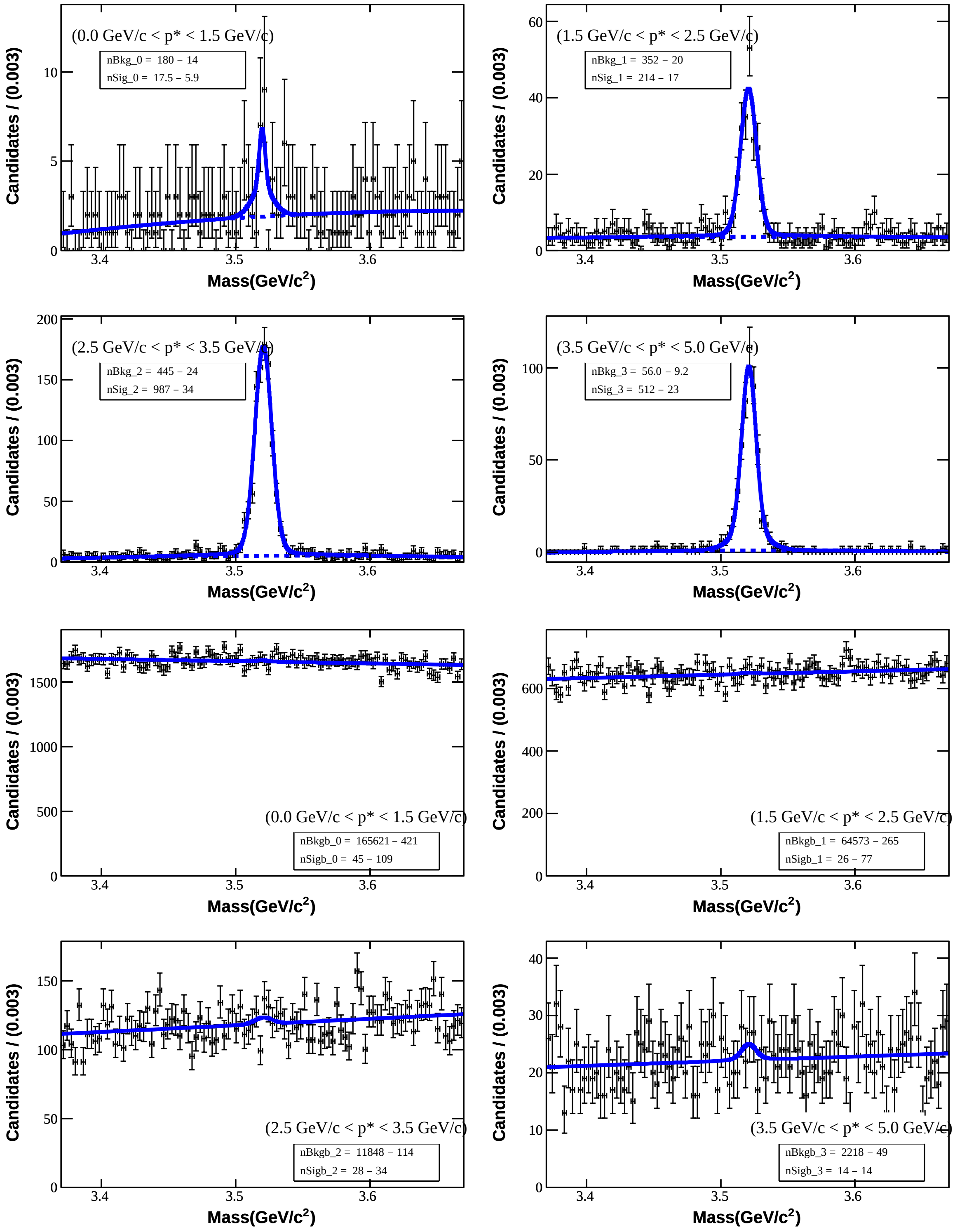

Figure 7.4: Invariant mass distributions of $R(3520)$ candidates in the SP6051 sample of Monte Carlo (top four plots) and data (bottom four plots) for the decay mode $p\ \pi^-\ K^+\ K^{*-}$ with best candidate selection applied on the K^{*-} candidates for each $p*$ bin.

Table 7.3: The upper limit on the differential cross section on the production of the $R(3520)$ for the decay mode K_S^0 K^+ p π^- π^- using SP6050 Monte Carlo after selection of the best K_S^0 candidates.

Bin	1		2		3		4	
Method	Fit	Truth	Fit	Truth	Fit	Truth	Fit	Truth
p* (GeV/c)	0.00-1.50		1.50-2.50		2.50-3.50		3.50-5.00	
Fitted Yield	$73.71^{+203.26}_{-205.15}$		$94.51^{+127.02}_{-127.15}$		$34.57^{+54.21}_{-53.54}$		$17.18^{+22.33}_{-21.54}$	
Shift	0.00		0.00		0.00		0.00	
Raw Efficiency (%)	5.71	6.50	7.08	7.23	8.73	8.89	10.04	10.16
Track eff. corr.(%)	96.34	96.12	95.92	95.83	95.76	95.78	95.90	95.93
PID eff. corr. (%)	99.06	98.84	98.68	98.32	97.94	97.96	97.96	97.97
K_S^0 eff. corr. (%)	102.91	102.19	100.37	100.55	101.59	100.53	101.02	100.67
Corrected Efficiency (%)	5.61	6.31	6.72	6.85	8.32	8.39	9.53	9.61
Raw UL (events)	409.09		304.10		124.01		54.02	
MC Stat error	9.58	8.94	2.83	2.79	1.26	1.25	1.68	1.67
Tracking Syst error	1.83	1.94	2.04	2.09	2.12	2.11	2.05	2.04
PID Syst error	0.47	0.58	0.66	0.84	1.03	1.02	1.02	1.01
K_S^0 Syst error	1.46	1.09	0.19	0.27	0.79	0.27	0.51	0.34
Total Syst.	9.93	9.30	3.72	3.76	3.00	2.89	3.09	3.05
Corrected UL	417.18	416.19	305.30	305.33	124.30	124.28	54.17	54.16
Luminosity (fb^{-1})	227.89		227.89		227.89		227.89	
Branching Fraction	0.35		0.35		0.35		0.35	
Upper Limit (fb/ GeV/c)	62.88	55.73	57.60	56.56	18.96	18.79	4.81	4.76

Table 7.4: Upper limit on the differential cross section on the production of the $R(3520)$ for the decay mode K^{*-} K^+ p π^- using SP6051 Monte Carlo after selection of the best K^{*-} candidates.

Bin	1		2		3		4	
Method	Fit	Truth	Fit	Truth	Fit	Truth	Fit	Truth
p* (GeV/c)	0.00-1.50		1.50-2.50		2.50-3.50		3.50-5.00	
Fitted Yield	$45.45^{+108.65}_{-108.63}$		$25.76^{+77.77}_{-77.27}$		$27.53^{+34.44}_{-33.70}$		$14.36^{+14.77}_{-13.93}$	
Shift	0.00		0.00		0.00		0.00	
Raw Efficiency (%)	4.30	3.69	5.72	5.31	6.47	6.37	6.96	6.69
Track eff. corr.(%)	95.88	95.96	95.98	95.83	95.77	95.84	95.59	95.81
PID eff. corr. (%)	93.58	94.33	97.87	98.34	98.02	97.95	97.38	97.46
K_S^0 eff. corr. (%)	103.04	100.67	100.42	100.12	102.27	100.93	102.03	100.53
Corrected Efficiency (%)	3.98	3.37	5.40	5.01	6.21	6.03	6.61	6.28
Raw UL (events)	224.72		154.09		84.36		38.73	
MC Stat error	23.41	25.34	6.63	6.90	3.08	3.10	4.26	4.35
Tracking Syst error	2.06	2.02	2.01	2.08	2.11	2.08	2.21	2.10
PID Syst error	3.21	2.84	1.07	0.83	0.99	1.03	1.31	1.27
K_S^0 Syst error	1.52	0.34	0.21	0.06	1.13	0.46	1.02	0.27
Total Syst.	23.80	25.60	7.10	7.34	4.17	4.05	5.20	5.12
Corrected UL	250.46	254.28	155.61	155.71	84.80	84.77	39.08	39.07
Luminosity (fb^{-1})	227.89		227.89		227.89		227.89	
Branching Fraction	0.17		0.17		0.17		0.17	
Upper Limit (fb/ GeV/c)	106.53	127.71	73.11	78.81	34.64	35.64	10.00	10.52

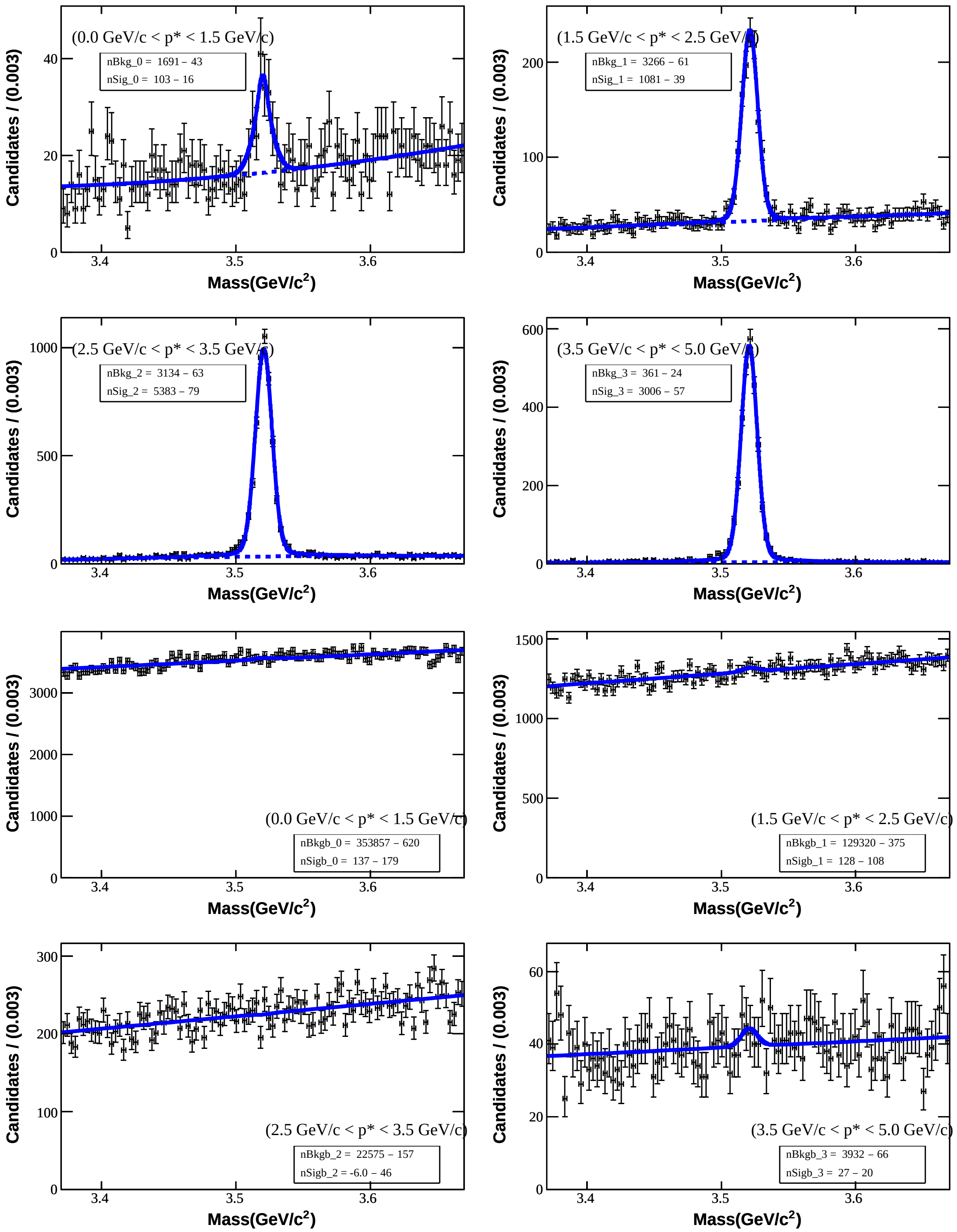

Figure 7.5: Invariant mass distributions of $R(3520)$ candidates with the tighter selection in SP6050 Monte Carlo (top four plots) and data (bottom four plots) for the decay mode $p\ \pi^-\ \pi^-\ K^+\ K^0_S$ for each $p*$ bin.

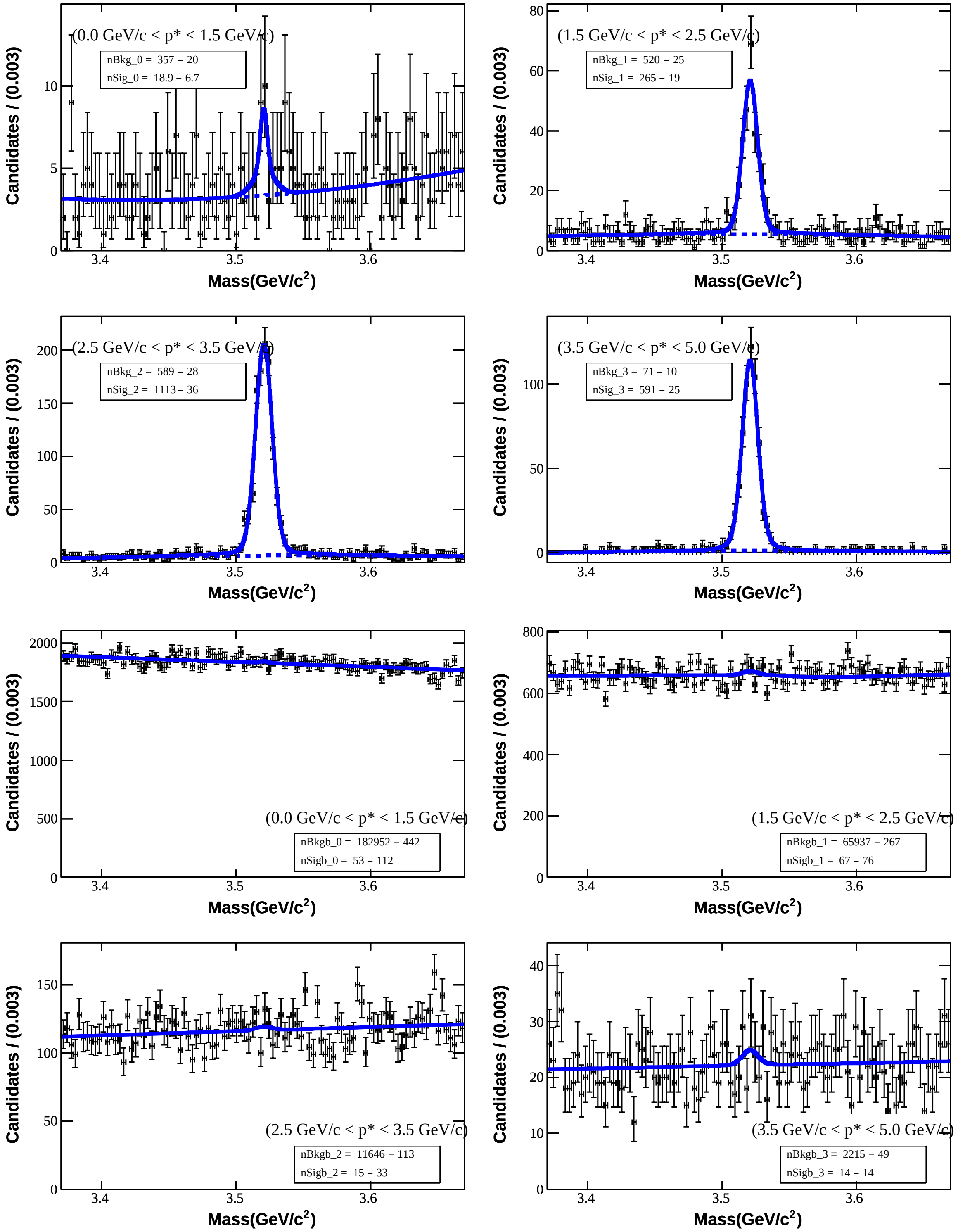

Figure 7.6: Invariant mass distributions of $R(3520)$ candidates in SP6051 Monte Carlo (top four plots) and data (bottom four plots) with tighter selection for the decay mode $p\ \pi^-\ K^+\ K^{*-}$ for each $p*$ bin.

Table 7.5: The upper limit on the differential cross section on the production of the $R(3520)$ for the decay mode K^0_S K^+ p π^- π^- using SP6050 Monte Carlo with tighter selection.

Bin	1		2		3		4	
Method	Fit	Truth	Fit	Truth	Fit	Truth	Fit	Truth
p* (GeV/c)	0.00-1.50		1.50-2.50		2.50-3.50		3.50-5.00	
Fitted Yield	$136.53^{+178.33}_{-179.46}$		$128.30^{+107.75}_{-107.56}$		$-5.98^{+46.27}_{-45.52}$		$26.88^{+20.24}_{-19.35}$	
Shift	0.00		0.00		5.98		0.00	
Raw Efficiency (%)	5.74	6.39	6.57	6.69	8.20	8.36	9.46	9.55
Track eff. corr.(%)	96.12	96.11	95.94	95.79	95.75	95.76	95.93	95.94
PID eff. corr. (%)	98.61	98.66	98.84	98.36	97.95	97.99	97.95	97.99
K^0_S eff. corr. (%)	103.30	102.35	100.44	100.52	101.51	100.54	100.93	100.65
Corrected Efficiency (%)	5.62	6.20	6.26	6.34	7.81	7.88	8.97	9.04
Raw UL (events)	430.78		306.09		76.35		60.28	
MC Stat error	9.55	9.02	2.94	2.91	1.31	1.29	1.74	1.73
Tracking Syst error	1.94	1.94	2.03	2.10	2.13	2.12	2.04	2.03
PID Syst error	0.69	0.67	0.58	0.82	1.03	1.01	1.03	1.01
K^0_S Syst error	1.65	1.18	0.22	0.26	0.76	0.27	0.47	0.33
Total Syst.	9.97	9.39	3.79	3.85	3.01	2.91	3.10	3.07
Corrected UL	443.10	441.73	307.86	307.92	76.44	76.44	60.53	60.53
Luminosity (fb^{-1})	227.89		227.89		227.89		227.89	
Branching Fraction	0.35		0.35		0.35		0.35	
Upper Limit (fb/ GeV/c)	66.65	60.20	62.41	61.61	12.41	12.30	5.71	5.66

Table 7.6: Upper limit on the differential cross section on the production of the $R(3520)$ for the decay mode K^{*-} K^+ p π^- using SP6051 Monte Carlo with tighter selection.

Bin	1		2		3		4	
Method	Fit	Truth	Fit	Truth	Fit	Truth	Fit	Truth
p* (GeV/c)	0.00-1.50		1.50-2.50		2.50-3.50		3.50-5.00	
Fitted Yield	$53.03^{+111.77}_{-111.86}$		$67.36^{+76.02}_{-75.50}$		$15.28^{+33.59}_{-32.85}$		$14.32^{+14.76}_{-13.94}$	
Shift	0.00		0.00		0.00		0.00	
Raw Efficiency (%)	4.65	4.19	7.06	6.51	7.29	7.16	8.04	7.82
Track eff. corr.(%)	97.18	95.86	95.75	95.75	95.81	95.85	95.67	95.86
PID eff. corr. (%)	93.99	95.74	98.09	98.19	97.73	97.75	97.56	97.65
K^0_S eff. corr. (%)	95.56	101.07	101.75	100.20	102.14	100.81	102.18	100.72
Corrected Efficiency (%)	4.05	3.88	6.75	6.13	6.97	6.76	7.67	7.37
Raw UL (events)	237.46		192.79		70.71		38.67	
MC Stat error	22.49	23.74	5.93	6.19	2.89	2.91	3.94	4.00
Tracking Syst error	1.41	2.07	2.13	2.13	2.10	2.07	2.17	2.07
PID Syst error	3.00	2.13	0.95	0.91	1.14	1.12	1.22	1.17
K^0_S Syst error	2.22	0.53	0.87	0.10	1.07	0.40	1.09	0.36
Total Syst.	22.86	23.96	6.52	6.70	4.05	3.93	4.91	4.80
Corrected UL	263.99	266.45	195.41	195.56	70.97	70.95	38.99	38.98
Luminosity (fb^{-1})	227.89		227.89		227.89		227.89	
Branching Fraction	0.17		0.17		0.17		0.17	
Upper Limit (fb/ GeV/c)	110.10	116.01	73.43	80.86	25.82	26.61	8.60	8.94

7.2.4 Summary

The upper limits on the differential cross section on the production of the $R(3520)$ obtained with all methods used are summarised in Table 7.7 and Table 7.8, respectively. The upper limits are given for each p* bin for the decay modes $p\ K^+\ \pi^-\ \pi^-\ K^0_S$ and $p\ K^+\ \pi^-\ K^{*-}$, respectively. The upper limits are given for the $R(3520)$ candidates: with the loose selection(called Loose in the tables), after the selection of the best K^0_S and K^{*-} candidates(called Best), and the tight selection(called Tight).

Table 7.7: Upper limits on the differential cross section on the production of the $R(3520)$ for the decay mode $p\ K^+\ \pi^-\ \pi^-\ K^0_S$ (in fb/ GeV/c)

Bin	1		2		3		4	
Method	Fit	Truth	Fit	Truth	Fit	Truth	Fit	Truth
p* (GeV/c)	0.00-1.50		1.50-2.50		2.50-3.50		3.50-5.00	
Loose	59.93	51.14	59.34	58.17	18.82	18.65	4.73	4.69
Best	62.91	55.74	57.62	55.82	18.98	18.70	4.80	4.75
Tight	66.65	60.20	62.41	61.61	12.41	12.30	5.71	5.66

Table 7.8: Upper limits on the differential cross section on the production of the $R(3520)$ for the decay mode $p\ K^+\ \pi^-\ K^{*-}$ (in fb/ GeV/c)

Bin	1		2		3		4	
Method	Fit	Truth	Fit	Truth	Fit	Truth	Fit	Truth
p* (GeV/c)	0.00-1.50		1.50-2.50		2.50-3.50		3.50-5.00	
Loose	128.00	119.96	74.41	80.11	35.44	36.57	8.90	9.29
Best	106.52	127.70	73.15	78.11	34.65	35.35	10.00	10.50
Tight	110.10	116.01	73.43	80.86	25.82	26.61	8.60	8.94

The upper limits on the differential cross sections are displayed as a function of p* in Figure 7.7 for the decay modes $p\ K^+\ \pi^-\ \pi^-\ K^0_S$(left) and $p\ K^+\ \pi^-\ K^{*-}$(right), respectively. The differential cross sections with the signal efficiency calculated using the extended maximum likelihood fits (Monte Carlo Truth information) are shown by the solid (dashed) line.

In general, it can be seen that the upper limits on the differential cross sections decreased with p* for both decay modes. This was due to the combination of a decrease of the upper limit of the maximum number of events, N_{Max}, with an increase of the signal efficiency.

The corrected signal efficiency increased as a function of p* for a number of reasons. Firstly, for the decays of $R(3520)$, with higher p* it was more likely that the decay products had a momentum which was higher than the threshold in the GoodTracksAccLoose selection criteria. Secondly, the higher the p* of the generated $R(3520)$ candidates the more jet-like their decays were. Therefore, it was more likely that all six tracks were within the acceptance of the detector hence the efficiency was higher at high p*.

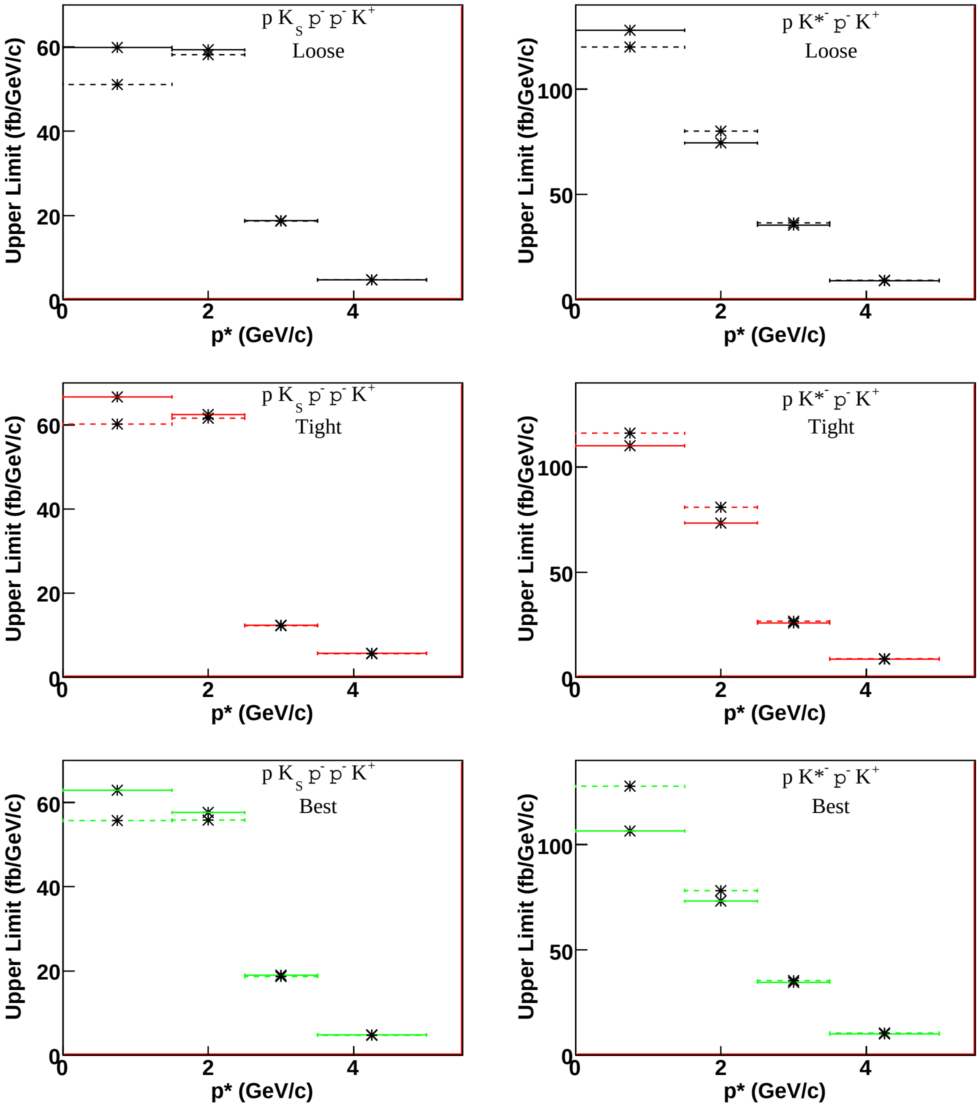

Figure 7.7: Upper limit on the differential cross section as a function of p*. The differential cross sections with the signal efficiency calculated using the extended maximum likelihood fits (Monte Carlo Truth information) are shown by the solid (dashed) line.

In general, N_{Max} decreased as a function of p* because it was dependent on the error on the yield returned from the extended maximum likelihood fit on the data in the p* bin. This error was inversely proportional to the square root of the number of the $R(3520)$ candidates in the p* bin. The number of the reconstructed $R(3520)$ candidates in a p* bin decreased as a function of p*.

However, N_{Max} was also dependent on the number of $R(3520)$ candidates returned from the unbinned extended maximum likelihood fit on the data. In the absence of any signal, this number can be expected to fluctuate around zero in a Gaussian fashion with the magnitude dependent on the number of the $R(3520)$ candidates in the p* bin.

It can be seen that the upper limits on the differential cross sections for the decay mode $p\ K^+\ \pi^-\ \pi^-\ K^0_S$ were similar in the first two p* bins whereas for the decay mode $p\ K^+\ \pi^-\ K^{*-}$ the upper limits were higher in the first p* bin than in the second p* bin. This difference was due to a combination of the following factors: the width of the first p* bin (1.5 GeV/c) was larger than the second p* bin(1 GeV/c), the signal efficiencies were different for the two decay modes, and also there were differences in N_{Max} for the two decay modes.

The signal efficiencies were lower for the decay mode $p\ K^+\ \pi^-\ K^{*-}$ than for the decay mode $p\ K^+\ \pi^-\ \pi^-\ K^0_S$ for two reasons. Firstly, the cuts used for the K^{*-} selection for the $p\ K^+\ \pi^-\ K^{*-}$ mode did not have a signal efficiency of 100%. Secondly, the kinematics of the decay particles were different in the two samples of signal Monte Carlo simulated data used for the two decay modes. In both samples of signal Monte Carlo the generated $R(3520)$ candidates decayed using the phase space model in `JETSET`. For the decay mode $p\ K^+\ \pi^-\ \pi^-\ K^0_S$ the two π^- produced in the $R(3520)$ decay had roughly the same momentum. For the decay mode $p\ K^+\ \pi^-\ K^{*-}$ the π^- originating directly from the $R(3520)$ decay have a larger momentum on average than the π^- that decays through the K^{*-}. The π^- which originated from the K^{*-} decay was therefore more likely to fail the momentum cut in the GoodTracksAccLoose selection criteria and this was more likely for the $R(3520)$ candidates with low p*. Therefore, the ratio of the efficiency in the first p* bin to the efficiency in second p* bin was smaller for the decay mode $p\ K^+\ \pi^-\ K^{*-}$ than for the decay mode $p\ K^+\ \pi^-\ \pi^-\ K^0_S$.

The upper limits also depended on the number of the $R(3520)$ candidates returned from the extended maximum likelihood fit on the data. For the decay mode $p\ K^+\ \pi^-\ K^{*-}$ the fitted yield was roughly the same in the first two p* bins, but because the first bin contained more $R(3520)$ candidates the error on the yield was higher in first p* bin than in the second p* bin. This, combined with the larger systematic error due to the limited statistics in the sample of signal Monte Carlo simulated data, resulted in N_{Max} being about 1.5 times larger in the first p* bin than in the second p* bin. The signal efficiency was lower in the first p* bin than in the second p* bin by a factor of 1.5. This was cancelled out by the first p* bin being 1.5 times larger than the second p* bin. Thus, the upper limit was 1.5

times larger in the first p* bin than in the second p* bin.

For the decay mode $p\ K^+\ \pi^-\ \pi^-\ K^0_S$, N_{Max} was slightly higher in the first p* bin than in the second p* bin. The signal efficiency was also smaller in the first p* bin than in the second p* bin. However, the increase in the upper limit in the first p* bin compared with that in the second p* bin was cancelled out because, as above, the first p* bin was 1.5 times larger than the second p* bin.

With the exception of the first p* bin, it can be seen that the upper limits on the differential cross sections obtained with the signal efficiency calculated using the extended maximum likelihood fit were similar to the upper limits calculated using the truth information in the Monte Carlo simulated data, indicating that similar results could be obtained with both methods.

The differences in the first p* bin obtained with the two methods were caused by differences in the signal efficiency.

There were fewer signal $R(3520)$ candidates generated in the first p* bin of the samples of the signal Monte Carlo simulated data because the production mode for the $R(3520)$ was assumed to be through the decay of the $c\,\overline{c}$ states produced in e^+e^- interactions in the Monte Carlo simulation. As the multiplicity of the particles produced in such events is lower than in the $B\ \overline{B}$ events and the mass of the $R(3520)$ is quite high, the p* of most of the generated $R(3520)$ candidates was generally high. The reconstruction efficiencies were also lowest in the first p* bin. The combination of these two factors resulted in the number of the signal $R(3520)$ candidates in the Monte Carlo simulated data being the lowest in the first p* bin.

In the first p* bin the number of the combinatorial background $R(3520)$ candidates reconstructed in the Monte Carlo simulated data was similar to the numbers of background candidates reconstructed in the second and third p* bins. However, because there were far fewer signal candidates in the first p* bin, the extended maximum likelihood fit was more sensitive to the fluctuations in the distribution of the background candidates in this bin than in the higher p* bins. The number of signal $R(3520)$ candidates returned from the extended maximum likelihood fit and, hence, the signal efficiency would be lower if there were a downwards fluctuation in the distribution of the background candidates in the vicinity of the peak. Conversely, if there were an upwards fluctuation in the distribution of the background candidates in the vicinity of the peak then the number of signal $R(3520)$ candidates returned from the fit would be higher.

In the SP6050 sample of Monte Carlo simulated data there was a downwards fluctuation directly under the signal peak which caused the signal efficiency calculated using the number of signal candidates returned from the fit to be lower than the efficiency calculated using the truth information in the Monte Carlo simulated data. For the decay mode $p\ K^+\ \pi^-\ \pi^-\ K^0_S$ with the loose selection applied the number of truth matched candidates in the first p* bin was 120 and the total number returned from the fit was $106.7^{+17.2}_{-16.6}$. The difference between the two values was less than the error, therefore the signal efficiencies obtained with the two methods were consistent.

The number of truth-matched $R(3520)$ candidates in the SP6051 sample for the decay mode $p\ K^+\ \pi^-\ K^{*-}$ with the loose selection was 19 and the number of candidates returned from the fit was $19.1^{+7.2}_{-6.1}$. However, there were also fits involved in the calculations of the tracking, PID and K^0_S corrections which will have similar errors. The difference in the upper limits corresponded to a difference in the corrected efficiency of 1.2 candidates which was well within the errors returned by the fits showing the upper limits were consistent.

In can be seen that the upper limits on the differential cross sections for the decay mode $p\ K^+\ \pi^-\ \pi^-\ K^0_S$ were roughly half those for the decay mode $p\ K^+\ \pi^-\ K^{*-}$. This difference was due to the extra factor of 0.5 in the branching fraction to account for the K^{*-} decay.

It can also be seen that the selection of the best K^0_S or K^{*-} candidates had very little effect on the upper limits on the differential cross sections. For the decay mode $p\ K^0_S\ \pi^-\ \pi^-\ K^+$ the results were similar due to the selection of K^0_S candidates only affecting a small proportion of the events. The selection of the best K^{*-} candidates had little effect as the reduction of the yield and the associated errors were cancelled out by the reduction in the signal efficiency.

With the exception of the third p* bin, it can be seen that the upper limits on the differential cross sections for the decay mode $p\ K^0_S\ \pi^-\ \pi^-\ K^+$ with the tight selection were higher than those obtained with the loose selection. The tight selection reduced the number of the $R(3520)$ candidates in the data, which in turn reduced the fit error on the yield. This was balanced due to the small drop in the signal efficiency caused by the tighter selection criteria. However, the main reason for the differences in the upper limits was that there were larger upwards fluctuations in the first, second, and fourth p* bins and a downwards fluctuation in the third p* bin in the invariant mass distribution obtained with the tight selection than in the distribution obtained with the loose selection.

Finally, it can be seen that upper limits on the differential cross sections for the decay mode $K^{*-}\ K^+\ p\ \pi^-$ obtained with the tight selection were slightly lower than those obtained with the loose selection. This was due to a reduction in N_{Max} caused by the reduction in the error returned from the extended maximum likelihood fit. This was due the to the number of $R(3520)$ candidates being smaller after the tight selection.

As neither selection of the best K^0_S or K^{*-} candidates or the tighter selection had a great effect on the differential cross sections obtained, only the loose selection method was considered further.

7.3 Experimental results of the upper limits on the differential cross section — $\Gamma = 7\,\mathrm{MeV}/c^2$ hypothesis

The upper limits on the differential cross section were calculated with the alternative width hypothesis $\Gamma = 7\,\mathrm{MeV}/c^2$, because any cross section would be dependent on this width. Results of the calculation of the upper limits on the differential cross section for the production of $R(3520)$ candidates for the decay modes $K^0_S\ K^+\ p\ \pi^-\ \pi^-$ and $K^{*-}\ K^+\ p\ \pi^-$ are tabulated in Table 7.9 and Table 7.10, respectively. The signal efficiencies have been calculated using both the number of signal candidates returned from extended maximum likelihood fits and the number of signal candidates determined from the Monte Carlo truth information.

The upper limits on the differential cross sections are displayed in Figure 7.7 as a function of p*, together with those obtained for $\Gamma = 1$ for comparison.

As expected, the upper limits on the cross section were higher with the width hypothesis $\Gamma = 7\,\mathrm{MeV}/c^2$. This was due to the increase in the yield and the errors on the yield caused by the increased width.

The upper limits decreased as a function of p* for both decay modes due to the decrease in the numbers of the $R(3520)$ candidates in the data with higher p*.

7.4 Total cross section

The upper limits on the total cross section are presented in Table 7.11 together with the differential cross sections presented in the previous sections. The upper limits on the total cross section were obtained by the addition of the differential cross sections in the p* range 0-5 GeV/c^2.

In order to be able to quote limits on the production cross section, it is necessary either to know the momentum spectrum or to believe that the momentum spectrum does not vary rapidly on the scale of the bin size. The latter assumption was considered in the calculations of the total cross sections.

The branching fractions for K^0 or $\overline{K}^0$ to K^0_S and the branching ratio for K^{*-} to $\overline{K}^0\ \pi^-$ have been divided out. The branching fractions for the $R(3520)$ into other decay modes have not been divided out, because no other decay modes have been observed.

Any postulated momentum spectrum can be folded into this differential limit to obtain a limit on the total cross section assuming that spectrum. The integral which corresponded to a uniform distribution was the worst case and therefore could be used to set a conservative model independent limit.

For the decay mode $K^0_S\ K^+\ p\ \pi^-\ \pi^-$ the total cross sections were larger than for the decay mode

Table 7.9: Upper limit on the differential cross section on the production of the $R(3520)$ with $\Gamma = 7\,\mathrm{MeV}/c^2$ for the decay mode $K^0_S\ K^+\ p\ \pi^-\ \pi^-$ using SP6050 Monte Carlo.

Bin	1		2		3		4	
Method	Fit	Truth	Fit	Truth	Fit	Truth	Fit	Truth
p* (GeV/c)	0.00-1.50		1.50-2.50		2.50-3.50		3.50-5.00	
Fitted Yield	$227.80^{+260.68}_{-263.54}$		$135.13^{+162.79}_{-163.05}$		$50.10^{+68.60}_{-67.88}$		$20.56^{+28.15}_{-27.31}$	
Shift	0.00		0.00		0.00		0.00	
Raw Efficiency (%)	5.93	6.67	7.08	7.23	8.73	8.90	10.05	10.16
Track eff. corr.(%)	96.20	96.10	95.91	95.83	95.76	95.78	95.91	95.92
PID eff. corr. (%)	99.02	98.79	98.67	98.32	97.95	97.97	97.93	97.97
K^0_S eff. corr. (%)	102.82	102.10	100.37	100.55	101.59	100.53	101.07	100.67
Corrected Efficiency (%)	5.81	6.47	6.73	6.85	8.32	8.39	9.54	9.61
Raw UL (events)	657.91		403.73		163.30		67.00	
MC Stat error	9.39	8.82	2.82	2.79	1.26	1.25	1.68	1.67
Tracking Syst error	1.90	1.95	2.05	2.09	2.12	2.11	2.04	2.04
PID Syst error	0.49	0.60	0.67	0.84	1.03	1.02	1.03	1.01
K^0_S Syst error	1.41	1.05	0.18	0.27	0.80	0.26	0.54	0.33
Total Syst.	9.76	9.18	3.72	3.76	3.00	2.89	3.09	3.05
Corrected UL	677.56	675.34	405.45	405.48	163.71	163.68	67.18	67.17
Luminosity (fb^{-1})	227.89		227.89		227.89		227.89	
Branching Fraction	0.35		0.35		0.35		0.35	
Upper Limit (fb/ GeV/c)	98.59	88.31	76.41	75.05	24.95	24.73	5.95	5.91

Table 7.10: Upper limit on the differential cross section of the production of the $R(3520)$ with $\Gamma = 7\,\mathrm{MeV}/c^2$ for the decay mode $K^{*-}\ K^+\ p\ \pi^-$ using SP6051 Monte Carlo.

Bin	1		2		3		4	
Method	Fit	Truth	Fit	Truth	Fit	Truth	Fit	Truth
p* (GeV/c)	0.00-1.50		1.50-2.50		2.50-3.50		3.50-5.00	
Fitted Yield	$164.89^{+181.27}_{-181.98}$		$36.93^{+112.54}_{-112.14}$		$42.74^{+48.40}_{-47.61}$		$17.40^{+20.23}_{-19.38}$	
Shift	0.00		0.00		0.00		0.00	
Raw Efficiency (%)	4.71	4.68	7.24	6.75	7.63	7.50	8.35	8.09
Track eff. corr.(%)	96.02	95.82	95.73	95.77	95.82	95.84	95.67	95.87
PID eff. corr. (%)	93.22	95.47	98.06	98.31	97.75	97.76	97.50	97.53
K^0_S eff. corr. (%)	96.32	100.95	100.85	100.23	102.37	100.87	102.00	100.61
Corrected Efficiency (%)	4.06	4.32	6.86	6.37	7.31	7.08	7.94	7.61
Raw UL (events)	464.00		222.61		122.61		50.78	
MC Stat error	22.32	22.40	5.85	6.07	2.82	2.84	3.86	3.93
Tracking Syst error	1.99	2.09	2.14	2.11	2.09	2.08	2.16	2.06
PID Syst error	3.39	2.26	0.97	0.84	1.12	1.12	1.25	1.24
K^0_S Syst error	1.84	0.48	0.42	0.11	1.19	0.43	1.00	0.30
Total Syst.	22.76	22.64	6.41	6.58	4.02	3.88	4.84	4.75
Corrected UL	537.01	536.28	224.39	224.49	123.24	123.20	51.15	51.13
Luminosity (fb^{-1})	227.89		227.89		227.89		227.89	
Branching Fraction	0.17		0.17		0.17		0.17	
Upper Limit (fb/ GeV/c)	223.51	209.82	83.01	89.36	42.74	44.12	10.89	11.36

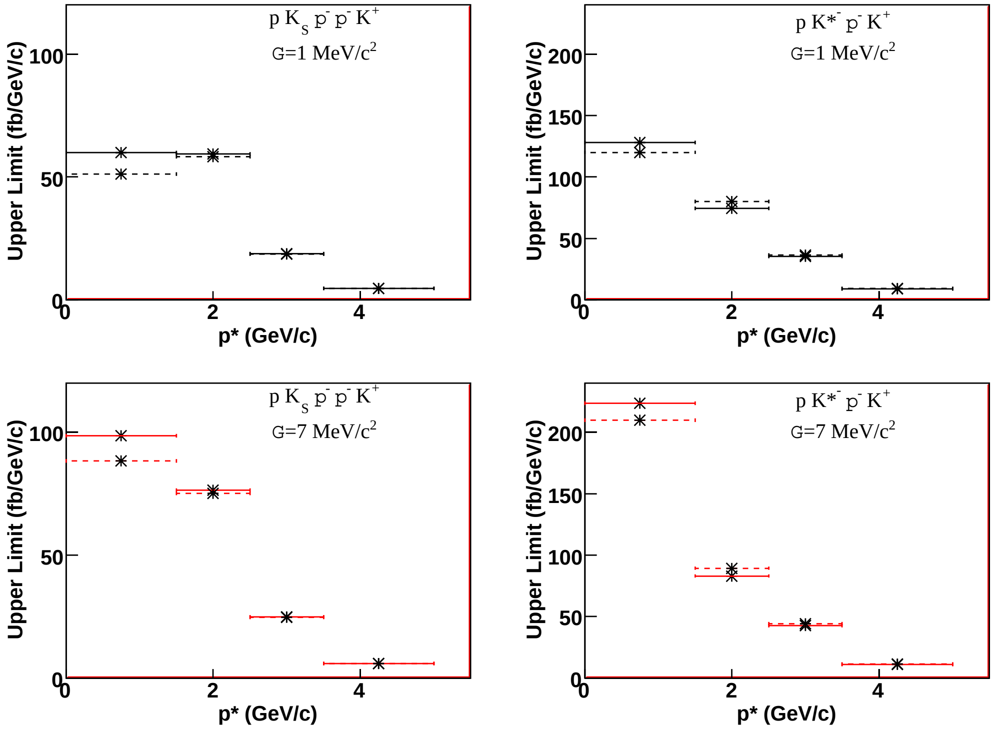

Figure 7.8: Upper limit on the differential cross section as a function of p* for the two width hypotheses. The differential cross sections with the signal efficiency calculated using the extended maximum likelihood fits (Monte Carlo Truth information) are shown by the solid (dashed) line.

Table 7.11: Upper limits on the total and differential cross sections in fb/ GeV/c

	$R(3520) \to p\ K_S^0\ \pi^-\ \pi^-\ K^+$				$R(3520) \to p\ K^{*-}\ \pi^-\ K^+$			
$p*$ Range	$\Gamma = 1\,\text{MeV}/c^2$ (fb/ GeV/c)		$\Gamma = 7\,\text{MeV}/c^2$ (fb/ GeV/c)		$\Gamma = 1\,\text{MeV}/c^2$ (fb/ GeV/c)		$\Gamma = 7\,\text{MeV}/c^2$ (fb/ GeV/c)	
(GeV/c)	Fit	Truth	Fit	Truth	Fit	Truth	Fit	Truth
0.0 - 1.5	59.93	51.14	98.59	88.31	128.00	119.96	223.51	209.82
1.5 - 2.5	59.34	58.17	76.41	75.05	74.41	80.11	83.01	89.36
2.5 - 3.5	18.82	18.65	24.95	24.73	35.44	36.57	42.74	44.12
3.5 - 5.0	4.73	4.69	5.95	5.91	8.90	9.29	10.89	11.36
Total	35.03	32.11	51.63	48.22	63.04	62.11	95.47	93.05

K^{*-} K^{+} p π^{-}. This was due to the extra factor of 0.5 in the branching fraction.

The total cross sections were larger with the $\Gamma = 7\,\mathrm{MeV}/c^{2}$ width hypothesis because there was a higher yield due to the broader resonance.

For the decay mode K^{0}_{S} K^{+} p π^{-} π^{-} the upper limits were slightly larger for the method where the signal efficiency was calculated using the extended maximum likelihood fit than that using the Monte Carlo truth information. The difference was caused by a downwards fluctuation in the background in the invariant mass distribution in the first p* bin of the sample of signal Monte Carlo simulated data.

For the decay mode K^{*-} K^{+} p π^{-} the upper limits were slightly larger for the method where the signal efficiency was calculated using the extended maximum likelihood fit than that using the Monte Carlo truth information. The difference was due to the low statistics in the sample of signal Monte Carlo simulated data in the first p* bin.

The upper limits on the total cross section were most sensitive to the differential cross sections in the bins with the lowest p*. In these low p* bins the most accurate measurement of the signal efficiency was calculated using the Monte Carlo truth information. Therefore, the total cross sections which should be regarded as the final results for this analysis were calculated using the Monte Carlo truth information to calculate the signal efficiency.

Chapter 8

Search for the $R(3520)$ with an associated $\overline{p}$ in the event

8.1 Introduction

In this section the search for the $R(3520)$ candidates with an associated $\overline{p}$ in the event is described. The analysis procedure was very similar to that presented in the previous chapters. All steps of the analysis were repeated with the additional requirement that there was an extra $\overline{p}$ in the event.

One change was made to the fit procedure. In the analysis presented in Section 7 the maximum likelihood fits to determine the signal shape were performed using the complete sample of signal Monte Carlo simulated data instead of that in the relevant p* bin. This was done, because the statistics at low p* were limited in both of the samples of signal Monte Carlo simulated data.

8.2 Selection criteria

In this section the search for the $R(3520)$ candidates with an associated $\overline{p}$ in the event is described. The candidates are only selected if there is an extra track in the event that is tightly identified as an $\overline{p}$. In order to remove those events where the $\overline{p}$ detected is the result of secondary interactions with the detector the same interaction region cuts are applied to the additional $\overline{p}$.

In summary, the $R(3520)$ candidates were selected with the following criteria.

- $R(3520)$ as identified in Section 6.1
- associated $\overline{p}$ identified as pLHTight (see Section 4.3)
- $|R_Z|$ of associated $\overline{p} \leq 2.9\,\mathrm{cm}$

- R_{XY} of associated $\overline{p} \leq 0.13\,\text{cm}$

This selection will be referred further as loose selection.

8.3 Invariant mass distributions of the $R(3520)$ candidates

The invariant masses of the $R(3520)$ candidates with an associated $\overline{p}$ in the event were calculated and their distributions were plotted in Figure 8.1 and Figure 8.2 for the decay modes $p\ K^0_S\ K^+\ \pi^-\ \pi^-$ and $p\ K^{*-}\ K^+\ \pi^-$, respectively. Plot a) in these figures shows the full spectrum while b), c) and d) show the spectrum in the ranges 2-3 GeV/c^2, 3-4 GeV/c^2, and 4-5 GeV/c^2, respectively. A maximum likelihood fit were performed on the data with a function of the form given in formula 6.1.

8.4 The multiplicity of $R(3520)$ candidates

Multiple $R(3520)$ candidates were reconstructed in the majority of events in which there was at least one candidate that passes the selection criteria. Figure 8.3 shows the multiplicities of $R(3520)$ candidates per event for the decay modes $p\ K^0_S\ K^+\ \pi^-\ \pi^-$ (left) and $p\ K^{*-}\ K^+\ \pi^-$ (right), respectively. The distributions have a number of peaks which were explained in Section 6.3. The average multiplicities were reduced slightly, because of the requirement that the track identified as the $\overline{p}$ was not one of the six tracks used to reconstruct the $R(3520)$ candidate.

8.5 Tighter selection of the $R(3520)$ candidates

In an attempt to reduce the background, additional cuts were applied on the $R(3520)$. The cut variables considered were the $P(\chi^2)$, $DOCA_{MT}$, R_Z, R_{XY} of the $R(3520)$ candidates. $DOCA_{MT}$ is the multi-track DOCA and is defined in Section 6.4.

The distributions of the variables $P(\chi^2)$, $DOCA_{MT}$, R_Z, R_{XY}, for $R(3520)$ candidates for the decay modes $p\ K^+\ \pi^-\ \pi^-\ K^0_S$ and $p\ K^+\ \pi^-\ K^{*-}$ are shown in Figure 8.4 and Figure 8.5, respectively. The candidates removed are shaded on the plots. The cut values have been chosen to be consistent with those used for K^0_S and K^{*-} selection. The cut variables applied are: $P(\chi^2) > 0.001$; $DOCA_{MT} \leq 0.32\,\text{cm}$; $|R_Z| < 2.9\,\text{cm}$; $R_{XY} \leq 0.13\,\text{cm}$.

The invariant mass of the $R(3520)$ candidates were calculated and their distributions were plotted in Figure 8.6 and Figure 8.7 for the decay modes $p\ K^+\ \pi^-\ \pi^-\ K^0_S$ and $p\ K^+\ \pi^-\ K^{*-}$, respectively. Plot a) in these figures shows the full spectrum while b), c) and d) show the spectrum in the ranges 2-3 GeV/c^2, 3-4 GeV/c^2, and 4-5 GeV/c^2, respectively. A maximum likelihood fit were performed on the data with a function of the form given in formula 6.1.

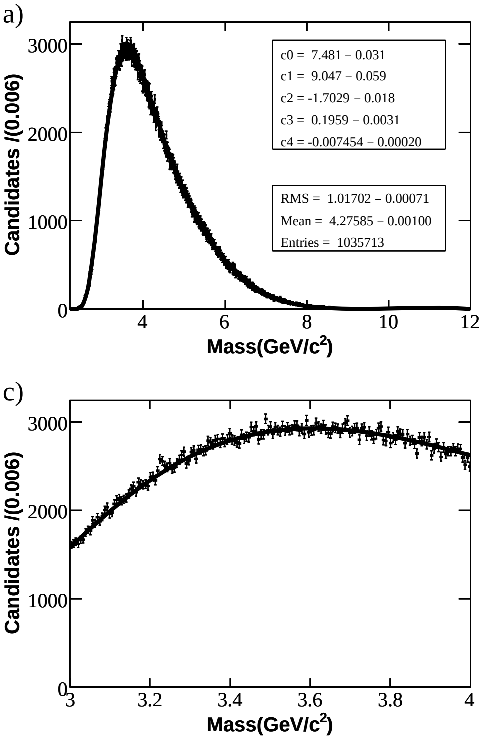

Figure 8.1: Invariant mass distributions of $R(3520)$ candidates for the decay mode $p\ K^+\ \pi^-\ \pi^-\ K_S^0$ with an associated $\overline{p}$.

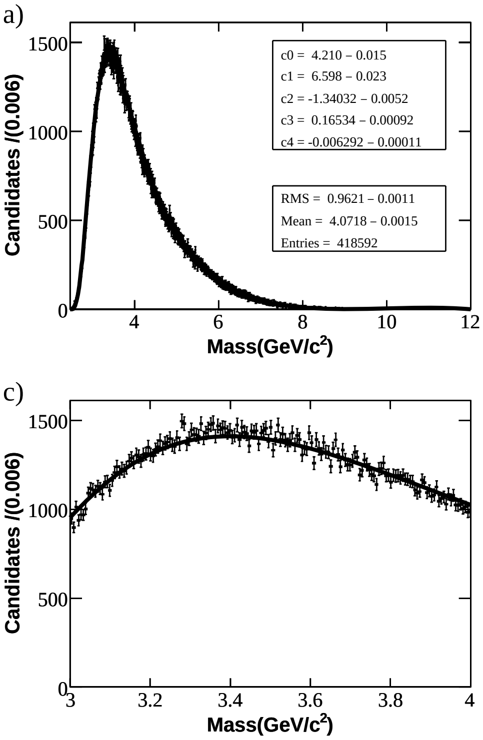

Figure 8.2: Invariant mass distributions of the $R(3520)$ candidates for the decay mode $p\ K^+\ \pi^-\ K^{*-}$ with an associated $\overline{p}$.

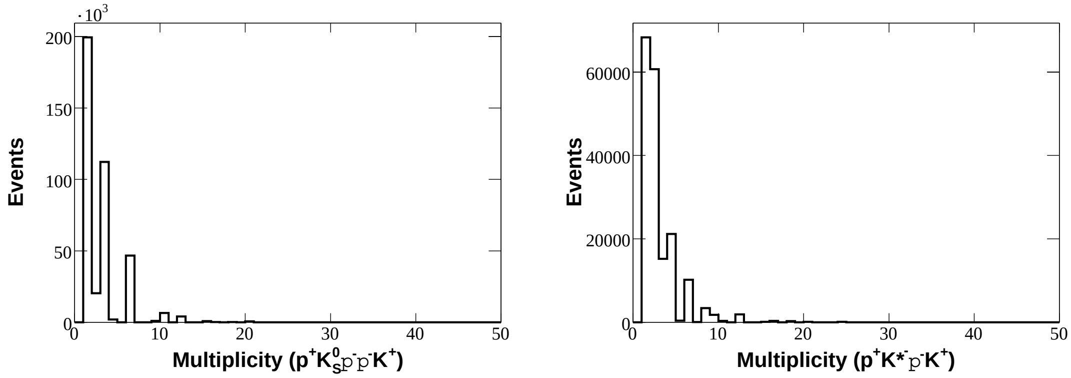

Figure 8.3: Multiplicities of $R(3520)$ candidates per event for the decay modes $p\ K^0_S\ K^+\ \pi^-\ \pi^-$ (left) and $p\ K^{*-}\ K^+\ \pi^-$ (right)

From these plots it can be seen that the selection on $P(\chi^2)$ is the most powerful of the cuts. The selection on the $DOCA_{MT}$ removes a few more candidates. The selections on $|R_Z|$ and R_{XY} do not remove many $R(3520)$ candidates. This is because these cuts have already been applied to the daughters of these candidates.

Figure 8.8 shows the multiplicities of $R(3520)$ candidates after tighter selection for the decay modes $p\ K^+\ \pi^-\ \pi^-\ K^0_S$ (left) and $p\ K^+\ \pi^-\ K^{*-}$ (right), respectively.

The combination of these cuts reduced the average multiplicity of $R(3520)$ candidates for the decay mode $p\ K^+\ \pi^-\ \pi^-\ K^0_S$ from 4.19 to 3.79. For the decay mode $p\ K^+\ \pi^-\ K^{*-}$ the average multiplicity of $R(3520)$ candidates was reduced from 3.65 to 3.42.

8.6 Effects of the cut on the $K^{*\pm}$ multiplicity

The invariant mass distributions of the $R(3520)$ candidates after cuts on the multiplicity of $K^{*\pm}$ candidates in an event were plotted in Figure 8.9 for the decay mode $p\ K^{*-}\ K^+\ \pi^-$. Plot a) in these figures shows the full spectrum while b), c) and d) show the spectrum in the ranges 2-3 GeV/c^2, 3-4 GeV/c^2, and 4-5 GeV/c^2, respectively. A maximum likelihood fit was performed on each of the invariant mass distribution with a function of the form given by the formula 6.1.

The mass distributions do not change much when a cut on events with a $nK^{*\pm} < 7$ is applied. The effects of a cut of $nK^{*\pm} < 5$ are more pronounced. There is more difference between the three curves at lower masses than at higher masses.

The multiplicities of $R(3520)$ candidates after cuts on the multiplicity of $K^{*\pm}$ are shown for $R(3520)$ candidates for the decay mode $p\ K^+\ \pi^-\ K^{*-}$with an associated $\overline{p}$ in the event in Figure 8.10. It can be seen from these graphs that the cut on the $K^{*\pm}$ multiplicity does not have a large effect on the $R(3520)$ multiplicity distributions. This is because the proportion of events with $nK^{*\pm} \geq 5$ ($nK^{*\pm} \geq 7$) is only

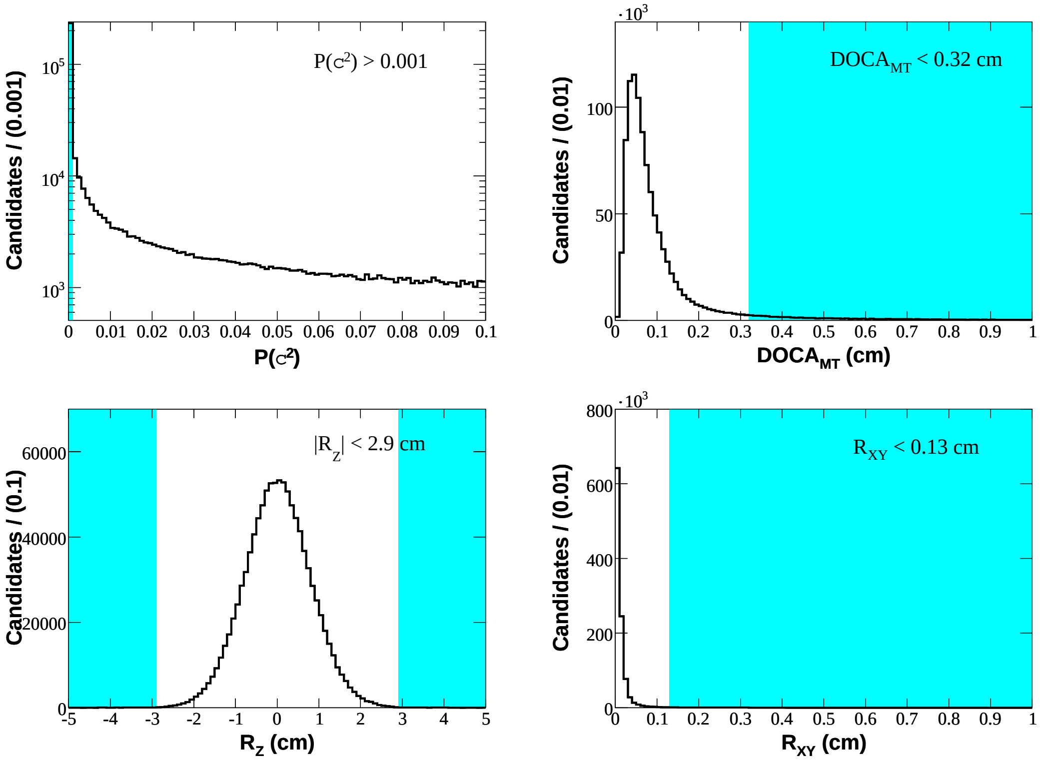

Figure 8.4: Distributions of $P(\chi^2)$, $DOCA_{MT}$, R_Z, R_{XY} variables used select $R(3520)$ candidates for the decay mode $p\ K^+\ \pi^-\ \pi^-\ K^0_S$. The candidates removed by the cuts are shaded.

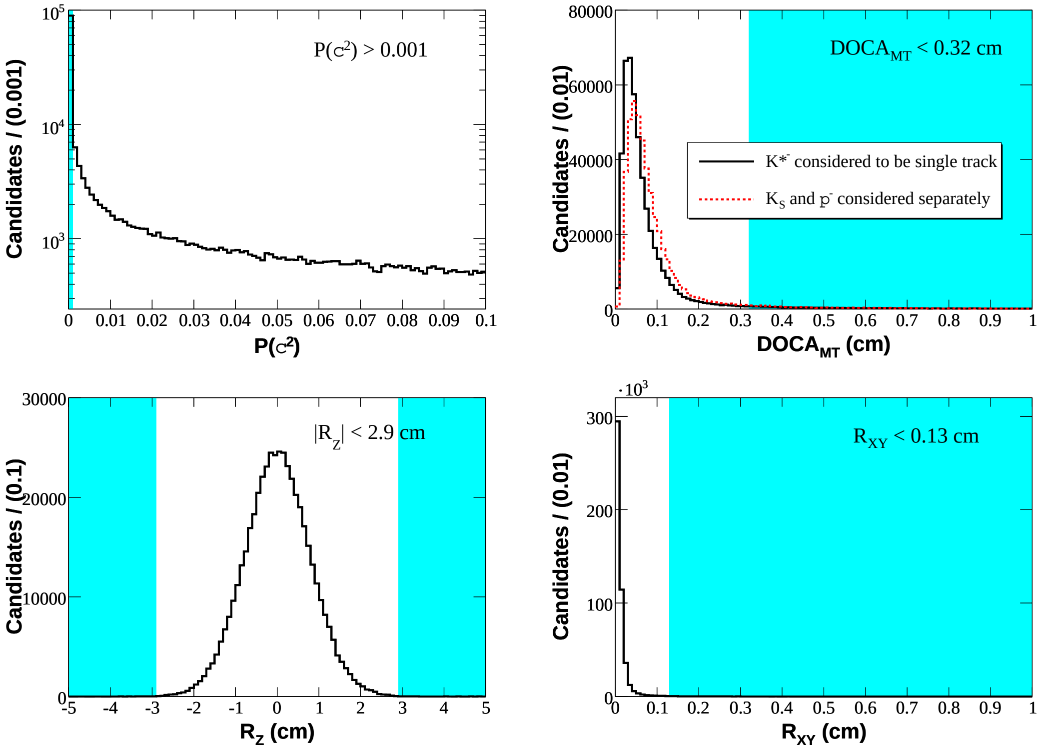

Figure 8.5: Distributions of $P(\chi^2)$, $DOCA_{MT}$, R_Z, R_{XY} variables used select $R(3520)$ candidates for the decay mode $p\ K^+\ \pi^-\ K^{*-}$. The candidates removed by the cuts are shaded.

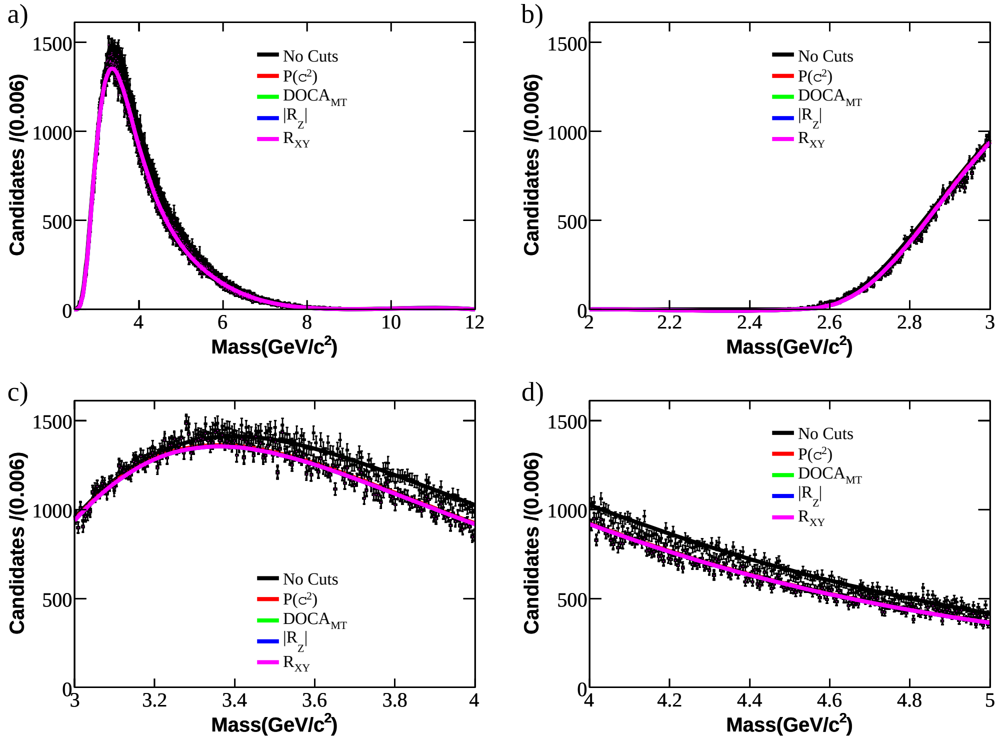

Figure 8.6: Invariant mass distribution of the $R(3520)$ candidates for the decay mode $p\ \pi^-\ \pi^-\ K^+\ K^0_S$ after the tighter selection with an associated $\overline{p}$.

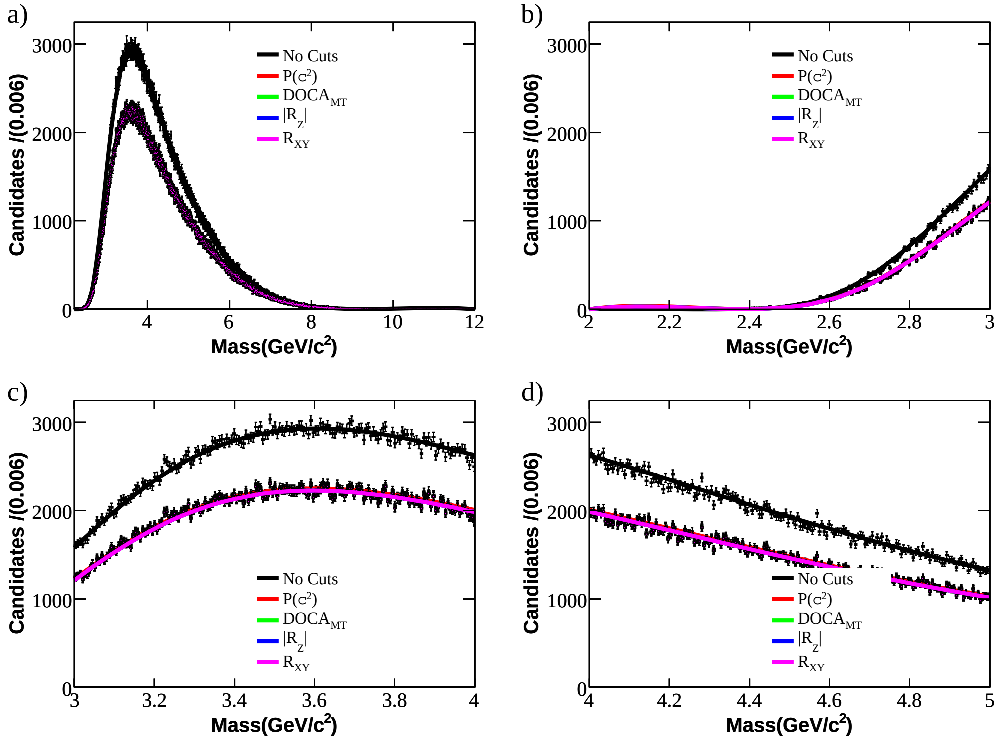

Figure 8.7: Invariant mass distribution of the $R(3520)$ candidates for the decay mode $p\ \pi^-\ K^+\ K^{*-}$ after the tighter selection with an associated $\overline{p}$.

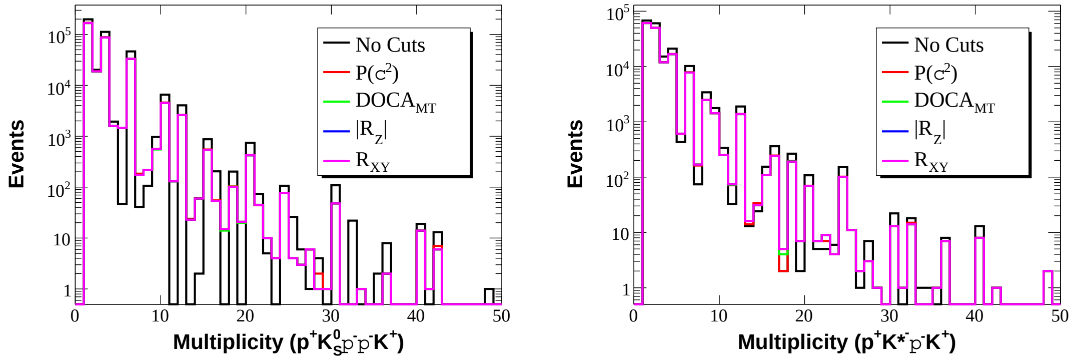

Figure 8.8: Multiplicities of $R(3520)$ candidates after tighter selection with an associated $\overline{p}$ for the decay modes $p\ \pi^-\ \pi^-\ K^+\ K_S^0$ (left) and $p\ K^+\ \pi^-\ K^{*-}$ (right).

3.0% (0.47%).

8.7 Best candidate selection of the K_S^0 and K^* candidates

The effects of selecting the best K_S^0 and K^{*-} candidates were investigated. The best K_S^0 candidates were selected as described in Section 5.2.7 using the flight length significance as the selection criteria. The best $K^{*\pm}$ candidates were selected as described in Section 5.3.5 using the difference of the $K^{*\pm}$ candidates mass from the PDG value.

The invariant mass distributions of the $R(3520)$ candidates were plotted before and after the selection of the best K_S^0 and $K^{*\pm}$ candidates in Figure 8.11 and Figure 8.12 for the decay modes $p\ K_S^0$ $K^+\ \pi^-\ \pi^-$ and $p\ K^{*-}\ K^+\ \pi^-$, respectively. The plots are shown before (after) the selection of the best K_S^0 or K^{*-} candidates in black (red). Plot a) in these figures shows the full spectrum while b), c) and d) show the spectrum in the ranges 2-3 GeV/c^2, 3-4 GeV/c^2, and 4-5 GeV/c^2, respectively. A maximum likelihood fit was performed on each of the invariant mass distributions with a function of the form, 6.1.

The multiplicity distributions of $R(3520)$ candidates before and after the selection of the best K_S^0 and K^{*-} candidates with an associated $\overline{p}$ in the event are shown in Figure 8.13 for the decay modes $p\ K^+\ \pi^-\ \pi^-\ K_S^0$ (left) and $p\ K^+\ \pi^-\ K^{*-}$ (right), respectively.

In the $K_S^0\ \pi^-\ \pi^-\ p\ K_S^0$ system it can be seen that selecting the best K_S^0 candidates in an event has a minor effect on the multiplicity of $R(3520)$ candidates. This is because $R(3520)$ candidates are only removed from those events where the K_S^0 candidates overlap, which account for only a small fraction of the total number of events. For the decay mode $K^{*-}\ \pi^-\ p\ K^+$ the average multiplicity of the $R(3520)$ candidates per event is reduced by about a third.

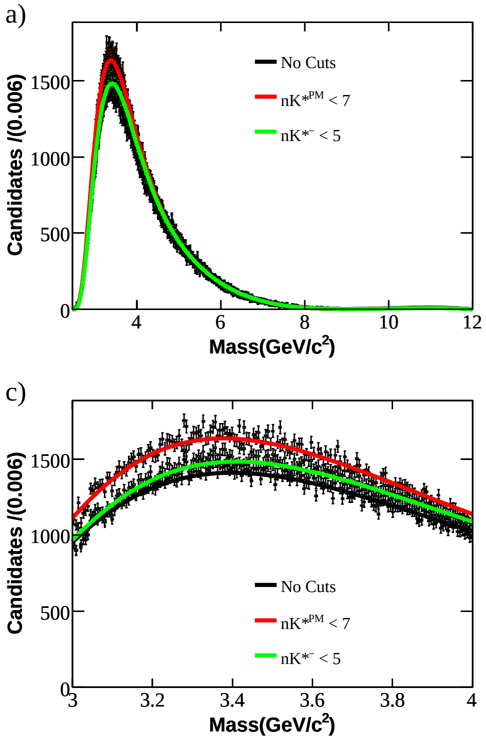

Figure 8.9: Invariant mass distributions of the $R(3520)$ candidates for the decay mode $p\ \pi^-\ K^+\ K^{*-}$ with an associated $\overline{p}$ in the event after selections on the $K^{*\pm}$ multiplicity.

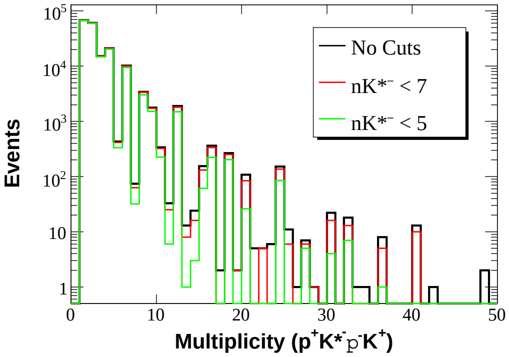

Figure 8.10: Multiplicity distributions of $R(3520)$ candidates for the decay mode $p\ \pi^-\ K^+\ K^{*-}$ system with an associated $\overline{p}$ in the event after selections on the $K^{*\pm}$ multiplicity.

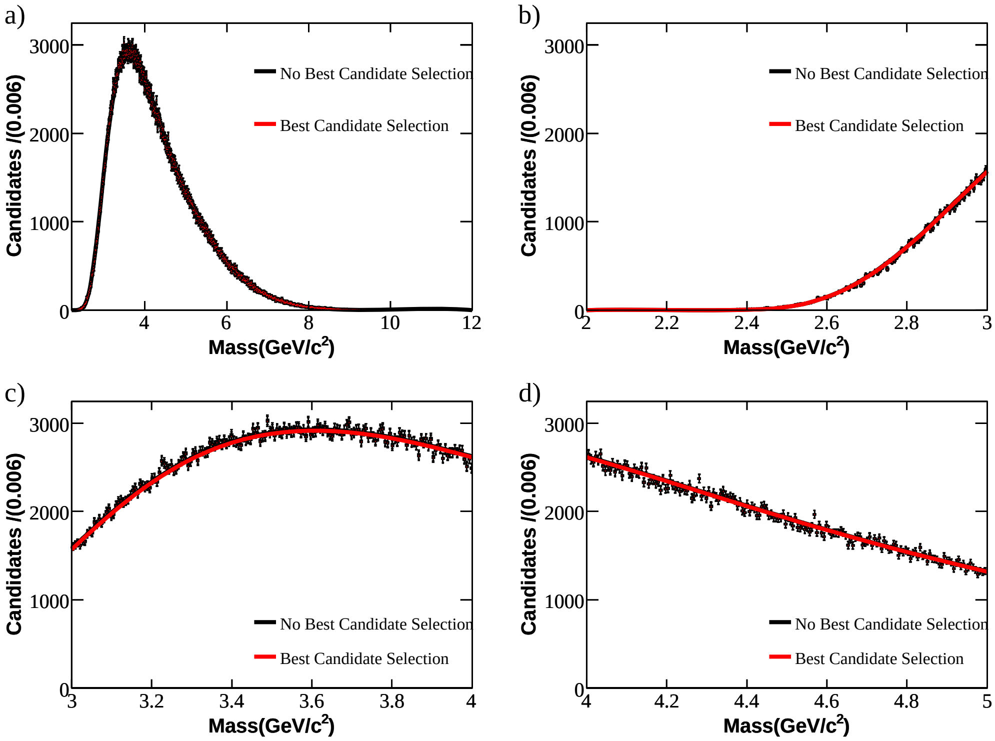

Figure 8.11: Invariant mass distributions of the $R(3520)$ candidates for the decay mode $p\ \pi^-\ \pi^-\ K^+\ K_S^0$ with an associated $\overline{p}$ in the event before and after the selection of the best K_S^0 candidates.

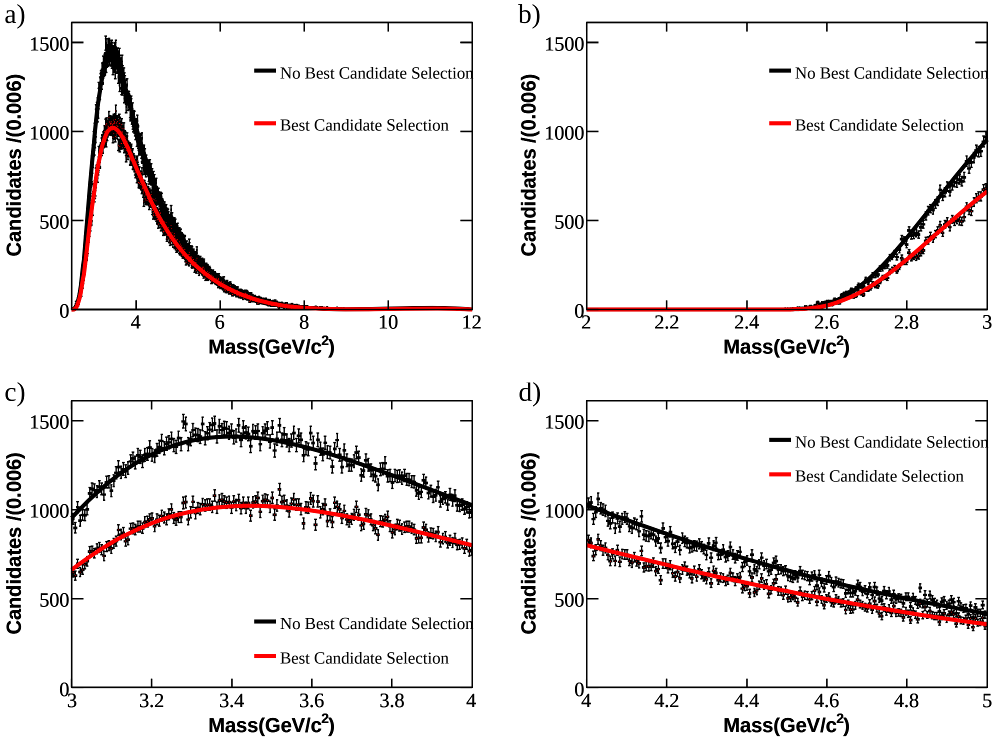

Figure 8.12: Invariant mass distributions of the $R(3520)$ candidates for the decay mode $p\ \pi^-\ K^+\ K^{*-}$ with an associated $\overline{p}$ in the event before and after selection of the best $K^{*\pm}$ candidates.

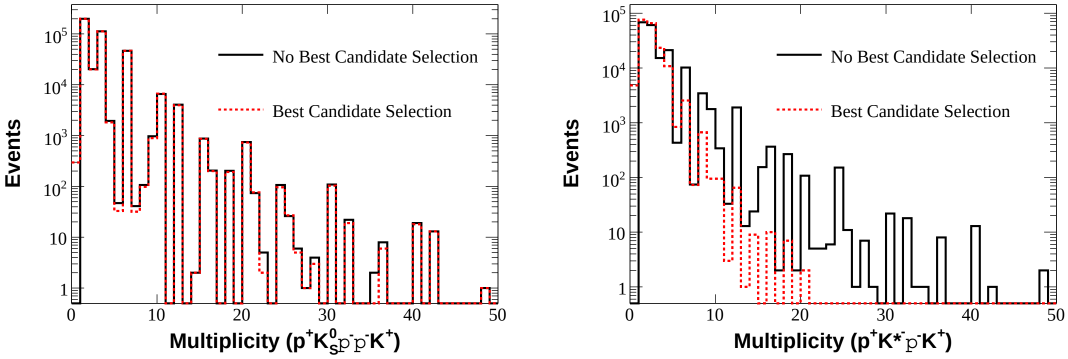

Figure 8.13: Multiplicity distributions of $R(3520)$ candidates for the decay modes $p\,\pi^-\,\pi^-\,K^+\,K^0_S$ (left) and $p\,\pi^-\,\pi^-\,K^+\,K^{*-}$ (right) system with an associated $\overline{p}$ before and after the selection of the best K^0_S or K^{*-} candidates.

8.8 Experimental results of the upper limits on the differential cross section — $\Gamma = 1\,\mathrm{MeV}/c^2$ hypothesis

The results from the calculations of the upper limit on the differential cross section for the production of $R(3520)$ candidates with an associated $\overline{p}$ in the event are detailed in this section. The calculation is described in detail in Section 7. The $p\,\pi^-\,\pi^-\,K^+\,K^0_S$ and $p\,\pi^-\,K^+\,K^{*-}$ results use the SP6050 and SP6051 samples of signal Monte Carlo simulated data, respectively, which were produced as described in Section 4.4. In order to make sure that the signal efficiency was as accurate as possible, events in the Monte Carlo simulation were only counted if there was an $\overline{p}$ in the Monte Carlo truth information, whose mother or grandmother was the same as the mother of the $R(3520)$.

8.8.1 Loose selection of the $R(3520)$ candidates

The invariant mass distributions for the decay modes $p\,\pi^-\,\pi^-\,K^+\,K^0_S$ and $p\,\pi^-\,K^+\,K^{*-}$ are shown in Figure 8.14 and Figure 8.15, respectively. In each figure, the top four plots are for signal Monte Carlo simulated data and the bottom four plots are for real data. The solid lines show the result of the extended maximum likelihood fit on these distributions, the dashed line shows the background component of these fits. The numbers of signal and background candidates are given on the plot.

Results are tabulated for the calculation of the upper limits on the differential cross section for the production of $R(3520)$ candidates for the decay modes $K^0_S\,K^+\,p\,\pi^-\,\pi^-$ and $K^{*-}\,K^+\,p\,\pi^-$ in Table 8.1 and Table 8.1, respectively. The signal efficiencies have been calculated using both the number of signal candidates returned from the extended maximum likelihood fits and the number of signal candidates determined from the Monte Carlo truth information.

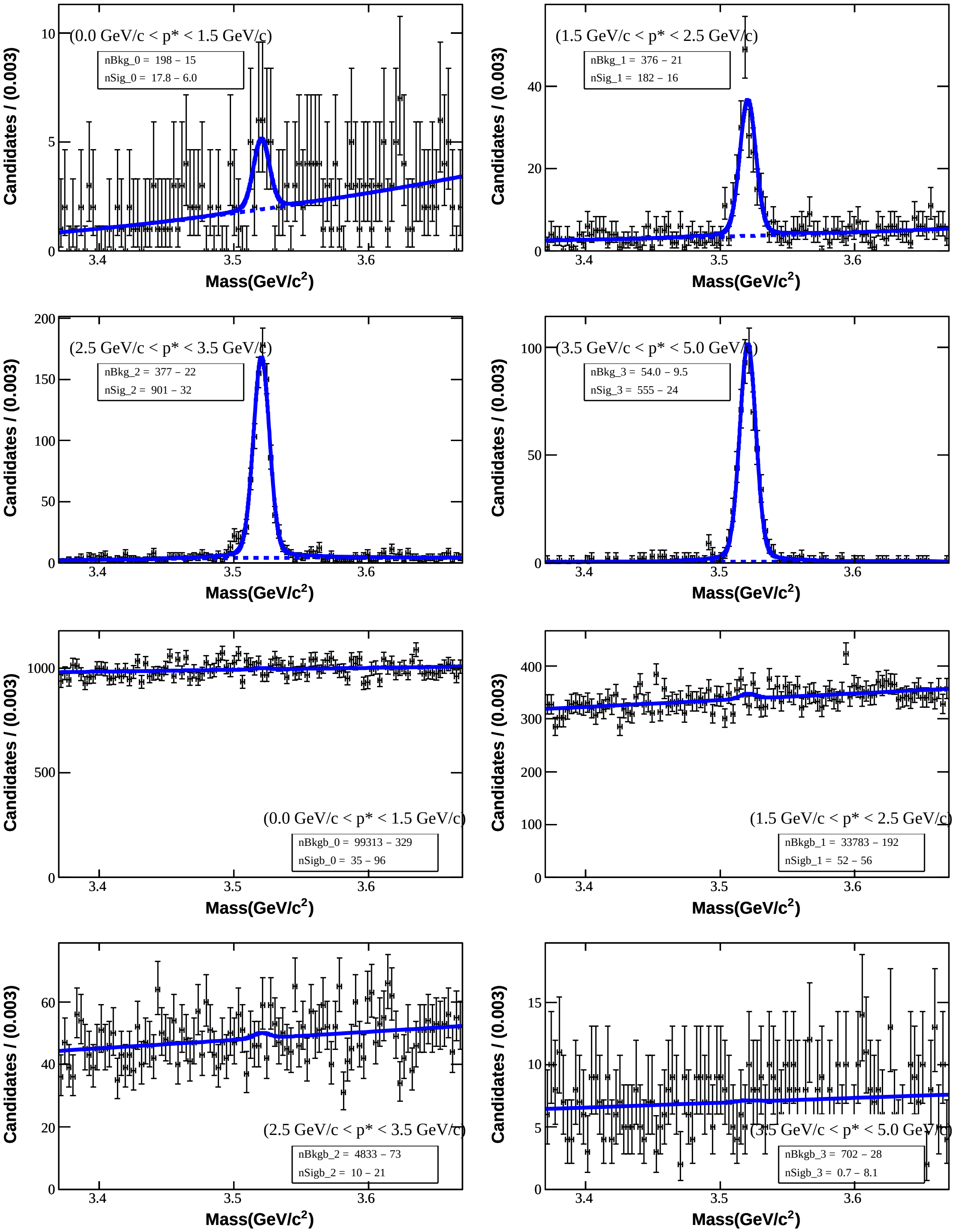

Figure 8.14: Invariant mass distributions of $R(3520)$ candidates in SP6050 Monte Carlo (top four plots) and data (bottom four plots) for the decay mode $p\ \pi^-\ \pi^-\ K^+\ K^0_S$ with an associated $\overline{p}$ in the event for each $p*$ bin.

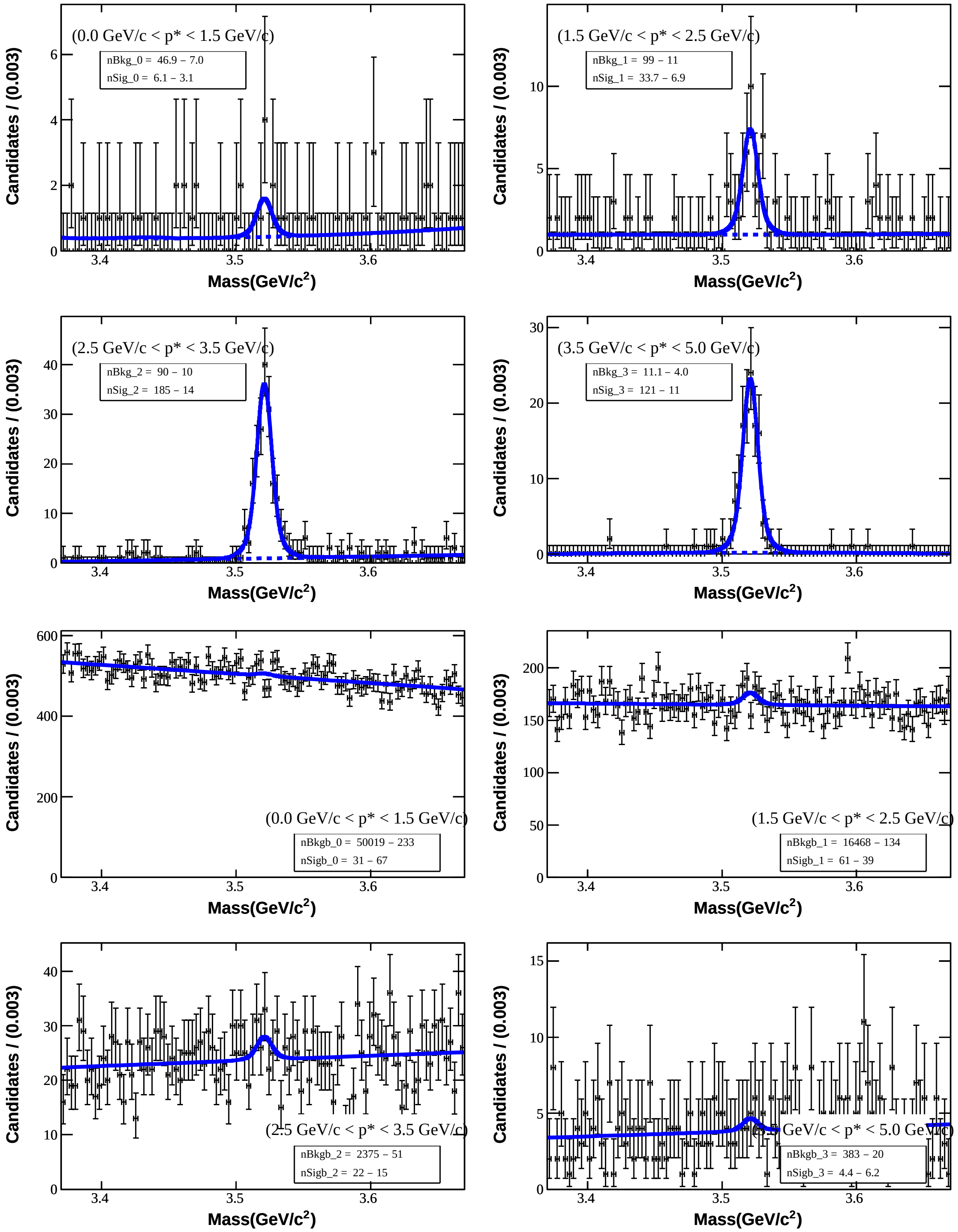

Figure 8.15: Invariant mass distributions of $R(3520)$ candidates in the SP6051 Monte Carlo (top four plots) and data (bottom four plots) for the decay mode $p\ \pi^-\ K^+\ K^{*-}$ with an associated $\overline{p}$ in the event for each $p*$ bin.

Table 8.1: Upper limit on the differential cross section on the production of the $R(3520)$ for the decay mode $K^0_S\ K^+\ p\ \pi^-\ \pi^-$ with an associated $\overline{p}$ in the event using SP6050 Monte Carlo.

Bin	1		2		3		4	
Method	Fit	Truth	Fit	Truth	Fit	Truth	Fit	Truth
p* (GeV/c)	0.00-1.50		1.50-2.50		2.50-3.50		3.50-5.00	
Fitted Yield	$35.18^{+96.50}_{-96.14}$		$52.19^{+56.77}_{-56.11}$		$9.59^{+21.80}_{-21.01}$		$0.72^{+8.48}_{-7.67}$	
Shift	0.00		0.00		0.00		0.00	
Raw Efficiency (%)	3.73	4.60	4.20	4.07	4.75	4.86	5.53	5.67
Track eff. corr.(%)	95.76	96.22	95.44	95.64	95.81	95.88	95.86	95.95
PID eff. corr. (%)	100.06	100.26	98.58	98.21	97.54	97.70	98.35	98.46
K^0_S eff. corr. (%)	103.04	101.46	99.75	99.69	101.26	100.42	100.38	100.27
Corrected Efficiency (%)	3.68	4.51	3.94	3.81	4.50	4.57	5.23	5.37
Raw UL (events)	194.39		145.87		45.56		14.71	
MC Stat error	23.25	20.82	7.26	7.38	3.25	3.21	4.13	4.07
Tracking Syst error	2.12	1.89	2.28	2.18	2.09	2.06	2.07	2.02
PID Syst error	0.03	0.13	0.71	0.90	1.23	1.15	0.83	0.77
K^0_S Syst error	1.52	0.73	0.12	0.15	0.63	0.21	0.19	0.13
Total Syst.	23.42	20.95	7.72	7.83	4.25	4.14	4.82	4.74
Corrected UL	214.95	211.00	148.71	148.79	45.74	45.73	14.76	14.76
Luminosity (fb^{-1})	227.89		227.89		227.89		227.89	
Branching Fraction	0.35		0.35		0.35		0.35	
Upper Limit (fb/ GeV/c)	49.41	39.60	47.85	49.55	12.90	12.68	2.38	2.32

Table 8.2: Upper limit on the differential cross section on the production of the $R(3520)$ for the decay mode $K^{*-}\ K^+\ p\ \pi^-$ with an associated $\overline{p}$ in the event using SP6051 Monte Carlo.

Bin	1		2		3		4	
Method	Fit	Truth	Fit	Truth	Fit	Truth	Fit	Truth
p* (GeV/c)	0.00-1.50		1.50-2.50		2.50-3.50		3.50-5.00	
Fitted Yield	$31.10^{+67.07}_{-66.48}$		$60.81^{+39.31}_{-38.54}$		$22.13^{+15.78}_{-14.79}$		$4.38^{+6.64}_{-5.86}$	
Shift	0.00		0.00		0.00		0.00	
Raw Efficiency (%)	5.69	3.70	3.35	3.18	4.20	4.28	5.17	5.17
Track eff. corr.(%)	96.86	97.04	95.40	96.08	95.94	95.98	95.55	96.04
PID eff. corr. (%)	99.52	97.75	97.77	97.55	97.94	97.89	96.59	97.47
K^0_S eff. corr. (%)	99.84	100.26	99.51	100.79	100.59	100.79	101.23	100.05
Corrected Efficiency (%)	5.47	3.52	3.11	3.00	3.97	4.05	4.83	4.84
Raw UL (events)	141.77		125.68		48.17		15.33	
MC Stat error	39.19	49.07	16.93	17.39	7.20	7.14	8.86	8.85
Tracking Syst error	1.57	1.48	2.30	1.96	2.03	2.01	2.22	1.98
PID Syst error	0.24	1.12	1.11	1.23	1.03	1.06	1.70	1.26
K^0_S Syst error	0.08	0.13	0.25	0.39	0.29	0.40	0.61	0.03
Total Syst.	39.24	49.11	17.16	17.59	7.64	7.58	9.37	9.22
Corrected UL	184.19	204.35	143.35	144.18	49.46	49.44	15.68	15.67
Luminosity (fb^{-1})	227.89		227.89		227.89		227.89	
Branching Fraction	0.17		0.17		0.17		0.17	
Upper Limit (fb/ GeV/c)	56.93	98.10	117.02	121.82	31.57	30.97	5.49	5.47

8.8.2 Best candidate selection of the K^0_S and K^{*-} candidates

The procedure followed to select the best K^0_S and K^{*-} candidates was that described in Section 5.2.7 and Section 5.3.5, respectively. The K^0_S candidates selected are those with the largest flight length significance and the K^{*-} candidates which are selected are those with the mass closest to the mass given in the PDG book [1].

The invariant mass distributions for the decay modes $p\ \pi^-\ \pi^-\ K^+\ K^0_S$ and $p\ \pi^-\ K^+\ K^{*-}$ are shown in Figure 8.16 and Figure 8.17, respectively. In each figure, the top four plots are for signal Monte Carlo simulated data and the bottom four plots are for real data. The solid lines show the result of the extended maximum likelihood fit on these distributions, the dashed line shows the background component of these fits. The numbers of signal and background candidates are given on the plot.

Results are tabulated in Table 8.3 and Table 8.4 for the calculation of the upper limits on the differential cross section for the production of $R(3520)$ candidates for the decay modes $K^0_S\ K^+\ p\ \pi^-\ \pi^-$ and $K^{*-}\ K^+\ p\ \pi^-$, respectively. The signal efficiencies have been calculated using both the number of signal candidates returned from the extended maximum likelihood fits and also the number of signal candidates determined from the Monte Carlo truth information.

8.8.3 Tight selection of the $R(3520)$ candidates

The invariant mass distributions of the $R(3520)$ candidates with the tighter selection criteria (see Section 6.4) applied for the decay modes $p\ \pi^-\ \pi^-\ K^+\ K^0_S$ and $p\ \pi^-\ K^+\ K^{*-}$ are shown in Figure 8.18 and Figure 8.19, respectively. In each figure, the top four plots are for signal Monte Carlo simulated data and the bottom four plots are for real data. The solid lines show the result of the extended maximum likelihood fit on these distributions, the dashed line shows the background component of these fits. The numbers of signal and background candidates are given on the plot.

Results are tabulated in Table 8.5 and Table 8.5 for the calculation of the upper limits on the differential cross section for the production of $R(3520)$ candidates for the decay modes $K^0_S\ K^+\ p\ \pi^-\ \pi^-$ and $K^{*-}\ K^+\ p\ \pi^-$, respectively. The signal efficiencies have been calculated using both the number of signal candidates returned from extended maximum likelihood fits and the number of signal candidates determined from the Monte Carlo truth information.

8.8.4 Summary

The upper limits on the differential cross section on the production of the $R(3520)$ with an associated $\overline{p}$ in the event are summarised in Table 8.7 and Table 8.8, respectively. The upper limits are given for each p* bin for the decay modes $p\ K^+\ \pi^-\ \pi^-\ K^0_S$ and $p\ K^+\ \pi^-\ K^{*-}$, respectively. The upper limits

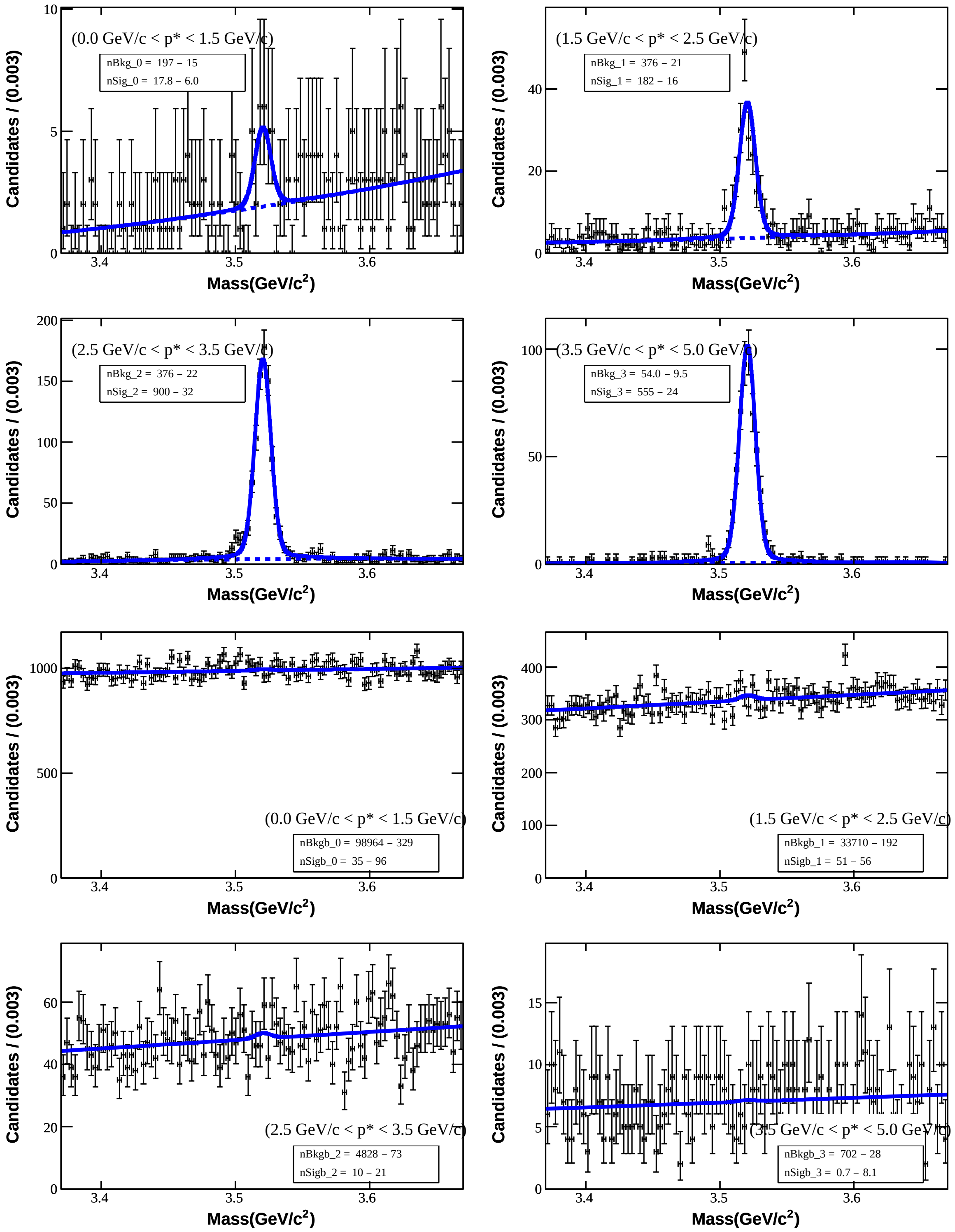

Figure 8.16: Invariant mass distributions of $R(3520)$ candidates with best candidate selection applied to the K^0_S candidates and an associated $\overline{p}$ in the event for each $p*$ bin in SP6050 Monte Carlo (top four plots) and data (bottom four plots) for the decay mode $p\ \pi^-\ \pi^-\ K^+\ K^0_S$.

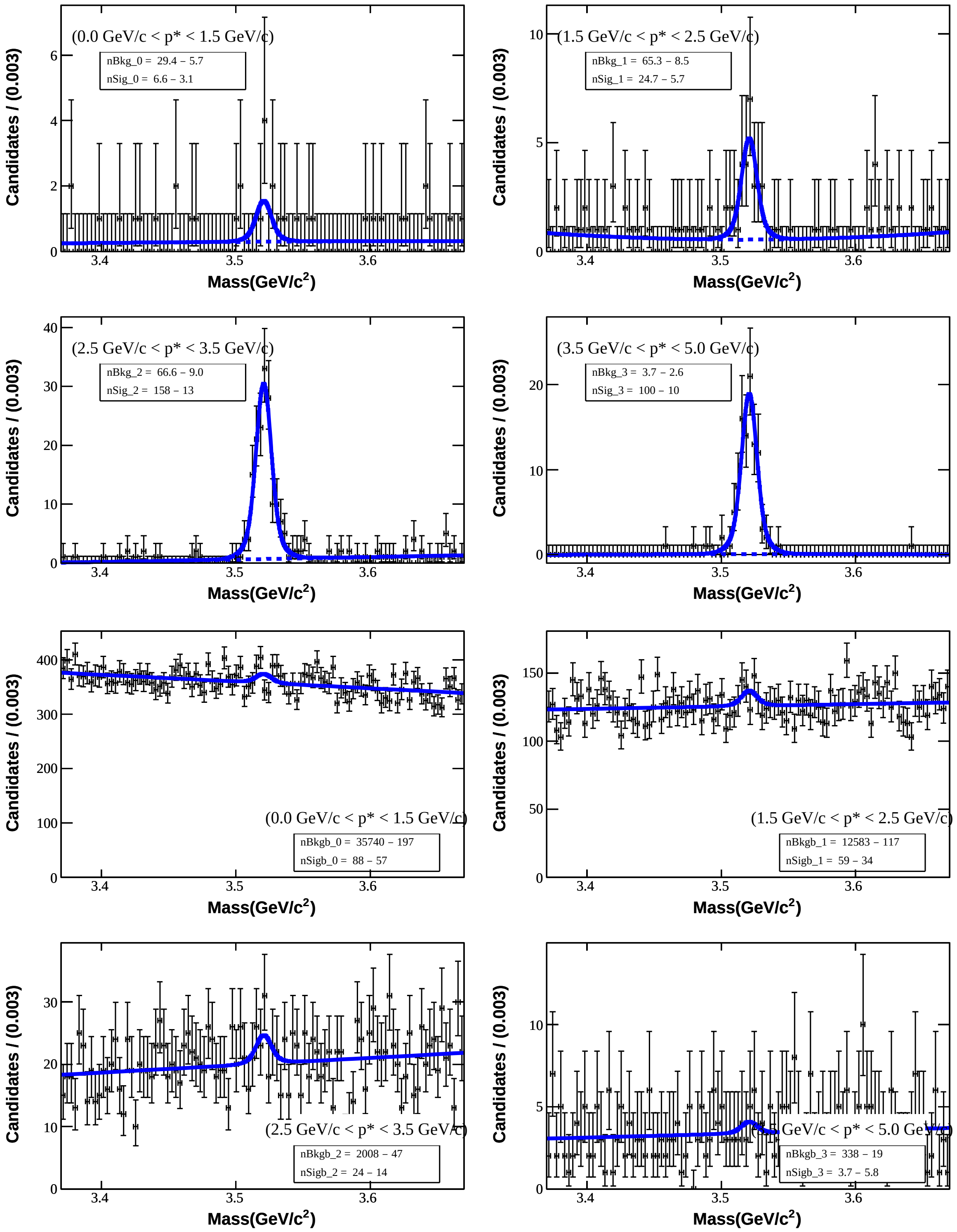

Figure 8.17: Invariant mass distributions of $R(3520)$ candidates with best candidate selection applied to the K^{*-} candidates and an associated $\overline{p}$ in the event for each $p*$ bin in SP6051 Monte Carlo (top four plots) and data (bottom four plots) for the decay mode $p\ \pi^-\ K^+\ K^{*-}$.

Table 8.3: Upper limit on the differential cross section on the production of the $R(3520)$ for the decay mode K^{*-} K^{+} p π^{-} after the selection of the best K^0_S candidates with an associated $\overline{p}$ using SP6050 Monte Carlo.

Bin	1		2		3		4	
Method	Fit	Truth	Fit	Truth	Fit	Truth	Fit	Truth
p* (GeV/c)	0.00-1.50		1.50-2.50		2.50-3.50		3.50-5.00	
Fitted Yield	$35.24^{+96.30}_{-95.94}$		$51.27^{+56.69}_{-56.03}$		$9.59^{+21.78}_{-20.99}$		$0.73^{+8.48}_{-7.67}$	
Raw Efficiency (%)	3.73	4.60	4.20	4.07	4.75	4.86	5.53	5.67
Track eff. corr.(%)	95.73	96.22	95.44	95.64	95.80	95.88	95.86	95.95
PID eff. corr. (%)	100.07	100.26	98.58	98.21	97.54	97.70	98.35	98.46
K^0_S eff. corr. (%)	103.04	101.46	99.75	99.69	101.29	100.42	100.38	100.27
Corrected Efficiency (%)	3.68	4.51	3.94	3.81	4.49	4.57	5.23	5.37
Raw UL (events)	194.14		144.81		45.52		14.72	
Shift	0.00		0.00		0.00		0.00	
MC Stat error	23.23	20.82	7.26	7.38	3.25	3.22	4.13	4.07
Tracking Syst error	2.14	1.89	2.28	2.18	2.10	2.06	2.07	2.02
PID Syst error	0.03	0.13	0.71	0.90	1.23	1.15	0.83	0.77
K^0_S Syst error	1.52	0.73	0.12	0.15	0.64	0.21	0.19	0.13
Total Syst.	23.40	20.95	7.72	7.83	4.26	4.14	4.82	4.74
Corrected UL	214.66	210.75	147.60	147.68	45.70	45.69	14.77	14.77
Luminosity (fb^{-1})	227.89		227.89		227.89		227.89	
Branching Fraction	0.35		0.35		0.35		0.35	
Upper Limit (fb/ GeV/c)	49.27	39.55	47.49	49.19	12.89	12.69	2.39	2.33

Table 8.4: Upper limit on the differential cross section on the production of the $R(3520)$ for the decay mode K^{*-} K^{+} p π^{-} after the selection of the best K^{*-} candidates with an associated $\overline{p}$ using SP6050 Monte Carlo.

Bin	1		2		3		4	
Method	Fit	Truth	Fit	Truth	Fit	Truth	Fit	Truth
p* (GeV/c)	0.00-1.50		1.50-2.50		2.50-3.50		3.50-5.00	
Fitted Yield	$88.19^{+57.64}_{-56.98}$		$59.35^{+34.72}_{-33.88}$		$24.40^{+14.67}_{-13.86}$		$3.70^{+6.19}_{-5.41}$	
Raw Efficiency (%)	6.15	3.70	2.46	2.38	3.60	3.62	4.29	4.23
Track eff. corr.(%)	95.67	97.04	95.88	95.67	95.50	95.93	96.15	96.19
PID eff. corr. (%)	97.60	97.75	97.23	97.32	97.88	98.10	97.00	97.66
K^0_S eff. corr. (%)	99.57	100.26	98.83	101.09	100.57	100.95	100.20	99.82
Corrected Efficiency (%)	5.71	3.52	2.26	2.24	3.39	3.44	4.00	3.97
Raw UL (events)	183.31		116.63		48.60		13.92	
Shift	0.00		0.00		0.00		0.00	
MC Stat error	37.60	49.07	19.85	20.17	7.80	7.79	9.77	9.84
Tracking Syst error	2.16	1.48	2.06	2.17	2.25	2.04	1.93	1.90
PID Syst error	1.20	1.12	1.39	1.34	1.06	0.95	1.50	1.17
K^0_S Syst error	0.21	0.13	0.58	0.55	0.29	0.47	0.10	0.09
Total Syst.	37.70	49.11	20.05	20.36	8.27	8.19	10.13	10.15
Corrected UL	286.17	339.94	140.61	141.31	50.39	50.36	14.28	14.28
Luminosity (fb^{-1})	227.89		227.89		227.89		227.89	
Branching Fraction	0.17		0.17		0.17		0.17	
Upper Limit (fb/ GeV/c)	84.68	163.20	157.50	159.78	37.74	37.18	6.03	6.09

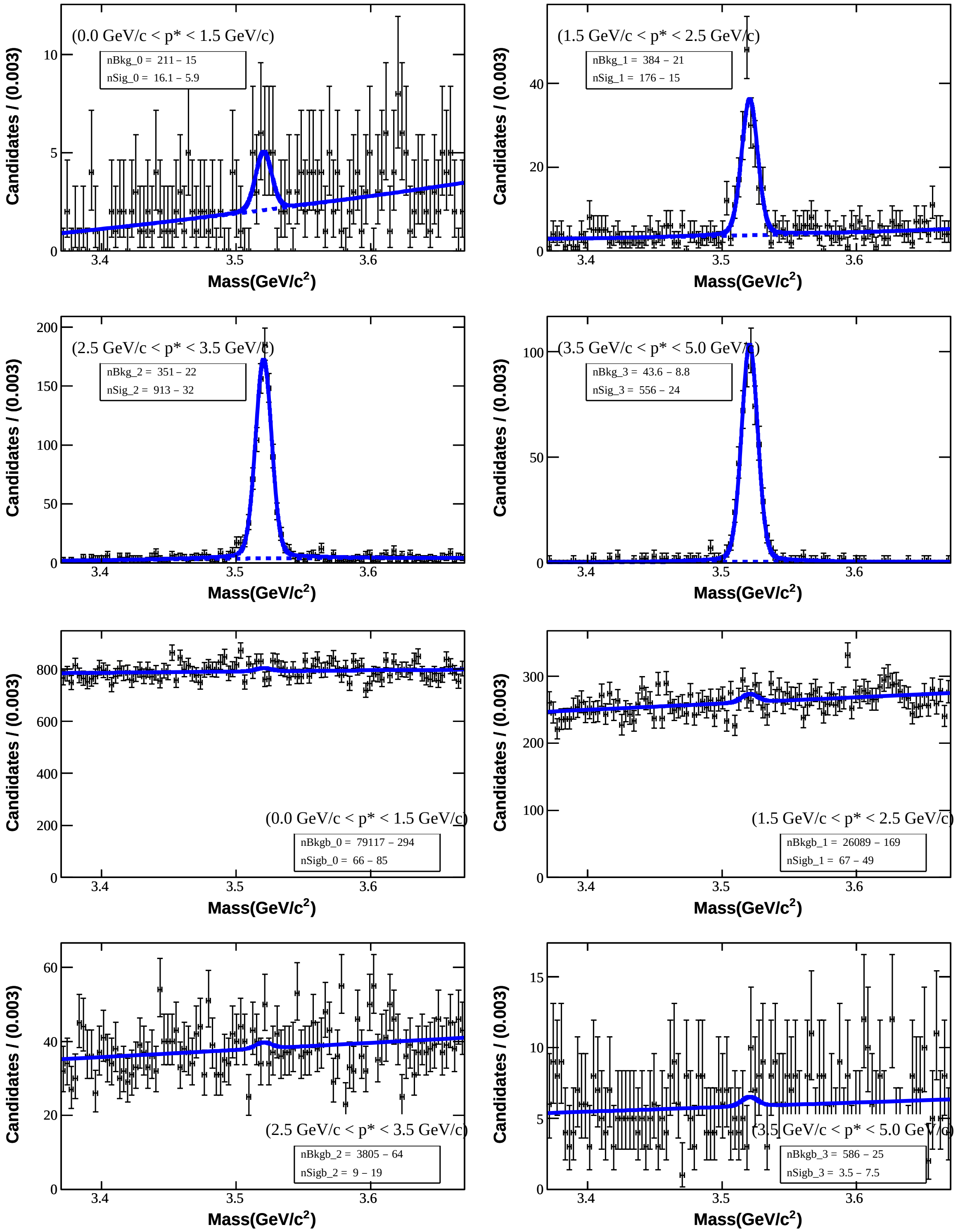

Figure 8.18: Invariant mass distributions of $R(3520)$ candidates in SP6050 Monte Carlo (top four plots) and data (bottom four plots) for the decay mode $p\ \pi^-\ \pi^-\ K^+\ K^0_S$ with an associated $\overline{p}$ in the event for each $p*$ bin.

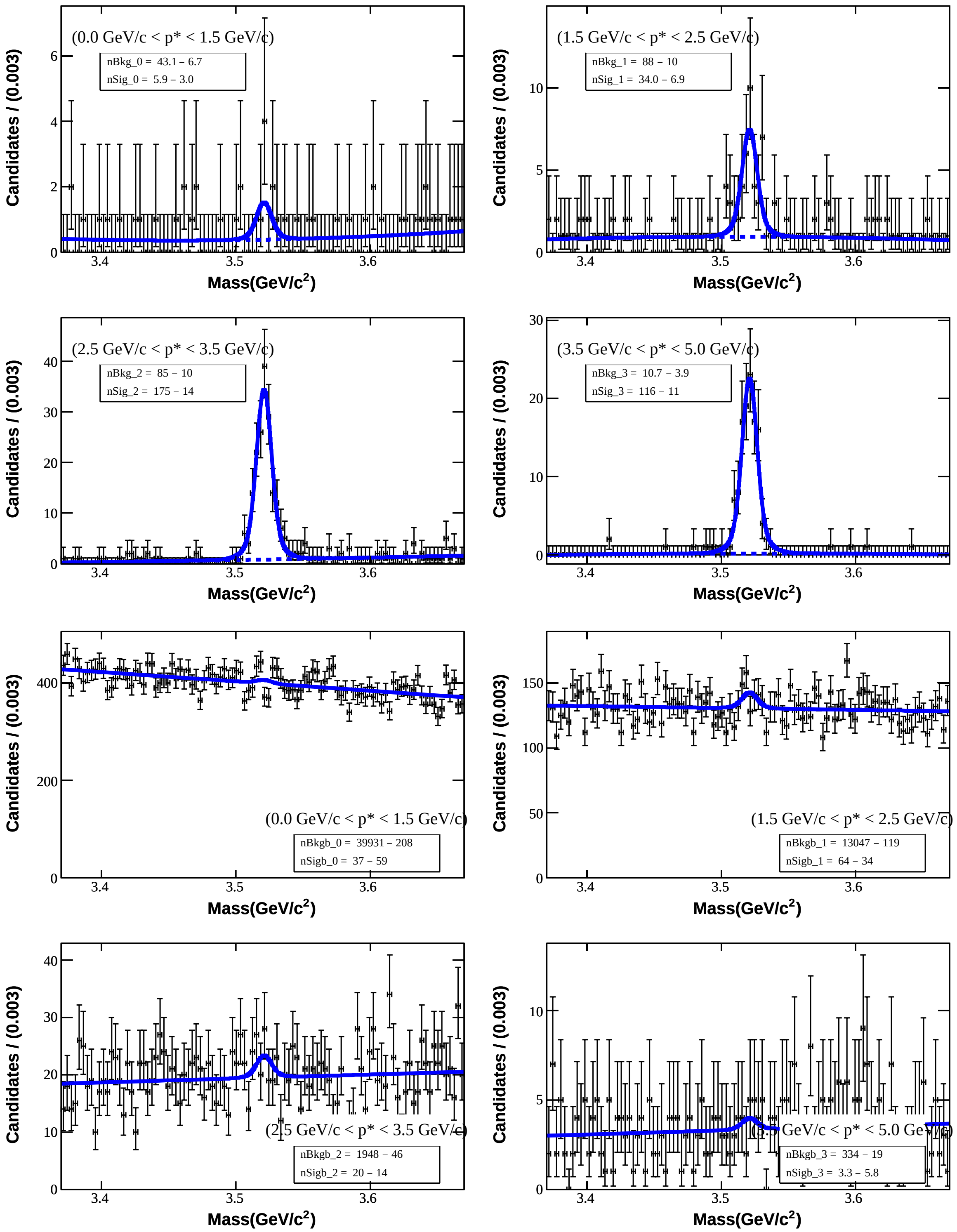

Figure 8.19: Invariant mass distributions of $R(3520)$ candidates in the SP6051 Monte Carlo (top four plots) and data (bottom four plots) for the decay mode $p\ \pi^-\ K^+\ K^{*-}$ with an associated $\overline{p}$ in the event for each $p*$ bin.

Table 8.5: Upper limit on the differential cross section on the production of the $R(3520)$ for the decay mode K^0_S K^+ p π^- π^- with an associated $\overline{p}$ in the event using SP6050 Monte Carlo.

Bin	1		2		3		4	
Method	Fit	Truth	Fit	Truth	Fit	Truth	Fit	Truth
p* (GeV/c)	0.00-1.50		1.50-2.50		2.50-3.50		3.50-5.00	
Fitted Yield	$66.42^{+85.41}_{-84.96}$		$66.91^{+49.59}_{-48.89}$		$9.05^{+19.10}_{-18.32}$		$3.53^{+7.96}_{-7.16}$	
Shift	0.00		0.00		0.00		0.00	
Raw Efficiency (%)	3.37	4.81	4.06	3.95	4.82	4.92	5.54	5.62
Track eff. corr.(%)	96.08	96.33	95.62	95.58	95.78	95.84	95.78	95.92
PID eff. corr. (%)	100.08	100.08	98.33	98.15	97.47	97.76	98.44	98.54
K^0_S eff. corr. (%)	103.97	101.63	99.72	99.59	101.14	100.39	100.45	100.27
Corrected Efficiency (%)	3.37	4.71	3.80	3.69	4.55	4.63	5.25	5.33
Raw UL (events)	207.34		148.73		40.57		16.67	
MC Stat error	24.50	20.34	7.39	7.49	3.23	3.19	4.12	4.09
Tracking Syst error	1.96	1.83	2.19	2.21	2.11	2.08	2.11	2.04
PID Syst error	0.04	0.04	0.84	0.93	1.27	1.12	0.78	0.73
K^0_S Syst error	1.98	0.81	0.14	0.20	0.57	0.20	0.22	0.13
Total Syst.	24.68	20.47	7.83	7.95	4.24	4.13	4.83	4.76
Corrected UL	241.71	231.54	152.78	152.90	40.73	40.73	16.75	16.75
Luminosity (fb^{-1})	227.89		227.89		227.89		227.89	
Branching Fraction	0.35		0.35		0.35		0.35	
Upper Limit (fb/ GeV/c)	60.68	41.52	50.93	52.53	11.36	11.16	2.70	2.66

Table 8.6: Upper limit on the differential cross section on the production of the $R(3520)$ for the decay mode K^{*-} K^+ p π^- with an associated $\overline{p}$ in the event using SP6051 Monte Carlo.

Bin	1		2		3		4	
Method	Fit	Truth	Fit	Truth	Fit	Truth	Fit	Truth
p* (GeV/c)	0.00-1.50		1.50-2.50		2.50-3.50		3.50-5.00	
Fitted Yield	$37.06^{+59.43}_{-58.80}$		$63.69^{+34.89}_{-34.03}$		$20.07^{+14.27}_{-13.38}$		$3.35^{+6.16}_{-5.38}$	
Shift	0.00		0.00		0.00		0.00	
Raw Efficiency (%)	5.47	3.70	3.37	3.18	3.97	4.03	4.97	5.00
Track eff. corr.(%)	96.55	97.04	94.85	96.08	95.70	95.99	95.32	96.04
PID eff. corr. (%)	100.77	97.75	97.63	97.55	97.81	97.97	97.25	97.82
K^0_S eff. corr. (%)	101.22	100.26	101.22	100.79	100.57	100.72	101.12	100.23
Corrected Efficiency (%)	5.39	3.52	3.16	3.00	3.74	3.81	4.66	4.71
Raw UL (events)	135.12		121.26		43.61		13.51	
MC Stat error	39.99	49.07	16.87	17.39	7.42	7.36	9.04	9.01
Tracking Syst error	1.72	1.48	2.57	1.96	2.15	2.01	2.34	1.98
PID Syst error	0.38	1.12	1.19	1.23	1.09	1.01	1.38	1.09
K^0_S Syst error	0.61	0.13	0.61	0.39	0.28	0.36	0.56	0.11
Total Syst.	40.04	49.11	17.15	17.59	7.88	7.79	9.52	9.36
Corrected UL	182.73	202.54	141.16	142.11	44.86	44.83	13.80	13.79
Luminosity (fb^{-1})	227.89		227.89		227.89		227.89	
Branching Fraction	0.17		0.17		0.17		0.17	
Upper Limit (fb/ GeV/c)	57.32	97.24	113.23	120.08	30.43	29.82	5.01	4.95

are given for the $R(3520)$ candidates: with the loose selection, after the selection of the best K^0_S and K^{*-} candidates, and the tight selection.

Table 8.7: Upper limits on the differential cross section on the production of the $R(3520)$ for the decay mode $p\ K^+\ \pi^-\ \pi^-\ K^0_S$ with an additional $\overline{p}$ in the event

Bin	1		2		3		4	
Method	Fit	Truth	Fit	Truth	Fit	Truth	Fit	Truth
p* (GeV/c)	0.00-1.50		1.50-2.50		2.50-3.50		3.50-5.00	
Loose	49.41	39.60	47.85	49.55	12.90	12.68	2.38	2.32
Best	49.27	39.55	47.49	49.19	12.89	12.69	2.39	2.33
Tight	60.68	41.52	50.93	52.53	11.36	11.16	2.70	2.66

Table 8.8: Upper limits on the differential cross section on the production of the $R(3520)$ for the decay mode $p\ K^+\ \pi^-\ K^{*-}$ with an additional $\overline{p}$ in the event

Bin	1		2		3		4	
Method	Fit	Truth	Fit	Truth	Fit	Truth	Fit	Truth
p* (GeV/c)	0.00-1.50		1.50-2.50		2.50-3.50		3.50-5.00	
Loose	56.93	98.10	117.02	121.82	31.57	30.97	5.49	5.47
Best	84.68	163.20	157.50	159.78	37.74	37.18	6.03	6.09
Tight	57.32	97.24	113.23	120.08	30.43	29.82	5.01	4.95

The upper limits on the differential cross sections are displayed as a function of p* in Figure 8.20 for the decay modes $p\ K^+\ \pi^-\ \pi^-\ K^0_S$(left) and $p\ K^+\ \pi^-\ K^{*-}$(right), respectively. The differential cross sections with the signal efficiency calculated using the extended maximum likelihood fits (Monte Carlo Truth information) are shown by the solid (dashed) line.

It can be seen that the requirement that there was an associated $\overline{p}$ in the event reduced the upper limits on the differential cross section for the decay mode $p\ K^+\ \pi^-\ \pi^-\ K^0_S$. This was due to the reduction in the number of the $R(3520)$ candidates reconstructed in the data which resulted in reduced errors returned from the maximum likelihood fit and this reduction increased with p*. However, some of this reduction was cancelled out because the signal efficiency decreased with the requirement that there was an additional $\overline{p}$ in the event. This decrease was because the additional track had to be detected and identified using the pLHTight PID selector. The GoodTracksAccLoose selection criteria was required for the additional $\overline{p}$ which also reduced the detection efficiency.

With the exception of the second p* bin, it can be seen that the requirement that there was an associated $\overline{p}$ in the event reduced the upper limits on the differential cross section for the decay mode $p\ K^+\ \pi^-\ K^{*-}$. This was due to the reduction in the number of the $R(3520)$ candidates reconstructed in the data which resulted in reduced errors returned from the maximum likelihood fit. This reduction increased with p*. However, some of this reduction was cancelled out

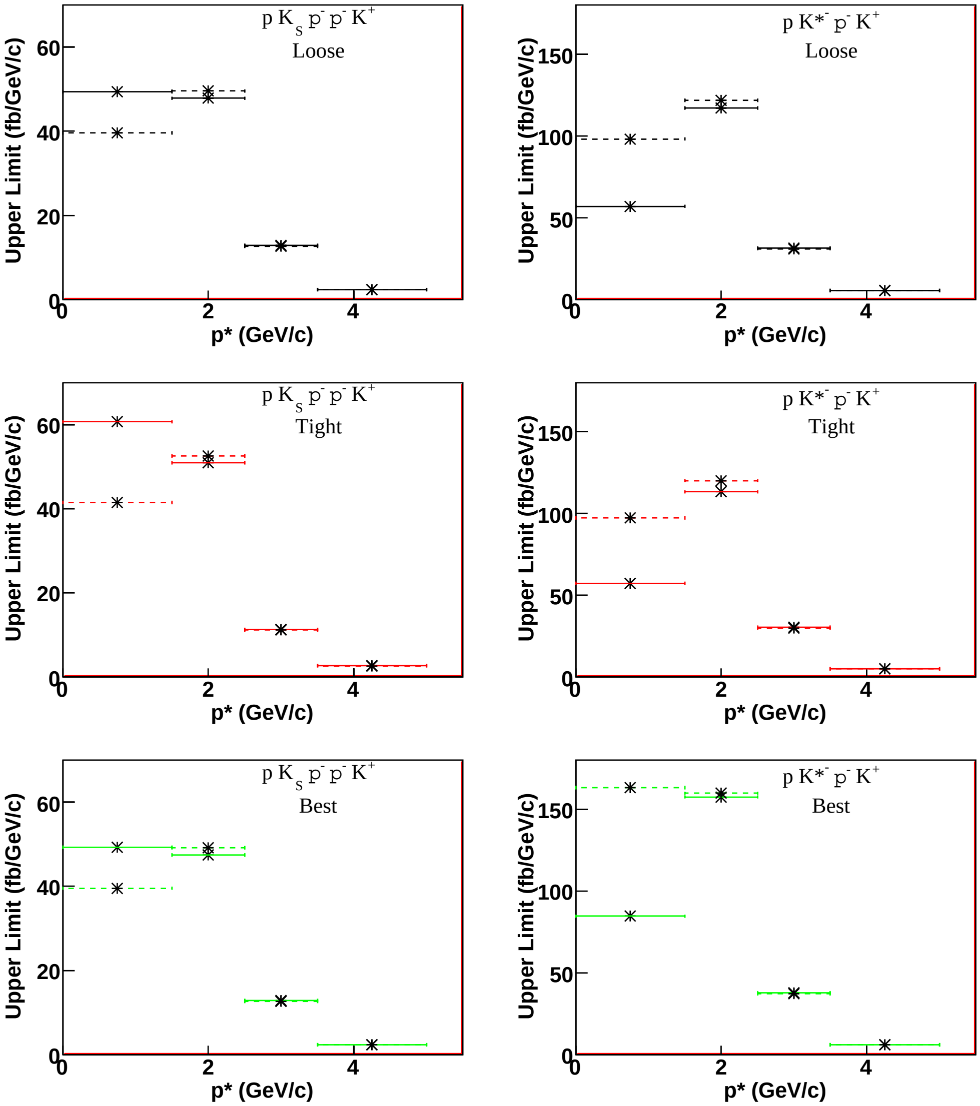

Figure 8.20: Upper limit on the differential cross section with an additional $\overline{p}$ in the event as a function of p*. The differential cross sections with the signal efficiency calculated using the extended maximum likelihood fits (Monte Carlo Truth information) are shown by the solid (dashed) line.

because the signal efficiency decreased with the requirement that there was an additional $\overline{p}$ in the event.

In the second p* bin there was an upwards fluctuation in the data where the peak was measured, as can be seen in Figure 8.15. The upper limit of N_{Max} was decreased from 200 to 126 with the requirement that there was an additional $\overline{p}$ in the event. The signal efficiency was reduced from 6.37% to 3.00%, and there was also a larger systematic error due to the limited statistics in the Monte Carlo simulated data. In the second p* bin, this systematic error increased the upper limit by 20%. It can be seen that the combination of these three factors resulted in a larger upper limit in the second p* bin with the requirement that there was an additional $\overline{p}$ in the event.

With the exception of the first p* bin, it can be seen that the upper limits on the differential cross sections obtained with the signal efficiency calculated using the extended maximum likelihood fit were similar to the upper limits calculated using the truth information in the Monte Carlo simulated data indicating that similar results could be obtained with both methods.

It can be seen that there were differences in the first two p* bins between the upper limits obtained using the maximum likelihood fit and the truth information in the Monte Carlo simulated data to calculate the signal efficiency. These differences in the upper limits were due to the differences in the signal efficiency because there were fewer events with $R(3520)$ candidates generated in this p* bin. Also, the requirement that there was an additional $\overline{p}$ in the event meant that the subsample of Monte Carlo simulated data was smaller than that used in Section 7.

In the SP6050 sample of Monte Carlo simulated data there happened to be a downwards fluctuation directly under the signal peak. With the loose selection for the decay mode $p\ K^+\ \pi^-\ \pi^-\ K_S^0$, the number of truth-matched candidates in the first p* bin was 22 and the total number returned from the fit was $17.7^{+6.4}_{-5.7}$. Since, the difference between the two values of the signal efficiency was less than the error and the values were consistent.

For the $p\ K^+\ \pi^-\ K^{*-}$ decay mode the statistics were even lower so the results looked weaker. The number of truth-matched candidates in the first p* bin was 4 and the total number returned from the fit was $6.1^{+3.2}_{-2.9}$. But it can be seen that the difference between the two values is less than the error so the values were consistent with each other.

It can be seen that for the decay mode $p\ K^+\ \pi^-\ \pi^-\ K_S^0$ the upper limits on the differential cross sections were similar in the first and second momentum bins and then reduced as a function of p*. The decrease as a function of p* was due to two factors: the signal efficiency increased as a function of p*, and the number of the $R(3520)$ candidates reconstructed in each p* bin decreased as a function of p* which decreased the errors returned from the fits. The signal efficiency increased as a function of p* for the reasons detailed in Section 7.2.4.

The upper limit in the first p* bin was similar to the upper limit in the second p* bin with the signal efficiency calculated using the number of candidates returned from the extended maximum likelihood fit. This was due to differences in the width of the momentum bin, the signal efficiency and N_{Max}. The value of N_{Max} was larger in the first p* bin than in the second p* bin because there were more $R(3520)$ candidates reconstructed in the first p* bin in the real data. The signal efficiency was much larger in the first p* bin than in the second p* bin. However, as the number of signal $R(3520)$ candidates in the Monte Carlo sample was very low in this bin, it was unclear if this effect was caused by kinematics or a statistical fluctuation in the reconstruction efficiency. The first p* bin was 1.5 times larger than the second p* bin which reduced the upper limit in the first p* bin.

The upper limit in the first p* bin was smaller than the upper limit in the second p* bin with the signal efficiency calculated using the truth information in the Monte Carlo simulated data. This was due to differences in the width of the momentum bin, the signal efficiency, and N_{Max}. The value of N_{Max} was larger in the first p* bin than in the second p* bin again because there were more $R(3520)$ candidates reconstructed in the first p* bin in the data. The signal efficiency was larger in the first p* bin than in the second p* bin. However, as the number of the signal $R(3520)$ candidates in the Monte Carlo sample was very low in this bin it was unclear if this effect was caused by kinematics or a statistical fluctuation in the reconstruction efficiency. The first p* bin was 1.5 times larger than the second p* bin which reduced the upper limit in the first p* bin.

It can be seen that for the decay mode $p\ K^+\ \pi^-\ K^{*-}$ the upper limits on the differential cross sections increased from the first p* bin to the second p* bin and then decreased as a function of p*. This was due to a combination of differences in the yield, the signal efficiency and the width of the p* bin.

There was a larger upwards fluctuation in the invariant mass distribution in the second p* bin than in the first p* bin, as can be seen in Figure 8.15, which resulted in the value of N_{Max} being similar in both p* bins.

The signal efficiency was also larger in the first p* bin than in the second p* bin. However, as the number of signal $R(3520)$ candidates was very low in the first p* bin this could be a statistical fluctuation.

It can be seen that the selection of the best K^0_S candidates had very little effect on the upper limits on the differential cross sections. For the decay mode $p\ K^0_S\ \pi^-\ \pi^-\ K^+$ the results were similar due to the selection of K^0_S candidates only affecting a small proportion of the events.

Also, it can be seen that the selection of the best K^{*-} candidates increased the upper

limits on the differential cross section for the decay mode K^{*-} K^+ p π^-. This was due to a decrease in the signal efficiency that was not cancelled out by the reduction of the yield and the associated errors. The reduction in the yield and the associated errors were due to the reduction of the number of reconstructed $R(3520)$ candidates due to the best candidate selection process. However, as the selection of the best K^{*-} candidates was not 100% efficient, the signal efficiency decreased.

With the exception of the third p* bin, it can be seen that the upper limits on the differential cross sections for the decay mode p K^0_S π^- π^- K^+ with the tight selection were higher than those obtained with the loose selection. The tight selection reduced the number of the $R(3520)$ candidates in the data which in turn reduced the fit error on the yield. This was balanced due to the small drop in the signal efficiency caused by the addition of the tighter selection criteria. However, the main reason for the differences in the upper limits were that there were larger upwards fluctuations in the first, second, and fourth p* bins and a downwards fluctuation in the third p* bin in the invariant mass distribution obtained with the tight selection than in the distribution obtained with the loose selection.

As neither the tight selection or the selection of the best K^0_S or K^{*-} candidates had a great effect on the differential cross sections obtained, only the loose selection was considered further.

8.9 Experimental results of the upper limits on the differential cross section — $\Gamma = 7\,\mathrm{MeV}/c^2$ hypothesis

The upper limits on the differential cross section were calculated with the alternative width hypothesis $\Gamma = 7\,\mathrm{MeV}/c^2$, because any cross section would be dependent on this width. Results of the calculation of the upper limits on the differential cross section for the production of $R(3520)$ candidates for the decay modes K^0_S K^+ p π^- π^- and K^{*-} K^+ p π^- are tabulated in Table 8.9 and Table 8.10, respectively. The signal efficiencies have been calculated using both the number of signal candidates returned from extended maximum likelihood fits and the number of signal candidates determined from the Monte Carlo truth information.

The upper limits on the differential cross sections with an additional $\overline{p}$ in the event are displayed for the two width hypotheses as a function of p* in Figure 8.21 for the decay modes p K^+ π^- π^- K^0_S(left) and p K^+ π^- K^{*-}(right), respectively. The differential cross sections with the signal efficiency calculated using the extended maximum likelihood fits (Monte Carlo Truth information) are shown by the solid (dashed) line.

Table 8.9: Upper limit on the differential cross section on the production of the $R(3520)$ with $\Gamma = 7\,\mathrm{MeV}/c^2$ for the decay mode $K^0_S\ K^+\ p\ \pi^-\ \pi^-$ with an additional $\overline{p}$ in the event using SP6050 Monte Carlo.

Bin	1		2		3		4	
Method	Fit	Truth	Fit	Truth	Fit	Truth	Fit	Truth
p* (GeV/c)	0.00-1.50		1.50-2.50		2.50-3.50		3.50-5.00	
Fitted Yield	$102.39^{+123.17}_{-122.81}$		$64.02^{+72.04}_{-71.34}$		$13.14^{+27.68}_{-26.84}$		$1.57^{+10.87}_{-9.95}$	
Shift	0.00		0.00		0.00		0.00	
Raw Efficiency (%)	3.73	4.60	4.20	4.07	4.75	4.86	5.53	5.67
Track eff. corr.(%)	95.72	96.22	95.44	95.64	95.81	95.88	95.86	95.95
PID eff. corr. (%)	100.01	100.26	98.58	98.21	97.54	97.70	98.35	98.46
K^0_S eff. corr. (%)	102.99	101.46	99.75	99.69	101.26	100.42	100.38	100.27
Corrected Efficiency (%)	3.67	4.51	3.94	3.81	4.50	4.57	5.23	5.37
Raw UL (events)	305.62		182.88		58.82		19.50	
MC Stat error	23.25	20.82	7.26	7.38	3.25	3.21	4.13	4.07
Tracking Syst error	2.14	1.89	2.28	2.18	2.09	2.06	2.07	2.02
PID Syst error	0.01	0.13	0.71	0.90	1.23	1.15	0.83	0.77
K^0_S Syst error	1.50	0.73	0.13	0.15	0.63	0.21	0.19	0.13
Total Syst.	23.42	20.95	7.72	7.83	4.25	4.14	4.82	4.74
Corrected UL	353.47	344.45	186.36	186.46	59.06	59.04	19.58	19.57
Luminosity (fb^{-1})	227.89		227.89		227.89		227.89	
Branching Fraction	0.35		0.35		0.35		0.35	
Upper Limit (fb/ GeV/c)	81.33	64.64	59.97	62.10	16.65	16.38	3.16	3.08

Table 8.10: Upper limit on the differential cross section of the production of the $R(3520)$ with $\Gamma = 7\,\mathrm{MeV}/c^2$ for the decay mode $K^{*-}\ K^+\ p\ \pi^-$ with an additional $\overline{p}$ in the event using SP6051 Monte Carlo.

Bin	1		2		3		4	
Method	Fit	Truth	Fit	Truth	Fit	Truth	Fit	Truth
p* (GeV/c)	0.00-1.50		1.50-2.50		2.50-3.50		3.50-5.00	
Fitted Yield	$62.85^{+85.29}_{-84.69}$		$67.60^{+49.43}_{-48.67}$		$26.86^{+19.71}_{-18.74}$		$5.57^{+8.29}_{-7.43}$	
Shift	0.00		0.00		0.00		0.00	
Raw Efficiency (%)	5.68	3.70	3.35	3.18	4.20	4.28	5.17	5.17
Track eff. corr.(%)	96.88	97.04	95.46	96.08	95.94	95.98	95.55	96.04
PID eff. corr. (%)	99.54	97.75	97.83	97.55	97.94	97.89	96.59	97.47
K^0_S eff. corr. (%)	99.87	100.26	99.57	100.79	100.59	100.79	101.23	100.05
Corrected Efficiency (%)	5.47	3.52	3.11	3.00	3.97	4.05	4.83	4.84
Raw UL (events)	203.58		149.16		59.38		19.24	
MC Stat error	39.20	49.07	16.94	17.39	7.20	7.14	8.86	8.85
Tracking Syst error	1.56	1.48	2.27	1.96	2.03	2.01	2.22	1.98
PID Syst error	0.23	1.12	1.09	1.23	1.03	1.06	1.70	1.26
K^0_S Syst error	0.07	0.13	0.22	0.39	0.29	0.40	0.61	0.03
Total Syst.	39.25	49.11	17.16	17.59	7.64	7.58	9.37	9.22
Corrected UL	278.95	313.69	167.97	168.86	60.93	60.90	19.70	19.68
Luminosity (fb^{-1})	227.89		227.89		227.89		227.89	
Branching Fraction	0.17		0.17		0.17		0.17	
Upper Limit (fb/ GeV/c)	86.17	150.60	136.95	142.68	38.89	38.15	6.90	6.87

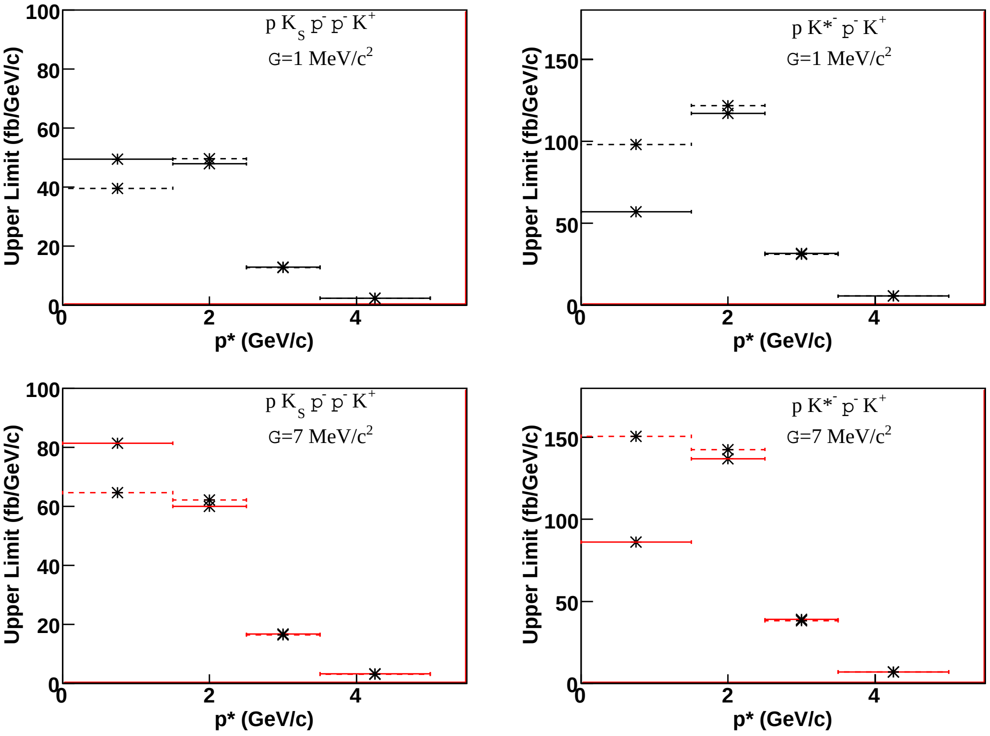

Figure 8.21: Upper limit on the differential cross section with an additional $\overline{p}$ in the event as a function of p* for the two width hypotheses. The differential cross sections with the signal efficiency calculated using the extended maximum likelihood fits (Monte Carlo Truth information) are shown by the solid (dashed) line.

In general, the upper limits increased with the width hypothesis, $\Gamma = 7\,\mathrm{MeV}/c^2$ because there was a larger yield due to the broader resonance.

8.10 Upper limit on the total cross section

The upper limits on the total cross section are presented in Table 7.11 together with the differential cross section presented in the previous sections. The upper limits on the total cross section were obtained by the addition of the differential cross sections in the p* range 0-5 GeV/c^2.

Table 8.11: Upper limits on the total and differential production cross sections in fb/ GeV/c

	$R(3520) \to p\ K_S^0\ \pi^-\ \pi^-\ K^+$				$R(3520) \to p\ K^{*-}\ \pi^-\ K^+$			
$p*$ Range	$\Gamma = 1\,\mathrm{MeV}/c^2$ (fb/ GeV/c)		$\Gamma = 7\,\mathrm{MeV}/c^2$ (fb/ GeV/c)		$\Gamma = 1\,\mathrm{MeV}/c^2$ (fb/ GeV/c)		$\Gamma = 7\,\mathrm{MeV}/c^2$ (fb/ GeV/c)	
(GeV/c)	Fit	Truth	Fit	Truth	Fit	Truth	Fit	Truth
0.0 - 1.5	49.41	39.6	81.33	64.64	56.93	98.1	86.17	150.6
1.5 - 2.5	47.85	49.55	59.97	62.1	117.02	121.82	136.95	142.68
2.5 - 3.5	12.9	12.68	16.65	16.38	31.57	30.97	38.89	38.15
3.5 - 5.0	2.38	2.32	3.16	3.08	5.49	5.47	6.9	6.87
Total	27.69	25.02	40.67	36.01	48.44	61.63	63.09	83.41

For the decay mode $K_S^0\ K^+\ p\ \pi^-\ \pi^-$ the total cross sections were larger than for the decay mode $K^{*-}\ K^+\ p\ \pi^-$. This was due to the extra factor of 0.5 in the branching fraction.

The total cross sections were larger with the $\Gamma = 7\,\mathrm{MeV}/c^2$ width hypothesis because of the higher yield due to the broader resonance.

For the decay mode $K_S^0\ K^+\ p\ \pi^-\ \pi^-$ the upper limits were larger for the method where the signal efficiency was calculated using the extended maximum likelihood fit than that using the Monte Carlo truth information. The difference was caused by a downwards fluctuation in the background in the invariant mass distribution in the first p* bin of the sample of signal Monte Carlo simulated data.

For the decay mode $K^{*-}\ K^+\ p\ \pi^-$ the upper limits were lower for the method where the signal efficiency was calculated using the extended maximum likelihood fit than that using the Monte Carlo truth information. The difference was mainly due to the low statistics in the sample of signal Monte Carlo simulated data in the first p* bin.

The upper limits on the total cross section were most sensitive to the differential cross sections in the bins with the lowest p*. In these low p* bins the most accurate measurement of the signal efficiency was calculated using the Monte Carlo truth information. Therefore, the total cross sections which should be regarded as the final results for this analysis were calculated using the Monte Carlo truth information to calculate the signal efficiency.

Chapter 9

Event selection with Gene Expression Programming

9.1 Introduction

This chapter describes a new algorithm and how it was used for event selection for a subsample of data used in the analysis presented in this thesis. The purpose of this study was to analyse the feasibility of this algorithm for solving such problems in high energy physics. This study was not developed enough in order to base the physics analysis presented in the previous chapters on such a novel method.

The results of the study were published in 2008, (L. Teodorescu and D. Sherwood, High Energy Physics event selection with Gene Expression Programming, Computer Physics Communications, Volume 178, Number 6, Pages 209-219) [181]. The author of this thesis contributed to this study by performing the manual optimisation and some of the GEP runs described further in the chapter.

Evolutionary algorithms(EAs) are computer algorithms which are inspired by the theories of evolutionary biology. Evolutionary algorithms encode candidate solutions to the problem being solved into a form that is understood by the computer, these are called chromosomes. The optimal solution to the problem is sought through an optimisation process. A fitness function is used to evaluate how good each solution is. The optimisation process uses a generate and test cycle.

An initial set of candidate solutions, called a generation, is created. This is normally done randomly. New solutions are then generated from the current ones by the application of a set of operators on the chromosomes. These operators are called genetic operators and simulate genetic reproduction in the evolutionary theories in biology. New solutions are then tested with fitness functions and the best of these are selected for reproduction.

Traditionally, the evolutionary algorithms contain four types of algorithm: Genetic Algorithms

(GAs) [182], Genetic Programming (GP) [183], Evolutionary Strategies (ES) [184], and Evolutionary Programming (EP) [185]. The main differences between these are in the way that the chromosomes are represented and the methods used for reproduction. The chromosomes are represented in ES and EP as vectors of real numbers, whilst the chromosomes are represented usually in GA as a fixed length binary string and in GP as a LISP expression that is translated graphically into a tree. The common reproduction methods are based on mutation and cross-over operators which are defined differently in each algorithm. These operators are applied to the candidate solutions directly which limits the algorithms' performance. For example, in GP many syntactically invalid structures are produced which wastes valuable computational resources.

Gene Expression Programming (GEP) [186] is a new type of evolutionary algorithm which overcomes some of the limitations of GA and GP. GEP works with two entities called the chromosome and the expression tree. The chromosome encodes the candidate solution which is translated into the expression tree. The expression tree is the actual candidate solution. The process of translating the chromosome into an expression tree can be seen as being analogous with the expression of biological genes encoded in DNA into proteins. The genetic operators are applied to the chromosomes and not directly to the candidate solutions. The combination of the reproduction process with the process by which the chromosomes are translated into expression trees enables the unconstrained genetic modifications whilst only producing valid expression trees. It has been shown in previous studies [187] that these characteristics enable GEP to outperform GP by 2 to 4 orders of magnitude in terms of the convergence speed in benchmark classification and symbolic regression problems.

A number of fields have started to utilise GEP for a number of applications. More information can be found in the papers referenced in [181].

9.2 Gene Expression Programmig

9.2.1 Algorithm

The first and most difficult steps in GEP or in any EA are the definition of the problem, the encoding of the candidate solution and the definition of a suitable fitness function. The encoding and fitness functions are specific to the individual problem and should be tailored to suit. In order for a successful outcome it is important that the right choices are made. To make these decisions knowledge about the problem and its expected solution should be utilised.

The next stage is the running of the GEP algorithm itself. A basic flowchart representation of the GEP algorithm is shown in Figure 9.1.

The process begins with the random creation of an initial population of chromosomes. Each of these

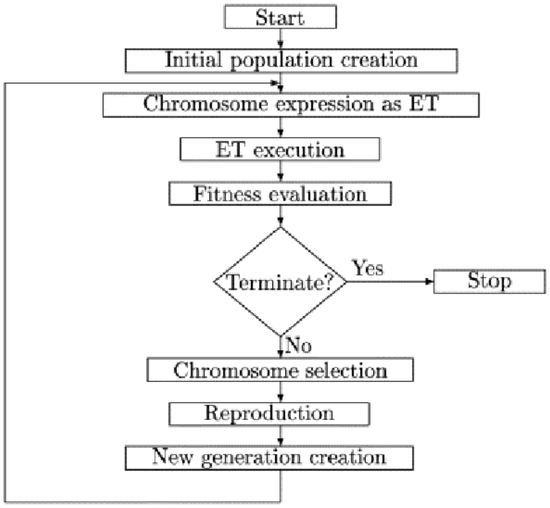

Figure 9.1: Basic GEP algorithm. [181]

chromosomes are translated into expression trees and then into a mathematical expressions which are executed. For each chromosome the fitness function is evaluated and the its fitness is determined. These fitnesses are checked against the termination criterion to verify if a solution of the required quality was found or a set number of iterations had been run. If the termination criterion is not met then some of the chromosomes are selected and allowed to reproduce. This results in a new population of chromosomes which replaces the old generation. This process continues until the termination criteria is met. The chromosome with the best fitness is then decoded to produce the optimal solution to the problem developed by the algorithm.

9.2.2 Chromosome encoding

To represent a candidate solution, GEP works with two entities: the chromosome and the expression tree (ET).

The chromosome is a list of functions and terminals (constants and variables) which are organised in one or more genes of equal length. The functions and variables are input information whilst the constants are created by the algorithm in a user defined range. Each gene consists of a head made up of functions and terminals and a tail composed entirely of terminals. The length of the head (h) is an input parameter whilst the length of the tail is given by:

$$t = h(n-1) + 1 \tag{9.1}$$

where n is the largest number of arguments taken by any of the functions used in the gene's head.

The organisation of the gene in to a head and a tail ensures that each function within a gene has the requisite number of terminals available and therefore ensures that each expression has the correct syntax.

Each of a chromosome's genes is translated (decoded) into an expression tree with the following rules:

- the first element of the gene is placed on the first line of the expression tree and this constitutes its root.
- a number of elements that is equal to the number of arguments of the functions on the previous line are placed on each new line of the ET,
- the process is repeated until a line is formed that contains only terminals.

In the reverse process, the encoding of an ET tree into a gene the ET is read from left to right and from top to bottom.

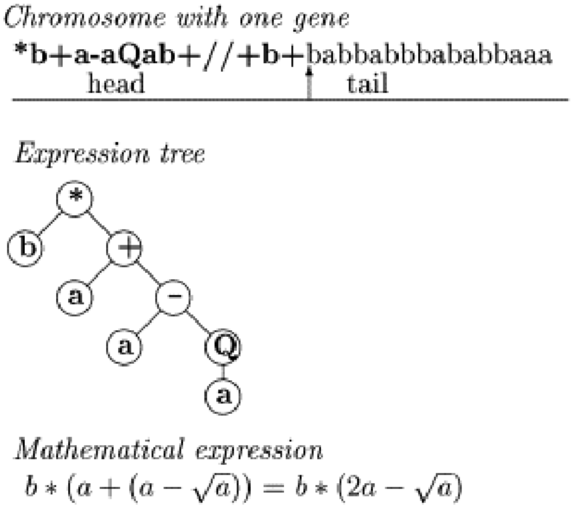

Figure 9.2: Unigenic chromosome, the decoded expression tree and its corresponding mathematical expression. [181]

An example of a chromosome with a head length equal to 15 constructed from five functions Q, /, *, +, and - (where Q is the square root function) and two terminals a and b is displayed in Figure 9.2 along with its encoded ET and the corresponding mathematical expression.

It can be seen that the ET ends before the end of the gene. This shows that genes in GEP can have regions which are not expressed, this mirrors the situation with biological genes which can have regions that are not expressed by proteins. This additional information that is encoded within a gene is used whenever it is needed in the process of genetic variation in order to ensure that the created expression trees are syntactically correct.

When a chromosome consists of more than one gene, the ETs that correspond to individual genes are connected with a user defined linking function. The candidate solution to the problem is the mathematical function associated with these combined ETs.

9.2.3 Reproduction

The chromosomes reproduce through two mechanisms: elitism and reproduction with modification.

Elitism is the process by which the chromosome with the best fitness is replicated unchanged into the next generation, which preserves the best genetic material from one generation to the next.

Reproduction with modification is the process by which the chromosomes are selected and modified using genetic operators to produce new chromosomes. In GEP the genetic operators are applied to chromosomes and not to the ET, which is done in GP. This feature along with the head-tail description of the genes enables the GEP algorithm to always produce structure that are syntactically correct during the process of evolution.

The selection of chromosomes for reproduction is carried out using the roulette-wheel method [188]. In which the individual candidate solutions are mapped to contiguous segments of a line, such that each individual's segment is equal in size to its fitness. A random number is generated and the individual whose segment spans the random number is selected. This process is repeated until the desired number of candidates are obtained. This method makes

In contrast to GA and GP which mainly use recombination and mutation operators, GEP uses three classes of genetic operators for reproduction with modification: mutation, transposition and recombination [186].

The mutation operator randomly changes one element in a chromosome into another element, whilst preserving the rule that the tails can contain only terminals. In the head of a gene a function can be replaced with another function or terminal and vice versa. In the tail a terminal can only be replaced with another terminal.

The transposition operator moves randomly one part of a chromosome to another location within the same chromosome. GEP has three different types of transposable elements:

- short fragments with either a function or a terminal are transposed into the head of genes, except at the root. A sequence containing the same number of elements is deleted from the end of the gene's head to maintain the organisation of the structure of the gene.
- short fragments with a function in the first position are transposed to the root of the gene. A

sequence containing the same number of elements is deleted from the end of the gene's head.

- an entire gene is transposed to the beginning of the chromosome.

The recombination or cross-over operator exchanges parts of a pair of randomly chosen chromosomes. In GEP there are three different types of recombination:

- one-point recombination in which the two parent chromosomes are paired and split after the same point. The material after the recombination point is exchanged between the two chromosomes to form two daughter chromosomes.
- two-point recombination in which two parent chromosomes are paired and two points are chosen randomly and the chromosomes are split at these points. The material between these two points is swapped between the two chromosomes creating two new daughter chromosomes.
- gene recombination in which entire genes are swapped between two chromosomes.

The probability with which each genetic operator is applied to a population of chromosomes is called the operator rate. The values of the operator rates are chosen and optimised by the user. Mutation is the most powerful of the operators and creates diversity within the population. The mutation operator rate which is defined as the probability of mutating each element of the population is recommended to be set at low values (0.01-0.1) [187]. The transposition operator creates additional diversity whilst the recombination operator has a homogeneous effect. The transposition and recombination rates are defined as the probability for each chromosome within a population to be subjected to the respective operator. For these two operators moderate rates are recommended(0.1-0.4) [187].

9.3 Method

GEP was applied to an event selection problem using a supervised statistical learning approach. The GEP algorithm was used to extract the selection criteria for the separation of signal from background in samples of training data in which the classification of each event was known. The extracted selection criteria were tested on similar independent data samples to check how applicable the solution was in the general case. The classifications of events provided by these selection criteria were then compared with the known classifications.

The performance of the GEP algorithm for the solution of this problem was analysed in terms of the classification accuracy that was obtained with the developed selection rules. Other quantities which were also used to analyse the performance of the GEP algorithm were the signal efficiency, background rejection, the signal significance and the purity of the data sample. These quantities were defined as follows:

- classification accuracy (A_{cc}) — ratio of the total number of signal and background K_S^0 candidates correctly classified to the total number of candidates in the data sample.
- signal efficiency (ϵ_S) — ratio of the total number of K_S^0 candidates classified correctly as signal to the total number of signal candidates in the sample.
- background rejection (ϵ_B) — ratio of the number of K_S^0 candidates correctly classified as background to the number of background K_S^0 candidates in the sample.
- purity of the data sample (P) — ratio of the number of K_S^0 candidates classified correctly as signal to the total number of K_S^0 candidates classified as signal.
- signal significance (S_{Sig}) — ratio of the number of K_S^0 candidates classified correctly as signal to the square root of the total number of K_S^0 candidates classified as signal. This is the same quantity which was used for optimisation in the K_S^0 and K^{*-} selection studies in Section 5.2 and Section 5.3.

The statistical errors associated with these quantities except the signal significance were calculated using the formula:

$$\Delta\epsilon = \sqrt{\frac{\epsilon(1-\epsilon)}{N}} \tag{9.2}$$

where ϵ was A_{cc}, ϵ_S, ϵ_B, P, and N was the total number of the corresponding type of candidates in the data sample. This was the total number of K_S^0 candidates for A_{cc}, the total number of signal K_S^0 candidates for ϵ_S, the total number of background candidates for ϵ_B and the total number of K_S^0 candidates classified as signal for P.

The statistical error associated with the signal significance was calculated using the formula, which can be derived from the formula above:

$$\Delta S_{Sig} = \sqrt{P(1-\epsilon)} \tag{9.3}$$

The data samples used were from the same Monte Carlo simulated events as presented in Table 4.3. The classification problem to be solved was the separation of signal K_S^0 candidates from background in $K_S^0 \to \pi^+\pi^-$ decays.

This process was chosen because it is well understood both theoretically and experimentally and also well modelled in the Monte Carlo simulation. It provided a moderately complicated event selection problem to evaluate the performance of the GEP algorithm.

For each K_S^0 candidate used for K_S^0 selection were $DOCA_{\pi^+\pi^-}$, R_Z, R_{XY}, $|\cos\theta^{\pi^+}_{Helicity}|$, SFL and F_{Sig}.

The GEP implementation within the software package APS 3.0 (Automatic Problem Solver) [189] was used. APS is a Windows based commercial software suite for function finding, classification and time series analysis using GEP. This was the only software implementation that was available at the time of this study. This software was only capable of processing a maximum of 5000 data instances which constrained the analysis to use data samples for training and testing with that number of events or K_S^0 candidates. The input information to the GEP algorithm was the variables for K_S^0 selection detailed earlier together with the set of mathematical functions listed in Tables 9.1 and 9.2. The GEP chromosomes were constructed with these variables and floating point constants in the range between -10 and 10 which were given as the input to the algorithm.

Table 9.1: GEP input functions — Set 1

Function	Definition
AND1	if $x < 0$ AND $y < 0$ then 1 else 0
AND2	if $x \geq 0$ AND $y \geq 0$ then 1 else 0
OR1	if $x < 0$ OR $y < 0$ then 1 else 0
OR2	if $x \geq 0$ OR $y \geq 0$ then 1 else 0
IFB1	if $x < y$ then 1 else 0
IFB2	if $x > y$ then 1 else 0
IFB3	if $x \leq y$ then 1 else 0
IFB4	if $x \leq y$ then 1 else 0
IFB5	if $x = y$ then 1 else 0
IFB6	if $x \neq y$ then 1 else 0

Table 9.2: GEP input functions — Set 2

Functions
+,-,×,/
<,>,≤, ≥
=,≠
Pow, Pow10
Sqrt, Inv
Ln, Log, Exp
Abs, Neg, Mod
Sin, Cos, Tan
Asin, Acos, Atan

Other input parameters to the GEP analysis were: the length of the gene head which was varied between 1 and 20, the number of chromosomes per generation was 100 and the maximum number of generations was varied between 3000 and 20000 depending on the chromosomes' complexity. The genetic operator rates were kept at the values recommended in [187] with rates of 0.044 for mutation, 0.3 for transposition and 0.1 for recombination.

The fitness function used in the GEP analysis was the number of hits which was the number of candidates correctly identified as either signal or background. Whilst other fitness functions such as the purity or the signal significance may have been more interesting, the number of hits was the only fitness function suitable for the problem that was implemented in the APS 3.0 software [189].

9.4 Analysis

Two analyses were performed with two sets of input functions on datasets with the signal to background ratio set to 0.25, 1 and 5.

9.4.1 GEP analysis with 10 input functions

In this analysis the ten logical functions listed in Table 9.1 were used as input information for the GEP algorithm, along with the variables and constant range detailed in the previous section.

The initial unigenic chromosomes were filled randomly with the functions, variables and constants from the from the input information. The chromosomes were evolved through a number of generations until the search process converged. The convergence of the search process was indicated by a plateau in the distribution of the fitness of the best individual within a generation plotted as a function of the number of generations.

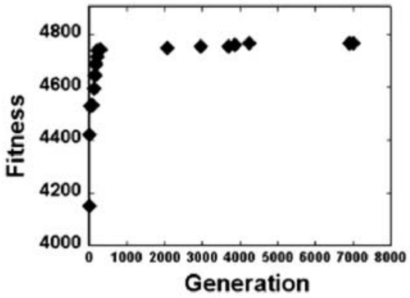

Figure 9.3: Fitness function of the best individual per generation as a function of the number of generations with the length of the gene head equal to 10 using the training dataset with S/B=0.25.

An example of one such distribution is shown in Figure 9.3 for a chromosome with the length of the gene head equal to ten. In can be seen that a high quality solution is found very early in the process of evolution, in less than 500 generations. The expression tree which is associated with the final solution is shown in Figure 9.4.

Table 9.3 shows the evolution of the solution as the complexity of the chromosomes increased for the dataset with S/B=0.25 along with the training and test classification accuracies along with their associated statistical errors.

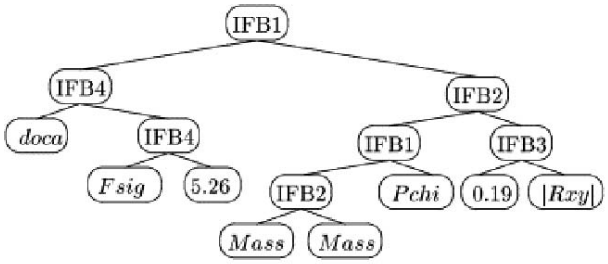

Figure 9.4: Expression tree corresponding to the solution found with a gene with head length equal to 10 using the set of 10 input functions.

Table 9.3: GEP classification criteria and classification accuracies for the datasets with S/B=0.25 with the 10 input functions in Set 1.

Head	Selection criteria	Training	Test
1	$F_{Sig} > 9.93$	83.34 ± 0.53	83.06 ± 0.53
2	$F_{Sig} > 8.80$, $DOCA_{\pi\pi} < 1$	90.76 ± 0.41	91.40 ± 0.40
3	$F_{Sig} > 3.67$, $R_{XY} \leq P(\chi^2)$	94.88 ± 0.31	94.76 ± 0.32
4	$F_{Sig} > 3.67$, $R_{XY} \leq P\chi^2$	94.88 ± 0.31	94.76 ± 0.32
5	$F_{Sig} > 3.63$, $\lvert R_{XY}\rvert \leq 2.65$, $R_{XY} < P(\chi^2)$	95.04 ± 0.31	94.80 ± 0.31
7	$F_{Sig} > 3.64$, $R_{XY} < P(\chi^2)$, $P(\chi^2) > 0$	95.04 ± 0.31	94.90 ± 0.31
10	$F_{Sig} > 5.26$, $R_{XY} < 0.19$, $DOCA_{\pi^+\pi^-} < 1$, $P_{\chi^2} > 0$	95.36 ± 0.30	95.20 ± 0.30
20	$F_{Sig} > 4.10$, $R_{XY} < 0.20$, $P(\chi^2) > 0$, $SFL > 0.20$, $DOCA_{\pi\pi} > 0$, $R_{XY} > Mass$	95.40 ± 0.30	95.28 ± 0.30

The highest classification accuracy was obtained with a chromosome with the length of the gene head equal to 20. The effect of each component cut within the corresponding selection criteria is shown in Table 9.4 which contains the purity of the data sample, the signal efficiency, the background rejection, the classification accuracy after the selection criteria have been applied one after the other on the training data sample with $S/B = 0.25$. The corresponding statistical errors were also reported.

Table 9.4: Table showing the K_S selection efficiency using GEP, Data S/N=0.25

Cut	P %	ϵ_S %	ϵ_B %	A_{CC} %	S_{Sig}
No Cut	20.00 ± 0.06	100.00	0.00	20.00 ± 0.06	14.12 ± 0.16
$F_{Sig} \geq 4.1$	52.60 ± 1.19	92.72 ± 0.82	79.03 ± 0.64	81.78 ± 0.55	37.19 ± 0.25
$F_{Sig} \geq 4.1$, $R_{XY} < 0.2cm$	80.38 ± 1.20	88.24 ± 1.02	94.59 ± 0.36	93.32 ± 0.35	56.84 ± 0.16
$F_{Sig} \geq 4.1$, $R_{XY} < 0.2cm$, $P(\chi^2) > 0$	89.02 ± 1.00	86.54 ± 1.08	97.32 ± 0.26	95.16 ± 0.30	62.95 ± 0.10
$F_{Sig} \geq 4.1$, $SFL > 0.2cm$, $R_{XY} < 0.2cm$, $P(\chi^2) > 0$	90.01 ± 0.98	85.44 ± 1.11	97.90 ± 0.23	95.40 ± 0.30	63.65 ± 0.09
$F_{Sig} \geq 4.1$, $SFL > 0.2cm$, $R_{XY} < 0.2cm$, $P(\chi^2) > 0$, $DOCA > 0$	90.01 ± 0.98	85.44 ± 1.11	97.90 ± 0.23	95.40 ± 0.30	63.65 ± 0.09
$F_{Sig} \geq 4.1$, $SFL > 0.2cm$, $R_{XY} < 0.2cm$, $P(\chi^2) > 0$, $DOCA > 0$, $R_{XY} < Mass$	90.01 ± 0.98	85.44 ± 1.11	97.90 ± 0.23	95.40 ± 0.30	63.65 ± 0.09

The last two of the selection rules, $DOCA > 0$ and $R_{XY} < Mass$ did not have any influence on the selection, as they were satisfied always. They were found early in the selection process and were superseded later by more powerful selection rules. For example the rule $R_{XY} < Mass$ was superseded by the rule $R_{XY} < 0.2$ which was found later in the selection process. This was always true because $Mass > 0.2$ of the K_S^0 candidates in the sample. This is a case of computer science imitating biology.

It can also be seen that GEP found alternative powerful selection rules, such as $R_{XY} < P(\chi^2)$, which produced high quality results. This can be seen in Table 9.3 for the results with the length of the gene head equal to 5 and 7. Although these cuts do not have a physics interpretation and may not be useful for the analysis of K_S^0 decays in this study, the ability of the algorithm to find alternative correlations between the variables could Selection rules such as this define volumes in the multidimensional phase space of the input variables which provide good separation between signal and background candidates.

The four most powerful cuts developed by the GEP algorithm, those on F_{Sig}, R_{XY}, $P(\chi 2)$ and SFL, were similar to those used in standard cut based analyses such as the one presented in this thesis. However, the K^0_S selection study described in Section 5.2 differed in three important aspects. Firstly, the signal to background ratio was equal 0.181 in the K^0_S selection study compared with $S/B = 0.25$ in the GEP analysis. Secondly, the GEP analysis used the classification accuracy as its fitness function whilst the study in Section 5.2 used the signal significance. Finally, the numbers of signal and background candidates were obtained from a χ^2 fit in Section 5.2 as opposed to the Monte Carlo truth information used in the GEP analysis. Hence, whilst the optimised cut values presented in Section 5.2 were similar to those found in the GEP analysis they were not directly comparable.

Two manual optimisation studies were performed: one optimised the signal significance, and the other optimised the classification accuracy. These studies were performed on a Monte Carlo simulated data sample containing 500,000 K^0_S candidates with a signal to background ratio of 0.25. The numbers of signal and background candidates were determined using the truth information in the Monte Carlo simulated data. In both manual optimisation studies, cuts on each selection variable were applied one after the next until the values of the cuts stabilised.

The results of the optimisation of the signal significance are presented in Figure 9.5 and Table 9.5. Figure 9.5 shows the signal significance as a function of the value of the cut variable being optimised. The arrow on each plot indicates the value of the cut which gave the highest signal significance. Table 9.5 contains the manually optimised cuts along with the signal purity, the signal efficiency, the background rejection, the classification accuracy and the signal significance after the cuts had been applied one after the other on the data sample.

The results of the optimisation of the classification accuracy are presented in Figure 9.6 and Table 9.6. Figure 9.6 shows the classification accuracy as a function of the value of the cut variable being optimised. The arrow on each plot indicates the value of the cut which gave the highest classification accuracy. Table 9.6 contains the manually optimised cuts along with the signal purity, the signal efficiency, the background rejection, the classification accuracy and the signal significance after the cuts had been applied one after the other on the data sample.

It can be seen that the cuts optimised using the signal significance are similar to those cuts optimised using the classification accuracy. This is good as this means that the GEP algorithm is not handicapped unduly by the choice of fitness function.

The cuts manually optimised using the two fitness functions were very similar to those which were found and optimised by the GEP algorithm. The values of A_{cc}, ϵ_S, ϵ_B, P and S_{Sig} for each of the three studies were also similar in each of three analyses. The additional cuts which were used in the

Table 9.5: Table showing the optimisation of the K_S selection efficiency using the signal significance, Data S/N=0.25, 500k

Cut	Purity %	ϵ_S %	ϵ_B %	A_{CC} %	S_{Sig}
No Cut	20.00 ± 0.06	100.00	0.00	20.00 ± 0.06	141.43 ± 0.40
$F_{Sig} \geq 4$	52.68 ± 0.12	93.04 ± 0.08	79.10 ± 0.06	81.89 ± 0.05	221.38 ± 0.50
$F_{Sig} \geq 4$, $R_{XY} < 0.21cm$	82.03 ± 0.12	88.81 ± 0.10	95.14 ± 0.03	93.87 ± 0.03	269.90 ± 0.38
$F_{Sig} \geq 4$, $R_{XY} < 0.21cm$, $P(\chi^2) \geq 0.001$	90.69 ± 0.09	85.40 ± 0.11	97.81 ± 0.02	95.33 ± 0.03	278.30 ± 0.29
$F_{Sig} \geq 4$, $R_{XY} < 0.21cm$, $P(\chi^2) \geq 0.001$, $SFL > 0cm$	90.81 ± 0.09	85.36 ± 0.11	97.84 ± 0.02	95.34 ± 0.03	278.42 ± 0.28
$F_{Sig} \geq 4$, $R_{XY} < 0.21cm$, $P(\chi^2) \geq 0.001$, $SFL > 0cm$, $\|R_Z\| < 3.2$	91.40 ± 0.09	85.26 ± 0.11	97.99 ± 0.02	95.45 ± 0.03	279.14 ± 0.28
$F_{Sig} \geq 4$, $R_{XY} < 0.21cm$, $P(\chi^2) \geq 0.001$, $SFL > 0cm$, $\|R_Z\| < 3.2$, $DOCA < 2.05cm$	91.66 ± 0.09	85.16 ± 0.11	98.06 ± 0.02	95.48 ± 0.03	279.38 ± 0.28
$F_{Sig} \geq 4$, $R_{XY} < 0.21cm$, $P(\chi^2) \geq 0.001$, $SFL > 0cm$, $\|R_Z\| < 3.2$, $\|\cos\theta^{Helicity}\| < 0.98$, $DOCA < 2.05cm$	92.10 ± 0.09	84.74 ± 0.11	98.18 ± 0.02	95.49 ± 0.03	279.35 ± 0.27

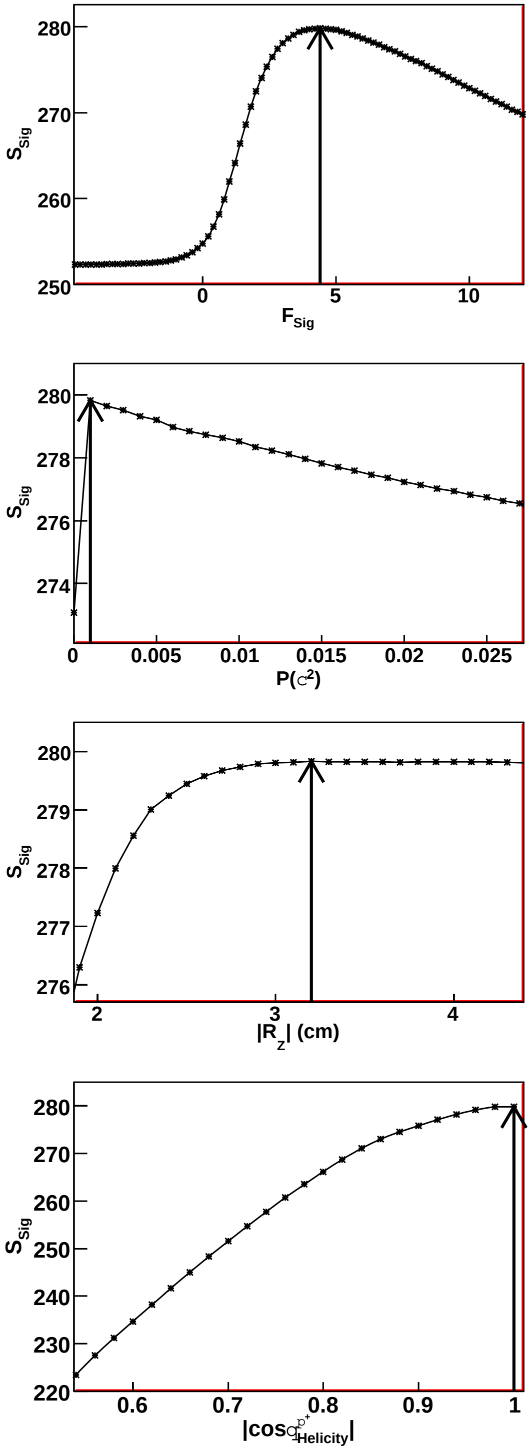

Figure 9.5: Signal significance as a function of the value of the cut applied on $P(\chi^2)$, $DOCA_{K_S^0\pi^-}$, $\pi^\pm$ R_Z, $\pi^\pm$ R_{XY}, R_Z, R_{XY}, $|\cos\theta^{\pi^+}_{Helicity}|$.

Table 9.6: Optimisation of the K_S selection efficiency using the classification efficiency, Data S/N=0.25, 500k

Cut	Purity %	ϵ_S %	ϵ_B %	A_{CC} %	S_{Sig}
No Cut	20.00 ± 0.06	100.00	0.00	20.00 ± 0.06	141.43 ± 0.40
$F_{Sig} \geq 5$	53.70 ± 0.12	91.63 ± 0.09	80.24 ± 0.06	82.52 ± 0.05	221.82 ± 0.50
$F_{Sig} \geq\ 5$, $R_{XY} < 0.21cm$	83.82 ± 0.11	87.51 ± 0.10	95.78 ± 0.03	94.12 ± 0.03	270.83 ± 0.37
$F_{Sig} \geq 5$, $R_{XY} < 0.21cm$, $P(\chi^2) \geq 0.001$,	92.12 ± 0.09	84.15 ± 0.12	98.20 ± 0.03	95.39 ± 0.02	278.43 ± 0.09
$F_{Sig} \geq 5$, $R_{XY} < 0.21cm$, $P(\chi^2) \geq 0.001$, $SFL > 0cm$	92.21 ± 0.09	84.13 ± 0.12	98.22 ± 0.02	95.40 ± 0.03	278.52 ± 0.26
$F_{Sig} \geq 5$, $R_{XY} < 0.21cm$, $P(\chi^2) \geq 0.001$, $SFL > 0cm$, $\lvert R_Z \rvert < 3.2$	92.80 ± 0.09	84.03 ± 0.12	98.37 ± 0.02	95.50 ± 0.03	279.23 ± 0.25
$F_{Sig} \geq 5$, $R_{XY} < 0.21cm$, $P(\chi^2) \geq 0.001$, $SFL > 0cm$, $\lvert R_Z \rvert < 3.2$, $DOCA < 2.05cm$	93.07 ± 0.09	83.93 ± 0.12	98.44 ± 0.02	95.54 ± 0.03	279.48 ± 0.25
$F_{Sig} \geq 5$, $R_{XY} < 0.21cm$, $P(\chi^2) \geq 0.001$, $SFL > 0cm$, $\lvert R_Z \rvert < 3.2$ $\lvert \cos\theta_{Helicity} \rvert < 0.98$, $DOCA < 2.05cm$	93.48 ± 0.09	$83.55 \pm 0.12\%$	98.54 ± 0.02	$95.54 \pm 0.03\%$	279.46 ± 0.25

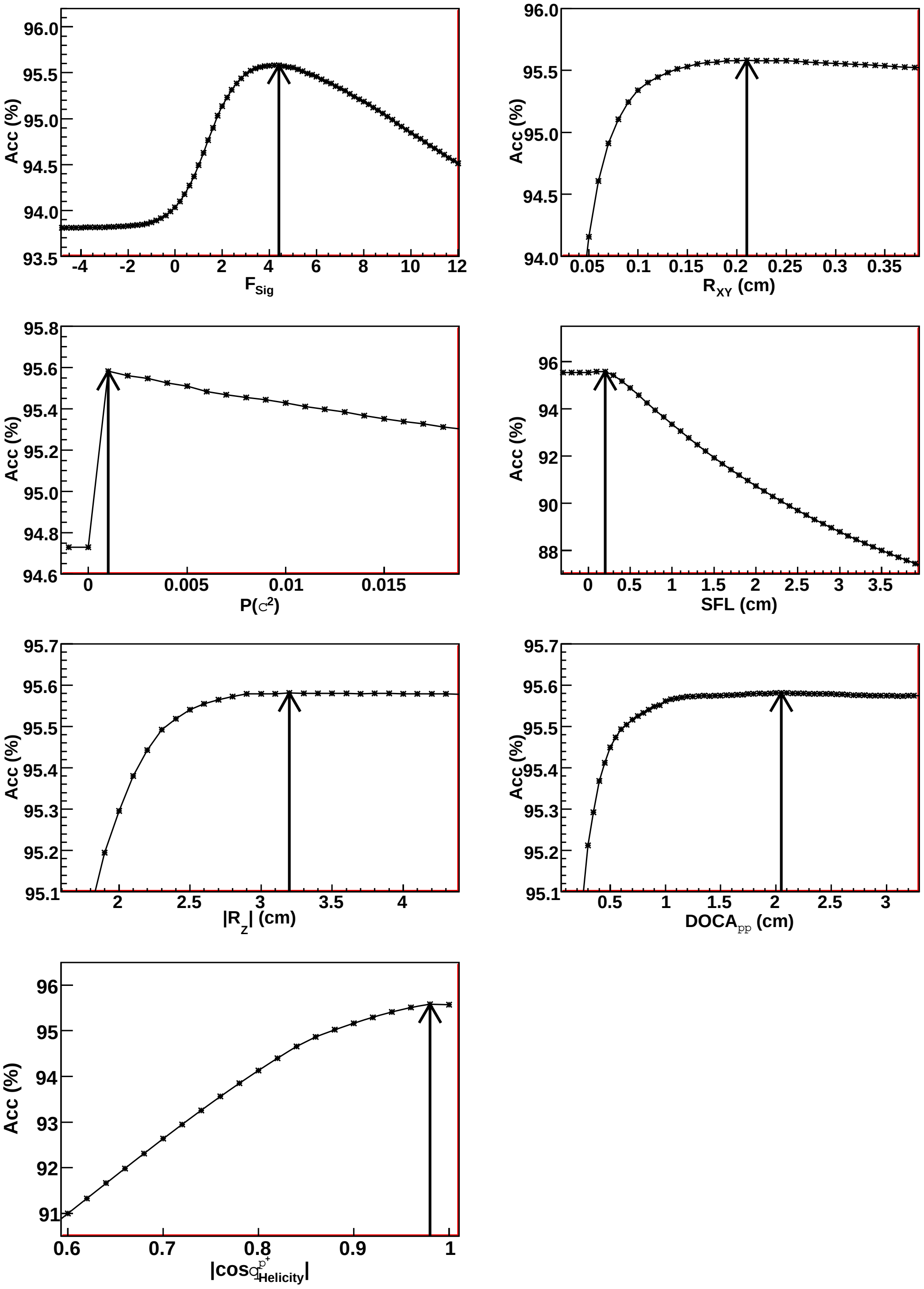

Figure 9.6: Classification accuracy as a function of the value of the cut applied on $P(\chi^2)$, $DOCA_{K^0_S\pi^-}$, $\pi^\pm\ R_Z$, $\pi^\pm\ R_{XY}$, $|R_Z|$, R_{XY}, $|\cos\theta^{\pi^+}_{Helicity}|$.

two manual optimisations, those on R_Z, $DOCA_{\pi\pi}$ and $|\cos\theta^{\pi^+}_{Helicity}|$, only improved the classification accuracy by 0.14% compared with the results achieved with only the four most powerful cuts found in the manual optimisation. This additional improvement to the classification accuracy was not achieved by the GEP analysis, which was probably mostly due to the lower statistics.

A second independent sample of another 500,000 K^0_S candidates with a signal to background ratio of 0.25 was used for a direct comparison of the manually optimised cuts with those developed by the GEP algorithm. The cuts were applied to this sample. The values obtained for the purity of the data sample, signal efficiency, background rejection, classification accuracy and signal significance are displayed in Table 9.7. Slightly higher classification accuracies and signal significances were obtained with the manually optimised cuts. The difference in the classification accuracy was about 0.5% . The background rejections and the sample purities achieved were higher with the manually optimised cuts.

Table 9.7: GEP and standard cuts applied to a test data sample of 500,000 events

Cut	P %	ϵ_S %	ϵ_B %	A_{CC} %	S_{Sig}
Manual analysis(S_{Sig}) $F_{Sig} \geq 4.4$, $R_{XY} < 0.23cm$, $P(\chi^2) \geq 0.001$, $SFL > 0.1cm$	91.48 ± 0.09	84.78 ± 0.11	98.03 ± 0.02	95.38 ± 0.03	278.49 ± 0.28
Manual analysis(S_{Sig}) $F_{Sig} \geq 4.4$, $R_{XY} < 0.23cm$, $P(\chi^2) \geq 0.001$, $SFL > 0.1cm$, $\lvert R_Z \rvert < 3.2$, $\lvert \cos\theta^{Helicity} \rvert < 0.98$, $DOCA < 2.00cm$	92.43 ± 0.09	84.55 ± 0.11	98.27 ± 0.02	95.52 ± 0.03	279.55 ± 0.26
Manual analysis(A_{CC}) $F_{Sig} \geq 4.4$, $R_{XY} < 0.21cm$, $P(\chi^2) \geq 0.001$, $SFL > 0.2cm$	92.22 ± 0.09	83.87 ± 0.12	98.23 ± 0.02	95.36 ± 0.03	278.11 ± 0.27
Manual analysis(A_{CC}) $F_{Sig} \geq 4.4$, $R_{XY} < 0.21cm$, $P(\chi^2) \geq 0.001$, $SFL > 0.2cm$, $\lvert R_Z \rvert < 3.2$ $\lvert \cos\theta_{Helicity} \rvert < 0.98$, $DOCA < 2.05cm$	93.51 ± 0.08	83.22 ± 0.12	98.56 ± 0.02	95.49 ± 0.03	278.92 ± 0.25
GEP analysis $F_{Sig} \geq 4.1$, $SFL > 0.2cm$, $R_{XY} < 0.2cm$, $P(\chi^2) > 0$, $DOCA > 0$, $R_{XY} < Mass$	88.31 ± 0.10	86.39 ± 0.11	97.14 ± 0.03	94.99 ± 0.03	276.20 ± 0.32

The overall similarity of the results proves that the GEP algorithm worked correctly finding automatically powerful selection criteria that separated the signal and background well. This is a remarkable result for GEP, taking into account that the only inputs it used were a list of functions and variables, without any physics knowledge about the process. Studies with higher statistics are required to evaluate the full potential of the GEP algorithm.

The GEP analysis was also performed on data samples with $S/B = 1$ and 5. The results are summarised in Table 9.8 which contains the classification accuracies with their statistical errors obtained with the selection rules found by GEP with the gene head length varying between 1 and 20. Figure 9.7 shows the classification accuracy as a function of the length of the gene head for all of the training and test datasets analysed.

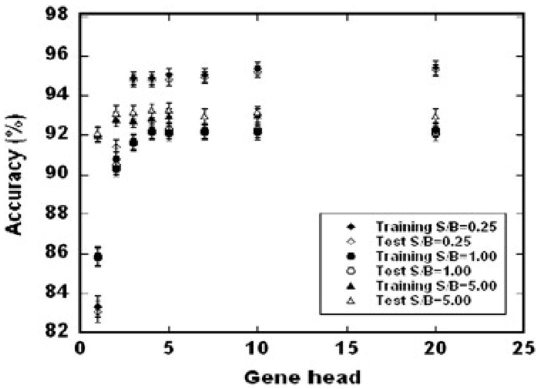

Figure 9.7: Classification accuracy as a function of the length of the gene head for the training (full symbols) and test (open symbols)data samples with S/B =0.25, 1, 5(Set 1 and Set 2 input functions).

Table 9.8: Optimisation of the K_S selection efficiency using the signal significance, Data S/N=0.25, 500k

Head	A_{cc} (%)			
	$S/B = 1$		$S/B = 5$	
	Training	Test	Training	Test
1	85.82 ± 0.49	85.88 ± 0.49	91.98 ± 0.38	92.08 ± 0.38
2	90.32 ± 0.42	90.44 ± 0.42	92.80 ± 0.36	93.12 ± 0.36
3	91.66 ± 0.39	91.60 ± 0.39	92.76 ± 0.37	93.14 ± 0.36
4	92.22 ± 0.38	92.18 ± 0.38	92.84 ± 0.36	93.26 ± 0.35
5	92.10 ± 0.38	92.24 ± 0.38	92.96 ± 0.36	93.28 ± 0.35
7	92.22 ± 0.38	92.16 ± 0.38	92.96 ± 0.36	92.96 ± 0.36
10	92.14 ± 0.38	92.18 ± 0.38	92.98 ± 0.36	93.18 ± 0.36
20	92.28 ± 0.38	92.12 ± 0.38	92.96 ± 0.36	92.96 ± 0.36

The classification accuracy obtained was high, over 90%, for almost all cases. Its values in the test dataset followed closely the values obtained on the the training data, being equal within the limit of the statistical errors. This indicated a high generalisation power of the solutions.

For most of the configurations the central value of the classification accuracy was slightly higher in the training dataset than in the test dataset. For some configurations with (S/B=1 and 5) the situation was reversed. However, within the statistical errors the two classification accuracies were equal.

In order to check that the search process used by the GEP algorithm was not trapped at a local optimum, for each chromosome configuration the analysis was repeated ten times with identical input information (input functions and parameters in addition to the input data), and the average and standard deviations of the classification accuracies were calculated and presented in Figure 9.9 (the statistical errors associated with the limited data sample were not included). The variations from one run to the next were due to the stochastic character of the algorithm (random creation of the initial population, probabilistic character of the genetic operators and the selection method). The values of the variations were under 1% which indicates that the algorithm converged towards similar solutions each time the analysis was repeated.

Table 9.9: Classification accuracy of solutions found by GEP for training and test datasets with S/B=0.25,1 and 5, using Set 1 of input functions and averaging over 10 identical runs.

Head	A_{cc} (%)					
	S/B=0.25		S/B=1		S/B=5	
	Training	Test	Training	Test	Training	Test
1	83.34 ± 0.00	83.06 ± 0.00	85.81 ± 0.01	85.83 ± 0.03	91.99 ± 0.02	92.05 ± 0.02
2	90.93 ± 0.12	91.37 ± 0.11	90.18 ± 0.19	90.62 ± 0.31	92.47 ± 0.40	92.71 ± 0.54
3	94.87 ± 0.01	94.76 ± 0.03	90.88 ± 0.66	91.45 ± 0.26	92.46 ± 0.23	92.49 ± 0.33
4	94.87 ± 0.01	94.75 ± 0.08	91.38 ± 0.82	91.74 ± 0.47	92.72 ± 0.25	93.04 ± 0.34
5	94.94 ± 0.07	94.81 ± 0.09	91.65 ± 0.24	91.91 ± 0.27	92.86 ± 0.09	93.22 ± 0.12
7	95.00 ± 0.06	94.88 ± 0.10	91.88 ± 0.33	92.20 ± 0.09	92.89 ± 0.08	93.11 ± 0.10
10	94.96 ± 0.33	94.89 ± 0.39	91.86 ± 0.18	92.21 ± 0.08	92.90 ± 0.08	93.21 ± 0.04
20	95.11 ± 0.18	94.98 ± 0.17	91.89 ± 0.75	91.92 ± 0.98	92.90 ± 0.08	93.20 ± 0.09

9.4.2 GEP analysis with 36 input functions

The GEP analysis described in Section 9.4.1 was repeated with the 36 mathematical input functions that are listed in Table 9.1 and Table 9.2.

An example of a solution found in this case is shown in Figure 9.8 for a unigenic chromosome with the length of the gene's head equal to 10 on the training dataset with $S/B = 0.25$. The classification accuracies obtained with all chromosome configurations and all training and test datasets are summarised in Table 9.10 and plotted in Figure 9.9 together with the associated statistical errors.

The solutions found by the GEP algorithm in this case were more complex, with combinations of mathematical and logical functions. However, the classification accuracies were not improved significantly with these solutions over those found with the logical functions. The best solutions are developed by the GEP algorithm with the logical functions, while the addition of the mathematical functions creates inactive regions in the solutions, making them larger but not significantly better.

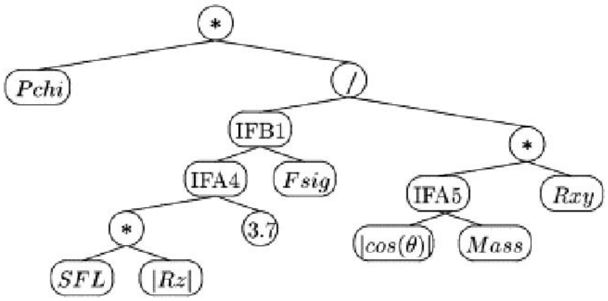

Figure 9.8: Expression tree corresponding to the solution found with a gene with head length equal to 10 using Set 1 and Set 2 input functions. ($S/B = 0.25$ training dataset)

Table 9.10: Classification accuracy of solutions found by GEP for training and test datasets with S/B=0.25,1 and 5, using Sets 1 and 2 of input functions

Head	A_{cc} (%)					
	$S/B = 0.25$		S/B=1		S/B=5	
	Training	Test	Training	Test	Training	Test
1	89.60 ± 0.43	88.80 ± 0.45	87.12 ± 0.47	86.94 ± 0.48	91.98 ± 0.38	92.10 ± 0.38
2	93.58 ± 0.35	93.10 ± 0.36	90.32 ± 0.42	89.98 ± 0.43	92.92 ± 0.36	93.30 ± 0.35
3	94.90 ± 0.31	94.82 ± 0.31	90.22 ± 0.42	90.02 ± 0.42	92.98 ± 0.36	93.32 ± 0.35
4	95.36 ± 0.30	95.32 ± 0.30	91.22 ± 0.40	90.90 ± 0.41	92.98 ± 0.36	93.32 ± 0.35
5	95.18 ± 0.30	94.84 ± 0.31	91.44 ± 0.40	90.94 ± 0.41	93.12 ± 0.35	93.46 ± 0.35
7	95.32 ± 0.30	95.18 ± 0.30	92.10 ± 0.38	92.12 ± 0.38	93.12 ± 0.36	93.34 ± 0.35
10	95.34 ± 0.30	94.72 ± 0.32	92.42 ± 0.37	92.32 ± 0.38	93.12 ± 0.36	93.30 ± 0.35
20	95.54 ± 0.29	95.40 ± 0.30	92.56 ± 0.37	92.26 ± 0.38	93.28 ± 0.35	93.20 ± 0.36

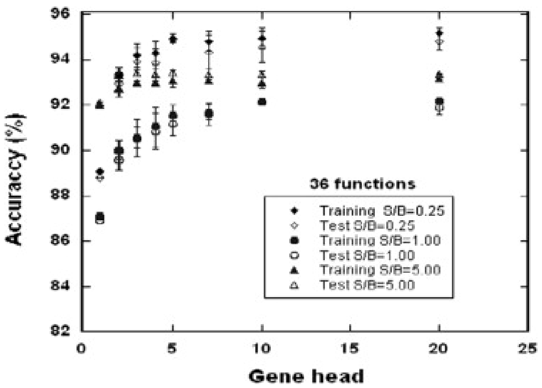

Figure 9.9: Classification accuracy as a function of the length of the gene head for the training (full symbols) and test (open symbols)data samples with S/B =0.25, 1, 5(Set 1 and Set 2 input functions).

Within the limits of the errors, similar classification accuracies were obtained on the training and test datasets which indicated that these more complex solutions also have a good generalisation power. This suggests that the inactive regions within the solutions did not affect their generalisation power.

The convergence of the solutions was tested by the repetition of the GEP analyses with identical input information. The average values and the standard deviations of the classification efficiencies for each configuration are presented in Table 9.11. (statistical errors associated with limited size of the input data samples were not included.

Table 9.11: Classification accuracy of solutions found by GEP for training and test datasets with S/B=0.25,1 and 5, using Sets 1 and 2 of input functions and averaging over 10 identical runs

Head	A_{cc} (%)					
	S/B=0.25		S/B=1		S/B=5	
	Training	Test	Training	Test	Training	Test
1	89.11 ± 0.16	88.80 ± 0.00	87.12 ± 0.00	86.94 ± 0.00	91.98 ± 0.01	92.06 ± 0.02
2	93.29 ± 0.51	92.96 ± 0.22	89.94 ± 0.45	89.48 ± 0.58	92.61 ± 0.30	93.02 ± 0.44
3	94.30 ± 0.50	94.08 ± 0.62	90.82 ± 0.74	90.54 ± 0.83	92.94 ± 0.04	93.39 ± 0.08
4	94.46 ± 0.46	94.10 ± 0.67	91.07 ± 0.71	90.82 ± 0.82	92.96 ± 0.01	93.31 ± 0.08
5	94.62 ± 0.49	94.44 ± 0.64	91.57 ± 0.41	91.46 ± 0.53	93.03 ± 0.11	93.42 ± 0.10
7	94.83 ± 0.41	94.65 ± 0.62	91.63 ± 0.52	91.69 ± 0.52	93.16 ± 0.28	93.36 ± 0.09
10	94.95 ± 0.41	94.64 ± 0.51	92.22 ± 0.30	92.08 ± 0.42	93.06 ± 0.07	93.28 ± 0.14
20	95.33 ± 0.23	95.16 ± 0.22	92.23 ± 0.18	92.02 ± 0.60	93.20 ± 0.11	93.37 ± 0.13

9.5 Summary

The suitability of an alternative method of event selection was analysed. Gene Expression Programming, a recently developed evolutionary algorithm was applied to find selection criteria for the selection of K_S^0 signal candidates decaying to $\pi^+ \pi^-$ from the background candidates produced in the Monte Carlo simulation.

To search for the optimal selection criteria, the GEP algorithm used a list of event variables and a list of mathematical functions as the input information, and the classification accuracy was used as the fitness function to guide the selection process. With only this information, the algorithm automatically determined and optimised the selection criteria that enabled the signal and background to be separated with classification accuracies in the range 92-95% in datasets with S/B=0.25,1,5.

Using logical input functions, the cut-type selection criteria developed by the algorithm were very similar to those chosen due to physics considerations and manually optimised. The similarity of these selection criteria proved that the algorithm worked correctly.

With the addition of mathematical input functions, more complex selection rules were developed without an improvement in the quality of the selection. This indicated that for the problem studied the logical functions were the optimal input functions from which the algorithm can develop the best solutions.

All of the solutions developed by the algorithm had good generalisation power as on both the training and test data samples the classification accuracies were equal within the statistical errors due to the data samples' limited size. For some configurations the classification accuracies achieved on the test data were higher than on the training data, but the values remained equal within the errors.

The convergence of the GEP algorithm was tested by the repetition of each analysis ten times under identical conditions with identical input data, GEP parameters, and input functions. The classification accuracies varied by under 1% in all cases which indicated that the search process was not trapped at some local optimum.

Chapter 10

Conclusions

The analysis presented in this thesis has described an inclusive search for the $R(3520)$, a possible crypto-exotic state using the data collected with the *BaBar* detector at the asymmetric energy PEP-II e^+e^- collider. The decay modes $p\,\pi^-\,\pi^-\,K^+\,K^0_S$, with $K^0_S \rightarrow \pi^+\pi^-$, and the $p\,\pi^-\,K^+\,K^{*-}$, with $K^{*-} \rightarrow K^0_S\pi^-$ and $K^0_S \rightarrow \pi^+\pi^-$, have been investigated for evidence of $R(3520)$ production in e^+e^- interactions at a centre of mass energy of 10.58 GeV. The data sample used in this search corresponded to the $227.78\,\mathrm{fb}^{-1}$ of data collected in the data collection periods Runs 1-4. The search was also repeated with the additional requirement that each event also contained an additional $\overline{p}$ in order to ensure the conservation of the baryon number.

The invariant mass spectra were analysed and no evidence for the state was observed. Therefore, upper limits were set on the differential cross section for the production of the $R(3520)$ state as a function of the momentum in the centre of mass frame. Using these differential cross sections the total cross sections were calculated with two different hypotheses for the state's width $1\,\mathrm{MeV}/c^2$ and $7\,\mathrm{MeV}/c^2$, with the additional assumption that the momentum spectrum for the production of state were flat. The upper limits for the total cross section production of the $R(3520)$ for the decay mode $p\,\pi^-\,\pi^-\,K^+\,K^0_S$ were calculated to be $32\,\mathrm{fb}/\,\mathrm{GeV}/c$ ($48\,\mathrm{fb}/\,\mathrm{GeV}/c$) with the $1\,\mathrm{MeV}/c^2$ ($7\,\mathrm{MeV}/c^2$) width. For the decay mode $p\,\pi^-\,K^+\,K^{*-}$ the upper limits on the total cross section were $62\,\mathrm{fb}/\,\mathrm{GeV}/c$ ($93\,\mathrm{fb}/\,\mathrm{GeV}/c$) for the $1\,\mathrm{MeV}/c^2$ ($7\,\mathrm{MeV}/c^2$) width hypotheses.

The studies were repeated with the additional requirement that there was an additional antiproton in the event. The invariant mass spectra were analysed and no evidence for the state was found. Therefore, upper limits were calculated on the total and differential cross sections for the production of this state. The upper limits for the total cross section production of the $R(3520)$ for the decay mode $p\,\pi^-\,\pi^-\,K^+\,K^0_S$ were calculated to be $25\,\mathrm{fb}/\,\mathrm{GeV}/c$ ($36\,\mathrm{fb}/\,\mathrm{GeV}/c$) with the $1\,\mathrm{MeV}/c^2$ ($7\,\mathrm{MeV}/c^2$) width. For the decay mode $p\,\pi^-\,K^+\,K^{*-}$ the upper limits on the total cross section were $62\,\mathrm{fb}/\,\mathrm{GeV}/c$

(83 fb/ GeV/c) for the 1 MeV/c^2 (7 MeV/c^2) width hypotheses. This shows that the nonobservance of the state was unaffected by the condition that the baryon number was conserved in the event.

The upper limits on the cross section obtained in this analysis calculated by these analyses are roughly a billion times smaller than the cross section of $14 \pm 3\,\mu$b reported by Karnaukhov et al. [156]. It is difficult to compare the cross sections from the two experiments because of the different production mechanisms. It is likely that the cross section for the production of the $R(3520)$ state may be higher in the π^- p collisions than in the electro-production because the events already contain a baryon. The two experiments could be compared using the ratio of the cross sections of production of the $R(3520)$ state with that of some other state. Cross sections for the production of the Ξ^- and the $\bar{\Xi}^+$ of $17.51 \pm 1.16\,\mu$b and $1.16 \pm 0.67\,\mu$b, respectively were measured in the same bubble chamber experiment which reported the $R(3520)$ state [190]. These cross sections are of the same order of magnitude as that of the $R(3520)$. So one might expect the cross sections for the production to be similar for the Ξ^- and the $R(3520)$ at *BABAR*. Unfortunately, the cross section for the production of the Ξ^- has not been measured at *BABAR* but the observation of 290,000 Ξ^- candidates in 83 fb^{-1} of data suggests that cross sections for the two states differ by at least 2-3 orders of magnitude. This indicates that if the $R(3520)$ state exists then its production at *BABAR* must be very highly suppressed compared with that of other baryons.

There is scope for the improvement of the results produced in this thesis. The dataset used could be enlarged to include the entire dataset collected by the *BABAR* detector. The generation of more Monte Carlo simulated data would reduce the largest systematic in the bins with low $p*$. For the decay mode $p\ \pi^-\ K^+\ K^{*-}$ the extended maximum likelihood fit could be extended to also include a fit of the distribution of the K^{*-} mass. Possibly, the area where there is the greatest potential for improvement is in the removal of the combinatorial background. It is possible that with the application of new analysis techniques such as GEP that progress could be made in this area. However, it is likely that the result of a search with these improvements would be a slightly better negative result.

The question of the existence of the $R(3520)$ could only be proven one way or the other by a high statistics π^- p experiment with more accurate particle identification at a similar energy.

The results presented here should be considered preliminary as the official review by the *BABAR* collaboration has not taken place yet. The results will be submitted for review following the submission of this thesis.

In addition, the suitability of an alternative method of event selection was analysed. Gene Expression Programming, a recently developed evolutionary algorithm was applied to find selection criteria for the selection of K^0_S signal candidates decaying to π^+ π^- from background candidates produced in the Monte Carlo simulation.

The inputs for the GEP algorithm were a list of variables for each K_S^0 candidate and a list of mathematical functions, and the classification accuracy as the fitness function used to guide the search for the optimal selection criteria. With only this information, the algorithm automatically determined and optimised the selection criteria that enabled the signal and background to be separated with classification accuracies in the range 92-95% in the datasets with S/B=0.25,1,5.

When logical input functions were used, the GEP algorithm developed cut-type selection criteria which were similar to the cuts chosen on the basis of physics considerations and optimised manually. The similarity of these cuts proved that the algorithm worked correctly.

With the addition of common mathematical functions to the list of input functions the GEP algorithm was able to develop more complex selection rules. However, this did not improve the quality of the selection criteria. This indicated that for the problem studied the logical functions are the optimal input functions from which a solution can be developed.

All solutions developed by the GEP algorithm had a good generalisation power. Within the limits of the statistical errors due to the limited size of the dataset, the classification accuracies were equal for both the training and test datasets.

The convergence of the GEP algorithm was tested by the repetition of each analysis 10 times with identical input data. The classification accuracy varied by less than 1% in all cases which proved that the algorithm was not getting stuck at some local minima.

In conclusion, the results obtained with the GEP were very promising and it will be interesting to see how this algorithm evolves to fulfil its full potential.

Bibliography

[1] Particle Data Group, W. M. Yao *et al.*, J. Phys. **G33**, 1 (2006).

[2] P. W. Higgs, Phys. Rev. Lett. **13**, 508 (1964).

[3] A. D. Sakharov, Pisma Zh. Eksp. Teor. Fiz. **5**, 32 (1967).

[4] J. H. Christenson, J. W. Cronin, V. L. Fitch, and R. Turlay, Phys. Rev. Lett. **13**, 138 (1964).

[5] BABAR, B. Aubert *et al.*, Phys. Rev. Lett. **87**, 091801 (2001), hep-ex/0107013.

[6] Belle, K. Abe *et al.*, Phys. Rev. Lett. **87**, 091802 (2001), hep-ex/0107061.

[7] D. J. Gross and F. Wilczek, Phys. Rev. **D8**, 3633 (1973).

[8] H. D. Politzer, Phys. Rept. **14**, 129 (1974).

[9] M. Gell-Mann, Phys. Lett. **8**, 214 (1964).

[10] G. Zweig, CERN-TH-401.

[11] M. Gell-Mann, CTSL-20.

[12] Y. Ne'eman, Nucl. Phys. **26**, 222 (1961).

[13] M. Gell-Mann, Phys. Rev. **125**, 1067 (1962).

[14] H. L. Anderson, E. Fermi, E. A. Long, and D. E. Nagle, Phys. Rev. **85**, 936 (1952).

[15] V. E. Barnes *et al.*, Phys. Rev. Lett. **12**, 204 (1964).

[16] M. Y. Han and Y. Nambu, Phys. Rev. **139**, B1006 (1965).

[17] O. W. Greenberg, Phys. Rev. Lett. **13**, 598 (1964).

[18] JADE, W. Bartel *et al.*, Phys. Lett. **B91**, 142 (1980).

[19] L. G. Landsberg, Lectures at Summer School on Hadron Spectroscopy, College Park, MD, Aug 1992.

[20] N. A. Tornqvist, Z. Phys. **C68**, 647 (1995), hep-ph/9504372.

[21] J. D. Weinstein and N. Isgur, Phys. Rev. **D27**, 588 (1983).

[22] J. D. Weinstein and N. Isgur, Phys. Rev. Lett. **48**, 659 (1982).

[23] R. L. Jaffe, Phys. Rev. **D15**, 267 (1977).

[24] R. L. Jaffe, Phys. Rev. **D15**, 281 (1977).

[25] R. L. Jaffe, Phys. Rev. **D17**, 1444 (1978).

[26] R. L. Jaffe and K. Johnson, Phys. Lett. **B60**, 201 (1976).

[27] L. Maiani, F. Piccinini, A. D. Polosa, and V. Riquer, Phys. Rev. Lett. **93**, 212002 (2004), hep-ph/0407017.

[28] C. J. Morningstar and M. J. Peardon, Phys. Rev. **D60**, 034509 (1999), hep-lat/9901004.

[29] MARK-III, W. Dunwoodie, AIP Conf. Proc. **432**, 753 (1998).

[30] BES, M. Ablikim *et al.*, Phys. Rev. Lett. **96**, 162002 (2006), hep-ex/0602031.

[31] N. Isgur and J. E. Paton, Phys. Rev. **D31**, 2910 (1985).

[32] UKQCD, P. Lacock, C. Michael, P. Boyle, and P. Rowland, Phys. Lett. **B401**, 308 (1997), hep-lat/9611011.

[33] MILC, C. W. Bernard *et al.*, Phys. Rev. **D56**, 7039 (1997), hep-lat/9707008.

[34] T. Barnes, F. E. Close, F. de Viron, and J. Weyers, Nucl. Phys. **B224**, 241 (1983).

[35] E852, D. R. Thompson *et al.*, Phys. Rev. Lett. **79**, 1630 (1997), hep-ex/9705011.

[36] E852, S. U. Chung *et al.*, Phys. Rev. **D60**, 092001 (1999), hep-ex/9902003.

[37] E862, G. S. Adams *et al.*, Phys. Lett. **B657**, 27 (2007), hep-ex/0612062.

[38] E852, G. S. Adams *et al.*, Phys. Rev. Lett. **81**, 5760 (1998).

[39] E852, E. I. Ivanov *et al.*, Phys. Rev. Lett. **86**, 3977 (2001), hep-ex/0101058.

[40] SELEX, A. V. Evdokimov *et al.*, Phys. Rev. Lett. **93**, 242001 (2004), hep-ex/0406045.

[41] L. Maiani, F. Piccinini, A. D. Polosa, and V. Riquer, Phys. Rev. **D70**, 054009 (2004), hep-ph/0407025.

[42] BABAR, B. Aubert *et al.*, (2004), hep-ex/0408087.

[43] E. S. Swanson, Phys. Rept. **429**, 243 (2006), hep-ph/0601110.

[44] S. L. Olsen, (2008), arXiv:0801.1153 [hep-ex].

[45] Belle, S. K. Choi *et al.*, Phys. Rev. Lett. **91**, 262001 (2003), hep-ex/0309032.

[46] K. Abe *et al.*, (2005), hep-ex/0505038.

[47] CDF II, D. E. Acosta *et al.*, Phys. Rev. Lett. **93**, 072001 (2004), hep-ex/0312021.

[48] CDF, A. Abulencia *et al.*, Phys. Rev. Lett. **98**, 132002 (2007), hep-ex/0612053.

[49] D0, V. M. Abazov *et al.*, Phys. Rev. Lett. **93**, 162002 (2004), hep-ex/0405004.

[50] G. Gokhroo *et al.*, Phys. Rev. Lett. **97**, 162002 (2006), hep-ex/0606055.

[51] BABAR, B. Aubert *et al.*, Phys. Rev. **D77**, 011102 (2008), arXiv:0708.1565 [hep-ex].

[52] K. Abe *et al.*, Phys. Rev. Lett. **98**, 082001 (2007), hep-ex/0507019.

[53] Belle, K. Abe *et al.*, Phys. Rev. Lett. **94**, 182002 (2005), hep-ex/0408126.

[54] BaBar, B. Aubert *et al.*, (2007), arXiv:0711.2047 [hep-ex].

[55] K. Abe *et al.*, (2005), hep-ex/0507033.

[56] Belle, K. Abe *et al.*, (2006), hep-ex/0612006.

[57] Belle, K. Abe *et al.*, (2007), arXiv:0708.3812 [hep-ex].

[58] BABAR, B. Aubert *et al.*, Phys. Rev. Lett. **95**, 142001 (2005), hep-ex/0506081.

[59] CLEO, T. E. Coan *et al.*, Phys. Rev. Lett. **96**, 162003 (2006), hep-ex/0602034.

[60] BABAR, B. Aubert *et al.*, Phys. Rev. Lett. **98**, 212001 (2007), hep-ex/0610057.

[61] Belle, X. L. Wang *et al.*, Phys. Rev. Lett. **99**, 142002 (2007), arXiv:0707.3699 [hep-ex].

[62] Belle, K. Abe *et al.*, (2007), arXiv:0708.1790 [hep-ex].

[63] N. A. Tornqvist, Phys. Lett. **B590**, 209 (2004), hep-ph/0402237.

[64] F. E. Close and P. R. Page, Phys. Lett. **B578**, 119 (2004), hep-ph/0309253.

[65] C.-Y. Wong, Phys. Rev. **C69**, 055202 (2004), hep-ph/0311088.

[66] E. Braaten and M. Kusunoki, Phys. Rev. **D69**, 114012 (2004), hep-ph/0402177.

[67] E. S. Swanson, Phys. Lett. **B588**, 189 (2004), hep-ph/0311229.

[68] L. Maiani, A. D. Polosa, and V. Riquer, Phys. Rev. Lett. **99**, 182003 (2007), arXiv:0707.3354 [hep-ph].

[69] L. Maiani, F. Piccinini, A. D. Polosa, and V. Riquer, Phys. Rev. **D71**, 014028 (2005), hep-ph/0412098.

[70] TWQCD, T.-W. Chiu and T.-H. Hsieh, Phys. Lett. **B646**, 95 (2007), hep-ph/0603207.

[71] F. E. Close and P. R. Page, Phys. Lett. **B628**, 215 (2005), hep-ph/0507199.

[72] L. Maiani, V. Riquer, F. Piccinini, and A. D. Polosa, Phys. Rev. **D72**, 031502 (2005), hep-ph/0507062.

[73] Y. S. Kalashnikova and A. V. Nefediev, (2008), arXiv:0801.2036 [hep-ph].

[74] E. Kou and O. Pene, Phys. Lett. **B631**, 164 (2005), hep-ph/0507119.

[75] X. Liu, X.-Q. Zeng, and X.-Q. Li, Phys. Rev. **D72**, 054023 (2005), hep-ph/0507177.

[76] F. J. Llanes-Estrada, Phys. Rev. **D72**, 031503 (2005), hep-ph/0507035.

[77] Z.-G. Wang, Nucl. Phys. **A791**, 106 (2007), hep-ph/0610171.

[78] L. Maiani, A. D. Polosa, and V. Riquer, (2007), arXiv:0708.3997 [hep-ph].

[79] G.-J. Ding, (2007), arXiv:0711.1485 [hep-ph].

[80] E. Braaten and M. Lu, (2007), arXiv:0712.3885 [hep-ph].

[81] J. L. Rosner, Phys. Rev. **D76**, 114002 (2007), arXiv:0708.3496 [hep-ph].

[82] C. Meng and K.-T. Chao, (2007), arXiv:0708.4222 [hep-ph].

[83] D. V. Bugg, (2007), arXiv:0709.1254 [hep-ph].

[84] BABAR, B. Aubert *et al.*, Phys. Rev. **D74**, 091103 (2006), hep-ex/0610018.

[85] BES, and others, (2007), arXiv:0712.1143 [hep-ex].

[86] G.-J. Ding and M.-L. Yan, Phys. Lett. **B650**, 390 (2007), hep-ph/0611319.

[87] Belle, K. F. Chen *et al.*, (2007), arXiv:0710.2577 [hep-ex].

[88] M. Karliner and H. J. Lipkin, (2008), arXiv:0802.0649 [hep-ph].

[89] A. J. G. Hey and R. L. Kelly, Phys. Rept. **96**, 71 (1983).

[90] Particle Data Group, M. Aguilar-Benitez *et al.*, Phys. Lett. **B170**, 1 (1986).

[91] Particle Data Group, G. P. Yost *et al.*, Phys. Lett. **B204**, 1 (1988).

[92] T. H. R. Skyrme, Nucl. Phys. **31**, 556 (1962).

[93] LEPS, N. Muramatsu, Nucl. Phys. **A721**, 112 (2003).

[94] D. Diakonov, V. Petrov, and M. V. Polyakov, Z. Phys. **A359**, 305 (1997), hep-ph/9703373.

[95] A. R. Dzierba, C. A. Meyer, and A. P. Szczepaniak, J. Phys. Conf. Ser. **9**, 192 (2005), hep-ex/0412077.

[96] NA49, C. Alt *et al.*, Phys. Rev. Lett. **92**, 042003 (2004), hep-ex/0310014.

[97] H. G. Fischer and S. Wenig, Eur. Phys. J. **C37**, 133 (2004), hep-ex/0401014.

[98] H1, A. Aktas *et al.*, Phys. Lett. **B588**, 17 (2004), hep-ex/0403017.

[99] ZEUS, S. Chekanov *et al.*, Eur. Phys. J. **C38**, 29 (2004), hep-ex/0409033.

[100] LEPS, T. Nakano *et al.*, Phys. Rev. Lett. **91**, 012002 (2003), hep-ex/0301020.

[101] CLAS, S. Stepanyan *et al.*, Phys. Rev. Lett. **91**, 252001 (2003), hep-ex/0307018.

[102] CLAS, V. Kubarovsky *et al.*, Phys. Rev. Lett. **92**, 032001 (2004), hep-ex/0311046.

[103] SAPHIR, J. Barth *et al.*, Phys. Lett. **B572**, 127 (2003), hep-ex/0307083.

[104] COSY-TOF, M. Abdel-Bary *et al.*, Phys. Lett. **B595**, 127 (2004), hep-ex/0403011.

[105] P. Z. Aslanyan, V. N. Emelyanenko, and G. G. Rikhkvitzkaya, Nucl. Phys. **A755**, 375 (2005), hep-ex/0403044.

[106] SVD, A. Aleev *et al.*, Phys. Atom. Nucl. **68**, 974 (2005), hep-ex/0401024.

[107] DIANA, V. V. Barmin *et al.*, Phys. Atom. Nucl. **66**, 1715 (2003), hep-ex/0304040.

[108] DIANA, V. V. Barmin *et al.*, Phys. Atom. Nucl. **70**, 35 (2007), hep-ex/0603017.

[109] A. E. Asratyan, A. G. Dolgolenko, and M. A. Kubantsev, Phys. Atom. Nucl. **67**, 682 (2004), hep-ex/0309042.

[110] L. Camilleri, Nucl. Phys. Proc. Suppl. **143**, 129 (2005).

[111] NOMAD, O. Samoylov *et al.*, Eur. Phys. J. **C49**, 499 (2007), hep-ex/0612063.

[112] HERMES, A. Airapetian *et al.*, Phys. Lett. **B585**, 213 (2004), hep-ex/0312044.

[113] ZEUS, S. Chekanov *et al.*, Phys. Lett. **B591**, 7 (2004), hep-ex/0403051.

[114] ALEPH, S. Schael *et al.*, Phys. Lett. **B599**, 1 (2004).

[115] BABAR, B. Aubert *et al.*, (2004), hep-ex/0408064.

[116] BABAR, B. Aubert *et al.*, Phys. Rev. **D73**, 091101 (2006), hep-ex/0604006.

[117] J. P. Coleman, *Search for the* $\Theta_5\,(1540)^+$ *strange-pentaquark candidate in* $e^+\,e^-$ *annihilation, hadroproduction and electroproduction with the BaBar detector*, PhD thesis, Liverpool University, 2005.

[118] Belle, K. Abe *et al.*, Phys. Lett. **B632**, 173 (2006), hep-ex/0507014.

[119] M. Z. Wang *et al.*, Phys. Lett. **B617**, 141 (2005), hep-ex/0503047.

[120] BES, J. Z. Bai *et al.*, Phys. Rev. **D70**, 012004 (2004), hep-ex/0402012.

[121] CDF, A. Abulencia *et al.*, Phys. Rev. **D75**, 032003 (2007), hep-ex/0612066.

[122] CDF, D. O. Litvintsev, Nucl. Phys. Proc. Suppl. **142**, 374 (2005), hep-ex/0410024.

[123] CDF, I. V. Gorelov, (2004), hep-ex/0408025.

[124] CLAS, V. Kubarovsky *et al.*, Phys. Rev. Lett. **97**, 102001 (2006), hep-ex/0605001.

[125] CLAS, R. De Vita *et al.*, Phys. Rev. **D74**, 032001 (2006), hep-ex/0606062.

[126] CLAS, S. Niccolai *et al.*, Phys. Rev. Lett. **97**, 032001 (2006), hep-ex/0604047.

[127] CLAS, B. McKinnon *et al.*, Phys. Rev. Lett. **96**, 212001 (2006), hep-ex/0603028.

[128] COMPASS, E. S. Ageev *et al.*, Eur. Phys. J. **C41**, 469 (2005), hep-ex/0503033.

[129] LEP, C.-H. Lin, Prepared for 32nd International Conference on High-Energy Physics (ICHEP 04), Beijing, China, 16-22 Aug 2004.

[130] E690, D. C. Christian *et al.*, Phys. Rev. Lett. **95**, 152001 (2005), hep-ex/0507056.

[131] KEK-PS E522, K. Miwa *et al.*, Phys. Lett. **B635**, 72 (2006), nucl-ex/0601032.

[132] FOCUS, J. M. Link *et al.*, Phys. Lett. **B639**, 604 (2006), hep-ex/0606014.

[133] FOCUS, J. M. Link *et al.*, (2007), arXiv:0708.1010 [hep-ex].

[134] FOCUS, J. M. Link *et al.*, Phys. Lett. **B622**, 229 (2005), hep-ex/0506013.

[135] H1, A. Aktas *et al.*, Phys. Lett. **B639**, 202 (2006), hep-ex/0604056.

[136] HERA-B, K. T. Knopfle, M. Zavertyaev, and T. Zivko, J. Phys. **G30**, S1363 (2004), hep-ex/0403020.

[137] HERA-B, I. Abt *et al.*, Phys. Rev. Lett. **93**, 212003 (2004), hep-ex/0408048.

[138] HERMES, A. Airapetian *et al.*, Phys. Rev. **D71**, 032004 (2005), hep-ex/0412027.

[139] HyperCP, M. J. Longo *et al.*, Phys. Rev. **D70**, 111101 (2004), hep-ex/0410027.

[140] J. Napolitano, J. Cummings, and M. Witkowski, (2004), hep-ex/0412031.

[141] G. De Lellis *et al.*, Nucl. Phys. **B763**, 268 (2007).

[142] S. R. Armstrong, Nucl. Phys. Proc. Suppl. **142**, 364 (2005), hep-ex/0410080.

[143] A. Panzarasa *et al.*, Nucl. Phys. **A779**, 116 (2006).

[144] PHENIX, C. Pinkenburg, J. Phys. **G30**, S1201 (2004), nucl-ex/0404001.

[145] SELEX, A. Blanco-Covarrubias and J. Engelfried, J. Phys. Conf. Ser. **37**, 11 (2006).

[146] SPHINX, V. F. Kurshetsov *et al.*, Phys. Atom. Nucl. **68**, 439 (2005).

[147] SPHINX, Y. M. Antipov *et al.*, Eur. Phys. J. **A21**, 455 (2004), hep-ex/0407026.

[148] WA89, M. I. Adamovich *et al.*, Phys. Rev. **C72**, 055201 (2005), hep-ex/0510013.

[149] WA89, M. I. Adamovich *et al.*, Phys. Rev. **C70**, 022201 (2004), hep-ex/0405042.

[150] ZEUS, S. Chekanov *et al.*, Phys. Lett. **B610**, 212 (2005), hep-ex/0501069.

[151] M. Karliner and H. J. Lipkin, Phys. Lett. **B575**, 249 (2003), hep-ph/0402260.

[152] R. L. Jaffe and F. Wilczek, Phys. Rev. Lett. **91**, 232003 (2003), hep-ph/0307341.

[153] BGR (Bern-Graz-Regensburg), K. Holland and K. J. Juge, Phys. Rev. **D73**, 074505 (2006), hep-lat/0504007.

[154] Birmingham-CERN-Glasgow-Michigan State-Paris, T. Amirzadeh *et al.*, Phys. Lett. **B89**, 125 (1979).

[155] D. Aston *et al.*, Phys. Rev. **D32**, 2270 (1985).

[156] V. M. Karnaukhov, V. I. Moroz, C. Coca, and A. Mihul, Phys. Atom. Nucl. **57**, 790 (1994).

[157] SPHINX, V. F. Kurshetsov and L. G. Landsberg, Nuovo Cim. **A107**, 2441 (1994).

[158] J. Hofmann and M. F. M. Lutz, Nucl. Phys. **A763**, 90 (2005), hep-ph/0507071.

[159] H. J. Lipkin, Phys. Lett. **B195**, 484 (1987).

[160] BABAR, e. Harrison, P. F. and e. Quinn, Helen R., Papers from Workshop on Physics at an Asymmetric B Factory (BaBar Collaboration Meeting), Rome, Italy, 11-14 Nov 1996, Princeton, NJ, 17-20 Mar 1997, Orsay, France, 16-19 Jun 1997 and Pasadena, CA, 22-24 Sep 1997.

[161] W. Kozanecki, Nucl. Instrum. Meth. **A446**, 59 (2000).

[162] BABAR, B. Aubert *et al.*, Nucl. Instrum. Meth. **A479**, 1 (2002), hep-ex/0105044.

[163] BABAR, Babar operations, `http://www.slac.stanford.edu/BFROOT/www/Detector/Operations/Operations.%html`.

[164] M. Bona *et al.*, Report of the tracking efficiency task force, *BABAR* Analysis Document # 324.

[165] T. Allmendinger *et al.*, Tracking efficiency studies in release 12 and 14, *BABAR* Analysis Document # 867.

[166] P. Billoir, Nucl. Instrum. Meth. **A225**, 352 (1984).

[167] `http://www.slac.stanford.edu/BFROOT/www/doc/workbook_kiwi/eventstore/nano%microsummary/Micro/CandLists.html`, `http://www.slac.stanford.edu/BFROOT/www/doc/workbook_kiwi/eventstore/na%nomicrosummary/Micro/CandLists.html`.

[168] W. D. Hulsbergen, Nucl. Instrum. Meth. **A552**, 566 (2005), physics/0503191.

[169] BABAR, A. Roodman, A short description of the lh selectors, `http://www.slac.stanford.edu/BFROOT/www/Physics/Tools/Pid/Hadrons/Descr%iption\%5Fof\%5Fthe\%5FLH\%5Fselectors.html`.

[170] BABAR, Pid likelihood selectors, `http://www.slac.stanford.edu/BFROOT/www/Physics/Tools/Pid/PidOnMc/pidon%mc.html`.

[171] D. J. Lange, Nucl. Instrum. Meth. **A462**, 152 (2001).

[172] T. Sjostrand, (1995), hep-ph/9508391.

[173] GEANT4, S. Agostinelli *et al.*, Nucl. Instrum. Meth. **A506**, 250 (2003).

[174] F. James and M. Roos, Comput. Phys. Commun. **10**, 343 (1975).

[175] BABAR, A. Telvov, Performing particle id on monte carlo, `http://www.slac.stanford.edu/BFROOT/www/Physics/Tools/Pid/PidOnMc/pidon%mc.html`.

[176] A. V. Telnov and A. F. Gritsan, Ks→ $\pi^+\pi^-$ reconstruction efficiency in *BaBar*: Release-10 data vs. sp4 monte carlo, *BaBar* Analysis Document # 677.

[177] BABAR, Tracking efficiency task force [r18/sp8], `http://www.slac.stanford.edu/BFROOT/www/Physics/TrackEfficTaskForce/Tra%ckingTaskForce-recipe.html`.

[178] R. Barlow *et al.*, Recommended statistical procedures for *BaBar*, *BaBar* Analysis Document # 318.

[179] R. Barlow, *Statistics: a Guide to the Use of Statistical Methods in the Physical Sciences* (Wiley, 1989).

[180] R. Gamet and C. Touramanis, Luminosity measurement for the runs 1,2 and 3 data sample using release 12 and sp5 simulation, *BaBar* Analysis Document # 1312.

[181] L. Teodorescu and D. Sherwood, Computer Physics Communications **178**, 409 (2008).

[182] J. H. Holland, *Adaptation in Natural and Artificial Systems* (University of Michigan Press., 1975).

[183] J. H. Koza, *Genetic Programming: On the Programming of the Computers by Means of Natural Selection* (MIT Press, 1992).

[184] H. P. Schwefel, *Numerical Optimization of Computer Models* (John Wiley and Sons, 1981).

[185] M. W. Fogel L. J., Owens A. J., *Numerical Optimization of Computer Models* (John Wiley and Sons, 1966).

[186] C. Ferreira, Complex Syst. **85**, 87 (2001).

[187] C. Ferreira, *Gene Expression Programming: Mathematical Modeling by an Artificial Intelligence* (Angra do Heroismo, 2002).

[188] D. E. Goldberg, *Genetic Algorithms in Search, Optimisation, and Machine Learning* (Addison-Wesley, 1989).

[189] Automatic problem solver version 3, `www.gepsoft.com`.

[190] E. Balea *et al.*, Nucl. Phys. **B150**, 345 (1979).